Application of scanning ion conductance microscopy to localised patch clamp recording from presynaptic terminals

Matthew Caldwell

2012

A thesis submitted to UCL
for the Degree of Doctor of Philosophy

Neuroscience, Physiology and Pharmacology
UCL
Gower Street
London WC1E 6BT

Declaration

I, Matthew Caldwell, confirm that the work presented in this thesis is my own. Where information has been derived from other sources, I confirm that this has been indicated in the thesis.

Abstract

The spatial distribution of ion channels in different subcellular regions is a key determinant of neuronal behaviour. Patch clamp electrophysiology allows characterisation of ion channel activity, but precise localisation is more difficult. This is particularly true for very small, specialised compartments such as synaptic terminals, which are inaccessible by conventional, direct patch recording methods.

Scanning ion conductance microscopy (SICM) generates high resolution topographic images by using a precisely positioned probe to measure ion currents. The development of a new 'hopping' mode allows convoluted neuronal networks to be imaged using the SICM probe. Some details of the implementation of this mode are described. The geometry of SICM pipette tips is examined, and the interaction between the probe and the cell membrane is shown to differ from the standard account.

Application of SICM to localised patch clamp recording has previously been demonstrated in several cell types and here is extended to record from presynaptic sites. Control experiments are performed and a model is introduced to explain how the use of fine-tipped SICM pipettes may give rise to artefacts seen in some of these experiments. The technique is then applied to synaptic boutons in primary cerebellar culture and a number of successful recordings are presented, along with some attempts to combine the advantages of SICM positioning with those of more conventional patch clamp pipettes. Experimental limitations of these approaches are discussed.

Acknowledgements

I am indebted to my supervisors Trevor Smart, Guy Moss and Yuri Korchev for their guidance and support throughout this project. Ian Duguid and James Cottam donated the GAD65-EGFP transgenic mice. Pavel Novak and Andrew Shevchuk contributed detailed information and troubleshooting advice on SICM in general and hopping mode in particular.

None of this work would have been possible without the constant assistance, interest and critical input of everyone in the Moss and Smart groups. I am especially grateful to David Benton and Phil Thomas for patient instruction in the dark arts of electrophysiology, tissue culture and all aspects of laboratory practice. Simon Hughes helped navigate the early forays into the treacherous waters of smart patching with good humour and a breezy disregard for the laws of physics. Samantha Del Linz provided invaluable SICM modelling data, as well as insight and perspective, while Alan Robertson was ever-generous with his formidable knowledge of presynaptic ion channels and receptor pharmacology.

I am grateful to CoMPLEX, both as an institution and as a collection of brilliant individuals, for enabling this research. It remains a beacon of scientific eclecticism in an often fragmentary and over-compartmentalised world.

Finally, I would like to thank my family and loved ones for their patience, understanding and encouragement through all the ups and downs. This thesis is dedicated to my father Peter, who sadly did not live to see it completed; and to Ian, without whom it would not have been.

Contents

Front Matter **2**
Declaration 2
Abstract 3
Acknowledgements 4

Contents **5**

List of Figures **9**

List of Tables **12**

Symbols and Abbreviations **13**

1 Introduction **15**
1.1 Ion channel localisation is important for neuronal behaviour . 15
1.2 Presynaptic NMDA receptors and DPI 17
1.3 Determining functional localisation is difficult 19
1.4 Scanning ion conductance microscopy 21
1.4.1 Principles of scanning probe microscopy 21
1.4.2 Early development and scanning tunnelling microscopy 23
1.4.3 Atomic force microscopy 25
1.4.4 Near-field optical microscopy 27
1.4.5 SICM probe is a microelectrode pipette 29
1.4.6 Hopping mode allows imaging of convoluted cells . . 33
1.5 Smart patch clamp 35

2 Methods and materials **37**
2.1 Tissue culture 37
2.1.1 Glass-bottomed dishes 37

2.1.2 Cell lines . . . 38
2.1.3 Cerebellar neurons . . . 38
2.1.4 Hippocampal neurons . . . 40
2.2 Transfection . . . 41
2.2.1 Calcium phosphate co-precipitation . . . 41
2.2.2 Lipofectamine . . . 42
2.3 Immunocytochemistry . . . 42
2.4 Live cell staining . . . 43
2.4.1 FM loading . . . 43
2.4.2 Cell tracing . . . 45
2.5 Optical microscopy . . . 45
2.5.1 Widefield imaging . . . 45
2.5.2 Confocal imaging . . . 46
2.6 Scanning ion conductance microscopy . . . 47
2.6.1 Equipment . . . 47
2.6.2 Pipettes . . . 49
2.7 Electrophysiology . . . 50
2.7.1 Smart patch clamp protocol . . . 51
2.8 Electron microscopy . . . 52
2.9 Data analysis . . . 53
2.10 Software . . . 54
2.11 Solutions . . . 55
2.12 Materials and suppliers . . . 57
2.12.1 Prepared media and solutions . . . 57
2.12.2 Drugs and peptides . . . 58
2.12.3 Dyes and markers . . . 58
2.12.4 Reagents . . . 58
2.12.5 Consumables and glassware . . . 59
2.12.6 Hardware and testing . . . 59
2.12.7 Suppliers and distributors . . . 60

3 SICM and hopping mode implementation 62
3.1 Mechanics of the hopping protocol . . . 62
3.1.1 Mixed mode . . . 62
3.1.2 Adaptive sampling density . . . 63
3.1.3 Order of sampling . . . 65
3.1.4 Split mode and the PicoCube . . . 66

3.2 Disadvantages of hopping mode . . . 68
3.2.1 Speed . . . 68
3.2.2 Confounding space and time . . . 69
3.3 Testing . . . 71
3.3.1 Using the hopping probe to check system stability . . 71
3.3.2 Testing lateral consistency . . . 74
3.4 Imaging control samples . . . 76
3.5 Imaging neurons . . . 78

4 SICM pipette tip geometry and approach characteristics 84
4.1 Estimating pipette tip geometry . . . 84
4.1.1 Geometry measured by scanning electron microscopy 84
4.1.2 Proportional wall thickness is not conserved . . . 88
4.1.3 Comparing estimated tip geometry with resistance . . 90
4.2 Surface detection . . . 93
4.2.1 Implications for SICM imaging and smart patching . . 97

5 Consequences of pipette size for patch clamp recording 100
5.1 Recording from control cells . . . 100
5.1.1 Rates of success and failure . . . 101
5.1.2 Accuracy of conductance estimates . . . 104
5.1.3 Qualitative variation . . . 106
5.1.4 Vesicle formation might explain current behaviour . . 111
5.2 Modelling current behaviour in the presence of a vesicle . . . 113
5.2.1 Analytical description of the model . . . 113
5.2.2 Numerical implementation . . . 115
5.2.3 Inclusion of stochastic effects . . . 122
5.2.4 Multiple channel openings . . . 125
5.2.5 Effect of filtering on peak current detection . . . 126
5.2.6 Estimating the conductance between the vesicle and the cell . . . 129
5.2.7 Stochastic behaviour of the internal conductance . . . 134
5.2.8 Relationship of vesicle volume to pipette geometry . . 137
5.3 Discussion . . . 139

6 Application of smart patch to cerebellar terminals 142
6.1 GAD65-EGFP cerebellar culture . . . 142
6.2 Smart patching in cerebellar culture . . . 147

6.2.1 Experimental variations . . . 147
6.2.2 Rates of success and failure . . . 149
6.2.3 Proportion of empty recordings . . . 150
6.2.4 Smart bouton recording #1 . . . 150
6.2.5 Smart recordings #2–#8 . . . 156
6.2.6 Smart recording #9 . . . 166
6.3 Recording with large pipettes . . . 168
6.4 Discussion of results . . . 177

7 Discussion **180**
7.1 Applicability of the techniques . . . 180
7.1.1 Hopping mode SICM allows imaging of neuronal networks . . . 180
7.1.2 Limitations of patching with SICM pipettes . . . 181
7.1.3 Localised patching is possible with larger pipettes using SICM positioning . . . 182
7.2 Presynaptic patching . . . 183
7.3 Future work . . . 185

Appendices **186**

A Software and source code **187**
A.1 IMG file format . . . 187
A.2 IonView . . . 189
A.3 Vesicle model . . . 190
A.4 Other source code . . . 191

References **192**

List of Figures

1.1 Principle of scanning probe microscopy 21
1.2 Simple schematic of SICM 28
1.3 Current-distance approach curve 29
1.4 Hopping mode SICM 34

2.1 Plating pattern for cerebellar neuronal cultures 39
2.2 Main component connections for the SICM system 47

3.1 Adaptive sampling based on local roughness 64
3.2 Interpolation of sample data 65
3.3 Boustrophedon scanning pattern 66
3.4 Split mode hopping 67
3.5 Linear drift manifests in non-linear steps 70
3.6 'Stairstep' artefacts in simulated scans 70
3.7 Measuring relative positional stability by hopping 72
3.8 Effect of pressure on current and position 74
3.9 Optical tests of lateral consistency 75
3.10 Artefacts in scan of CD grooves 77
3.11 Better scan of CD grooves 78
3.12 Scan of TGG01 AFM target 79
3.13 Early attempts at scanning neurons 80
3.14 Hippocampal culture scanned at different compression levels . . 81
3.15 Zooming into a low-resolution scan 83

4.1 Scanning electron microscopy of pipette tip geometry 85
4.2 Tip measurements for Sutter #77 and Intracel #95 pipettes 87
4.3 Estimated exterior profile of Sutter #77 tip 87
4.4 OD:ID ratio is not conserved at tip 88

4.5 Model interior profile of Sutter #77 tip 89
4.6 Variation of head resistance with segment lengths l_t and l_b 92
4.7 Variation of head resistance with tip radius 93
4.8 Approach to a hard surface agrees with finite element model . . 94
4.9 Approach curves to HEK soma obtained in hopping mode 96
4.10 Single approach to HEK soma 98

5.1 Outcome proportions of HEK-bslo experiments 102
5.2 Variation of conductance estimates with tip resistance 105
5.3 Good quality HEK-bslo recording 107
5.4 Empty HEK-bslo recording 107
5.5 Currents decaying after channel opening 108
5.6 Current decay after multiple openings 109
5.7 Visible change of recording state 110
5.8 Poor recording 111
5.9 Vesicle formation in the pipette tip 112
5.10 Schematic of compartments in the vesicle model 113
5.11 Baseline current time course of the vesicle model 116
5.12 Single parameter variations of the vesicle model 117
5.13 Voltage drop and spatial effects 119
5.14 Varying P_{open} in the vesicle model 121
5.15 More realistic kinetics with noise and filtering 124
5.16 Multiple channel openings 127
5.17 Vesicle volume affects detectability of artefacts 128
5.18 Effect of vesicle on conductance estimates 130
5.19 Estimated γ_2 decreases with pipette resistance 131
5.20 Relationship between internal channel resistance and pipette resistance 132
5.21 Variation of pore resistance with geometry 134
5.22 Varying P_{open} and β for the internal conductance 135
5.23 Stochastic openings on both sides of the vesicle 136
5.24 Vesicle geometry is constrained by pipette tip 138
5.25 Vesicle volume as a function of length 139
5.26 Resistance distribution by experimental outcome 140

6.1 Fluorescent protein expression in GAD65-EGFP cerebellar slice . 143
6.2 Antibody staining for parvalbumin and VIAAT 144

6.3 Antibody staining for Tau 145
6.4 Antibody staining for MAP2 146
6.5 Locations of some empty recordings 151
6.6 Location of smart recording #1 152
6.7 Smart recording #1 154
6.8 Peak current–voltage relation changes over time 155
6.9 Possible voltage dependence of burst rate 156
6.10 Smart recording #2 158
6.11 Smart recording #3 159
6.12 Smart recording #4 160
6.13 Smart recording #5 161
6.14 Smart recording #6 162
6.15 Smart recording #7 163
6.16 Smart recording #8 164
6.17 Summary plots of smart bouton recording results 165
6.18 Smart recording #9 167
6.19 Location of big pipette recording #1 170
6.20 Big pipette recording #1 171
6.21 Location of big pipette recording #2 172
6.22 Big pipette recording #2 174
6.23 Possible maxi-anion channel activity from smart recording #4 . . 176
6.24 Possible maxi-anion channel activity from smart recording #9 . . 177

List of Tables

2.1 Antibody combinations and dilutions 43
2.2 Capillary glasses for pulling SICM pipettes 49
2.3 P-2000 pipette puller programs 49

4.1 Tip geometry measurements made from scanning electron micrographs 86

5.1 Experimental outcomes using large and small pipettes 102
5.2 Parameter values for traces in Figure 5.12 116

6.1 Outcomes of smart patching in cerebellar culture 149
6.2 Summary results for smart cell-attached bouton recordings . . . 157
6.3 Outcomes of large pipette patching in cerebellar culture 168

A.1 Important fields in the IMG file header 188

Symbols and Abbreviations

$m \backsim n$	Median (m) and median absolute deviation (n)
$m \pm n$	Mean (m) and standard deviation (n)
$[n]$	Solution recipe n in the solutions table (§2.11)
[X*]	Concentration of ion X*
$[X^*]_\mathbf{i}$	Intracellular concentration of ion X*
$[X^*]_\mathbf{o}$	Extracellular concentration of ion X*
ADC	Analogue to digital converter
AFM	Atomic force microscopy
AIS	Axon initial segment
AP	Action potential
AP5	(2*R*)-amino-5-phosphonopentanoate, a competitive blocker of the glutamate binding site of NMDARs
CD-R	Recordable compact disc
CICR	Calcium-induced calcium release
DAC	Digital to analogue converter
DIV	Days *in vitro*
DPI	Depolarisation-induced potentiation of inhibition
DSE	Depolarisation-induced suppression of excitation
DSI	Depolarisation-induced suppression of inhibition
DSP	Digital signal processor
EDTA	Ethylenediaminetetraacetic acid
EGFP	Enhanced green fluorescent protein
GABA	γ-aminobutyric acid
GAD65	Glutamic acid decarboxylase (65 kDa isoform)
GAD65-EGFP	Transgenic mouse strain expressing EGFP under control of the promoter for GAD65

HEK	Human embryonic kidney cell line
HVA	High voltage amplifier (for piezo control)
ID	Inner diameter
IN	Interneuron, especially cerebellar basket or stellate cell
IN-PC	Interneuron–Purkinje cell synapse
IPSC	Inhibitory post-synaptic current
MAD	Median absolute deviation
MAP2	Microtubule associated protein 2
NMDA	*N*-methyl D-aspartate
NMDAR	NMDA receptor: ionotropic glutamate receptor sensitive to the artificial agonist NMDA
OD	Outer diameter
OLS	Ordinary least-squares regression
OTF	Optical transfer function
PC	Cerebellar Purkinje cell
PSF	Point spread function
RP	Rebound potentiation
SEM	Scanning electron microscopy
SICM	Scanning ion conductance microscopy
SNOM	Scanning near-field optical microscopy
SPM	Scanning probe microscopy
STM	Scanning tunnelling microscopy
TTX	Tetrodotoxin
VDAC	Voltage-dependent anion channel
VGCC	Voltage-gated Ca^{2+} channel
VIAAT	Vesicular inhibitory amino acid transporter

Chapter 1

Introduction

1.1 Ion channel localisation is important for neuronal behaviour

Ion channels are protein complexes that selectively mediate the ability of different ions to pass across the otherwise largely impermeable plasma membrane of a cell. Such mediation was recognised as important for cell function long before the channel proteins themselves were known to exist or could be identified and characterised. Notably, Hodgkin and Huxley (1952a, b, c) showed that changes in permeability to different ion species underlay the electrical excitability of cells such as nerves and muscle fibres. The changes were gated by the membrane potential, which was itself modified by the resulting ion fluxes, to produce a propagating voltage pulse, the action potential (AP).

Other channel gating mechanisms were subsequently identified. Many processes already described in terms of the binding of agonists to receptors turned out to produce their effects through the opening of ion channels. In some cases there are additional signalling steps in between the ('metabotropic') receptor and the channel, while in other cases the ('ionotropic') receptor is an intrinsic feature of the channel itself. Among other biological functions, the latter type of 'ligand-gated' channels provide the basis of fast signal transmission at chemical synapses: neurotransmitters released from presynaptic sites, known as terminals or boutons, bind to post-synaptic receptors and cause the channels to open.

The computational behaviour of a neuron is to a significant extent the product of such channel activity. Ion flows through open channels at many synapses combine to produce polarisation shifts that can initiate or inhibit AP firing. Neuronal output is thus an integrative function of the synaptic inputs. Broadly, channels selectively permeable to anions, in particular Cl^-, are inhibitory, while those allowing passage of cations such as K^+ are excitatory, though this depends on the ionic conditions inside and outside the cell and the resulting net flow across the membrane.

As the mechanisms of selective permeability came to be better understood, additional roles for channels in the modulation of cellular chemistry and signal transduction were discovered. Many cellular processes are critically sensitive to local ionic concentrations, and in particular to Ca^{2+} ions, which are normally maintained at a very low level inside cells. Changes in $[Ca^{2+}]_i$ can trigger complex cascades of biochemical activity. These changes commonly arise from ions moving through Ca^{2+}-permeable ion channels, either entering from the extracellular space or being released from intracellular stores. An important case is the process of vesicular fusion by which neurotransmitter release occurs from presynaptic boutons, which is driven by Ca^{2+} influx through voltage-gated calcium channels (VGCCs) opened by an invading AP (Katz and Miledi 1965; Miledi 1973; Hille 2001).

Ion flow through channels is 'passive', in the sense that the ions diffuse down their electrochemical gradients. The movements are thermodynamically favourable and do not require additional energy expenditure. As a result they can be very efficient and fast—at least at short range. Because ions are driven by diffusion, the effective speed falls with distance. Moreover, the passage of just a small number of ions can cause a significant change in concentration over a small volume, whereas the effect on a larger volume would be negligible. The impact of individual channel openings thus exhibits an important spatial dependence.

Cells in general are not spatially uniform, and neurons in particular are highly asymmetric, exhibiting a great deal of structural differentiation with many specialised subcompartments. Distribution of proteins and other functional molecules is similarly varied, and this is certainly true of ion channels. Different neuronal compartments may express completely distinct channel populations. The composition of these populations substantially determines the local electrochemical behaviour, and thus how each compartment con-

tributes to the signalling and computational activity of the neuron.

A textbook example of the importance of ion channel localisation for function is the dense clustering of Na^+ and K^+ channels at the nodes of Ranvier in myelinated axons (Shrager 1989; Rasband et al. 1998). These allow for the rapid depolarisation necessary for fast passive signal propagation through the insulated internodal regions. Similarly, a high density of Na^+ channels localised to the axon initial segment (AIS) is required for the initiation of action potentials (Moore et al. 1983; Clark et al. 2005; Kole et al. 2008).

Channel localisation is also crucial for synaptic communication: the speed and fidelity of neurotransmission depends on the close proximity of VGCCs in the presynaptic terminal to the vesicular release machinery that is triggered by their Ca^{2+} influx (Llinás et al. 1995; Zucker and Regehr 2002). On the receiving side, the nature and strength of the response is determined by which specific receptors are present in the post-synaptic membrane.

Channel populations are often dynamic, changing with development and with factors such as environmental stress or, importantly, neuronal activity. By locally varying the number and type of channels present, for example on the receiving side of a synapse, the relative contribution of a neuronal input can be altered. This is one mechanism for 'synaptic plasticity', the tuning of the strength of neural connections, which is believed to underpin memory and learning.

Because of the many aspects of neuronal function that depend crucially on the localisation of different ion channel types, it is important to be able to determine that localisation in order to understand how it contributes to the larger scale processes by which the brain and nervous system work.

1.2 Presynaptic NMDA receptors and DPI

As a specific example of neuronal behaviour for which channel localisation is significant, we consider a form of synaptic plasticity occurring in the cerebellar cortex, at synapses from molecular-layer basket and stellate interneurons onto Purkinje cells (IN-PC synapses). These inhibitory synapses help to tune the principal outputs of the cerebellar cortex and play an important role in motor coordination.

Following repeated depolarisation of the post-synaptic Purkinje cell, there is a short-term decrease in presynaptic release probability, lasting $\sim$ 1 min and termed depolarisation-induced suppression of inhibition (DSI) (Llano et al. 1991; Vincent et al. 1992; Pitler and Alger 1992; Marty and Llano 1995), followed by a more sustained increase in release probability lasting $\sim$ 8 min or even longer, termed depolarisation-induced potentiation of inhibition (DPI) (Duguid and Smart 2004). Both of these presynaptic effects have been demonstrated to be mediated by retrograde messengers released post-synaptically in response to elevated $[Ca^{2+}]_i$. The latter elevation also drives a functional up-regulation of post-synaptic receptors for the neurotransmitter γ-aminobutyric acid (GABA). This underlies a third component of plasticity, rebound potentiation (RP), which manifests as a long term increase in the amplitude of inhibitory post-synaptic currents (IPSCs) (Llano et al. 1991; Kano et al. 1992).

In the case of DSI, the messenger is the endocannabinoid 2–arachidonoylglycerol (2-AG), acting on presynaptic CB1 receptors (Diana et al. 2002; Yoshida et al. 2002; Szabo et al. 2006). For DPI, the messenger is glutamate or a glutamate analogue acting on glutamate receptors sensitive to the artificial agonist *N*-methyl-D-aspartate (NMDA) (Duguid and Smart 2004). Evidence for the involvement of NMDA receptors (NMDARs) is strong: DPI can be mimicked by NMDA application, and abolished by NMDAR blockers such as AP5. However, the location of these receptors is contentious.

There are several lines of evidence suggesting that they must be located on or very close to the presynaptic terminal itself (Glitsch and Marty 1999; Huang and Bordey 2004; Duguid and Smart 2004). In particular, the effect occurs in a dissociated 'nerve-bouton' preparation in which only the attached terminals are present (Duguid et al. 2007). However, there is also contradictory evidence from calcium imaging experiments. The latter is important because the proposed mechanism for DPI relies on Ca^{2+} entry through the NMDARs, amplified by calcium-induced calcium release (CICR) from intracellular stores, to effect the release probability change. Christie and Jahr (2008) failed to observe such Ca^{2+} entry, although they did artificially deplete the internal stores.

Antibody staining experiments have shown that NMDAR subunits are expressed at the interneuron terminals, but functional ion channels were not directly observed (Duguid and Smart 2004).

1.3 Determining functional localisation is difficult

The previous example illustrates the difficulty of proving that specific functional ion channels are located in given subcellular compartments. For many proteins, antibody staining for known epitopes is sufficient to demonstrate localisation. However, ion channels are multimers whose components must be correctly coassembled and inserted into the membrane in order to function. Immunocytochemical evidence of the presence of the necessary subunits in a given compartment is suggestive but not conclusive.

Since a channel's function is to pass an ion current, that functionality is best demonstrated by electrophysiological measurement of the current. This is commonly achieved using the patch clamp technique (Neher and Sakmann 1976; Hamill et al. 1981; Sakmann and Neher 1995). This allows direct recording of ion flows using a glass microelectrode attached to the cell membrane via a very high resistance 'gigaseal'. In 'single channel' configurations (cell-attached, inside-out and outside-out), the recording is taken from an isolated patch of membrane, typically containing only a small number of channels. In the 'whole cell' configuration, the recording is of the aggregate activity of channels in the whole membrane of the cell (or a spatially well-defined subcompartment).

Channel identity is usually established pharmacologically, based on differing channel sensitivities to agonists and blockers. In most cases, pharmacological approaches involve aggregate or secondary effects and provide only indirect evidence for localisation. Single channel configurations, by definition, record from an isolated region of membrane, but the practicalities of obtaining the seal mean that patches are most often made on the cell soma and scope for more defined positioning is limited. Nevertheless, because of the importance of channel localisation, numerous attempts have been made to patch from smaller structures, with some success.

One approach has been the use of severely reduced preparations in which the tissue is homogenised and the membrane regions of interest separated. In some cases the detached compartments may be used directly, as with the 'neurosecretosomes' isolated from peptide-secreting nerve terminals in rat neurohypophysis (Nordmann et al. 1982; Lemos and Nowycky 1989; Lim et al. 1990). Alternatively, synaptic membrane fractions can be isolated from lysed homogenate by centrifugation in a density gradient (Jones and Matus

1974; Dunkley et al. 1986). Recordings can then be made from reconstituted 'giant synaptosomes' (Rahamimoff et al. 1988; Edry-Schiller et al. 1991) or from vesicles formed in a membrane multilayer on a coverslip (Hall et al. 1993).

Patching from subcompartments of intact neurons has most often been attempted in dendrites, which are usually larger and more accessible than axons and boutons. The process has particularly been applied to the apical dendrites of large central neurons such as neocortical pyramidal cells (Stuart et al. 1993; Stuart and Sakmann 1994) and cerebellar Purkinje cells (Stuart and Häusser 1994; Martina et al. 2003). Some experimenters have specifically isolated patched dendrites from the soma by compression with a micropipette, in order to better distinguish differences in channel population (Delmas et al. 2000).

Patching of presynaptic terminals has usually been limited to atypically large, specialised cases such as the calyx of Held (Forsythe 1994; Borst et al. 1995; Borst and Sakmann 1996; Forsythe et al. 1998; Wang et al. 2008). A few notable successes have been achieved in smaller terminals where the anatomy provides a favourable density of defined synapses surrounding the soma, such as mossy fibre boutons onto cerebellar granule cells (Rancz et al. 2007) and the pericellular basket and pinceau structure of cerebellar basket interneurons (Southan and Robertson 1998; Southan et al. 2000; Southan and Robertson 2000). The latter experiments patched the same IN-PC terminals where the presence of NMDARs is expected to give rise to DPI. No evidence of NMDARs was reported in those recordings, but the pharmacology was not tailored to reveal such channels.

Putative cerebellar interneuron terminals have also been patched in a culture in which chronic exposure to NMDA has produced enlarged varicosities, and in this case NMDARs were found in a proportion of single channel patches (Fiszman et al. 2005). This again supports the contention that presynaptic NMDARs are in fact present, although the non-physiological preparation leaves the relevance open to question. Furthermore, the recordings were obtained from very young cultures of 3–4 days *in vitro* (DIV), before synapses would be expected to form. The GAD65-EGFP transgenic mouse line used for these experiments is the same as for those described later in this thesis (Chapter 6).

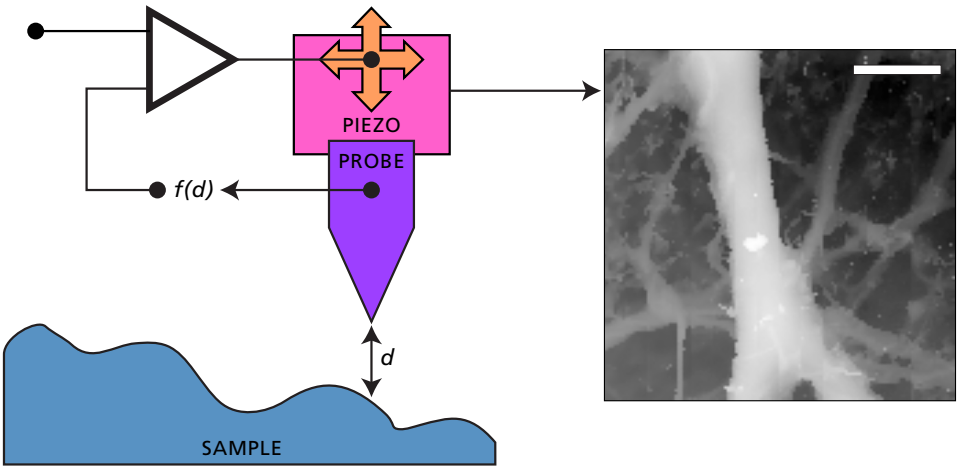

Figure 1.1: Principle of scanning probe microscopy. The probe produces a signal, $f(d)$, as a function of its distance d from the sample. The probe is scanned across the sample via a piezoelectric positioning system, using feedback to maintain $f(d)$ at a constant value. The height of the piezo at each lateral position is used to build a topographic map of the sample. (Example image shows an SICM scan of processes in primary hippocampal culture. Height is represented by greyscale value, with lighter points higher. Scale bar 5 µm.)

1.4 Scanning ion conductance microscopy

1.4.1 Principles of scanning probe microscopy

Scanning ion conductance microscopy (SICM) belongs to a family of imaging techniques known collectively as scanning probe microscopies (SPMs) (Wickramasinghe 1990, 2000). While these techniques vary significantly in their details and application, they derive from a common principle for measuring topography, illustrated in Figure 1.1. A probe is used that generates some signal that varies with proximity. This probe is moved over the surface of a target sample using a high precision positioning system. By monitoring the relationship between the detected signal and the position, a topographic map of the surface can be built up.

The exact distance dependence is not necessarily known for a given probe. Moreover, the range over which a useful signal change occurs may be much shorter than the height variation in the sample. Thus, the signal level alone

often cannot be used as an absolute measure of the sample surface topography. Instead, a feedback system is used to maintain the signal at some predetermined level, known as the reference value or (particularly in the context of SICM) the *set point*. Assuming the surface–probe distance is the dominant factor affecting the signal, a constant signal level will correspond to a constant separation. The probe position can then be taken as measuring the surface position, with some unknown but approximately constant offset.

The operation of such a system depends crucially on the ability to adjust the relative positions of the probe and sample with high accuracy. This is done using piezoelectric actuators, based on materials such as lead zirconate titanate (PZT) that exhibit small but very consistent mechanical deformation in response to an applied electric field (Jaffe et al. 1971). The increasing sophistication of such devices since the 1970s has been instrumental in the development of viable SPM techniques.

SPM does not involve far-field image formation and so is not subject to the Abbe diffraction limit of optical microscopy. Instead, limits to resolution arise from the need for positional stability and from the nature of the proximity-detecting signal. The physical process that generates the signal is an interaction between the probe and the surface, and this can never be perfectly one-dimensional. Instead, there is a space over which the interaction is effective, and the signal integrates over that space. The effect is analogous to an optical transfer function, with a convolution between the spatial properties of the sample and those of the detector (Stark et al. 2005; Vázquez et al. 2006). This places a bound on the imaging resolution of the probe. For most SPM techniques, a key determinant of the interaction volume is the geometry of the probe tip. Broadly, a larger tip will integrate over a larger area of surface and thus be less able to distinguish small details.

The concept of 'resolution' is well defined in classical optics (Born and Wolf 1999; Hecht 2002), but in SPM there is not a single accepted definition. The term is often used quite loosely, and claims of achieving a particular resolution may not be directly comparable. Three useful ways of formalising resolution are:

Detection How small a particle can the system detect in an otherwise empty field?

Accuracy Given that a lone particle or boundary has been detected, how precisely can its size or location be determined?

Separability Given two detectable particles, how far apart do they need to be before they can be resolved as distinct objects rather than appearing as a single peak?

The last sense is closest to that usually used for optical imaging. Despite some attempts to define resolution this way for SPM (Rheinlaender and Schäffer 2009; Del Linz 2011), the first definition predominates in common usage.

Whereas in a classic widefield optical system all points are imaged in parallel, SPM techniques measure only one location at a time and require the probe and sample to be physically moved relative to one another before the next location can be measured. As a result, image acquisition can be substantially slower than with optical microscopy, and there is a risk that time-varying properties of the sample can confound spatial measurements. This is particularly important for living biological samples, which are often highly dynamic.

1.4.2 Early development and scanning tunnelling microscopy

A number of precursors to modern SPM can be identified in the literature. The basis of what would become scanning near-field optical microscopy (§1.4.4) was first proposed more than 80 years ago (Synge 1928), and the same author also conceived the use of piezoelectric positioning for what we would now call raster scanning (Synge 1932). A similar near-field optical aperture approach was suggested by O'Keefe (1956), though he concluded that the positioning precision required was unattainable with the technology of the time. The principle was eventually demonstrated on a coarser scale by Ash and Nicholls (1972), using 3 cm microwaves with a 1.5 mm aperture. The same year saw publication of the 'Topografiner', an instrument for non-contact measurement of surface topography by field emission, using piezo positioning (Young et al. 1972). In retrospect it is clear this was an SPM in all but name.

Nevertheless, the first 'true' SPM technique is generally held to be scanning tunnelling microscopy (STM) (Binnig et al. 1982a, b; Binnig and Rohrer

1983). Here, the probe is a metal electrode with a very sharp tip, and the sample—which must be a conductor—acts as a second electrode. The two are separated by an insulating gap, often a vacuum, and a bias voltage applied between them. The proximity-sensitive property is the ability of an electrical current to pass across the gap by quantum tunnelling. This occurs only at extremely short distances, and drops off approximately exponentially, losing an order of magnitude with each additional 0.1 nm.

Probe–sample separations for STM are < 1 nm, and the effective tip size can be as small as a single atom. Achievable resolution is on the order of 0.01 nm in the axial direction and 0.1 nm laterally, sufficient to distinguish individual atoms in a crystal lattice (Binnig et al. 1983). Scan sizes are typically in the 10–100 nm square range, though up to 1 µm is possible.

Because of the very short working distance, STM is usually limited to very flat specimens and its main areas of application have been in material and surface science. Images are often obtained in vacuum, although STM can also be performed in gaseous and even liquid environments, at some cost to stability and resolution (Coleman et al. 1985; Liu et al. 1986; Drake et al. 1986; Sonnenfeld and Hansma 1986; Schneir and Hansma 1987). The requirement for conductive, immobile, clean and flat samples means that STM is of relatively limited biological application. Some success was achieved with fixed biological macromolecules (Lindsay and Barris 1988; Smithson et al. 1991; Youngquist et al. 1991) and cell fragments (Baró et al. 1985; Dahn et al. 1988). Non-conductive samples have been imaged by applying a conductive coating (Amrein et al. 1988), and STM has also been used with freeze-fracture replicas of biological membranes (Zasadzinski et al. 1988). However, the use of STM in biology was largely overshadowed by the rise of atomic force microscopy (§1.4.3).

STM was immediately recognised as a remarkable breakthrough—Binnig and Rohrer were awarded the Nobel Prize for Physics in 1986—and it paved the way for a rapid explosion of other SPM techniques. Only a few will be discussed here, but there are many others: Wickramasinghe (2000) lists 23 varieties as just “some of the main ones.”

1.4.3 Atomic force microscopy

Probably the most widely used form of SPM is atomic force microscopy (AFM), which addresses the problem of scanning non-conductive samples. The initial implementation (Binnig et al. 1986) took a cue from an engineering instrumentation technique, stylus profilometry (Engel and Millis 1982; Teague et al. 1982; Guenther et al. 1984), to introduce a cantilever spring as a conductive proxy for the sample itself. The cantilever makes contact with the sample via a sharp conical or pyramidal tip. As the cantilever is scanned across the sample, height variations push or pull it away from its set position, and this deformation is detected by an STM probe located above the cantilever. The position of the combined STM-tip/cantilever assembly is then adjusted by the piezos to maintain a constant deformation and track the sample surface. Later developments replaced STM with laser interferometry as a more robust means of detecting cantilever movement (Martin et al. 1987; Meyer and Amer 1988; Alexander et al. 1989).

With the cantilever tip exerting a force on the sample during scanning, this 'contact mode' AFM can damage or distort the measured surface. This is particularly problematic for biological samples, which are often softer than the probe itself. An alternative 'non-contact' mode was devised whereby the cantilever tip is vibrated at high frequency very close to the sample and changes in the vibrational amplitude due to van der Waals interactions with the atoms of the surface are used to determine proximity (Martin et al. 1987; Anselmetti et al. 1994).

A third form, the 'tapping' or 'intermittent contact' mode, also uses a vibrating tip but touches the sample at the bottom of the oscillation. This allows contact-dependent force measurements to be made while reducing the risk of sample damage during scanning (Zhong et al. 1993; Hansma et al. 1993, 1994; Putman et al. 1994; Fritz et al. 1995; Hansma 2001). In a further variation, 'jumping mode', the probe is moved away from the sample during lateral movements and only brought into close proximity at each point of measurement (de Pablo et al. 1998; Moreno-Herrero et al. 2004; Sotres et al. 2007).

Typical tip sizes for normal topographic scanning with AFM are of the order 10 nm. Non-contact working distance is in the range 0.3–5 nm (Martin et al. 1987; Anselmetti et al. 1994). The achievable resolution depends very

much on the experimental conditions. For most practical purposes, a lateral resolution of 1 nm and axial of 0.1 nm are probably the limit (Möller et al. 1999; Muller and Engel 2007), although atomic resolution can be achieved under ideal conditions (Albrecht and Quate 1987; Ohnesorge and Binnig 1993; Giessibl 1995, 2005).

AFM has been used extensively in biological applications, not only for fixed biomolecules (Worcester et al. 1988; Butt et al. 1990; Bustamante et al. 1992; Lacapère et al. 1992) and cell fragments (Blackford et al. 1991), but also for dynamic samples in more physiological environments. Biochemical processes such as blood clotting (Drake et al. 1989), DNA degradation (Bezanilla et al. 1994), DNA transcription (Kasas et al. 1997) and ion channel oligomerisation (Hoogenboom et al. 2007) have been observed in isolated preparations. Imaging of live cells has been performed on numerous cell types, including glia (Henderson et al. 1992; Parpura et al. 1993), epithelial cells (Oberleithner et al. 1995; Schrot et al. 2005), cardiomyocytes (Shroff et al. 1995; Geisse et al. 2009) and cancer cells (Braet et al. 1998; Cross et al. 2007).

Because AFM monitors the force acting between the sample and the cantilever, it is not limited to the measurement of superficial topography. Mechanical properties of the sample can be tested by varying the degree of force applied (Radmacher et al. 1992, 1994; Muller and Engel 2007). Such 'force spectroscopic' approaches can detect subsurface structures such as the stiffer cytoskeleton beneath a cell's soft plasma membrane (Henderson et al. 1992; Chang et al. 1993). Varying the applied force has also been used to test mechanosensitivity (Gil et al. 1999; Langer et al. 2000). If the tip is bonded to a single protein or other biomolecule and the force monitored as the tip is moved away, elastic properties can be measured and corresponding conformational transitions deduced (Rief et al. 1997a, b; Oesterhelt et al. 2000; Bippes et al. 2005). By functionalising the tip with chemical or biological agents a wide range of interactions can be examined in relation to local topography, including the binding of ligands to receptors (Moy et al. 1994; Chtcheglova et al. 2008) and of antibodies to their epitopes (Hinterdorfer et al. 1996; Dufrêne and Hinterdorfer 2007).

Improvements in speed and operating conditions continue to be made and new twists on AFM continue to be devised. Commercial AFM systems are available from numerous vendors. It is unlikely to be challenged as the most mainstream SPM technique in the near future.

1.4.4 Near-field optical microscopy

The early near-field optical work by Synge, O'Keefe and others mentioned above (§1.4.2) was further developed in the light of the advances made in STM by Lewis and co-workers (Lewis et al. 1983, 1984; Betzig et al. 1986; Harootunian et al. 1986) and by Pohl and co-workers (Pohl et al. 1984; Fischer 1985; Fischer et al. 1988), to become scanning near-field optical microscopy (SNOM, also abbreviated NSOM). This uses light as its primary signal, detecting the near-field non-radiative evanescent wave at the surface of a specimen. This wave is not subject to the diffraction limit, but is detectable only at very short distances. The detector is usually a fine glass probe coated with a thin layer of metal, into which a sub-wavelength aperture has been introduced, although aperture-less probes have also been used (Fischer and Pohl 1989; Gleyzes et al. 1995; Bachelot et al. 1997).

The light carries information about the optical properties of the specimen in the vicinity of the aperture. In general, it is these optical properties that are of interest and they may vary independently of the topography, so the light signal itself cannot be used as a proximity measure. Instead, a second proximity signal is used to maintain the aperture at working distance from the surface. Early SNOM used a contact or tunnelled current for surface detection, but modern implementations more commonly use shear stress of the optical probe measured by changes in resonant vibration (Betzig et al. 1992), or else a simultaneous AFM signal (Shalom et al. 1992; Toledo-Crow et al. 1992; Muramatsu et al. 1995a, b; Baida et al. 1998). As will be discussed in the next section (§1.4.5), SICM has also been used as the proximity detector for SNOM.

The resolution of SNOM is limited by the size of the detector aperture, which in turn is limited by the thickness and absorption characteristics of the opaque material in which it is formed. Typical apertures are 50–100 nm in diameter, with a working distance of the order 10 nm and lateral resolution 10–50 nm. Since SNOM does not measure topography directly, axial resolution is instead limited by whatever mechanism is used for proximity detection. For shear stress measurement, this is of the order 10 nm (Durkan and Shvets 1995; Gheber et al. 1998).

SNOM can be used in combination with fluorescent probes (Harootunian et al. 1986) and in biologically-relevant environments (Betzig et al. 1986;

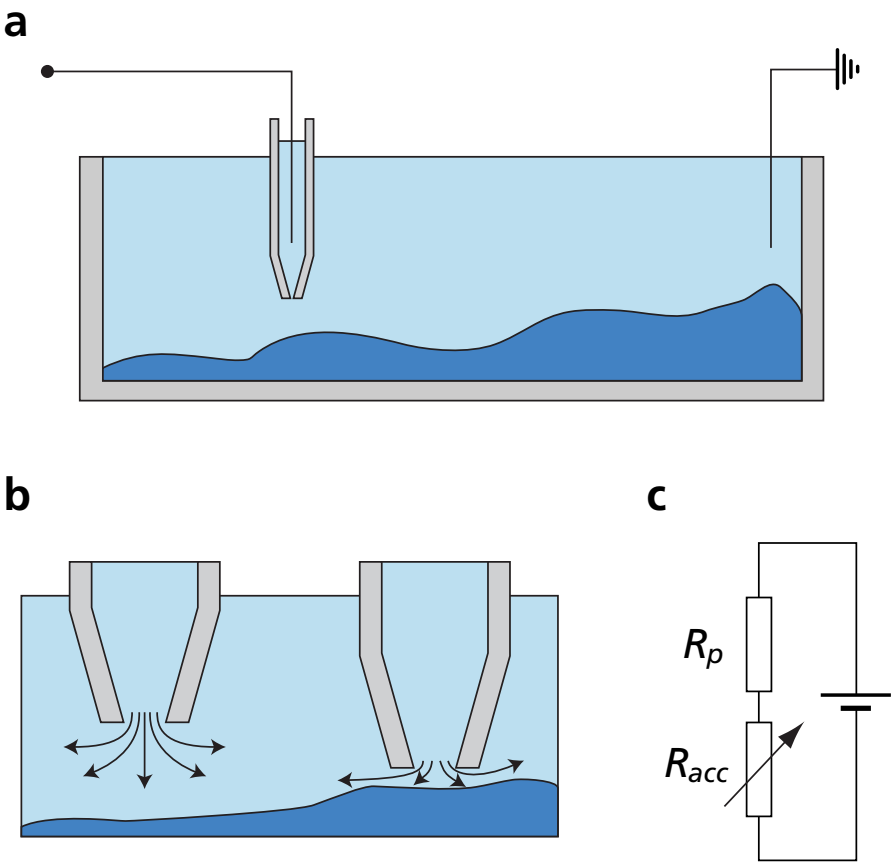

Figure 1.2: Simple schematic of SICM. **a** The SICM probe is a glass microelectrode pipette filled with electrolyte. An ion current flows when a voltage is applied. **b** When the tip is far from the sample surface, access resistance is negligible compared to the resistance of the pipette. When the tip is close, current flow is occluded and access resistance increases significantly. **c** Simple equivalent circuit. Pipette resistance R_p is constant, while access resistance R_{acc} varies with proximity. An applied voltage V will give rise to a current $I = \frac{V}{R_p + R_{acc}}$, which is used as the feedback signal.

Muramatsu et al. 1995b; Gheber et al. 1998). Because of the short working distance it is better suited to imaging flat samples (Betzig and Trautman 1992), although this depends very much on the proximity detection mechanism used.

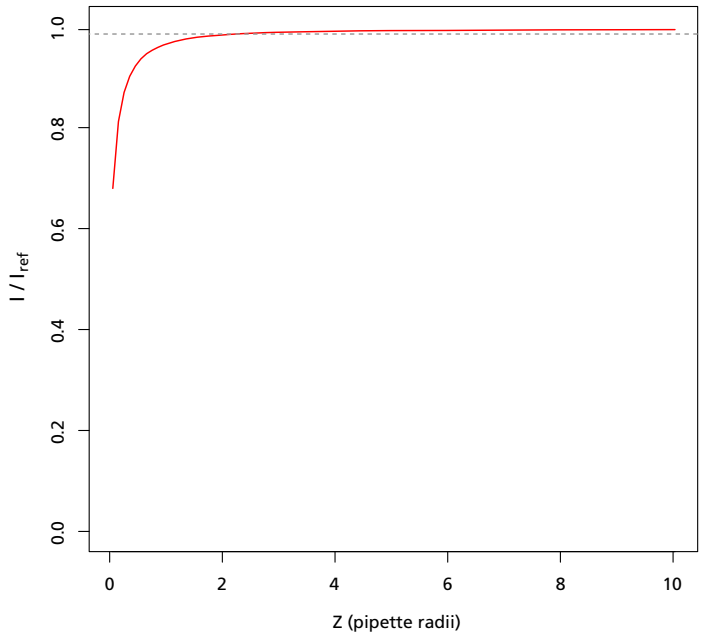

Figure 1.3: Current-distance approach curve. When the probe is far from the surface, current is approximately constant, determined by R_p. When separation is on the scale of the pipette tip radius, R_{acc} becomes significant and current varies steeply with distance. Dotted line indicates a SICM detection set point of 1%. (Curve based on finite element model data by Samantha Del Linz.)

1.4.5 SICM probe is a microelectrode pipette

In the case of SICM (Hansma et al. 1989), the proximity probe is a glass microelectrode pipette, similar to those used for electrophysiological recording (Sakmann and Neher 1983a; Brown and Flaming 1986). The pipette is filled with electrolyte solution and its tip immersed in an electrolyte bath. An Ag/AgCl wire is threaded into the pipette, and a second Ag/AgCl electrode is placed in the bath. When a bias voltage is applied between these electrodes an electric current flows, carried by the ions in the solution. If the probe is brought close to a relatively-insulating surface the ion flow is occluded and the current falls (Figure 1.2a–b). This reduction in conductance provides the proximity-sensing signal.

The situation can be represented by the simple equivalent circuit shown in Figure 1.2c. A constant resistance R_p is contributed by the pipette regardless of position, while a variable external access resistance R_{acc} depends on how freely ions can flow between the bath electrode and the tip. The total resistance $R = R_{acc} + R_p$ is dominated by R_p when the probe is far from the surface, but R_{acc} increases steeply when the tip is close. The result is a current–distance relation or *approach curve* such as that shown in Figure 1.3.

The exact shape of the approach curve depends on various experimental factors, but the dominant one in most realistic scenarios is the pipette tip geometry (Adenle and Fitzgerald 2005; Edwards et al. 2009; Rheinlaender and Schäffer 2009; Del Linz 2011). Typically, R_{acc} is approximately constant until the separation is of the order $2 - 4\times$ the pipette tip inner radius, r_i. This sets an upper bound on the working distance.

The corresponding lower bound depends on the nature of the sample and the size and shape of the tip. If both the sample and the tip were perfectly flat, then the tip could be operated arbitrarily close to the surface, but this is never the case in practice (and if it were, there would be little value in scanning the topography). Even small deviations from uniformity in either tip or sample will mean that the current never completely shuts down even when the tip is actually in contact with the surface. To maintain one of the major advantages of SICM, the working distance needs to be great enough to ensure that contact does not occur.

Working distance is specified indirectly in terms of the set point, S, at which the SICM is operated. This defines the current level I_s at which the pipette tip is the desired height above the surface. S is usually expressed as a percentage reduction relative to the baseline current, I_{ref}, measured when the probe is very far away from the surface:

$$S = \left(1 - \frac{I_s}{I_{ref}}\right) \times 100 \tag{1.1}$$

The choice of set point affects the behaviour of the scan. Because the approach curve is shallow in its upper range, at low set points the current is relatively insensitive to positional variation. The axial resolution is therefore poorer, and there is also a higher susceptibility to false detection due to current noise. Conversely, at high set points the approach curve is much

steeper and so axial resolution is better and less susceptible to current noise, but the working distance is very short, increasing the risk of collision.

In most cases, especially for fragile biological samples that can be easily damaged by contact with the pipette tip, collision avoidance is prioritised and a low set point (0.2–0.5%) is used. This corresponds to a working distance of the order $2r_i$.

Lateral resolution also depends on tip geometry. Finite element models have been used to examine resolution in the strict 'separability' sense mentioned in §1.4.1, predicting that objects can be distinguished at a distance of $3r_i$ (Rheinlaender and Schäffer 2009) or $2r_i$ (Del Linz 2011). The analogy with optical resolution is imperfect, however, as the system is non-linear. Resolution is affected by the topography of the sample and by the choice of set point. Experimental evidence suggests that individual features smaller than r_i can be detected (Gorelik et al. 2003; Shevchuk et al. 2006; Novak et al. 2009).

Tip size and shape vary with glass type and the parameters used to pull the pipette. In general, the tip geometry may be quite uncertain. The value of r_i is not known for a given pipette used for scanning, but instead estimated by comparing its measured R_p with resistance and size ranges obtained previously from similar pipettes. It is common to use pipettes with an expected range for r_i of 25–150 nm, and thus a working distance of 50–300 nm and a resolution of some tens of nm. Some data for the geometry of pipettes used for work in this thesis is presented in Chapter 4.

SICM is designed to operate in saline solutions at physiologically-relevant temperatures, so is ideally suited to imaging live biological specimens. This was noted by Hansma et al. (1989) in their original publication of the method, and subsequently developed by Korchev et al. (1997a, b, 2000a). The technique has been used to observe phenomena as diverse as volume changes in cultured cardiomyocytes, epithelial and cancer cells (Korchev et al. 2000a; Zhang et al. 2005; Gorelik et al. 2006) and neurons and oligodendrocytes (Happel et al. 2003; Mann et al. 2006; Novak et al. 2009), membrane dynamics in epithelial cells, organ of Corti and spermatozoa (Gorelik et al. 2003; Shevchuk et al. 2006) and vesicular fusion in bovine chromaffin cells (Shin and Gillis 2006).

SICM is well suited for use in tandem with other imaging methods, in par-

ticular optical microscopy. The SICM scan head is commonly placed on the stage of an inverted microscope so that targets can be viewed from below for visual identification and alignment. Standard biological fluorescence techniques have been applied in this configuration, including the use of calcium-sensitive dyes to study mechanosensitive responses in human sensory neurons (Sanchez et al. 2007) and FM 1-43 staining to identify presynaptic terminals in neuronal cultures (Novak et al. 2009).

Two special cases of combining optical microscopy with SICM are worth noting.

As mentioned in §1.4.4, SICM has been used in conjunction with SNOM, providing the surface detection component to generate topographic data and maintain the SNOM detector at an appropriate working distance (Korchev et al. 2000c; Mannelquist et al. 2001, 2002). SICM is well suited to this purpose because its glass microelectrode probe can be used as a light guide; indeed, a similar microelectrode is often used as the SNOM probe even in the absence of SICM (Betzig et al. 1986; Harootunian et al. 1986). Alternatively, a fluorescent dye inside the SICM pipette can be excited to provide the SNOM light source (Bruckbauer et al. 2002a; Rothery et al. 2003). A hybrid SICM-SNOM system has been used with a calcium sensitive fluorophore to observe Ca^{2+} fluctuations and relate them to volume changes in cardiomyocytes (Shevchuk et al. 2001).

Surface confocal microscopy (Gorelik et al. 2002b; Shevchuk et al. 2008) also combines SICM with optical microscopy at the scanned surface, but in this case using far-field confocal imaging. The light is gathered by a normal microscope objective on the underside of the sample. The SICM pipette is held in a fixed position relative to the objective, such that the confocal spot is aligned just in front of the tip. All piezo movement acts on the sample, which is scanned relative to the pipette, shifting in the Z direction to maintain the set point. Thus, the detected surface is always moved to coincide with the confocal volume. For each topographic location recorded, the optical intensity is also captured as a pixel in a confocal image. Whereas an ordinary confocal microscope scans a planar slice through the sample, the surface confocal image represents an optical map of the whole upper surface. This is particularly useful for studying fluorescent-tagged membrane proteins or surface interactions such as virus particle entry.

The SICM pipette can also be used for controlled electrophoretic deposition of charged molecules from the pipette solution to the scanned sample (Bruckbauer et al. 2002b, 2003; Ying et al. 2005; Rodolfa et al. 2006). In a biological context this has been used to deliver fluorescent markers to proteins in the cell membrane, enabling the observation of diffusion properties in different compartments (Bruckbauer et al. 2007), to control chimeric *E. coli* flagellar motors via Na^+ concentration (Piper et al. 2008), and for application of permeant ions to study ion channel localisation via a concurrently-recorded electrophysiological response (Korchev et al. 2000b).

1.4.6 Hopping mode allows imaging of convoluted cells

In the original continuous feedback configuration of SICM, the probe is kept at a constant distance from the sample as it scans back and forth. However, the region of sensitivity is highly localised at the probe tip and there is very limited scope for detection at the side. If the surface varies steeply, the probe may collide with the sample laterally before it can be detected (Figure 1.4a). This is particularly problematic for biological samples such as networks of neurons, which may have very convoluted and even overhanging topography.

To minimise this, several groups have developed variations of an alternative scanning mode, similar to the jumping mode of AFM. Referred to variously as pulse (Mann et al. 2002), backstep (Happel et al. 2003; Mann et al. 2006; Happel and Dietzel 2009), standing approach (Yamada et al. 2005; Takahashi et al. 2006, 2010), vertical approach (Rheinlaender et al. 2011) or (the term we will use here) hopping mode (Novak et al. 2009; Klenerman et al. 2011), this involves retracting the probe to a safe distance from the surface before lateral movement occurs (Figure 1.4b). The approach curve is then measured from scratch at each raster position. This has the additional benefit of constantly resampling the baseline current I_{ref}, which can otherwise be subject to drift due to bath evaporation or other environmental factors, requiring more complex modulation modes to compensate (Shevchuk et al. 2001; Pastré et al. 2001; Mannelquist et al. 2001).

One consequence of moving from a constant-distance scan to a sequence of quasi-independent approaches is that the location of each sample can be somewhat decoupled from that of the previous one. This allows the lateral

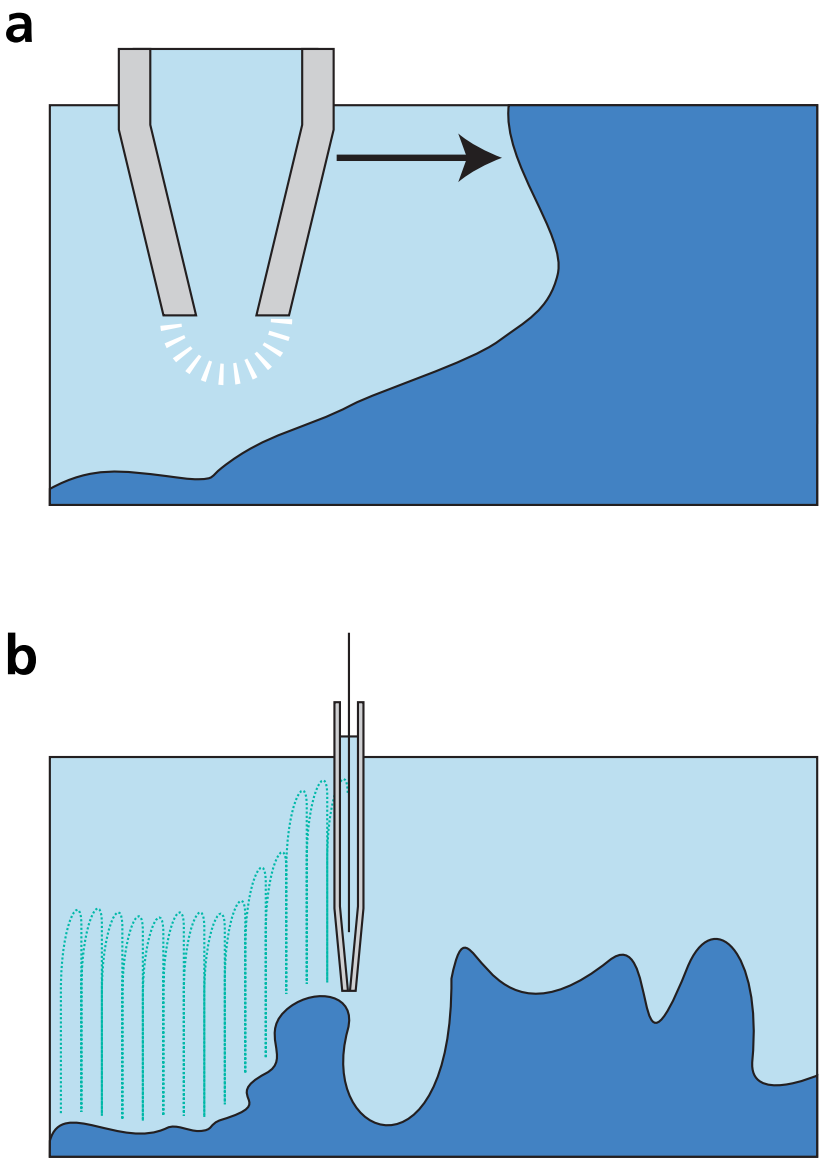

Figure 1.4: Hopping mode SICM. **a** Proximity detection is largely localised to the pipette tip and there is limited lateral sensitivity. If the probe is moved sideways while close to the surface of a steeply-varying sample, collisions may occur. **b** In hopping mode, the probe is withdrawn to a safe distance before lateral movement, and each location is measured by an independent vertical approach. This allows steeper and more convoluted samples to be imaged safely.

sampling rate to be varied adaptively according to some estimator of the local information density in different areas, which can significantly improve the speed of image acquisition (Novak et al. 2009).

For the work described in this thesis, hopping mode has been used more or less exclusively. Some issues concerning its implementation and deployment are discussed in Chapter 3.

1.5 Smart patch clamp

The SICM pipette is similar in form to the microelectrodes used for electrophysiology and—with some important limitations—it is possible to make patch clamp recordings with it (Gu et al. 2002; Gorelik et al. 2002a). Topographic data from a preliminary scan is used to guide the pipette placement, allowing the recording to be localised to a known position on the cell. This is termed the scanning patch clamp or 'smart' patch technique.

Given the importance of ion channel localisation discussed above (§1.1), smart patching would seem to promise considerable benefits. However, it has not been widely adopted and remains an immature technique. Despite some early proof-of-concept recordings from sensory neurons (Gorelik et al. 2002a), meaningful results using this method have largely been restricted to A6 kidney epithelial cells (Gorelik et al. 2005) and cardiomyocytes (Dutta et al. 2008). This can in part be attributed to lack of access to the underlying SICM technology, which only recently started to become commercially available. However, there are also some limitations that may have had an impact on uptake.

Because of the dependence of imaging resolution on tip size, SICM pipettes are usually very fine by patch clamp standards, akin to the 'sharp' electrodes used for intracellular recording (Brown and Flaming 1986). Such pipettes are not ideal for most patch clamp purposes, and in particular are unsuited for use in the whole cell configuration. The small aperture means it is not usually possible to break the membrane, and the high series resistance and restricted access to the interior would in any case make it difficult to maintain voltage clamp. Smart patching is thus generally restricted to recording single channel currents in the cell-attached and inside-out configurations. This limits the pharmacological interventions that can be used and, because

of the small area of membrane sampled in these configurations, can significantly increase the number of experiments that must be performed in order to obtain meaningful results.

The use of topographic imaging to identify location means that the technique can only be applied to the very uppermost surface of a sample. This excludes a wide range of productive investigations in tissue slices, where the outer surfaces tend to consist of dead cells and debris. Cells must be stable, clean and well isolated, so the technique is mainly applicable in sparse dissociated cultures.

Some further complications associated with smart patching are discussed below in Chapter 5.

Despite these limitations, the smart patch technique remains an attractive approach to questions of functional localisation of ion channels. The remainder of this thesis will describe exploratory studies using SICM applied to mammalian central neurons, with particular reference to identifying NMDA receptors in the presynaptic terminals of cerebellar interneurons (§1.2).

Chapter 2

Methods and materials

Note: all solution recipes are given in §2.11. Solution numbers are referred to in the text using square brackets: [1]. *Full details for commercially-prepared solutions referred to by an abbreviation such as HBSS are listed in §2.12.*

2.1 Tissue culture

2.1.1 Glass-bottomed dishes

Many experiments required the use of high magnification, short working distance fluorescence optics, so cell samples had frequently to be prepared on thin glass. The scanning ion conductance microscope (§2.6) is unsuited to use with loose cover slips, so instead glass-bottomed petri dishes were constructed.

12 mm ⌀ holes were drilled in the centre of the bottom of Nunc 35 mm plastic petri dishes, and any burring buffed away. The dishes were then soaked in 70% v/v ethanol to remove any grease picked up during drilling, and dried overnight in air at 60°C. 18 mm × 18 mm square, thickness 0 glass cover slips were washed with 100% ethanol and flamed, then attached to the bottom of the drilled dishes using a thin layer of freshly-mixed Sylgard elastomer. The liquid elastomer spread to seal the interface, but left the accessible region of the glass free for specimen preparation. The dishes were again stored at 60°C for at least 24 hours to allow the Sylgard to cure.

After curing, dishes were sterilised by UV illumination for at least 30 min.

Unless otherwise specified below, dishes were incubated overnight with borate-buffered poly-D-lysine [1] to provide a growth substrate. This solution was then removed and the glass washed 3× with tissue culture grade H_2O. The dishes were allowed to dry thoroughly before use.

2.1.2 Cell lines

Human embryonic kidney 293 (HEK 293) line cells were maintained as described by Thomas and Smart (2005).

Cells were grown in Nunc T25 air-filtered cell culture flasks in DMEM-based growth medium [2], incubated at 37°C in 95% air/5% CO_2. On reaching 85%–95% confluence, cells were passaged as follows.

Growth medium was discarded and the flask gently rinsed with HBSS to remove serum. Cells were then incubated in 2 ml Trypsin-EDTA for 2 min at room temperature. 10 ml of growth medium was added to stop the trypsin, and cells dislodged by striking the side of the flask. Cells were dissociated by trituration with a 10 ml plastic pipette. The suspension was transferred to a 15 ml centrifuge tube and spun for 3 min at 180×g. The supernatant was discarded and the cell pellet resuspended in 10 ml growth medium. This suspension was diluted 1:10–1:20 with fresh growth medium and transferred to new flasks to regrow, or plated for experimentation.

HEK cells were typically used for experiments not requiring high-magnification optics, so were usually plated onto Nunc 35 mm Nunclon-coated plastic petri dishes. In those cases for which glass-bottomed dishes were required, a poly-D-lysine substrate was applied as described in §2.1.1.

Cells were transfected, if required, after 12–24 hours, and used for experiments up to 72 hours after plating.

HEK lines were discarded after 25–30 passages.

2.1.3 Cerebellar neurons

Mixed cell-type cultures were prepared from the cerebella of GAD65-EGFP transgenic mice as follows.

Figure 2.1: Cerebellar neuronal cultures in glass-bottomed dishes. Suspension was plated in an X shape to maximise the lower-density periphery.

A mouse pup at post-natal day 5–8 was killed by cervical dislocation according to the Animals (Scientific Procedures) Act 1986, and the cerebellum quickly removed into ice-cold dissection medium [3]. Meninges and extraneous tissue were removed and the isolated cerebellum manually chopped into small fragments. The fragments were transferred to trypsin solution [4] and incubated for 25 min at 37°C in 95% air/5% CO_2.

The trypsinised fragments were transferred to a 15 ml centrifuge tube and washed in plating medium [5], then in serum-based growth medium [6] to inhibit the action of any remaining trypsin, then twice more in plating medium, leaving them in a final volume of 3 ml. The tissue was gently triturated in this solution 12× with each of three glass Pasteur pipettes fire-polished to decreasing sizes (roughly full bore, $\frac{1}{2}$ and $\frac{1}{4}$). The solution was then left at room temperature for 2–3 min to allow undissociated tissue to settle out.

The cell suspension was transferred to another tube and centrifuged for 5 min at 500×g. The supernatant was discarded and the cells resuspended in another 5 ml of plating medium.

This suspension was plated onto poly-D-lysine coated dishes (§2.1.1), ap-

plying 50 µl to each cover slip in an X shape using a 200 µl Gilson pipette (Figure 2.1). The cells were incubated for 2–3 hours at 37°C in 95% air/5% CO_2. The dishes were then topped up with 2 ml of plating medium per dish and returned to the incubator overnight.

After 24 hours incubation, the plating medium was removed and replaced with 2 ml per dish of the serum-based cerebellar growth medium [6]. The cells were incubated in this new medium for 2 days. The medium was then replaced with growth medium containing anti-mitotics [7] (1:500 dilution, final concentration 2 µM) and incubated for a further 3–4 hours. The anti-mitotic medium was then removed and replaced with fresh growth medium [6], and the cells returned to the incubator once again.

After this, cultures were fed once a week by replacing 1 ml of the old medium with fresh growth medium.

Cultures were used for experiments from DIV 8–24.

2.1.4 Hippocampal neurons

A Sprague-Dawley rat pup at post-natal day 4 was killed by cervical dislocated and decapitated. The brain was swiftly removed into ice-cold dissection medium [3], hemisected and sliced into 500 µm coronal sections with a MacIlwain tissue chopper.

The hippocampal CA1 and CA3 regions were dissected from the slices and transferred to trypsin solution [4]. This was incubated at 37°C in 95% air/5% CO_2 for 30 min, then the trypsin solution was replaced with fresh and the incubation continued for another 30 min.

The tissue was then transferred to a 15 ml centrifuge tube, washed 3× in bovine albumin-containing medium [8] to inhibit the trypsin, and left in a final volume of 2 ml. The tissue was gently triturated 10× with each of three glass Pasteur pipettes, fire-polished to decreasing sizes. After each pipette, the tube was centrifuged very briefly ($\sim$ 5 s) to settle the tissue fragments, and the supernatant and dissociated cells were transferred to a second tube. The hippocampal fragments were then resuspended in another 2 ml of medium for the next round of trituration.

The accumulated supernatant was centrifuged at 110×g for 5 min, and the cells resuspended in 3 ml of serum-based plating medium [9]. Approximately 250 µl per dish of this cell suspension was plated onto glass-bottomed dishes that had been first prepared as described in §2.1.1 and then washed with newborn calf serum 30 min before use. The dishes were incubated for 2–3 hours at 37°C in 95% air/5% CO_2, then topped up with 2 ml of plating medium per dish and returned to the incubator overnight.

After 24 hours, the plating medium was removed and replaced with 2 ml per dish of serum-free growth medium [10]. The dishes were returned to the incubator.

Cultures were used for experiments at DIV 8–14.

2.2 Transfection

Unless otherwise noted in relation to a particular experiment, neuronal cultures were transfected via the calcium phosphate method (§2.2.1), while HEK cells were transfected using Lipofectamine (§2.2.2).

Quantities given in protocols are for transfecting a single 35 mm petri dish of cells.

2.2.1 Calcium phosphate co-precipitation

15 µl of 2× HEPES-buffered saline (HBS) [11] was placed in a 1.5 ml microcentrifuge tube. 1–2 µg of cDNA plasmid was placed in a second tube, together with sufficient TE buffer to bring the volume to 13.5 µl.

1.5 µl of 2.5 M $CaCl_2$ solution was added dropwise to the second tube and swirled to mix. This DNA-$CaCl_2$ mixture was then added dropwise to the HBS and vortexed for 2–3 seconds.

The combined precipitate solution was incubated in darkness for 30 min, vortexing briefly every 5 min.

100 µl of 5× kynurenic acid [12] was combined with 400 µl of unsupplemented Neurobasal medium, pre-warmed to 37°C. The cells' usual growth medium was discarded and this kynurenic acid medium substituted.

The precipitate solution was added to the cells dropwise, and they were incubated for 30 min at 37°C in 95% air/5% CO_2.

The precipitate was removed from the cells, which were then washed 2× in warmed unsupplemented Neurobasal. Finally the dishes were refilled with the appropriate growth medium for the cells, and returned to the incubator.

Expression was usually observed after 2–3 days.

2.2.2 Lipofectamine

The proprietary chemical transfection agent Lipofectamine 2000 was used in accordance with the manufacturers instructions, as follows.

50 µl of Opti-MEM was placed in each of two 1.5 ml microcentrifuge tubes. 2 µl of Lipofectamine was added to one tube, while 2 µg of cDNA plasmid was added to the other. Both tubes were incubated at room temperature for 5 min.

The contents of the two tubes were combined and incubated at room temperature for a further 30 min.

The mixture was then added dropwise directly to the growth medium of the cells, which were then returned to the incubator.

Expression was typically observed after 12–24 hours.

2.3 Immunocytochemistry

The primary and secondary antibodies and dilutions listed in Table 2.1 were used with the following staining protocol.

Growth medium was removed from cells and they were washed 3× in phosphate-buffered saline (PBS) [13]. Cells were then fixed in paraformaldehyde [14] for 10 min at room temperature.

The fixing solution was removed and the cells rehydrated for 5 min in PBS, quenched for 10 min with ammonium chloride [15], and washed again in PBS for 5 min.

The fixed cells were then incubated for 1 hour in antibody blocking solution (ABS) [16] to permeabilise and reduce non-specific binding.

Primary	Source	Dilution	Secondary	Source	Dilution
Parvalbumin (mouse)	Sigma	1:200	TRITC goat anti-mouse	Jackson	1:50
VIAAT (rabbit)	Bruno Gasnier	1:1000	Cy5 goat anti-rabbit	Jackson	1:100
Tau (mouse)	Cell Signalling	1:200	TRITC goat anti-mouse	Jackson	1:50
MAP2 (chicken)	Abcam	1:100	Cy5 goat anti-chicken	Jackson	1:100

Table 2.1: Antibody combinations and dilutions used in immunofluorescence experiments.

Primary antibodies were suspended in ABS at an appropriate dilution and the cells incubated in this mixture for 1 hour.

Cells were washed 3× with Tween-20 [17].

Conjugated secondary antibodies were suspended in ABS at an appropriate dilution, and the cells again incubated for 1 hour.

Cells were again washed 3× with Tween-20 and finally left in plain PBS for imaging.

Widefield imaging was sometimes done immediately, but confocal imaging was typically performed the following day. In the latter case, stained cells were refrigerated overnight at 4 °C and protected from light prior to viewing.

2.4 Live cell staining

2.4.1 FM loading

Acute staining with the styryl dyes SynaptoRed (FM 4-64) and SynaptoGreen (FM 1-43) was used to identify regions of membrane internalisation associated with synaptic vesicle cycling. Choice of dye was dependent on what

other markers were being imaged in parallel. Staining protocols were the same for both dyes.

Two distinct loading approaches were used. Most commonly, exocytosis was stimulated by membrane depolarisation. This was effective but prone to damaging fragile cells. Where cell health was problematic, an alternative procedure was used to load via spontaneous activity only.

Stimulated loading

Growth medium was discarded and the cells washed 3–4× with the relevant external solution ([18] or [20]). The solution was then replaced with a high $[K^+]$ equivalent ([19] or [21]) containing the FM dye (5 µM) along with glutamate channel blockers (D-AP5 50 µM, DNQX 5 µM) to reduce excitotoxicity during depolarisation. Cells were incubated in this solution at room temperature for 1–2 min.

The solution was then replaced with the normal external solution ([18] or [20]) containing just the FM dye (5 µM), and the cells incubated at room temperature for a further 8–10 min. This "completion" step allowed time for vesicles exocytosed during depolarisation to be internalised again, taking the FM dye with them.

The FM solution was removed and the cells incubated for 1.5–2 min in external solution containing Advasep-7 (1 mM), to quench uninternalised dye and reduce background fluorescence. This in turn was removed and the cells washed for 3–4 min in normal external solution.

A second 1.5–2 min Advasep-7 incubation followed, and two further 3–4 minute external solution washes. The cells were then ready to view.

Spontaneous loading

1–2 µl of FM dye stock (10 mM in H_2O; final concentration 5–10 µM) was added directly to the $\sim$ 2 ml growth medium in which cells were maintained, and the dish returned to the incubator. Cells were incubated for a further 1–2 hours at 37°C in 95% air/5% CO_2.

The growth medium was removed, and cells washed 3–4× in external solution before being used for experimentation.

2.4.2 Cell tracing

For some experiments using large (10–20 MΩ) pipettes, 20 µM Alexa Fluor 568 was included in the pipette filler solution to confirm the location of recordings.

After a patch recording was obtained in the cell-attached configuration, a suction pulse was applied to rupture the membrane and switch to the whole-cell configuration. The membrane potential was held at −60 mV and the dye allowed to diffuse into the cell.

When successful, the dye was normally clearly visible to widefield epifluorescence imaging within 1–2 min.

2.5 Optical microscopy

2.5.1 Widefield imaging

The majority of optical microscopy was performed using a Nikon Eclipse TE-2000U inverted microscope equipped with the following Nikon objective lenses: Ph1 ADL 10× 0.25 NA (∞/1.2 WD 0.17); Ph2 ADL Plan Fluor ELWD 40× 0.6 NA (∞/0–2 WD 3.7–2.7); Plan Fluor 60× 0.85 NA (∞/0.11–0.23 WD 0.30); Plan 100× 1.25 NA oil immersion (∞/0.17 WD 0.17).

Brightfield illumination was provided by a Nikon T-DH 100W Dia-illuminator. The corresponding phase contrast apparatus had to be removed due to the space constraints of using the optical system in conjunction with the scanning ion conductance microscope (§2.6), so only the lamp and condenser were used.

Epifluorescence excitation was provided by a Nikon Intensilight C-HGFI source. A Semrock Brightline FITC filter set (465–495/505/515–555) was used to image FITC, GFP, EGFP and FM 1-43 dyes. FM 4-64, Alexa Fluor 568 and TRITC were imaged using a Chroma Technology HQ545/30x excitation filter and Q570LP dichroic, together with a Semrock EdgeBasic 580nm long pass emission filter.

Additional optical microscopy was performed using a Leica DM-IL inverted microscope equipped with the following Leica objectives: C Plan 10× 0.22

NA (∞/−/↑ 506075); C plan 40× 0.50 NA (∞/1.1 506149); HCX APO 100× 1.30 NA oil immersion (∞/0.17/D 506156).

As with the Nikon, phase contrast illumination was precluded by the space requirements of the SICM. Instead, brightfield illumination was provided by a bright white LED spotlight attached to a custom-built mount.

Epifluorescence excitation was provided by a Leica EL 6000 external mercury arc source. A Leica N2.1 filter set (515–560/580/590LP) was used for viewing FM 4-64, TRITC and Alexa Fluor 568. A Leica I3 filter set (450–490/510/515LP) was used for viewing FITC, GFP, EGFP, and FM 1-43. (Note that this set could not be used to image samples simultaneously labelled with red markers such as FM 4-64, because of the risk of crosstalk via the long pass emission filter.)

Watec WAT-120N cameras were attached to both microscopes, via the TE-2000U front light port and the DM-IL side camera port with standard C-mounts. The camera video signals were digitised by MatrixVision mvDelta capture boards mounted in Dell Optiplex 745 and 960 PCs running Microsoft Windows XP. Images were captured to the lossless PNG format using the VLC application in conjunction with MatrixVision's DirectShow drivers.

2.5.2 Confocal imaging

Confocal microscopy was performed using a Zeiss LSM 510 Meta laser scanning confocal system. The base microscope was an Axioscop FS equipped with the following Zeiss objective lenses: Plan-Neofluar 10× 0.3 NA (∞/0.17 WD 0.17); Achroplan 40× 0.8 NA water immersion (∞/0 440090); Achroplan 63× 0.95 NA water immersion (∞/0 440330).

Fluorescence excitation was provided by Argon (477, 488, 514 and 548 nm) and Helium-Neon (543 and 633 nm) lasers. Emissions were filtered using the inbuilt 505–530 bandpass filter for FITC, GFP, EGFP, FM 1-43; 560–615 bandpass for TRITC and FM 4-64; and Meta head 650 long pass for Cy5.

The microscope was controlled using Zeiss LSM 510 Version 3.0 SP3 software running on a Fujitsu Siemens 600 PC with Microsoft Windows 2000 SP2. Images were captured to LSM format, with metadata stored in an accompanying MDB database.

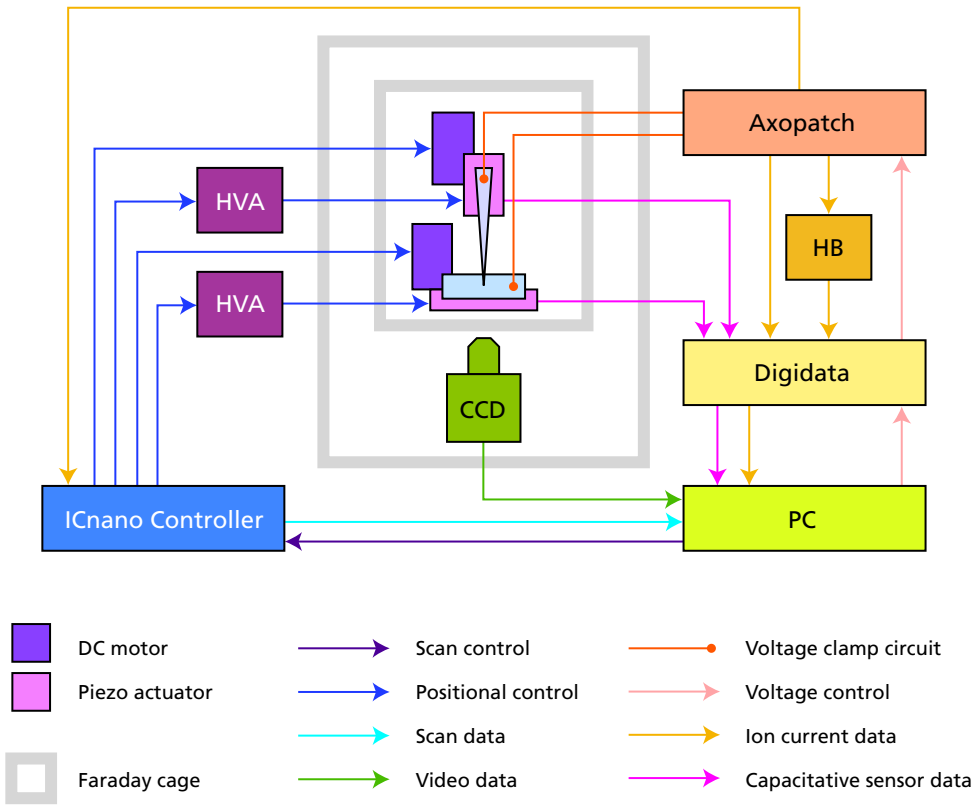

Figure 2.2: Main component connections for the SICM system. Abbreviations: HVA, high voltage piezo amplifier; HB, Humbug noise reduction filter (§2.7); CCD, video camera capturing optical microscopy (§2.5.1).

2.6 Scanning ion conductance microscopy

2.6.1 Equipment

Scanning ion conductance microscopy was performed using two IonScope ICnano SSH01 systems, with some customisation as described in Chapter 3. The major components of the system were as described below; see also Figure 2.2 for an overview of their interconnections.

Sample stage (XY) and pipette (Z) positioning were provided using Physik Instrumente closed loop DC motors for coarse control and piezo actuators for fine control. The stage DC motors were M-111.1DG with 15 mm range, and the piezos were Hera P-621.1CL with 100 µm range. Pipette DC motors

were M-112.1DG with 25 mm range, and the piezos were LISA P-753 with 25 µm range.

The positioning assembly was mounted inside a grounded anodized aluminium box acting as a Faraday cage to reduce electromagnetic interference. Also inside the box was the Axon Instruments CV203BU head stage used for primary ion current amplification.

Attached to the Z piezo was a sprung plastic clip into which could be inserted a Warner Instruments pipette holder appropriate for the pipette glass: ESP-F10P for 1.0 mm OD glass or ESP-F15P for 1.5 mm. The holder was connected to the head stage amplifier by a flying lead. Attached to the XY piezos was a 35 mm petri dish stage. A silver chloride electrode was attached to this stage to provide a ground connection that would move in synchrony with the dish.

This whole scan-head apparatus was placed on the 3-plate translation stage of one of the inverted optical microscopes described in §2.5.1, which were in turn mounted on Halcyonics Active Workstation 900-360 M6/25 vibration isolation tables. The microscope was enclosed in a large custom-built Faraday cage.

The piezos were driven by matched Physik Instrumente high-voltage amplifiers (E509, E505, E503). DC motors were driven by PI Mercury C-863 servo controllers built into the IonScope ICnano scanner control unit. The latter also contained a Texas Instruments SBC6711 digital signal processor (DSP) used to generate the positioning control signals and to collect the topographic image data. All control hardware was rack-mounted outside the microscope Faraday cage.

Pipette voltage was generated and ion current monitored using an Axon Instruments 200B patch clamp amplifier. This current signal was connected directly to the ICnano DSP, and also via an Axon Instruments Digidata 1440 interface to a Dell Optiplex PC running Microsoft Windows XP, allowing the signals to be monitored and recorded via Axon Instruments Clampex 10 software. Piezo driving signals and positional data from the piezo controllers' capacitive feedback sensors was also monitored directly via the Digidata interface and Clampex.

The ICnano system was controlled using the IonScope ScanIC client application, also running on the Windows XP PC, which was connected to the DSP

Manufacturer	OD (mm)	ID (mm)	Length (cm)	Catalogue #
Sutter Instruments	1.0	0.50	7.5	BF100–50–7.5
Intracel	1.0	0.58	7.5	01–002–06/A
World Precision Instruments	1.0	0.75	15	TW100F–6

Table 2.2: Capillary glasses for pulling SICM pipettes. All glass is of borosilicate type and includes an internal filament to aid filling.

Program	Line	Heat	Filament	Velocity	Delay	Pull
#75	1	350	4	60	200	100
#77	1	325	2	40	150	0
	2	260	2	27	160	200
#95	1	350	8	30	200	0
	2	220	2	27	160	250
#98	1	350	3	30	200	0
	2	260	2	27	160	200
#99	1	350	8	30	200	0
	2	250	2	27	160	250

Table 2.3: P-2000 pipette puller programs. Program numbers are arbitrary and used only for identification purposes.

via USB and to the DC motor controllers via RS232. Topographic images were captured to IonScope IMG format by this software.

2.6.2 Pipettes

SICM pipettes were pulled using a Sutter Instruments P-2000 laser puller. Numerous variations of glass and pull program were tried, but only a few were used consistently to obtain the data presented in this thesis. For brevity, these are referred to in the text using the name of the glass manufacturer and the number of the puller program used, for example: Sutter #77, Intracel #95. Glass details are in Table 2.2, while program settings are listed in Table 2.3.

Note that there appears to be significant variation in puller behaviour between different P-2000 units, so these specifications may not produce directly equivalent pipettes on a different puller.

2.7 Electrophysiology

Patch clamp experiments were performed on the SICM rigs (§2.6), using the same Axon Instruments CV203BU headstage, AxoPatch 200B amplifier, Digidata 1440 interface and Clampex 10 software for recording. The SICM DC motors and piezo actuators were used for coarse and fine positioning respectively, in place of traditional micro-manipulators.

Currents were low-pass filtered at 1–2 kHz using the internal 4-pole Bessel filter of the AxoPatch 200B, and sampled at 10 kHz. In the latter stages of the project, currents were processed prior to sampling using a Quest Scientific Hum Bug to subtract mains harmonic noise introduced by the ICnano scanner. Where this was done, the unprocessed signal was also recorded and the two compared to ensure that the Hum Bug did not introduce other artefacts.

Most recordings were made with high resistance SICM pipettes using the smart patch method described below (§2.7.1). These pipettes were pulled as specified in the previous section. More conventional patch pipettes were pulled from Harvard Instruments GC150F 1.5 mm OD/0.86 mm ID filamented borosilicate capillary glass using a List Medical L/M-3P-A puller, with a first pull heater current of 13.4 A and second pull 12.1 A. Tips were polished using a Narishige MF-9 microforge and in some cases coated with Sylgard 184 elastomer to reduce capacitance. Pipettes of this kind are abbreviated as 'Harvard F' in the text.

For most experiments, continuous gap-free recordings were made in the cell-attached configuration, with the pipette potential controlled manually. Other patch configurations were attempted in a number of cases, most commonly pulling inside-out patches. Whole cell configuration could not be achieved with fine pipettes, but a small number of whole-cell and whole-compartment recordings were tried with the larger pipettes, using suction to break the membrane after an initial cell-attached seal. Voltage pulse protocols were occasionally also recorded to look for voltage gating or rectifi-

cation. None of these attempts produced useful electrophysiological data. Almost all the recordings presented in this thesis are from the cell-attached configuration, with just a single inside-out recording in §6.2.6.

Two main bath solutions were used with neuronal preparations, a standard Krebs buffer [20] and an alternative derived from Fiszman et al. (2005) [18]. In most cases 100 nm tetrodotoxin (TTX) was added to the buffer to block action potential firing. HEK-bslo experiments were performed with either the standard Krebs bath [20] or a higher $[K^+]$ variant [27].

For cell-attached mode the pipette filler was typically of similar composition to the bath, supplemented with pertinent blockers and/or agonists. For NMDAR experiments, the filler included NMDA (25–100 µM) and glycine (10 µ). In most cases Mg^{2+} was omitted and buffered down with EDTA [22][23][24]. In a subset of experiments, Mg^{2+} was instead included [25], in an attempt to use the characteristic NMDAR voltage-dependent magnesium block as a marker of identity. Where there was the intention of attempting to go whole-cell or whole-compartment, a high-$[K^+]$, low-$[Ca^{2+}]$ pipette filler was used [26].

All recordings were made at room temperature (20–22 °C).

2.7.1 Smart patch clamp protocol

The smart patch technique used SICM imaging in combination with optical fluorescence microscopy for positional control. In order to apply the two techniques simultaneously, the SICM pipette had first to be aligned within the optical field. This was done as follows.

The sample was washed in bath solution and mounted on the SICM stage. A scanning pipette was filled and attached to the SICM scan head. The tip was immersed and checked for resistance and noise using the patch clamp amplifier. The tip was then brought close to the dish surface under manual control and centred in the microscope field of view using the positioning controls on the optical microscope's 3-plate stage. This process was repeated as necessary to locate the pipette with increasing precision within the fields of view of higher magnification, shorter working distance objectives. The pipette was then withdrawn ∼100 µm using the Z DC motor, to allow space to move the sample without colliding with the tip. In order to preserve

the alignment, no further movement of the 3-plate stage was permitted. All subsequent sample movement was performed instead with the SICM motors and piezos.

The dish was moved around using the XY DC motors until a suitable target was identified optically. This was positioned alongside the centre of the field of view, and the pipette lowered back down to the surface until it was 'under control'—hopping on the spot next to the target. Optical images were captured and then a SICM scan performed. By comparing these images, a patching location was selected within the area of the scan.

The pipette was retracted to the top of its Z piezo range and the sample moved to the XY piezo position corresponding to the chosen scan pixel. The Z piezo was then slowly lowered again until the cell surface was detected, and the pipette held static at that position. Light suction was applied while monitoring the current induced by a small (–10 mV) seal test pulse in Clampex. Once a seal was achieved, patch recording proceeded in the conventional way.

2.8 Electron microscopy

Samples were mounted on Agar Scientific 45° angled pin stubs, into the surface of which a groove with a 90° angled cross section had been milled. Pulled glass pipettes were glued into this groove using two-sided adhesive carbon tape, positioned so that the pipette tip was just within the body of the stub. Excess glass from the back end of the pipette was then trimmed away. To improve grounding, Agar Scientific quick drying colloidal silver was painted onto the pipette body to within a few mm of the tip and allowed to dry overnight in a ventilated fume hood.

The stub-mounted pipettes were attached to the SEM stage and this was placed in a Polaron E500 sputter coater for 2 min to deposit a coating of gold 10–15 nm thick.

The stage was transferred into the imaging chamber of a Jeol JSM-6480LV scanning electron microscope. The SEM was operated at potentials of 7–17 kV and magnifications ranging from 1000× to 200,000×. Images were captured using the JEOL SEM control software and saved in lossless TIFF format for further analysis.

SEM facilities were provided by the Rock and Ice Physics Laboratory in the UCL Department of Earth Sciences, with generous technical assistance from Jim Davy.

2.9 Data analysis

Whenever appropriate, robust and/or non-parametric statistics were used in preference to methods with stronger distributional assumptions. Central tendency and spread have usually been expressed in terms of median and median absolute deviation (MAD), using the notation $median \backsim MAD$. Where it was instead appropriate to use mean and standard deviation, these have been denoted $mean \pm SD$. The latter were particularly used when estimating values from a parametric model. When counts were very small, averages have been avoided and instead the individual observations shown.

Similarly, robust regression using iteratively re-weighted least-squares for M-estimation was preferred to ordinary least-squares (OLS) regression for fitting data (Venables and Ripley 2002). The former is more resistant to distortion by outliers, but the underlying model does not allow calculation of straightforward p-values for hypothesis tests. In some cases, both methods were applied in parallel and the OLS p-values reported when the results closely agreed. Where this was done it has been clearly stated in the text.

Basic distribution tests for categorical count data were performed using Fisher's exact test. In more complex cases it was sometimes necessary to apply parametric alternatives such as χ^2 and ANOVA. This has again been noted in the text.

More complex analyses were performed using publicly-available packages in the R environment, in combination with custom-written code. The latter is included on the accompanying CD (see Appendix A.4).

Single channel records were analysed both by visually placing cursors on the trace in ClampFit and by statistical fitting in R. Where the two methods substantially disagreed, those trace segments were not used. Records were idealised by threshold-crossing based on the estimated current levels.

Maximum likelihood fitting of distributions was done using numerical methods from the `MASS` (Venables and Ripley 2002) and `fitdistrplus` (Delignette-

Muller et al. 2010) packages, along with some custom density and cumulative distribution functions. Most optimisation was performed using the Nelder-Mead method, but simulated annealing was applied in some cases where the fit was poorer. For parameter estimates requiring it, propagation of errors was performed by Monte-Carlo simulation methods from the `qpcR` package (Spiess and Ritz 2010).

In dot and scatter plots with many observations at the same x-axis position, horizontal jitter has often been added for visibility. This is simply a presentational device and does not indicate actual variation in the predictor value.

2.10 Software

Most statistical analysis and much of the numerical modelling was done using the open source software R (R Development Core Team 2010). This was also used for the generation of many figures. Additional modelling and analysis was performed in Matlab (Mathworks), while Mathematica (Wolfram Research) was used for some algebraic computation. R and Matlab code can be found on the accompanying CD (Appendix A). A small number of graphs and traces were prepared with Igor Pro (WaveMetrics) and most experimental data was tabulated using Numbers (Apple).

SICM image data was primarily analysed and rendered using a custom-written Mac OS X application, IonView, described in Appendix A.2, and with IonScope's SICM Image Viewer software. An IonScope IMG file importer module was contributed to the open source SPM analysis program Gwyddion (Klapetek et al. 2004–2010), allowing that also to be used for particular analyses. In addition, some SICM data was exported from IonView in tab-delimited text format for further processing with Matlab and R.

Electrophysiological data was analysed using Clampfit 10 (Axon Instruments) or exported as text for analysis in R or Matlab.

Confocal microscope data was viewed and analysed using LSM Image Browser 4.2 (Zeiss) and Osirix 3.9.2 (Pixmeo).

Final preparation of graphs and vector art figures was done using Illustrator CS3 (Adobe). Bitmap image processing was performed using Photoshop

CS3 (Adobe) and Acorn (Flying Meat). Image distances and angles were measured with PixelStick (Plum Amazing).

The manuscript was prepared using TeXShop (http://www.texshop.org) and typeset with pdflatex (http://www.pdftex.org), using the Memoir class by Peter Wilson (http://www.ctan.org/pkg/memoir). References were managed using Papers (Mekentosj) and processed with BibTeX (http://www.bibtex.org).

2.11 Solutions

For basal media, salt solutions and other ingredients available in variant forms, product details are given in §2.12. Where no other base is specified, solutions were made up in 18.2 MΩ · cm H_2O.

Percentage values are v/v.

Solutions were filtered with a 0.22 µm filter prior to use.

[1]	Borate-buffered poly-D-lysine	Boric acid 50 mM, sodium tetraborate 12.5 mM, poly-D-lysine 50 µg/ml
[2]	HEK growth medium	DMEM 90%, fœtal bovine serum 10%, L-glutamine 2 mM, penicillin 100 units/ml, streptomycin 100 µg/ml
[3]	Dissection medium	GBSS, D-glucose 6 mg/ml, $MgCl_2$ 8 mM
[4]	Trypsin solution	HBSS, trypsin (type XI) 1 mg/ml, HEPES 8 mM
[5]	Cerebellar plating medium	Neurobasal-A 97%, B-27 2%, N2 1%, L-glutamine 2 mM, KCl 15 mM, penicillin 100 units/ml, streptomycin 100 µg/ml
[6]	Cerebellar growth medium	MEM 90%, horse serum 10%, L-glutamine 2 mM, KCl 20 mM, D-glucose 7 mM, penicillin 100 units/ml, streptomycin 100 µg/ml
[7]	Anti-mitotic solution	ARA-C 1 mM, FUDR 1 mM, uridine 1 mM
[8]	BSA solution	HBSS 90%, newborn bovine serum 10%, bovine albumin 1 mg/ml, $MgCl_2$ 8 mM
[9]	Hippocampal plating medium	Neurobasal 93%, newborn bovine serum 5%, B-27 2%, L-glutamine 0.5 mM
[10]	Hippocampal growth medium	Neurobasal 98%, B-27 2%, L-glutamine 0.5 mM

[11]	2× HEPES-buffered saline	NaCl 274 mM, KCl 10 mM, Na_2HPO_4 1.4 mM, D-glucose 15 mM, HEPES 42 mM; pH to 7.11 with NaOH
[12]	5× kynurenic acid	Neurobasal, kynurenic acid 10 mM
[13]	Phosphate-buffered saline (PBS)	NaCl 136.9 mM, KCl 2.7 mM, Na_2HPO_4 9.2 mM, KH_2PO_4 1.8 mM; pH to 7.2 with HCl
[14]	Paraformaldehyde solution	PBS, paraformaldehyde 40 mg/ml
[15]	Ammonium chloride solution	PBS, NH_4Cl 50 mM
[16]	Antibody blocking solution	PBS 89.9%, fœtal bovine serum 10%, Triton-X 0.1%, bovine albumin 5 mg/ml
[17]	Tween-20 solution	PBS 99%, Tween-20 1%
[18]	Fiszman external solution	NaCl 145 mM, KCl 5 mM, $MgCl_2$ 1 mM, $CaCl_2$ 1 mM, HEPES 5 mM, D-glucose 5 mM, sucrose 15 mM; pH to 7.4 with NaOH
[19]	High [K^+] Fiszman solution	NaCl 50 mM, KCl 100 mM, $MgCl_2$ 1 mM, $CaCl_2$ 1 mM, HEPES 5 mM, D-glucose 5 mM, sucrose 15 mM; pH to 7.4 with KOH
[20]	Krebs external solution	NaCl 140 mM, KCl 4.7 mM, $MgCl_2$ 1.2 mM, $CaCl_2$ 2.48 mM, HEPES 5 mM, D-glucose 11 mM; pH to 7.4 with NaOH
[21]	High [K^+] Krebs solution	NaCl 44.7 mM, KCl 100 mM, $MgCl_2$ 1.2 mM, $CaCl_2$ 2.48 mM, HEPES 5 mM, D-glucose 11 mM; pH to 7.4 with KOH
[22]	NMDA filler #2	NaCl 150 mM, KCl 2.5 mM, EDTA 1 mM, HEPES 10 mM, NMDA 100 µM, glycine 10 µM, TEA 10 mM, 4AP 1 mM, TTX 100 nM; pH to 7.4 with NaOH
[23]	NMDA filler #4	NaCl 136 mM, KCl 3 mM, HEPES 10 mM, EDTA 1 mM, NMDA 100 µM, glycine 10 µM, TTX 100 nM; pH to 7.4 with NaOH
[24]	NMDA filler #5	NaCl 136 mM, KCl 3 mM, HEPES 10 mM, EDTA 1 mM, NMDA 25 µM, glycine 10 µM, TTX 100 nM; pH to 7.4 with NaOH
[25]	NMDA filler #6	NaCl 140 mM, KCl 2.8 mM, $MgCl_2$ 1.2 mM, $CaCl_2$ 0.5 mM, HEPES 10 mM, EDTA 10 µM, D-glucose 5 mM, NMDA 100 µM, glycine 10 µM, TTX 100 nM; pH to 7.4 with NaOH

[26]	NMDA filler #7	KCl 150 mM, HEPES 10 mM, EDTA 1 mM, NMDA 100 µM, glycine 10 µM, TEA 1 mM, 4AP 1 mM, TTX 100 nM, PTX 100 µM
[27]	BK external solution	KCl 145 mM, HEPES 10 mM, $MgCl_2$ 1 mM, D-glucose 10 mM, $CaCl_2$ 100 µM; pH to 7.4 with KOH

2.12 Materials and suppliers

2.12.1 Prepared media and solutions

Name	Description	Supplier	Cat #
HBSS	Hank's Balanced Salt Solution (1×), [–] $CaCl_2$, [–] $MgCl_2$	Gibco	14170
GBSS	Gey's Balanced Salt Solution	Sigma	G9779
B27	B27 serum-free supplement (50×)	Gibco	17504
Neurobasal-A	Neurobasal-A medium (1×)	Gibco	10888
Neurobasal	Neurobasal medium (1×)	Gibco	21103
MEM	Minimum essential medium (1×), [+] Earle's, [–] L-glutamine	Gibco	21090
Opti-MEM	Optim-MEM reduced serum medium (1×), [+] L-glutamine	Gibco	31985
DMEM	Dulbecco's modified Eagle's medium (1×), 1 g/l D-glucose, [+] L-glutamine, [+] sodium pyruvate	Gibco	31885
Trypsin	Trypsin type XI from bovine pancreas	Sigma	T1005
BME	Basal Medium Eagle (1×), [+] Earle's, [–] L-glutamine	Gibco	41010
Trypsin-EDTA	Trypsin 0.5 g/l and EDTA·4Na 0.2 g/l in HBSS	Gibco	25300
N2	N2 serum-free supplement (100×)	Gibco	17502
Horse serum	Sterile-filtered adult horse serum, New Zealand origin	Gibco	16050

2.12.2 Drugs and peptides

Name	Description	Supplier	Cat #
D-AP5	D(–)-2-amino-5-phosphonopentanoic acid	Sigma	A8054
Poly-D-lysine	Poly-D-lysine hydrobromide, MW $> 300,000$	Sigma	P7405
DNQX	6,7-dinitroquinoxaline-2,3(1H,4H)-dione	Sigma	D0540
Kynurenic Acid	4-hydroxyquinoline-2-carboxylic acid	Sigma	K3375
PTX	Picrotoxin	Sigma	P-5753
4AP	4-aminopyridine	Sigma	A0152
TEA	Tetraethylammonium chloride	Sigma	T2265
NMDA	N-methyl D-aspartate	Tocris	0114
Glycine	Glycine	Tocris	0219

2.12.3 Dyes and markers

Name	Description	Supplier	Cat #
FM1-43	FM1-43	Invitrogen	T35356
FM4-64	SynaptoRed (FM 4-64)	Calbiochem	574799
Advasep-7	Advasep-7 $>$ 96% solid	Sigma	A3723
Lipofectamine	Lipofectamine-2000 transfection reagent	Invitrogen	11668

2.12.4 Reagents

Basic salts and reagents not individually specified below were of AnalaR grade and purchased from VWR.

Name	Description	Supplier	Cat #
HEPES	HEPES solution 1M, sterile filtered, pH 7.0–7.6	Sigma	H0887

$MgCl_2$	Magnesium chloride solution 1M, sterile filtered	Sigma	M1028
DMSO	Dimethyl sulfoxide	Sigma	154938
Para-formaldehyde	Paraformaldehyde	Sigma	P6148
Triton X-100	Triton X-100, molecular biology grade	Sigma	T8787
Tween-20	Tween-20, molecular biology grade	Promega	H5151
Sylgard	Sylgard 184 silicone elastomer	Dow Corning	1673921

2.12.5 Consumables and glassware

Description	**Supplier**	**Cat #**
8 mm two-sided adhesive carbon tape	Agar	G3939
45° angled pin stubs	Agar	G301E
Quick drying silver paint	Agar	G302
1.0/0.5 mm borosilicate capillaries	Sutter	BF100–50–7.5
1.0/0.58 mm borosilicate capillaries	Intracel	01–002–06/A
1.0/0.75 mm borosilicate capillaries	WPI	TW100F–6
1.5/0.86 mm borosilicate capillaries	Harvard	GC150F–15 (30–0058)
18 mm × 18 mm thickness 0 cover slips	VWR	631–0119
35 mm plastic petri dishes	Nunc	153066
T25 filtered tissue culture flask	Nunc	156367
Millex.GP 0.22 µm filter	Millipore	SLGP033RS

2.12.6 Hardware and testing

Description	**Supplier**	**Cat #**
500 nm AFM step target	BudgetSensors	HS–500MG
100 nm AFM step target	BudgetSensors	HS–100MG
1.8 µm AFM angled grating target	MikroMasch	TGG01

2.12.7 Suppliers and distributors

Listings are for UK distributors where available. Distributed and subsidiary brands are in parentheses.

Name	Address
Agar Scientific	Unit 7, M11 Business Link, Parsonage Lane, Stansted, CM24 8GF
Chroma	PO Box 489, Rockingham, VT 05101, USA
CN Technical Services (Mikromasch)	42 Bridge Street, Downham Market, PE38 9DJ
Digitimer (Quest Scientific)	37 Hydeway, Welwyn Garden City, AL7 3BE
Edmund Optics	Tudor House, Lysander Close, York, YO30 4XB
Farnell (Dow Corning)	Maybrook Industrial Estate, Castleton Road, Leeds, LS12 2EN
Fisher Scientific (BioTek)	Bishop Meadow Road, Loughborough, LE11 5RG
Harvard Apparatus (Warner Instruments)	PO Box 126, Kent, TN8 6WF
Intracel (Sutter Instruments)	Unit 4, Station Road, Shepreth, Royston, SG8 6PZ
Invitrogen (Gibco, Molecular Probes)	3 Fountain Drive, Inchinnan Business Park, Paisley, PA4 9RF
IonScope	A2 Ash House, Melbourn Science Park, Cambridge Road, Melbourn, SG8 6HB
Laser2000 (Semrock)	Britannia House, Denford Road, Ringstead, NN14 4DF
Leica Microsystems	Davy Avenue, Knowlhill, Milton Keynes, MK5 8LB
LGC Standards (ATCC)	Queens Road, Teddington, Middlesex TW11 0LY
Melles Griot	Second Avenue, Onchan, Isle of Man, IM3 4PA
Merck (Calbiochem)	Boulevard Industrial Park, Padge Road, Beeston, NG9 2JR
Millipore	Building 6, Croxley Green Business Park, Watford, WD18 8YH
Molecular Devices (Axon Instruments)	660 Eskdale Road, Wokingham, RG41 5TS
Nikon	380 Richmond Road, KT2 5PR
Pacer International (Perkin Elmer)	Unit 3, Horseshoe Park, Pangbourne, Reading, RG8 7JW

Physik Instrumente	Trent House, University Way, Cranfield, Bedford, MK43 0AN
Promega	Delta House, Southampton Science Park, SO16 7NS
Sarstedt	68 Boston Road, Beaumont Leys, Leicester, LE4 1AW
Sigma-Aldrich	The Old Brickyard, New Road, Gillingham, Dorset, SP8 4XT
SLS (BD Biosciences, Eppendorf, Ideal-Tek, Nalgene, Portex)	Orchard House, The Square, Hessle, HU13 0AE
Thorlabs	1 St Thomas Place, Ely, CB7 4EX
Tocris	Tocris House, IO Centre, Moorend Farm Avenue, Bristol, BS11 0QL
VWR (Nunc)	Hunter Boulevard, Magna Park, Lutterworth, LE17 4XN
Windsor Scientific (BudgetSensors)	264 Argyll Avenue, Slough, Berkshire, SL1 4HE
World Precision Instruments	Astonbury Farm Business Centre, Aston, Stevenage, SG2 7EG

Chapter 3

SICM and hopping mode implementation

For scans presented in this thesis, the SICM was operated in the hopping mode outlined in §1.4.6. This mode is explained in detail in Novak et al. (2009) and the associated Supplementary Methods. Here we provide only a brief description, focussing on specific problems encountered with implementation in our lab and on those aspects pertaining to the intended use of the smart patch clamp technique.

3.1 Mechanics of the hopping protocol

3.1.1 Mixed mode

The SICM was arranged as described in §1.4.5. The sample was mounted on a positioning stage with coarse DC motor and fine piezo controls in the lateral (XY) directions, while the pipette probe was attached to a vertical mount with DC motor and piezo controls in the Z direction. The DC motors were used to bring the pipette and sample sufficiently close together that all movement required during the scan was within the limited range of the piezos (100 µm XY and 25 µm Z). This was done initially under visual control, using the microscope brightfield image as a guide. The final vertical approach was automated, using the ion current signal to detect the

surface. Once the sample was positioned, the DC motors were locked off during scanning.

Scans were constructed from height measurements at different XY locations. Individual measurements were made as follows. First, the probe was retracted from the previously detected surface position, either by a specified relative distance or to a specified absolute height level. Retraction occurred at relatively high speed, typically 1000 nm/ms. Then, the sample was moved laterally so that it was at the desired measurement position. The probe was maintained at the specified distance for a delay of several ms, during which the average baseline current I_{ref} was measured. The probe was then lowered vertically at a slower rate, typically of the order 50 nm/ms, while simultaneously monitoring the instantaneous ion current I. As soon as $I < I_s$ (see Equation 1.1, p. 30) for four consecutive samples (200 µs at the scanner's 20 kHz sampling rate), the probe position was recorded. The probe was then quickly withdrawn and the process repeated for subsequent locations.

3.1.2 Adaptive sampling density

The hopping procedure potentially required the pipette to travel a considerable distance for each sample. The Z piezo was faster than those in XY, but the fall rate was limited by the need to avoid overshooting and colliding with the sample. There was thus a significant hop time cost for each position measured, and a concomitant benefit to avoiding unnecessary measurements.

Many samples of interest included empty regions that did not merit measurement at high levels of detail. It was therefore worthwhile to perform a 'pre-scan' step to estimate the level of detail for each region of the scan, as shown in Figure 3.1. The target area was first divided into a grid of square tiles, to be scanned in turn. For each tile, the four corner heights were first measured and the vertical span, h, taken as a metric of the tile's content or roughness. A simple threshold test was applied to this value, such that if h exceeded the threshold the tile would be scanned at higher density, otherwise lower. (Note that the corner measurements incurred a cost in terms of additional travel time, so for samples without substantial variations in roughness it might be preferable to scan at a single density level. No pre-scan was performed in that case.)

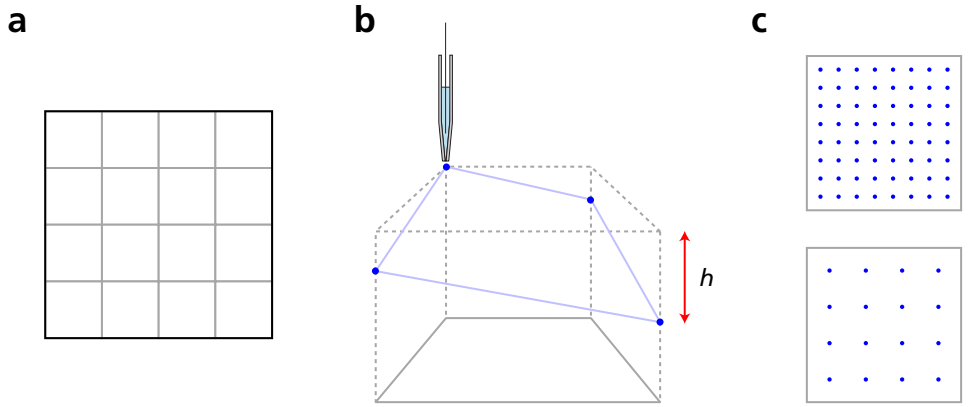

Figure 3.1: Adaptive sampling based on local roughness. **a** The scan area is divided into a grid of square tiles to be scanned in turn. **b** For each tile, a pre-scan is made, measuring the height at the four corners. The vertical span, h, is taken as the metric of roughness. **c** The tile topography is sampled at high density if h exceeds a chosen threshold value, at lower density otherwise.

The pre-scan measurements were typically taken with a relatively large hop height to reduce the likelihood of collisions with the sample while making the large lateral movements between the tile corners. Sampling within the tile was usually at a lower hop height based on the measured roughness.

The four-point roughness measure provided only a crude estimate and carried the risk of tall objects in the middle of a tile remaining undetected. There was thus a trade-off between the time saved by using fewer, larger tiles, and the corresponding increased risk of missed data and possible collisions with the sample.

The various scan parameters were adjusted according to the characteristics of the target and could span quite a range of values, but as an example, typical parameters for a 10 µm $\times$ 10 µm scan of a region of neuronal processes in culture might be: tile size 625 nm; pre-scan hop height 4 µm; minimum internal hop height 2 µm; roughness threshold 200 nm; high density sample spacing 156 nm; low density 312 nm. Where differences are important for data presented subsequently, the parameters used will be noted.

All images were produced with nominal pixel dimensions of 512 $\times$ 512. In most cases, only a fraction of those pixels were actually measured, with different densities in different tiles as seen in Figure 3.2. By default, images

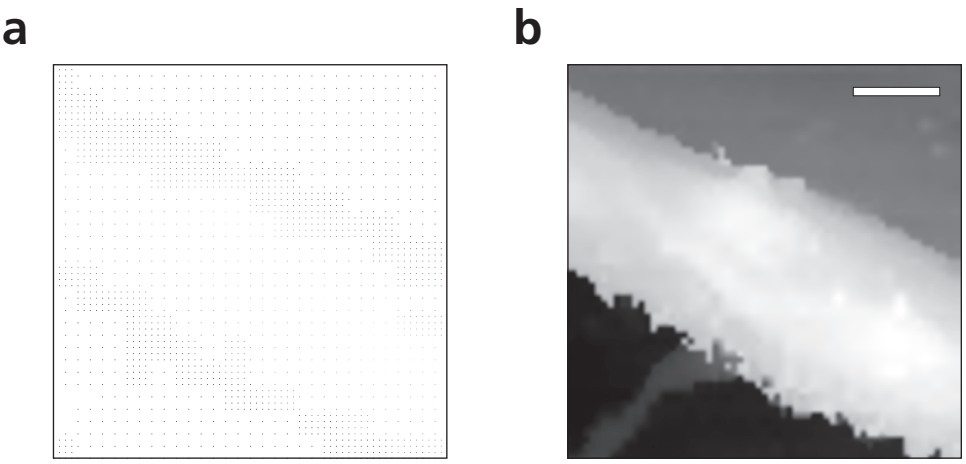

Figure 3.2: Interpolation of sample data. Image shown is a neuronal process from a primary cerebellar culture. **a** Actual measurements made, with tiles sampled at two different densities. Unsampled points are shown as white. **b** The same SICM image after bicubic spline interpolation. (Scale bar, 1 µm.)

were saved as both raw data and, separately, in interpolated form, with the missing data filled in bilinearly. Most of the images presented in this thesis were rendered from the raw data using bicubic spline interpolation instead of bilinear.

3.1.3 Order of sampling

The sample had to be physically moved between every measurement position. The scanning would therefore be most efficient if consecutive measurements were close together.

In traditional continuous-feedback SICM, there is often an asymmetry in the response to positive and negative height changes, meaning that the profile scanned in one direction may be different to that scanned in the reverse direction. It is therefore advisable to scan all raster lines for an image in the same direction. A common approach has been to acquire two images in parallel, one while scanning forward across the sample and the other while moving back. This makes use of the backward movement that would in any case have to occur and also allows for comparison of the two profiles to identify any discrepancies.

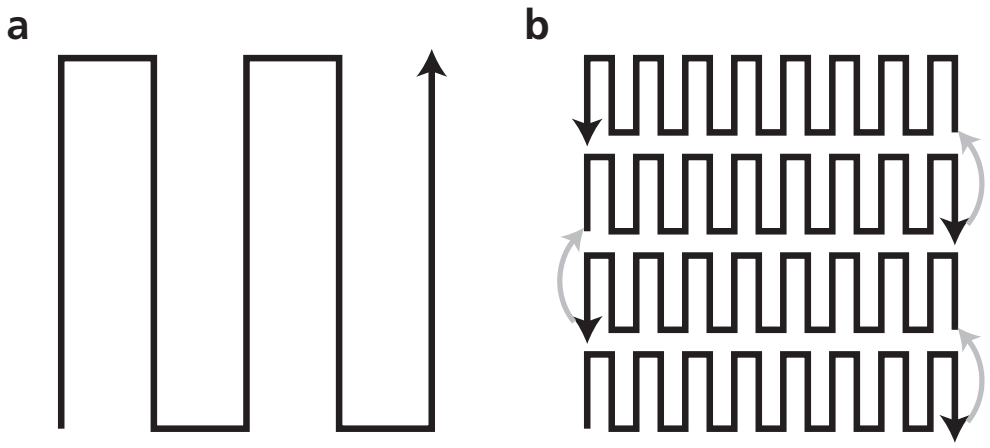

Figure 3.3: Boustrophedon scanning pattern. **a** Columns of pixels within each tile are scanned alternately bottom-to-top and top-to-bottom. **b** Similarly, alternate rows of tiles are scanned left-to-right and right-to-left.

With hopping mode, the approach to each point was made independently. In theory there should be no dependence on direction of lateral motion (but see §3.2.2). It therefore made sense to minimise superfluous movement by acquiring data in alternating directions across the sample. We termed this a 'boustrophedon' pattern, by analogy with bi-directional writing systems.

To allow for the use of adaptive sampling as described in the previous section, the image was acquired not in complete rows but as a series of smaller tiles. These tiles were also scanned in boustrophedon order, leading to a nested alternation, as shown in Figure 3.3. (For illustrative purposes the figure shows sampling at only a single density level; for adaptive sampling the scan pattern would be more complicated.)

This arrangement allowed for faster scanning, but also brought some artefacts of its own. The trade-offs involved are discussed in §3.2.

3.1.4 Split mode and the PicoCube

In the hopping implementation described above, the pipette piezo is responsible for all Z movement, so its position at any time combines both the modulating signal of the hops and the topographic information of surface height. This is referred to as 'mixed mode' hopping. By its nature, this

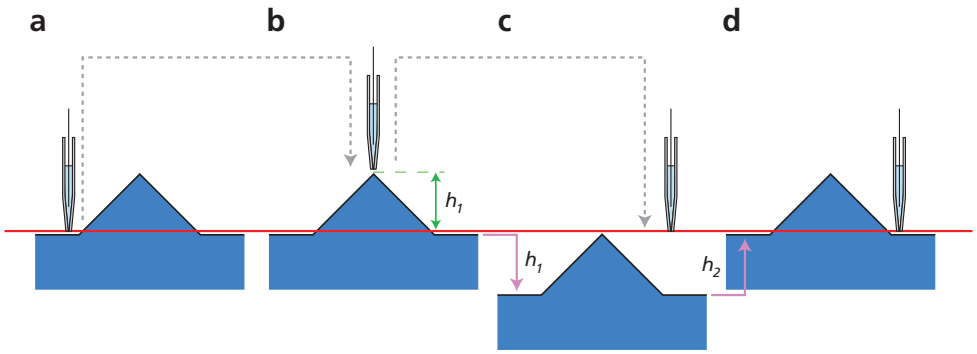

Figure 3.4: Split mode hopping. Datum level is indicated in red. From initial measured position (**a**), the pipette is withdrawn to the hop height and the sample moved laterally to the next location. Pipette is lowered toward surface. If the surface is detected before the datum is reached (**b**), the height h_1 is recorded. The pipette is immediately withdrawn, and the sample is also lowered by h_1 so that the detected point is once again aligned with the datum. If the approaching pipette reaches the datum without detecting the surface (**c**), the sample is raised towards the datum until detection occurs (**d**) and the topography determined from the distance raised, h_2.

is limited to scanning a sample whose height fits within the pipette piezo range while also leaving space for the hops.

In our original SICM instrument, the pipette piezo was a Physik Instrumente PicoCube with only a 5 µm vertical range. Since at least 2 µm is typically used for hopping, this could not accommodate usefully-large samples in mixed mode. However, the rig was also equipped with a stage Z piezo with 100 µm range. This was too slow to be used for the mixed mode Z movement, and in any case the resulting vibration of the sample would have risked undesirable side effects. Instead, an alternative form of hopping, known as 'split mode', was devised to allow larger samples to be scanned.

In split mode, the high frequency hopping signal was still performed by the pipette, but the lower frequency topographic signal was extracted and applied to the stage. After each hop, the sample Z position was adjusted so that the surface was at a 'datum' level with respect to the pipette, just within the latter's movement range. The process is illustrated in Figure 3.4.

Although split mode was implemented, in practice it proved highly unreliable and prone to error. The scans produced exhibited many 'stairstep'

artefacts and non-independence of sampling. Examples can be seen in Figure 3.13. Some of the issues were a consequence of the scan pattern and also occurred in mixed mode; these will be discussed in §3.2 below. However, there were also issues specific to the PicoCube and the split mode.

Most fundamentally, split mode measured distance in two competing frames of reference, depending on the sample topography. In effect, upward slopes were measured with the pipette piezo, while downward slopes were measured with the stage piezo. Any inconsistencies between the two systems would accumulate in the stage position and be interpreted as features of the sample. The cumulative error at any point in the scan would depend on the history of previous measurements, and thus the samples were not independent. The piezos were of substantially different sizes and characters, and in practice we were not able to calibrate them with sufficient accuracy to ensure measurement consistency.

Moreover, the PicoCube was a 3-axis actuator, providing XY positioning as well as Z; and the split mode also required three dimensional positioning on the stage. In both cases, we found that movements in each direction were not perfectly independent, with crosstalk between the vertical and lateral positions. These positional errors were reflected in the topographic measurements, contributing to the cumulative inconsistency.

Ultimately, split mode could not be made usable for our experiments and was abandoned. The PicoCube was removed and replaced with a single-axis piezo having 25 µm range; this is the configuration described in §2.6. The same specification was used when a second SICM rig was built. All subsequent scanning was performed in mixed mode.

3.2 Disadvantages of hopping mode

3.2.1 Speed

Hopping required the pipette to travel much further than it would in a conventional constant-distance scanning mode. The pipette piezo was faster than the stage piezo, but the vertical distance was often large compared to the lateral separation of points and could add considerably to the time taken to acquire an image.

Some improvement in scan speed was achieved by tuning the filtering and slew rate limiting of the piezo amplifiers to better match the mechanical resonances of the system. This was not a major focus and it is likely that further improvements could be made in this regard. Colleagues at Imperial College have managed considerable speed increases on some systems by careful customisation and selection of the electronic and mechanical components, but this work does not easily generalise.

For practical purposes, the scanning parameters themselves remained the principal means of adjusting scan speed. Scans were much faster with lower sampling densities and smaller hops. The cost of such improvement was a loss of spatial resolution and reduction in the ability to scan complex samples. The balance between these different properties depended on the purpose of the experiment, the nature of the sample and even the characteristics of the pipette. In many cases imaging was only a means to an end, and it was often necessary to sacrifice spatial resolution in favour of speed (see §3.5).

3.2.2 Confounding space and time

As with all SPM techniques, the hopping image was acquired serially, so time-varying properties of the sample could become confounded with the topography. The problem was exacerbated by the convoluted scan pattern, in which nearby points in adjacent rows would be scanned soon after one another at one end but separated by a long delay at the other. This is illustrated in its simplest form in Figure 3.5, which shows a scan of the flat bottom of a plastic petri dish in the presence of constant drift.

The drift introduced a gradient into the image, and because of the boustrophedon scanning this manifested as a pattern of steps with alternating slope. In this simple case, the artefacts were clearly identifiable and unlikely to be mistaken for sample features. That would not necessarily be true, however, if the drift were less uniform and the sample more complicated.

The delay between scanning consecutive points must always depend on the sample topography: the path from one point to the next is shorter going uphill than going down. So even with only a single compression level, there would be an interaction between the actual topography and any time-

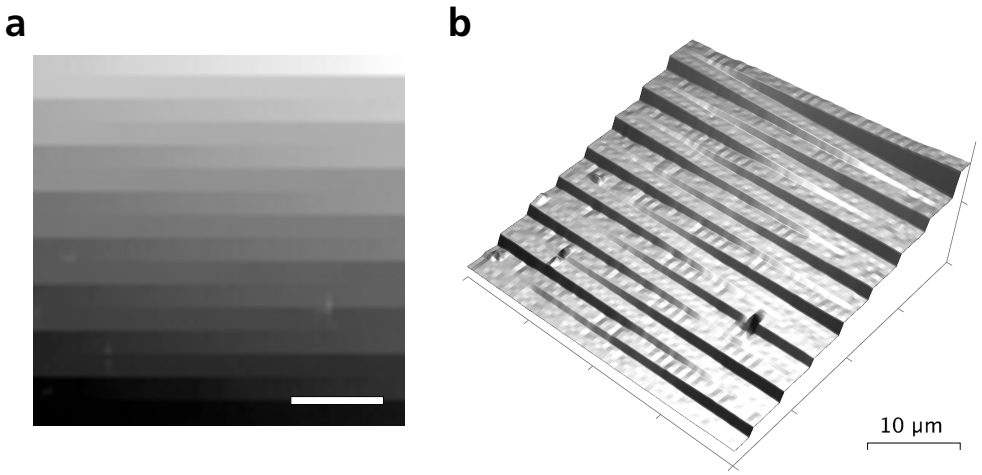

Figure 3.5: Linear drift manifests in non-linear stepping due to the boustrophedon scan pattern. The sample shown is flat but drifting upwards over the course of the scan.

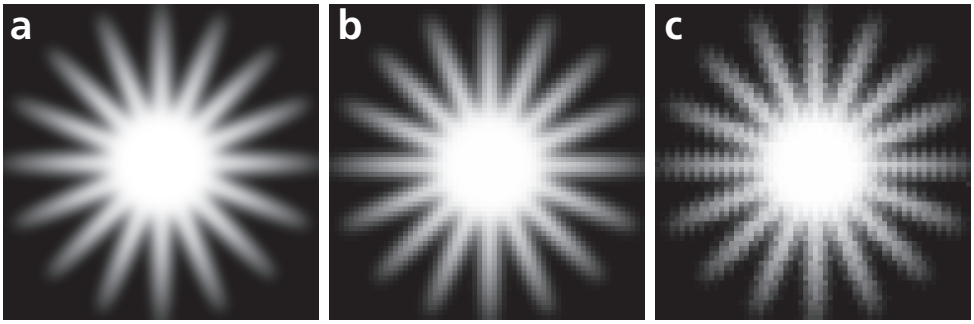

Figure 3.6: 'Stairstep' artefacts in simulated scans. **a** Model image. **b** Simulated image with low-resolution sampling and perfect positioning. **c** Simulated image with the same resolution but lateral lag such that the result at each postion is averaged with that at the previous location.

dependent errors. And the variability would be much greater with adaptive compression, when different areas might be scanned at different densities and hop heights.

Scan pattern artefacts could also arise if the synchronisation between lateral positioning and measurement were imperfect. This could occur in several ways, including lateral vibration of the probe tip and lag in the settling of the XY piezos to their target position. The result would again be a loss of

sampling independence.

Such an effect is illustrated in simulated form in Figure 3.6. (Note that the simulation is quite simplistic and omits several factors likely to make matters worse in practice.) Here the model image is sampled in boustrophedon fashion with a single compression level. With the lateral position perfectly synchronised as in Figure 3.6b, the object is reproduced correctly with resolution reduced according to the sampling density. In the presence of positional lag, the image becomes distorted with characteristic 'stairstep' artefacts (Figure 3.6c).

These artefacts occurred frequently in practice, especially during the early months of setting up the SICM, and were never wholly eliminated. Some extreme examples can be seen in Figure 3.13, and there are remnants, albeit at more acceptable levels, in Figures 3.11 and 3.15 and indeed most of the other scans presented in this thesis. An unfortunate feature of such artefacts is that they could have greater impact at higher sampling density. In many cases, increasing the scan resolution resulted in a worse image.

As with the scanning speed, some improvements were obtained by tuning the system to reduce positional ringing and resonance, but the major reduction came from *slowing down* the scan. Increasing the delays between different movement stages allowed the position to settle and vibrations to dampen before measurement.

Clearly this solution was at odds with the need to reduce artefacts arising from drift. Again, a balance had to be struck between contradictory requirements according to the nature of the particular sample and the goals of the experiment.

3.3 Testing

3.3.1 Using the hopping probe to check system stability

By maintaining the probe at a set lateral position and recording the pipette height as it repeatedly hopped on the spot we were able to monitor the stability of the system (Figure 3.7).

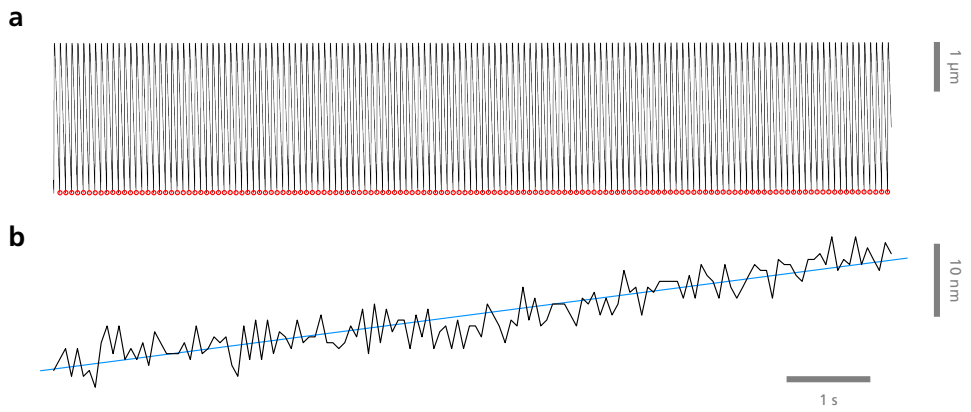

Figure 3.7: Measuring relative positional stability by hopping on the spot. The hop position gives a measure of the separation of probe and surface over time. **a** Full trace including hops. Surface is detected at positions indicated by red circles. **b** Detected surface position shown on a magnified scale. Blue line shows underlying drift of 1.5 nm/s (from linear regression). Noise in detected position is 9 nm RMS. Pipette resistance was 140 MΩ when filled with Krebs buffer [20].

The piezo signal provided only a one-dimensional measure of the positional state, whereas the system itself had several degrees of positional freedom, each of which might be subject to drift. When substantial drift was observed, it was not possible to be certain which underlying movement was the cause. Equally, the absence of observed vertical drift did not guarantee that the system was stable. However, in the former case we could be certain that there was *some* instability and attempt to correct it. In the latter, we had to assume there was a low probability that multiple sources of drift would compensate one another purely by chance.

It was not always possible to eliminate drift or identify its source. In some cases the drift was inherent to the sample and no adequate compensation was possible. But several sources were demonstrated experimentally and could usually be prevented or at least significantly reduced:

Thermal expansion Size changes due to heat flows between the sample and environment. A notable source of temperature change was the microscope brightfield lamp, which could have a significant warming effect if the sample was cold. Thermal drift problems could not always be

entirely eliminated, but were reduced by ensuring that the sample and equipment were properly equilibrated before attempting to scan.

Dish compression Concerns about dish movement during scanning, which had been observed particularly in split mode, led to several attempts to hold the dish more firmly on the sample platform. However, these entailed the dish and/or the holder experiencing sufficient force to cause ongoing deformation or displacement relative to the probe. Ultimately it was found that the sample was more stable when simply resting on the platform with no additional restraining force.

Air movement The stage was surprisingly susceptible to small movements induced by draughts. It was usually necessary to ensure that local sources of such movement such as air conditioning were kept off while scanning to reduce disturbance. This also helped with temperature consistency.

Because it was our intention to use the scanning pipette for smart patch clamping, a particular concern was that the application of suction necessary to obtain a gigaseal would perturb the pipette position. We therefore performed a number of tests in which the probe was again kept hopping at a fixed location and its height monitored while both negative and positive pressure pulses were applied. A representative example is shown in Figure 3.8.

A notable feature of this and all such tests ($n = 22$) was that the current flow through the pipette increased for the duration of the pressure pulse, slowly recovering after release (Figure 3.8a). Interestingly, this increase was independent of the direction of the pressure.

As can be seen from Figure 3.8c, a transient deflection in the pipette position occurred when pressure was applied, and another opposite deflection when it was released. The size of the deflection was estimated as $50 \backsim 15$ nm, while its duration was $280 \backsim 140$ ms (with time resolution limited by the hopping frequency to 70 ms).

The pipette itself was quite rigid, as were most of the materials of the holder. An exception was the rubber bung that gripped the pipette in place. One possible explanation of the pipette movement is that it reflects a brief

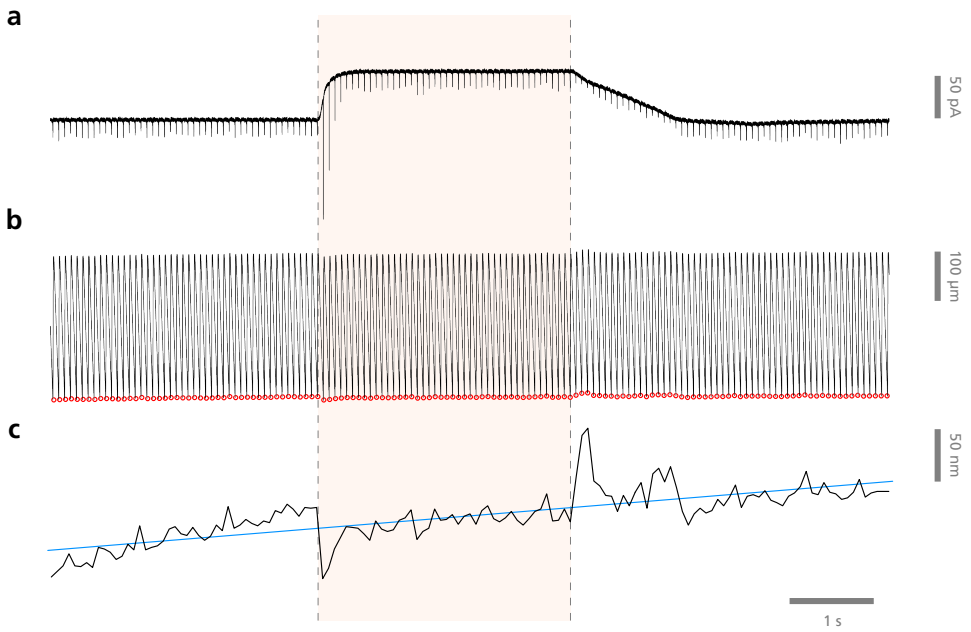

Figure 3.8: Effect of pressure on current and position. Suction was applied for the shaded period. **a** Current trace shows a sustained increase in the baseline current during the suction application, slowly recovering after release. **b,c** Detected surface position deflects briefly downward at the onset of suction, indicating a slight retraction of the pipette, and upward at release, indicating recovery to the original configuration. Deflection is $\sim$ 60 nm. There is underlying drift (blue line) of 7 nm/s and positional noise 20 nm RMS.

damped oscillation in the rubber in response to the pressure change; we have not attempted to confirm this experimentally.

Given the short length scale and duration of these perturbations, they were not considered to represent a major obstacle to smart patching. However, it was not possible to rule out their having some impact on patch success.

3.3.2 Testing lateral consistency

In order to return the pipette to a previously-scanned cellular compartment for patch clamping, the lateral positioning needed to remain consistent over time. To test this, brightfield optical images of a control sample (in this case a scratched plastic petri dish) were obtained while the scan position was

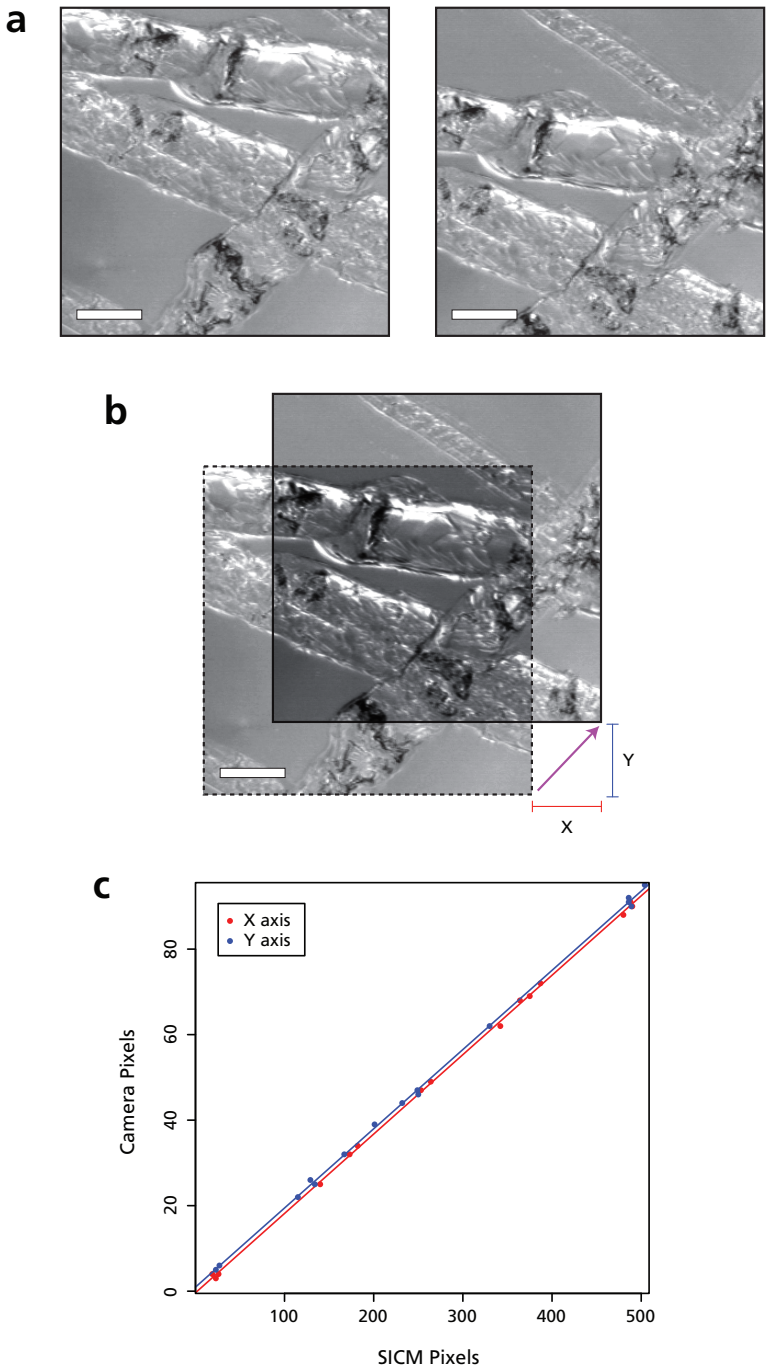

Figure 3.9: Optical tests of lateral consistency. **a** Sample is moved laterally using the SICM and optical microscope images captured at each position. **b** Pixel offset is measured for each optical image. **c** Optical offsets plotted against the corresponding SICM position. Full deflection for experiment shown is 80 µm. Relationship is strongly linear ($p < 10^{-10}$) in both directions, indicating a high degree of lateral consistency. (Scale bars, 50 µm.)

varied among a series of random locations. The relative displacement of each image was then measured and compared to the corresponding SICM coordinates.

Example optical images and a graph of the results from one such test are shown in Figure 3.9. In all cases the piezos were able to move reproducibly among arbitrary positions. There was also no measurable dependence between the X and Y positioning at this resolution.

We concluded that the lateral positioning system was sufficiently stable to allow for localised smart patch clamping, provided that the living cells used were also relatively immobile on the time scale of the scan.

3.4 Imaging control samples

Several control samples were employed at different times during the system development and implementation. The easiest and most frequently used, as already mentioned, was a plain plastic petri dish. This was useful for its simplicity and uniformity but lacked precise topographic features with which we could test the accuracy of scanning.

A well-defined target of appropriate scale was obtained from the polycarbonate substrate of a blank CD-R with the metallic film layer removed (Meenakshi et al. 2007). The surface features of such a sample are concentric grooves with depth 100–150 nm at a pitch of 1.5–1.6 µm (Tosello et al. 2010).

Initial scans were poor, exhibiting many of the problems described in previous sections. Although the CD grooves were detected, they were swamped by artefacts. An example is shown in Figure 3.10.

Extensive experimentation and tuning allowed the scanning to be improved to the extent that results like that shown in Figure 3.11 were possible. At this point it was feasible to compare the measured topography with that expected from the sample. Measurements from 10 apparently stable scans gave the pitch as $1.54 \backsim 0.05$ µm and the depth $140 \backsim 40$ nm, clearly within the expected range. We concluded that the SICM images were being acquired with acceptable accuracy for this sample.

Further control scans were subsequently performed using commercial targets designed for testing and calibration of AFM systems. Three such targets

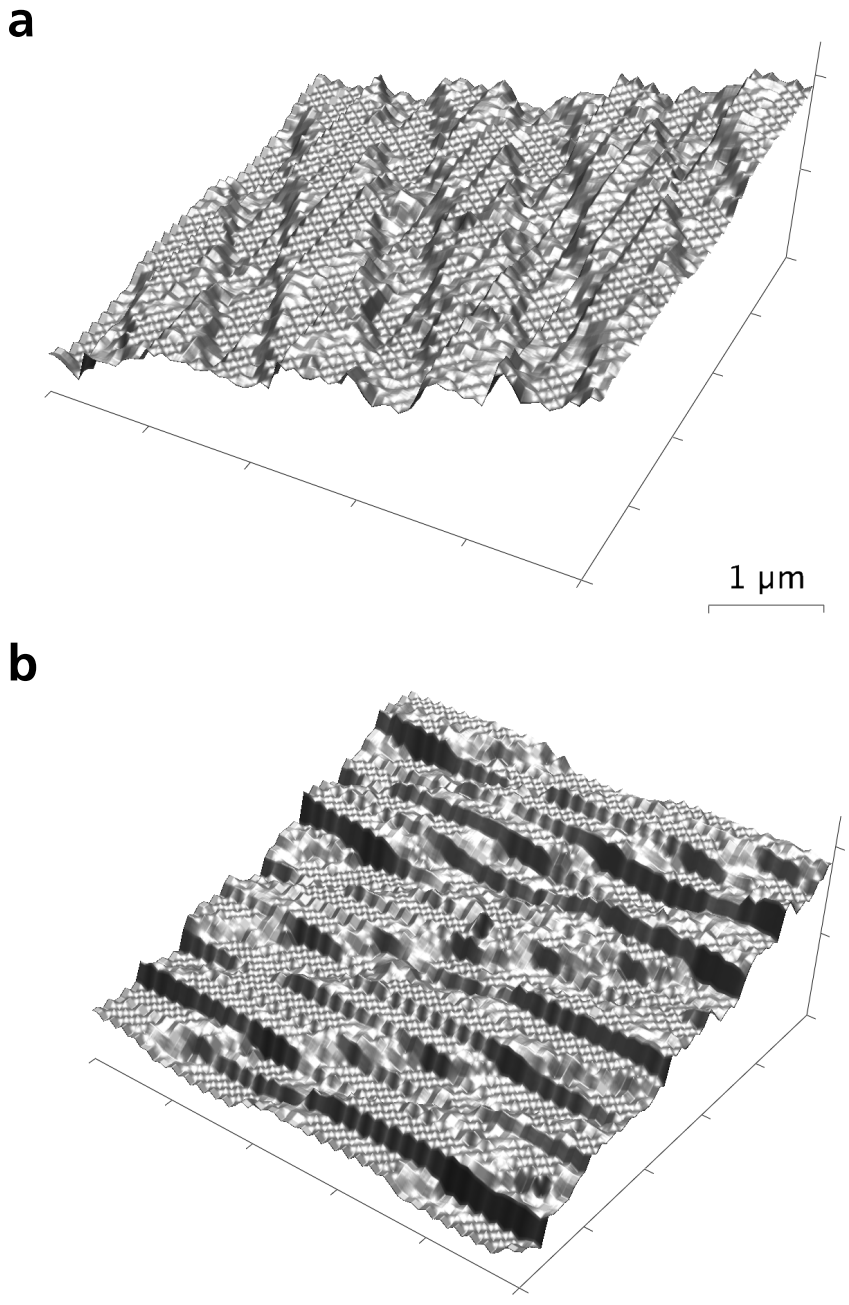

Figure 3.10: Artefacts in scan of CD grooves. The groove pattern is detected by the SICM, as can be seen if the row artefacts are aligned so as to be less intrusive (**a**). However, the artefacts are of the same size order as the real features (**b**).

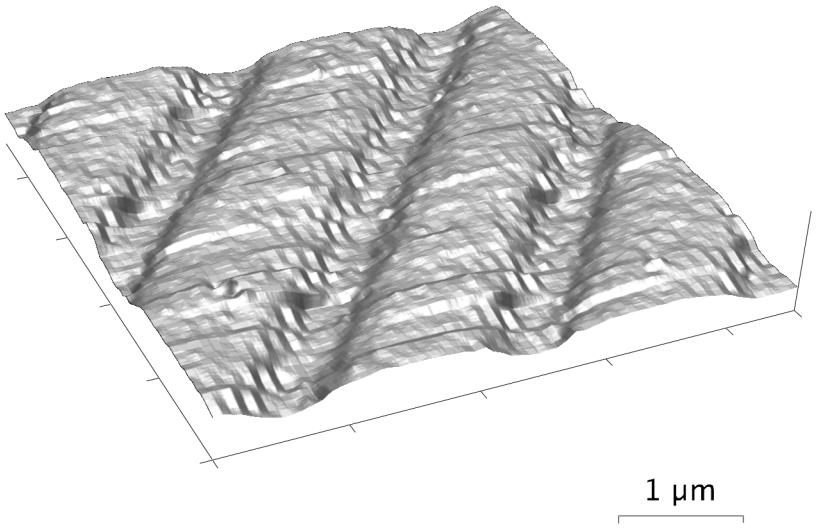

Figure 3.11: Improved scan of CD grooves with substantially reduced artefacts. Note that some residual scan pattern artefacts can still be seen, especially at the groove edges.

were used: BudgetSensors HS-100MG and HS-500MG step targets with 100 nm and 500 nm feature heights respectively, and a MikroMasch TGG01 target with 70° angled features of 1.8 µm height at a 3 µm line pitch. An example TGG01 scan is shown in Figure 3.12.

3.5 Imaging neurons

Many attempts to image complex cells such as cultured neurons were made in parallel to the control scans. Early results were very poor. Some relatively successful examples are shown in Figure 3.13; most scans were much less interesting, consisting essentially of noise and errors.

Artefacts were more pronounced for neurons than the control samples because the cultures were more convoluted and spanned a much greater range of feature sizes. Frequent collisions occurred with large objects such as the cell soma, due to inadequate hop heights, poor movement timing and otherwise unsuitable scan parameters. (With the PicoCube and split mode, for example, the maximum hop height was 4.9 µm, which we now recognise as

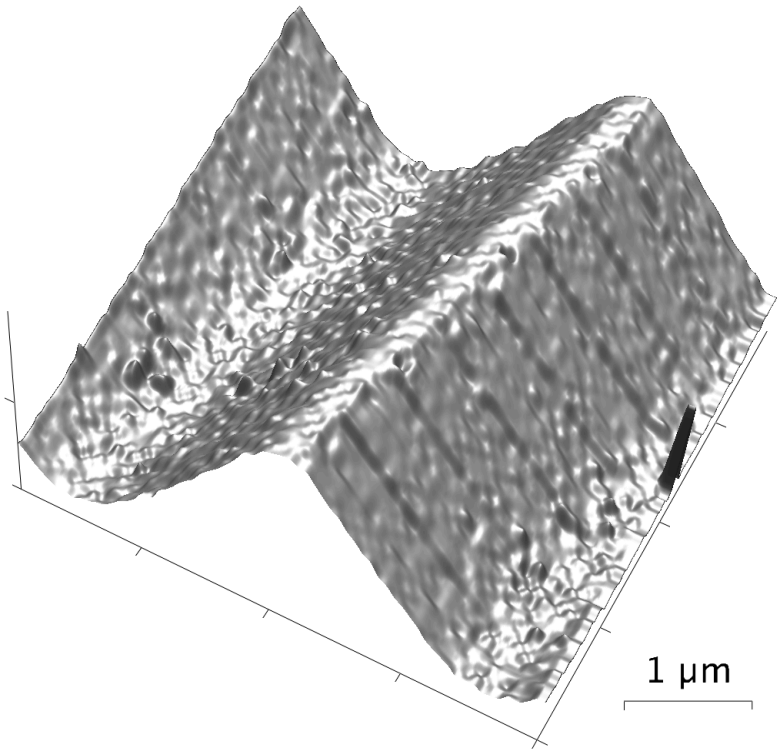

Figure 3.12: Scan of the MikroMasch TGG01 AFM target with 1.8 µm peak height. Slight drift is apparent between image rows.

insufficient to mount a large soma without collision.) In addition to optimising the many scan parameters, other aspects of the system such as the pipette pulling programs were also refined during this time.

Once many of the problems had been identified and ameliorated, we were able to obtain scans of neuronal topography such as those shown in Figure 3.14. Intricate networks of cellular processes could be imaged in detail, but at a significant cost in scanning time. Acquisition of the higher resolution scan 3.14b took nearly two hours (1:48), 16× as long as the lower resolution version (6.50). This sample was unusually stable, but there are nevertheless clear discontinuities along scan row edges. For more dynamic samples or those with a limited useful lifespan on the microscope, such long duration scans were not practical.

Scan times were primarily a function of the piezo speed and distance trav-

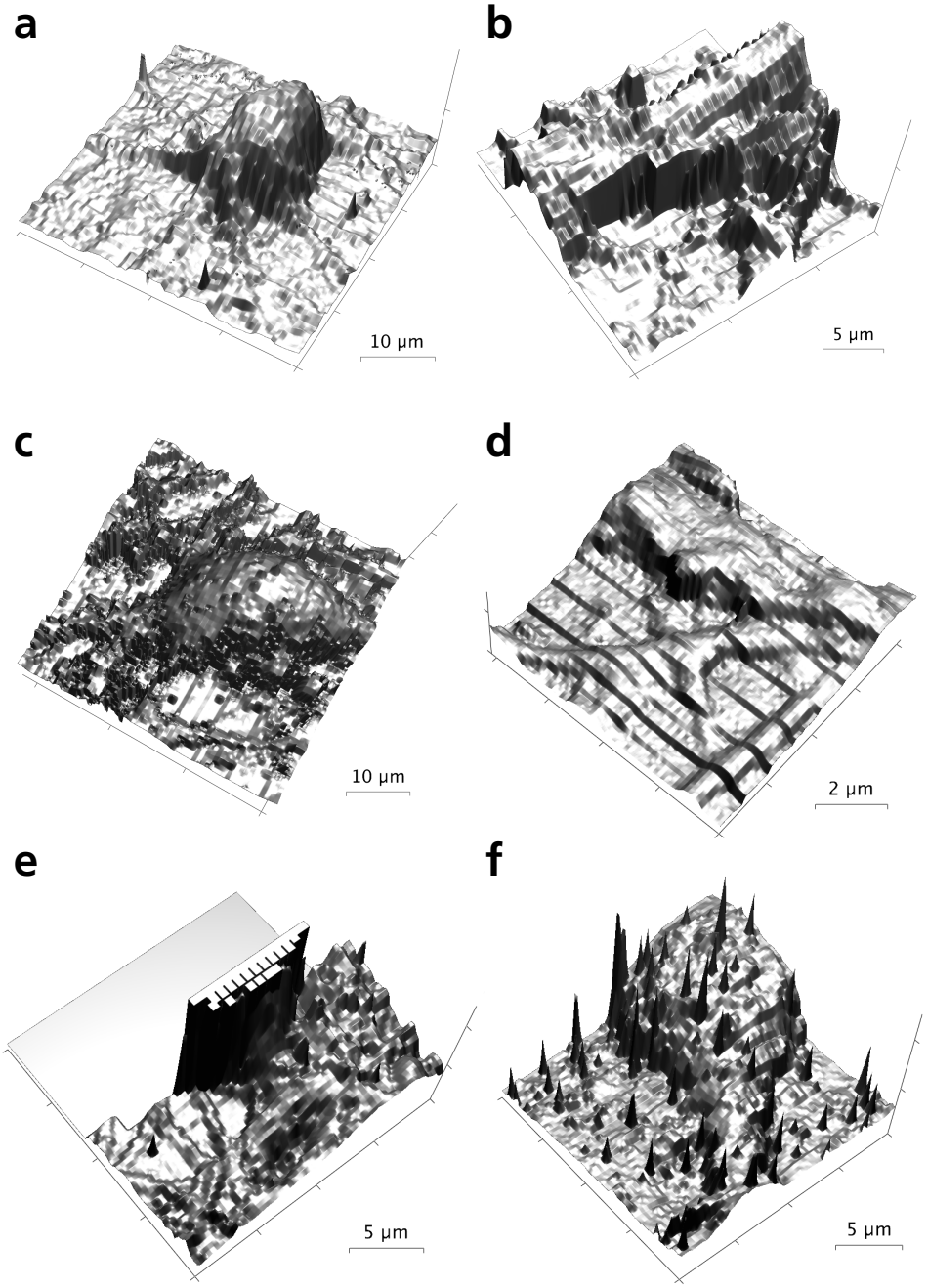

Figure 3.13: Early attempts at scanning neurons encountered many problems. Examples shown exhibit stairstep artefacts (**a**, **b**, **f**), positional instability (**d**, **f**), collision with steep features (**c**, **e**) and contamination of the tip (**f**). Scans **a**, **b** and **e** were acquired in split mode (§3.1.4).

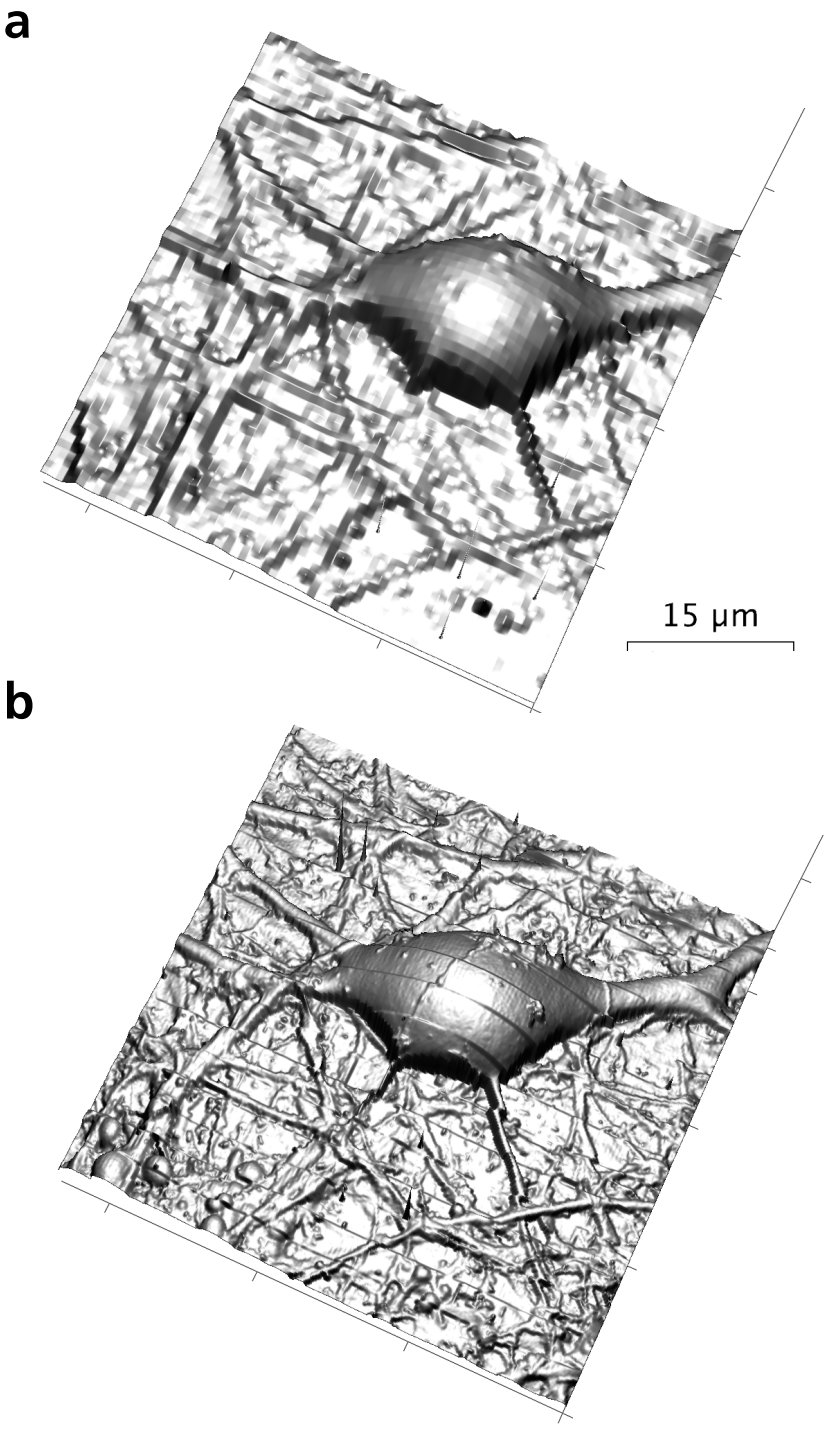

Figure 3.14: Scans of the same region of cultured hippocampal neurons at two different compression levels. In **a**, the sampling density is low and the resolution is poor, while in **b** there is much more detail but the much slower scan time leads to drift artefacts.

elled. Scanning large areas was slower than scanning small ones, even if the same number of points was acquired. Areas with a lot of height variation had to be scanned with larger hops and this added to the time taken. Scans could therefore be acquired more quickly by concentrating on flatter regions and measuring fewer points.

For most of our experiments, large scale topography was not the primary concern. Rather, the scans were required as a frame of reference for subsequent positioning. In such cases it was sufficient to scan at low resolution to identify possible targets, and then zoom in on a particular region of interest for more detailed examination (Figure 3.15). We were also often interested in synaptic contacts between processes, and could avoid the large cell bodies.

With such restrictions, together with tuning of the SICM equipment itself, we were able to reduce typical scan times to 2–5 min, making it practical to use scanning as part of a patching protocol. The images produced were typically not interesting in their own right and only a few contextually-relevant examples will be included in subsequent chapters.

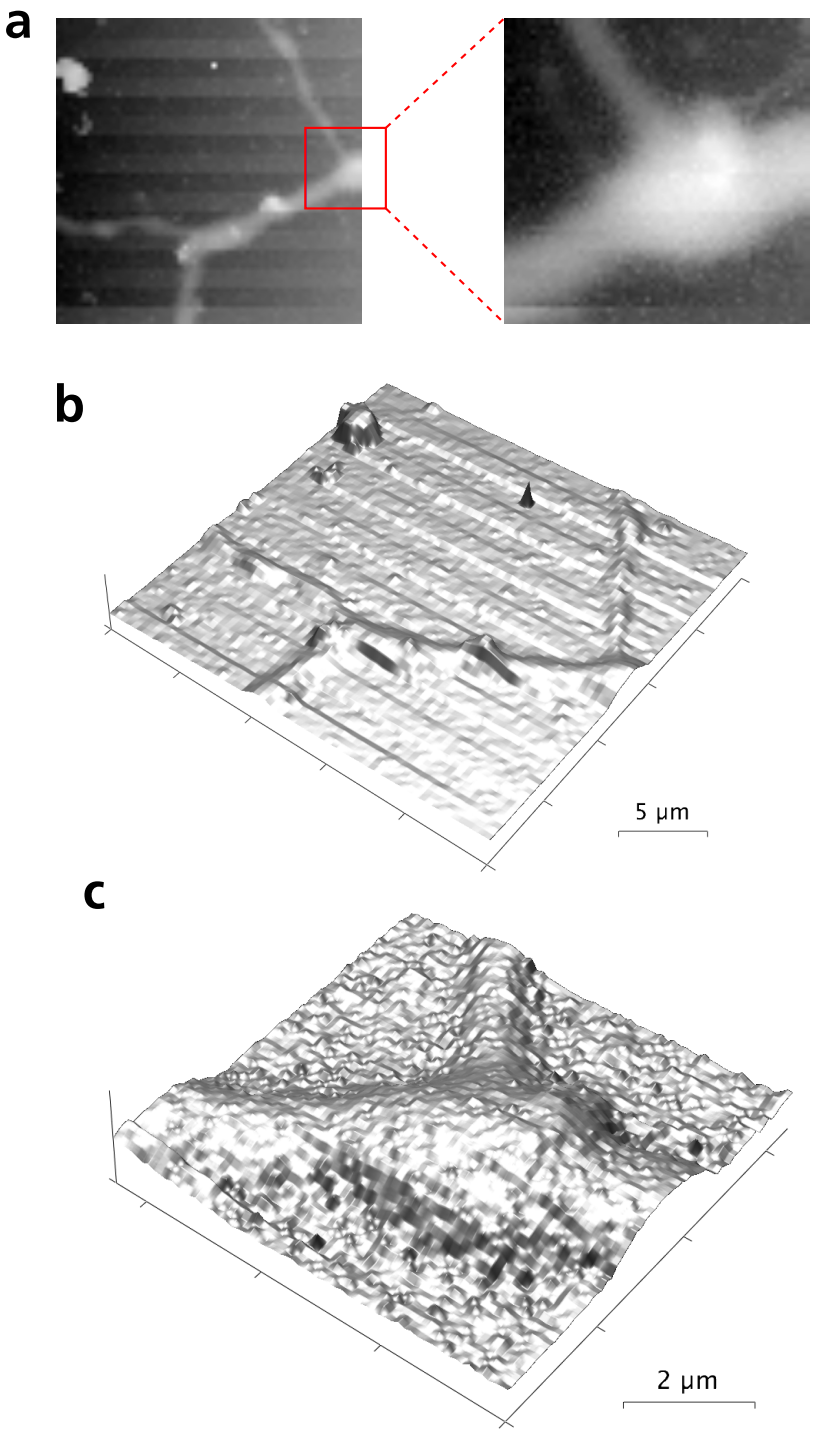

Figure 3.15: Zooming into a low-resolution scan. Initial sampling density is low, but provides a frame of reference. A region of interest, indicated by the red box, can be selected for higher resolution scanning. Scans show a possible synaptic contact between neuronal processes in cerebellar culture.

Chapter 4

SICM pipette tip geometry and approach characteristics

4.1 Estimating pipette tip geometry

SICM resolution and approach characteristics depend strongly on tip geometry. This is difficult to determine directly, so pipette resistance is often taken as a convenient proxy measure. However, it is a very imprecise metric.

In common with previous investigators, we found the resistance to vary in highly non-linear ways with glass type and pull parameters, and further that identical parameters could produce quite different results on different puller units.

Therefore, it was not ideal to rely on proxy measures alone, and some direct measurement was required to establish at least an approximate baseline for the geometric parameters of our particular pipettes.

4.1.1 Geometry measured by scanning electron microscopy

Sample SICM tips were drawn using the two main glass/pull combinations that we had in regular use. In addition, a small number were prepared using two other combinations for comparison purposes. The tips were imaged using scanning electron microscopy (SEM) as described in §2.8, capturing images from the side and also from directly towards the tip. Some example micrographs are shown in Figure 4.1.

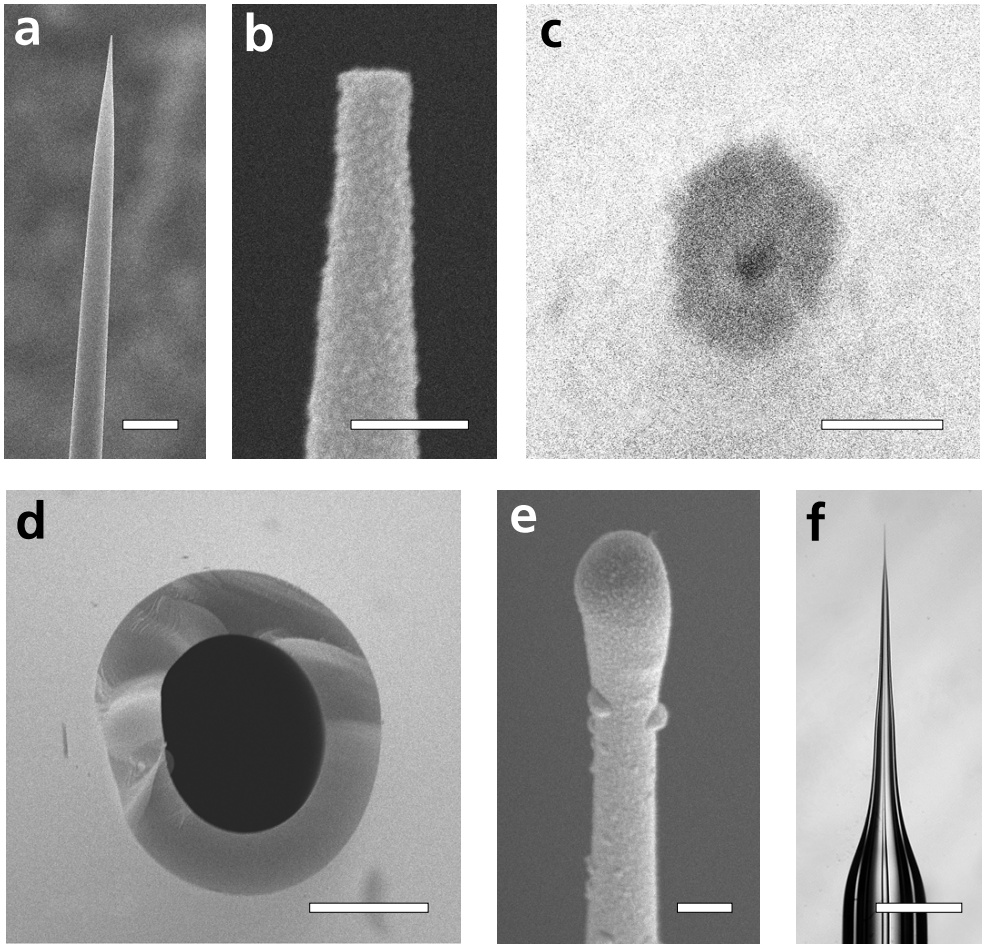

Figure 4.1: Scanning electron microscopy of pipette tip geometry
a-c Side and end views of the same tip. (Sutter #77; scale bars: 10 µm, 500 nm, 200 nm)
d Broken tip provides information about changes in relative thickness of the glass walls. (Sutter #77; scale bar 5 µm)
e Example of tip deformation. (Intracel #95; scale bar 1 µm)
f Optical image showing large scale geometry. (Sutter #77; scale bar 1 mm)

Where possible, the inner diameter (ID) and outer diameter (OD) at the pipette tip were measured from the SEM images, along with the cone angle close to the tip. In a small number of cases the tip was deformed or sealed over so that no meaningful measurement could be obtained (Figure 4.1e).

Due to the fragility of the tips, a proportion were broken during sample preparation, and these were also measured to provide some information on how the pipette geometry varies longitudinally. While the location of the break relative to the absent tip was unknown, the position could be broadly estimated by comparison with unbroken examples and, importantly, the ratio of OD:ID could be measured to reveal something of the internal geometry.

These measurements are summarised in Table 4.1, and the key values plotted in the graphs of Figure 4.2.

The sample sizes are small, so we can only draw tentative conclusions regarding population values. Nevertheless, the measurements for Sutter #77 pipettes are well clustered, and we can use these to estimate the geometry at

	Intracel #95	Sutter #77	Sutter #96	WPI #75
Pipettes	9	8	4	3
Broken	3	3	1	2
Deformed	3	0	0	0
Original Glass				
OD (mm)	1.0	1.0	1.0	1.0
ID (mm)	0.58	0.5	0.5	0.75
OD:ID	1.72	2.0	2.0	1.33
Unbroken Tip				
OD (nm)	445 ∽ 163	280 ∽ 30	360 ∽ 15	340
ID (nm)	230 ∽ 141	70 ∽ 15	150 ∽ 15	190
OD:ID	2.55 ∽ 0.82	4.00 ∽ 0.99	2.50 ∽ 0.11	1.79
Angle (°)	9.1 ∽ 1.2	8.5 ∽ 0.3	6.6 ∽ 0.4	—
Broken Tip				
OD:ID	1.37 ∽ 0.03	1.62 ∽ 0.04	1.55	1.17, 1.29
Angle (°)	6.2 ∽ 0.6	2.0 ∽ 1.0	7.7	—

Table 4.1: Tip geometry measurements made from scanning electron micrographs

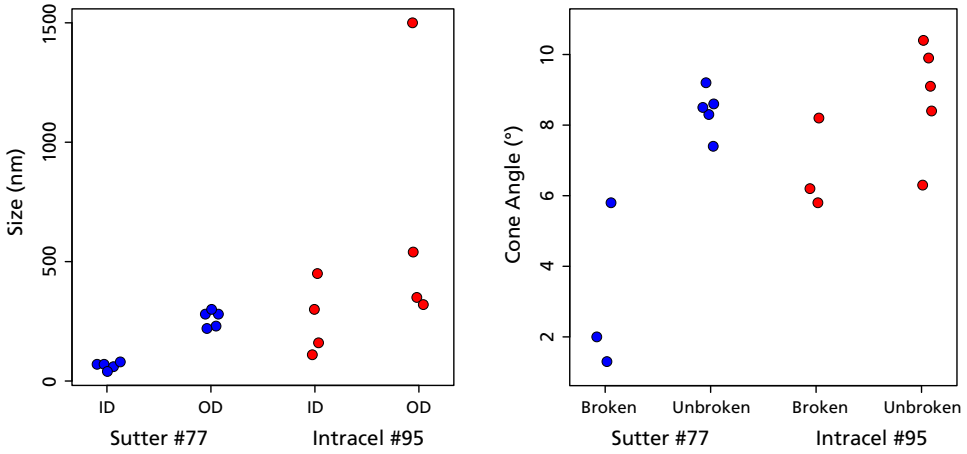

Figure 4.2: Tip measurements for Sutter #77 and Intracel #95 pipettes. ID and OD sizes are for unbroken tips.

the tip. Combined with measurements of larger scale geometry from optical micrographs like Figure 4.1f, we construct the model exterior profile shown in Figure 4.3. The segments are labelled for ease of reference in subsequent sections. Additional segments further up the pipette body were also estimated, but have been omitted here because their contribution to the pipette resistance is negligible (§4.1.3).

Since the pipette glass is virtually non-conducting in comparison with its filler, we are more interested in the interior geometry, but we have only very limited direct measurement of this and must extrapolate from the the OD:ID ratio.

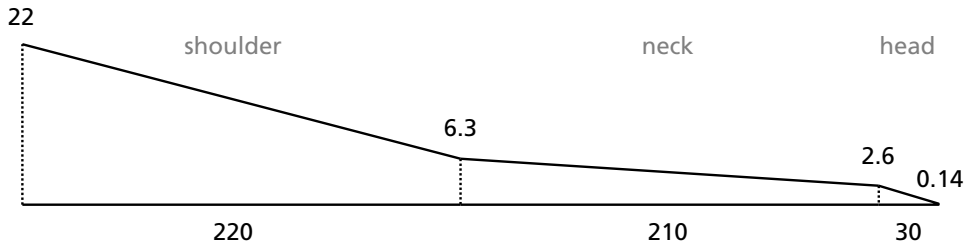

Figure 4.3: Estimated exterior profile of Sutter #77 tip. Sizes are shown in microns, with vertical scale exaggerated for visibility.

4.1.2 Proportional wall thickness is not conserved

A common rule of thumb for estimating interior geometry is that the OD:ID ratio is maintained along the pipette length (Corey and Stevens 1983; Brown and Flaming 1986). However, our measurements contradict this. We invariably observe that the ratio at the tip is increased relative to the original ratio of the glass—that is, the glass is thickened and the tip opening proportionally smaller—while the ratio further down the shank is decreased.

Figure 4.4 shows these results for the Sutter #77 and Intracel #95 pipettes; the observation also holds for all other pipettes measured (see Table 4.1). Considering these results purely as categorical counts, the consistency is highly significant ($p = 4.01 \times 10^{-7}$, Fisher's exact test).

Intuitively, this is not surprising. The pipette glass is under tension during the pull. When the glass shears and the tension is released, we would expect there to be some retraction of the extended glass back towards the tip. Note that this thickening is exactly the opposite of the results found by Brown and Flaming (1986). However, their pulling conditions are different enough that direct comparison may not be meaningful.

It is not clear from our observations how the difference in OD:ID ratio is distributed longitudinally. From the surviving geometry, it appears that the

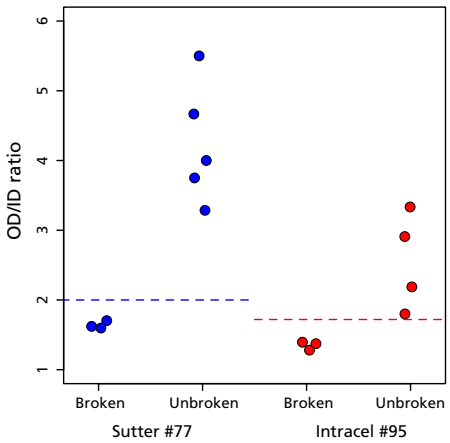

Figure 4.4: OD:ID ratios at and away from the pipette tip. Dashed lines indicate the original OD:ID ratio of the glass.

break points where we see the reduced thickness occur in the neck region. This suggests that the thickening of the glass walls is localised to the head. We will therefore assume that there is some transition within that segment, with the lower OD:ID ratio maintained elsewhere.

We represent this scenario using the model illustrated in Figure 4.5. The head segment is subdivided into three, with an intermediate transitional region interpolating between the two observed OD:ID levels.

In the next section we will attempt to put some bounds on the relative sizes of these regions. But even without doing so it is clear that the qualitative effect of this geometry is to increase the localisation of the pipette resistance at the tip, steepening the corresponding voltage drop ΔV and increasing the electric field $-\nabla V$. In addition, the hypothesised presence near the tip of

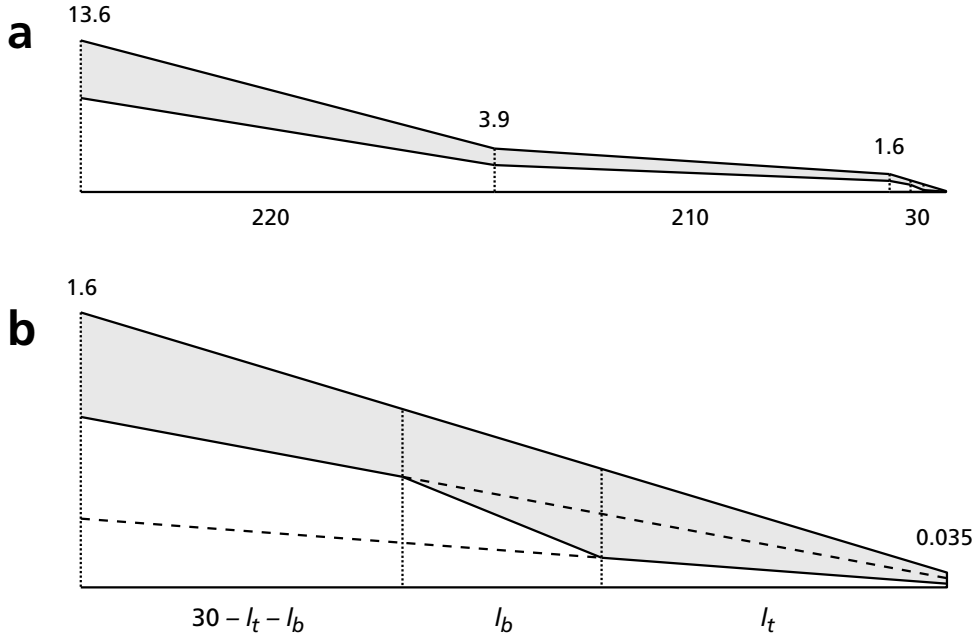

Figure 4.5: Model interior profile of Sutter #77 tip. Heights shown are internal, corresponding to the external ones in Figure 4.3. (Dimensions in microns.)
a The shoulder and neck segments maintain the low OD:ID ratio observed in broken pipettes.
b In the head segment, the low OD:ID applies at one end and the high OD:ID at the other. A boundary region, of unknown length l_b, is introduced to effect the transition between the two.

a narrow segment with a shallow cone angle has implications for the way the tip would interact with a cell membrane and the area of membrane that could be sampled during patch clamp recording. These matters are revisited in Chapter 5.

4.1.3 Comparing estimated tip geometry with resistance

If we ignore any conductivity through the glass walls, we can approximately model the resistance of a pipette as that of a shaped volume of the filler solution. Assuming cylindrical symmetry and a radial profile described by some function $f(x)$ of longitudinal position x, the resistance is given by (Snell 1969):

$$R = \frac{\rho}{\pi} \int \frac{1}{f^2(x)} \mathrm{d}x \tag{4.1}$$

where ρ is the resistivity of the filler.

Following the profiles obtained in previous sections, we approximate the pipette as a series truncated-conical segments. Each segment is described by a linear function, $f(x) = ax$. We can conveniently define the slope a in terms of the end radii r_1 and r_2 and either the segment length l or the cone angle θ, such that:

$$\begin{aligned} R_{con} &= \frac{\rho}{\pi} \cdot \cot\left(\frac{\theta}{2}\right) \cdot \left|\frac{1}{r_2} - \frac{1}{r_1}\right| \\ &= \frac{\rho}{\pi} \cdot \frac{l}{|r_1 - r_2|} \cdot \left|\frac{1}{r_2} - \frac{1}{r_1}\right| \end{aligned} \tag{4.2}$$

Taking the filler solution to be 150 mM KCl with $\rho \approx 51\ \Omega \cdot \mathrm{cm}$, and using the sizes determined in §4.1.2, we calculate a resistance for the shoulder segment ($r_1 = 13.6$ µm, $r_2 = 3.9$ µm, $l = 220$ µm) of 670 kΩ and for the neck ($r_1 = 3.9$ µm, $r_2 = 1.6$ µm, $l = 210$ µm) of 5.4 MΩ. Similar calculations for the much larger body segments of the pipette (not shown) suggest they contribute less then 500 kΩ altogether.

In addition, we can approximate the external access resistance using the formula of Hall (1975):

$$R_{acc} = \frac{\rho}{4r} \tag{4.3}$$

For our median measured tip radius of 35 nm, this predicts an access resistance of 3.6 MΩ.

In practice, pipettes of this kind with comparable high [K^+] filler (as used in experiments described in §5.1) had a median resistance of 155 MΩ. The vast majority of that resistance, ∼145 MΩ, thus remains to be attributed to the head.

Using the 3-segment model from Figure 4.5, we calculate head resistances for different values of the tip and boundary segment lengths l_t and l_b. (We have fixed the overall head length at 30 µm, so these two values fully determine the size of the other segment.) The results are shown in Figure 4.6.

It is clear that the head resistance is dominated by the length of the narrow tip segment. The split between the other two segments is much less important unless l_t is small.

We can see from the graph that if the tip is to contribute the expected ∼ 145 MΩ to the pipette resistance, l_t must lie within a narrow range of values, which we calculate to be 1.6–2.6 µm. In this range, the resistance curve is very steep for all values of l_b, and the spread between curves is also large. Thus, even small changes in geometry would lead to large variation in resistance.

The actual MAD of these recordings was 36 MΩ, so resistance was indeed quite variable. This spread is indicated by the dotted lines in Figure 4.6. Calculating the full range of parameter values consistent with this spread, the tip length l_t could be as small as 0.3 µm at the lower end of the resistance range (with the whole remaining length given over to l_b), or as much as 5.8 µm at the high end (with $l_b = 0$). This implies a significant level of uncertainty in our geometry estimate.

In practice, it is unrealistic to fix the external geometry and attribute all resistance changes to redistribution between these hypothetical internal segments. Recall from Table 4.1 that the tip diameter measurements had a MAD of 15 nm. If the same range of {l_t, l_b, resistance} curves shown in Figure 4.6 are plotted for different values of the tip radius, the results are as shown in Figure 4.7. We observe that small changes in tip radius substantially shift the whole envelope of resistance. The degree of tip size variation seen in

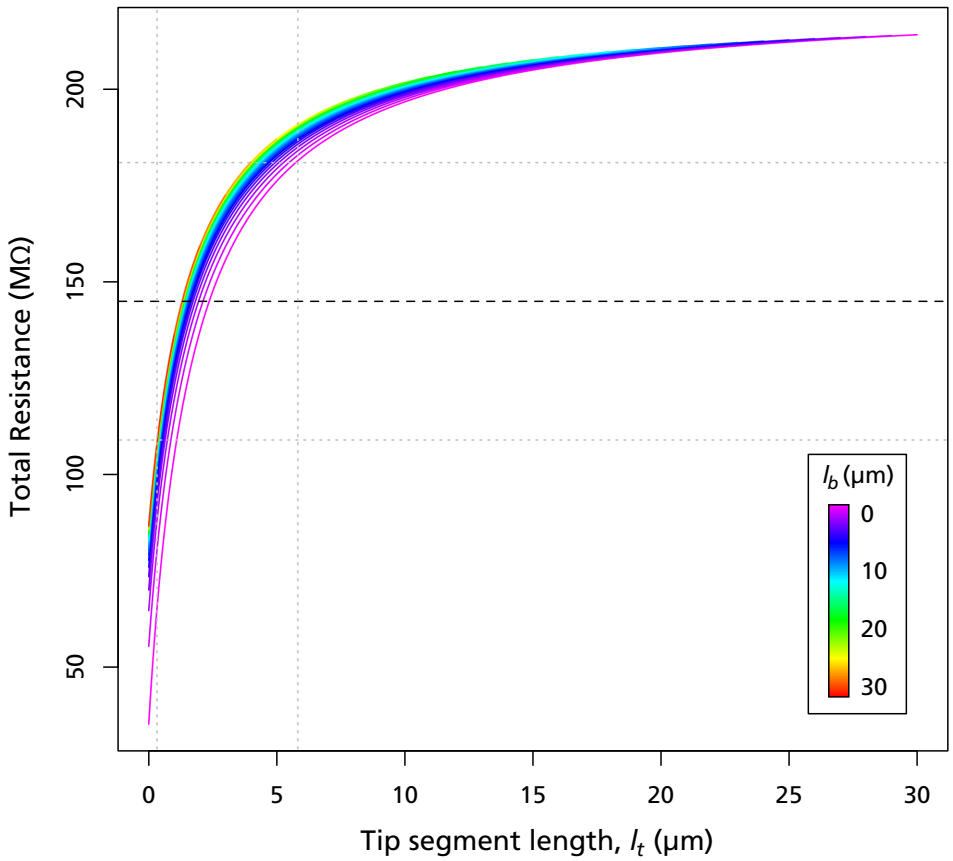

Figure 4.6: Variation of head resistance with l_t and l_b. For each curve, l_b is held at a fixed length between 0 and 30 µm, indicated by colour, while l_t is varied. The dashed line indicates median measured resistance. Dotted lines show the resistance MAD and the range of l_t consistent with it.

the SEM images is sufficient to account for the range of measured resistances without requiring large changes in the relative sizes of the internal segments.

Since the former has an empirical basis and the latter is speculative, we conclude that tip radius is probably the source of most of the resistance variation. While it remains possible that there is considerable variability in the internal geometry, comparison of the resistance MAD with the range spanned by the curves in Figure 4.7 suggests that l_t is more likely typically short, on the order of 1–2 µm.

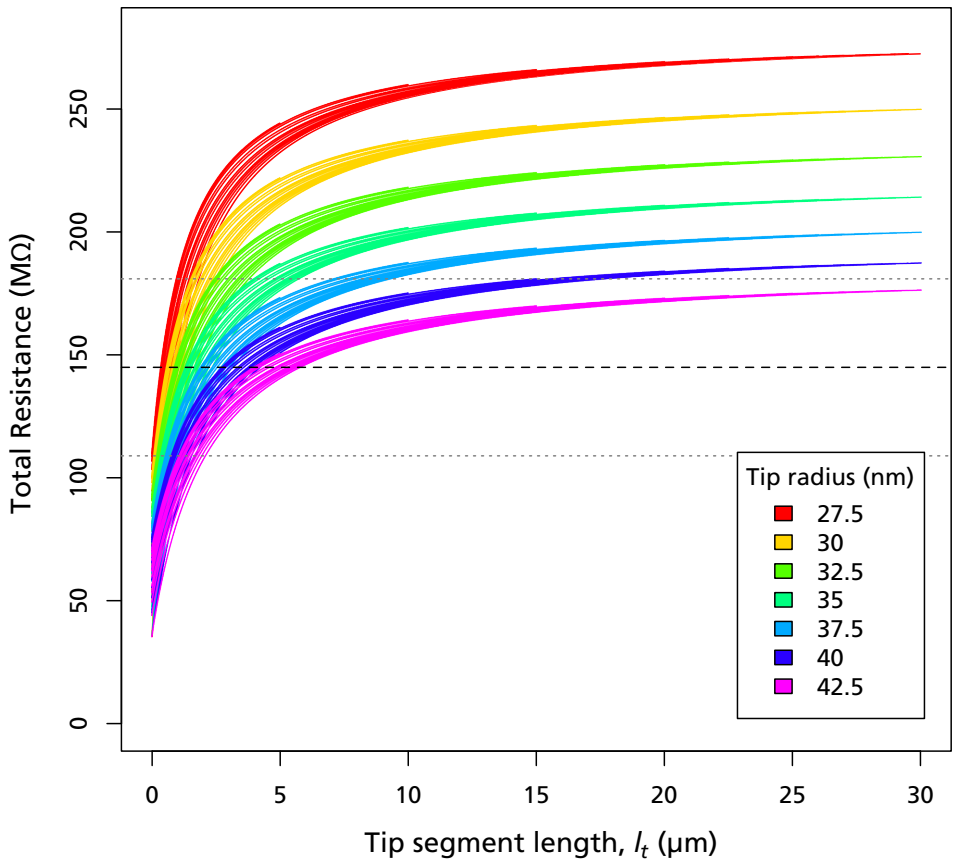

Figure 4.7: Variation of head resistance with tip radius. Each set of curves varies l_b and l_t as in Figure 4.6, for a given tip radius, indicated by colour. The dashed line shows the median expected resistance while the dotted lines show the MAD.

4.2 Surface detection

As explained in §1.4.5, SICM topographic imaging is based on the consistency of current drop-off with pipette tip proximity to a surface. For modelling purposes, it is typically assumed that the target is flat, immobile and uniformly non-conductive and that the effects of surface charge can be ignored. Under such circumstances, the experimental approach curve is stable and repeatable, and its characteristics can be well modelled using finite element approaches (Edwards et al. 2009; Rheinlaender and Schäffer 2009; Del Linz 2011). An example of such a model approach curve was shown in Figure 1.3.

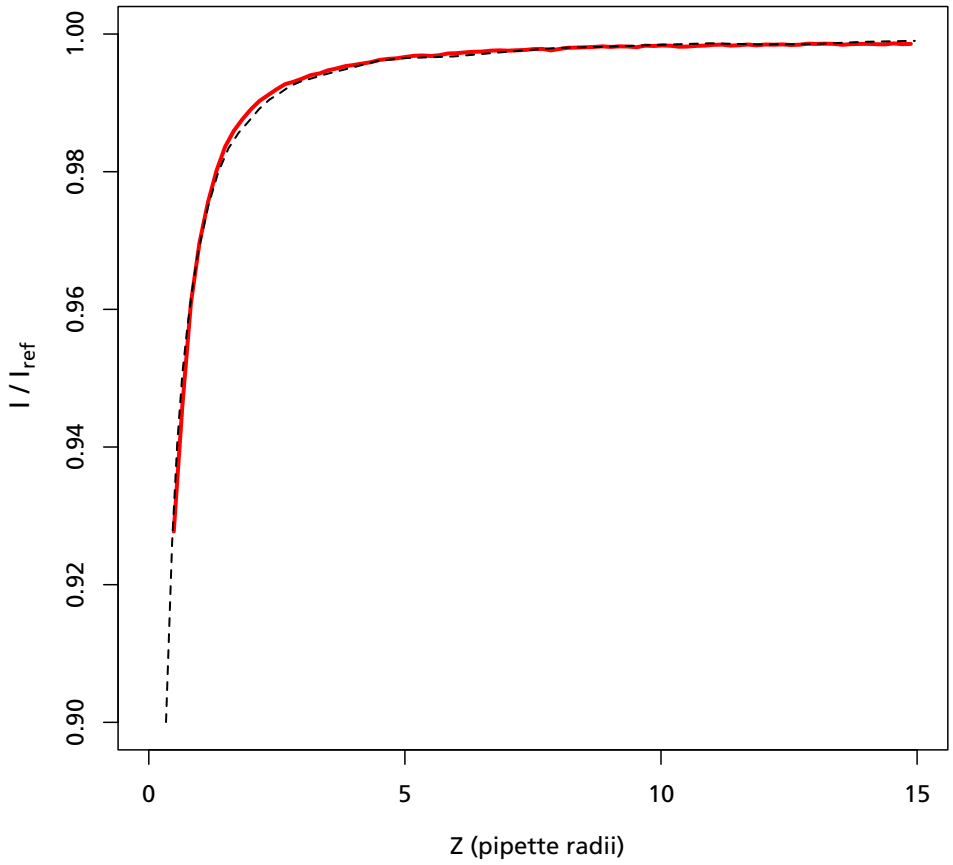

Figure 4.8: Approach to a hard surface agrees with that predicted by a finite element model. Dashed line shows current-distance relationship for geometry determined in §4.1. Red curve shows measured approach to plastic petri dish surface. Physical distances were scaled to maximise model fit, giving an estimated pipette radius of 27 nm.

Another simulated approach is shown in Figure 4.8, together with a curve measured experimentally by approaching the rigid surface of a plastic petri dish with a Sutter #77 pipette. The model results were generated by Samantha Del Linz, using the tip geometry estimated in the previous section. It can be seen that the shapes of the two curves are in very close agreement. The pipette radius corresponding to this fit was 27 nm.

Perfectly flat, static surfaces are not very interesting. We usually wish to apply SICM to samples which violate one or more of the model assumptions. The plasma membrane of a living cell, for example, will often be dynamic, deformable and topographically complex. To see how well the current behaviour in such cases compares to the model, approaches were measured to the surfaces of several cell types.

Two different approach protocols were used.

In one set of experiments, the approach was measured repeatedly using the SICM hopping mode with a gradually increased set point. The pipette fall rate was kept low (down to 1 nm/ms) to minimise overshoot. Each hop measured the portion of the approach curve up to the set point before retracting. The current–distance relationship was estimated by averaging over many hops.

The results from one such set of measurements are shown in Figure 4.9. These were made with the same pipette used for the rigid approach curve in Figure 4.8; the measured version of that approach curve is shown as a dashed line in each plot for comparison. It can be seen that even at the smallest set point shown, corresponding to a current reduction of just 0.3%, the approach curve is diverging from the one measured for a rigid surface. As the set point increases, so does the divergence.

The exact location of the cell surface in these experiments is not known. If we make the assumption that the most distant portion of the approach, which most closely resembles its rigid counterpart, is an accurate reflection of the true relationship, then we can align the two curves and use this to estimate the surface position. The grey lines on the graphs show this estimate. However, it is important to note that the assumption may be invalid. If the approach characteristics are not commensurate, then the true surface may be lower.

Nevertheless, it seems very likely that by the time we get to the higher set

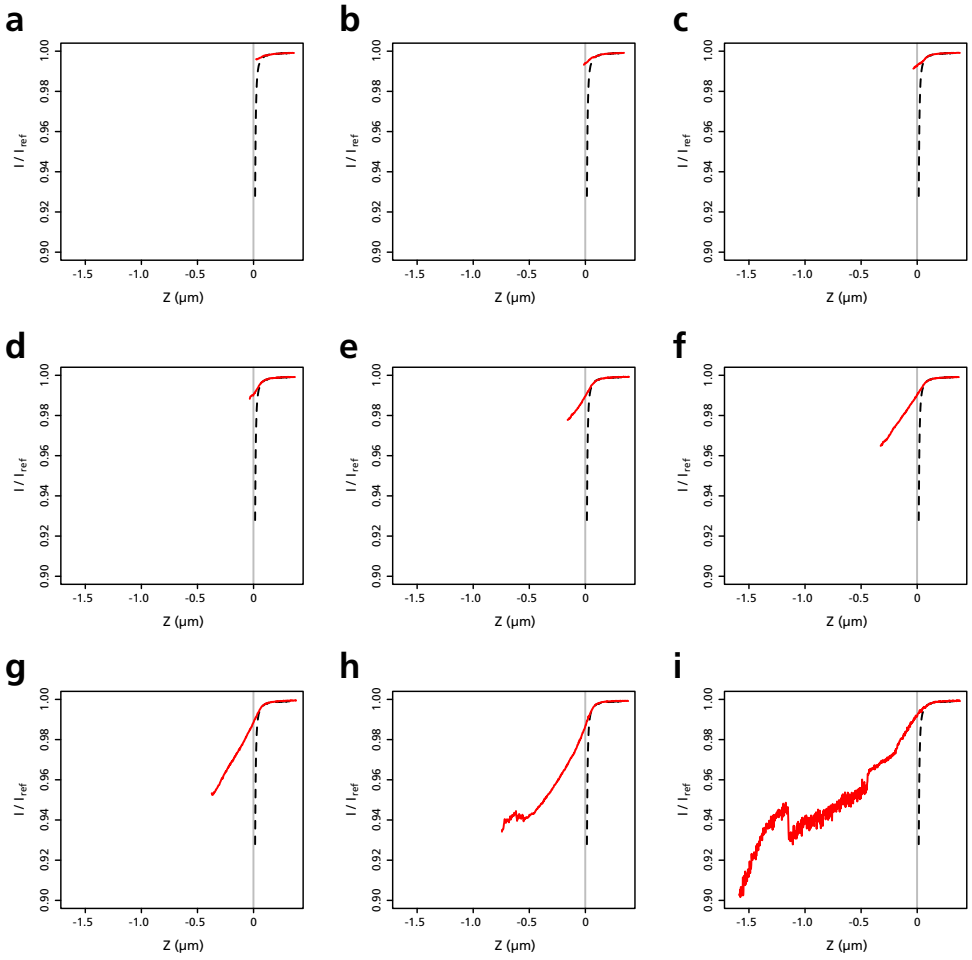

Figure 4.9: Approach curves to HEK soma obtained in hopping mode. Curves are shown for the same pipette as in Figure 4.8. Dashed line shows the previously measured approach to the dish surface. Z distances are shown relative to the estimated surface position. Set point was increased for each panel: **a** 0.3%; **b** 0.5%; **c** 0.7%; **d** 1%; **e** 2%; **f** 3%; **g** 4%; **h** 5%; **i** 10%.

points in panels e–i, some interaction is occurring between the pipette tip and the cell membrane, and this is distorting the approach curve. These lower reaches of the curve are not consistent from cell to cell or even over time on the same cell.

In a second set of experiments, single one-way approaches to the cell surface were measured, starting with the pipette several µm away from the surface and advancing it in 5 nm steps, with a 1 s pause between each step, until well below the surface. Figure 4.10a shows a representative example of such an approach.

Once again, the true surface position is not known. In this case we did not record a hard surface approach curve for comparison. The grey line indicates an arbitrary cut-off position corresponding to a set point of 1%. The dashed line corresponds to a more realistic scanning set point of 0.5%.

As with the hopping experiments, the measured approach differs significantly from the model curve and surface detection is ambiguous. The steepening current drop with proximity that is seen on approach to a rigid surface does not occur. Instead, it seems clear that the tip is interacting with the membrane, and it is likely that some form of contact with and/or deformation of the surface is taking place.

During the approach there was also an apparent increase in current noise, as shown in Figure 4.10b. This may correspond to contact between the tip and the membrane. However, it could also be simply a function of the steepness of the approach curve, reflecting some constant level of positional uncertainty, perhaps due to vibration of the tip. We note that the highest noise peaks correspond exactly with the steepest regions of the approach curve, consistent with the latter hypothesis.

4.2.1 Implications for SICM imaging and smart patching

In all cases where we have measured an approach curve to a cell membrane ($n = 17$ for hopping, 6 for one-way approaches), there has been gross deviation from the standard model. The details differ for every cell and pipette, but the basic features are consistent. The expected rapidly-increasing current drop does not occur. Indeed, the current change is typically not monotonic and there is some recovery as the pipette advances. We speculate that

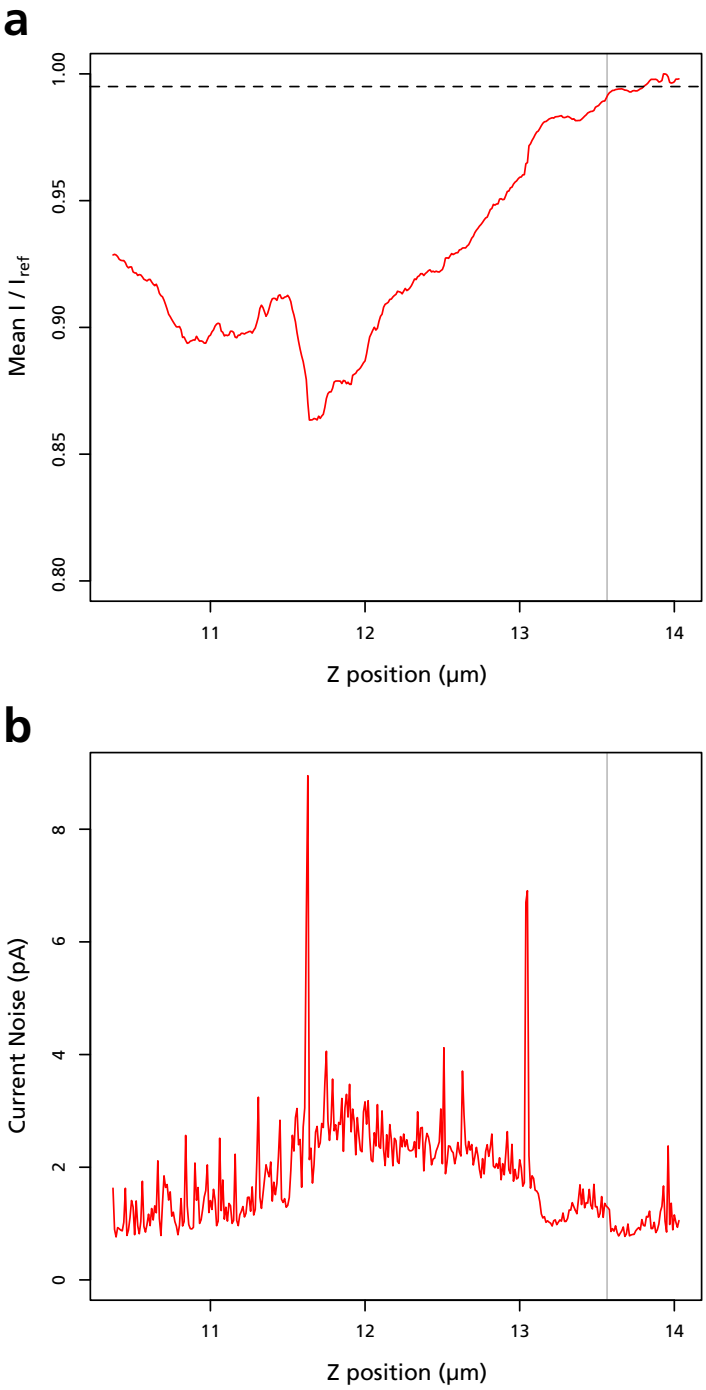

Figure 4.10: Single approach to HEK soma. **a** Mean current as pipette is lowered towards cell in 5 nm steps. Current is plotted as a fraction of the baseline current far from the surface. **b** Variation of current noise with position, calculated as the standard deviation during the period of recording at each distance.

this recovery might correspond to the tip penetrating the membrane, but we do not yet have any independent evidence for this suggestion.

The shape of the approach curve is important for the quality of SICM imaging. Nevertheless, we saw in Chapter 3 that images of cells can be obtained with reasonable reliability. This is probably due to the very low set points typically used when scanning such targets. The approach curve to a cell most closely resembles that to an ideal surface over this most distant range, when the likelihood of more complex tip–surface interactions is low.

In the case of smart patching, it is necessary to bring the pipette tip very close to the surface in order to obtain a seal. Because of the variability of the current drop near to cells, estimates of the surface position are necessarily unreliable. In particular, the lower reaches of the approach curve do not provide useful proximity information. Instead, we have adopted the strategy of halting at the position detected at a low set point and then advancing by an increment based on the estimated tip size. Given the many sources of error, such an approach is inevitably imperfect and patching will often fail. Nevertheless, as will be described in the following two chapters, successful recordings have been achieved.

Chapter 5

Consequences of pipette size for patch clamp recording

5.1 Recording from control cells

To test how differences in pipette size affect the viability of patch clamp recording in practice, control experiments were performed using a well-characterised, cloned ion channel transiently expressed in human embryonic kidney (HEK 293) line cells. The pore-forming subunit, **bslo**, of the high conductance potassium (BK) channel was chosen as a suitable target on the basis of its distinctive conductance and its voltage sensitivity, allowing for experimental modulation of open probability in the cell-attached patch configuration.

HEK cells were cultured as described in §2.1.2 and co-transfected with bslo and EGFP using Lipofectamine (§2.2.2). Transfected cells were identified using widefield epifluorescence.

Patch recordings were attempted using both SICM imaging pipettes (Sutter #77, 137 $\backsim$ 53 MΩ) and more conventional single-channel patch pipettes (Harvard F, 18.6 $\backsim$ 7.1 MΩ). All tests were performed on the same SICM rig and using the same approach protocol. Lateral positioning was performed under optical control, although in some cases when using SICM pipettes a topographic scan was also performed.

The conductance of bslo exhibits a strong dependence on the external K^+

concentration, ranging from ∼100 pS in a low [K^+] solution up to ∼250 pS in high [K^+]. We obtained recordings in both environments, using either standard Krebs bath solution [20] or a higher [K^+] BK solution [27] as the pipette filler for different experiments.

5.1.1 Rates of success and failure

Several experimental outcomes were possible. A proportion of experiments were abandoned without attempting a patch, usually due to the pipette becoming blocked. Additionally, patch attempts did not always result in formation of a gigaseal.

Where a seal was successfully obtained, the resulting recordings were classified as follows. When channels were present with measurable openings and the overall current trace was sufficiently well-behaved for a unitary conductance to be estimated, the recording was classified as "good" (Figure 5.3). If the recording was apparently clean and stable but showed no evidence of channel activity over a sustained period of time and a range of applied voltages, it was classified as "empty" (Figure 5.4).

In addition, a number of recordings exhibited peculiar artefacts or state changes, and these recordings were denoted "strange" (Figures 5.5–5.7). This category was not exclusive: some nominally good recordings also had strange features. We will more closely examine the nature of these artefacts in subsequent sections, but first we summarise the distribution of the different characteristics between the experimental groups.

Table 5.1 lists the counts and percentages broken down both by glass type and by filler solution, and the proportional results are graphed in Figure 5.1.

The most apparent differences in these results lie in the distribution of empty and strange recordings. With small pipettes, a third of all recordings were empty, whereas with the larger pipettes there were none at all. Further, of 10 recordings identified as strange, all but one were from recordings with small pipettes.

We tested the different recording outcomes for significance according to pipette size and filler type, using Fisher's exact test with a Holm-Bonferroni correction for multiple comparisons. By this measure, only two effects were found to be significant: pipette size had a clear effect the number of empty

	Harvard F		Sutter #77	
	High [K^+]	Low [K^+]	High [K^+]	Low [K^+]
Total Pipettes	54	58	27	71
Seal Attempted	25 (46%)	43 (74%)	22 (81%)	49 (70%)
Sealed	20 (80%)	26 (60%)	18 (81%)	42 (86%)
Good	16 (80%)	5 (19%)	5 (24%)	9 (21%)
Empty	0 (0%)	0 (0%)	6 (35%)	14 (33%)
Strange	0 (0%)	1 (3%)	4 (24%)	5 (12%)

Table 5.1: Experimental outcomes representing pooled data from both large and small pipettes. Percentages are given with respect to the closest containing set, ie: Attempted as a proportion of Total; Sealed as a proportion of Attempted; Good, Empty and Strange as a proportion of Sealed.

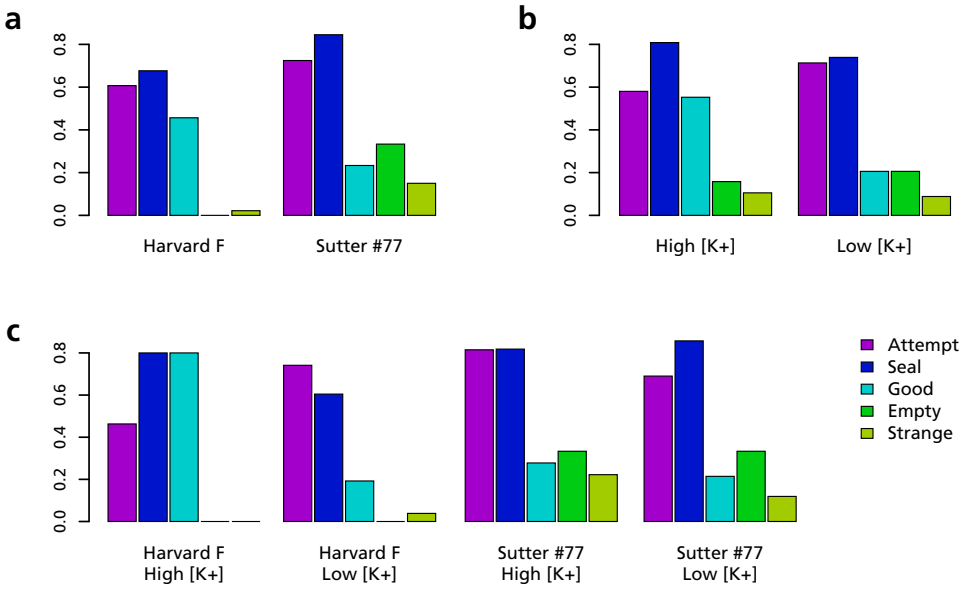

Figure 5.1: Graphs of outcome proportions, with respect to the containing set, as in Table 5.1 above. Experiments are grouped by **a** pipette type; **b** filler solution; **c** both.

recordings ($p = 1.4 \times 10^{-5}$), while the filler type affected the number of good recordings ($p = 0.002$).

The changes in incidence of good and strange recordings with pipette size were *not* significant after the Holm-Bonferroni correction ($p = 0.09$ and 0.12 respectively), although either would have been if taken in isolation. Nevertheless, the strangeness was interesting enough to merit further investigation.

We have implicitly assumed that the most important difference between the two pipette types is the size of the tip. In addition to the simple type classification, we also have available a continuous, albeit indirect, proxy for differences in size, the pipette resistance. We might therefore expect there to be a relationship between resistance and the recording outcome.

To test this, we performed a logistic regression to see whether the binary outcomes "good", "empty" and "strange" were significantly dependent on resistance. Taking p values from the regression Wald z statistic and again applying the Holm-Bonferroni correction, we found a significant negative dependence of goodness on resistance ($p = 0.02$) and a significant positive dependence of emptiness ($p = 1.5 \times 10^{-3}$) across the whole set of recordings. As with the count tests, the relationship between strangeness and resistance was not significant.

However, taking the Sutter #77 pipettes alone, the significance of the effect of resistance on goodness was only borderline ($p = 0.049$), and there was no significant effect on either emptiness or strangeness. Within the Harvard F group, no effects were significant.

Given that the resistance variation is so heavily coupled to the pipette type, we cannot exclude the possibility that some other, unidentified difference between the two pipette types was actually responsible for the differences in recording quality, and the resistance—and hence size—was merely incidental.

In the case of the empty recordings, there is nevertheless good reason to suppose that size is a key factor. In a given cell, any channels present will be distributed across some area of cell membrane in an unknown and hence effectively random fashion. In the absence of any better information guiding the patch position, the probability of encountering one or more of these channels depends on the fraction of available membrane that is actually

sampled. A smaller tip will sample a smaller region and thus be more likely to miss out on any channels.

A membrane patch is not strictly planar, so its area will be greater than that of the pipette tip opening, but the latter places a lower bound on the size and gives some idea of its order of magnitude.

From the measurements in §4.1, the Sutter #77 pipettes have an inner tip diameter of about 70 nm, and hence an area of 4.4×10^{-3} μm^2. We have not explicitly determined the size of our Harvard F tips, but if we take as an estimate the bottom end of the range measured for thick-walled patch pipettes by Sakmann and Neher (1983b), 0.5 μm diameter, then the corresponding area would be around 0.2 μm^2, 44 times larger than the SICM pipette. It is therefore unsurprising that the larger pipettes find channels more often.

It is worth noting that the small area sampled is not *necessarily* disadvantageous. In one set of transfected HEK cells used during the course of these experiments, bslo expression was dramatically higher than usual. The channel density was such that patches obtained with Harvard F tips could not be adequately voltage clamped and the resulting recordings were useless. By contrast, Sutter #77 pipettes produced several viable recordings from these cells. Despite the small patch size, each of these recordings contained multiple channels. The small pipette tip could thus prove beneficial in certain experimental situations, for example when studying single channel kinetics, where isolating an individual channel is desirable.

5.1.2 Accuracy of conductance estimates

Having obtained a number of apparently good bslo recordings using both large and small pipettes, these were analysed to see whether there was any difference in their viability.

For each recording, single channel currents were measured for each voltage at which they occurred. An IV plot was produced and a linear regression performed to estimate the K^+ reversal potential and the slope conductance of the channels. Where the plot deviated noticeably from linearity at more extreme potentials, the outer points were excluded from the regression to avoid underestimating the slope.

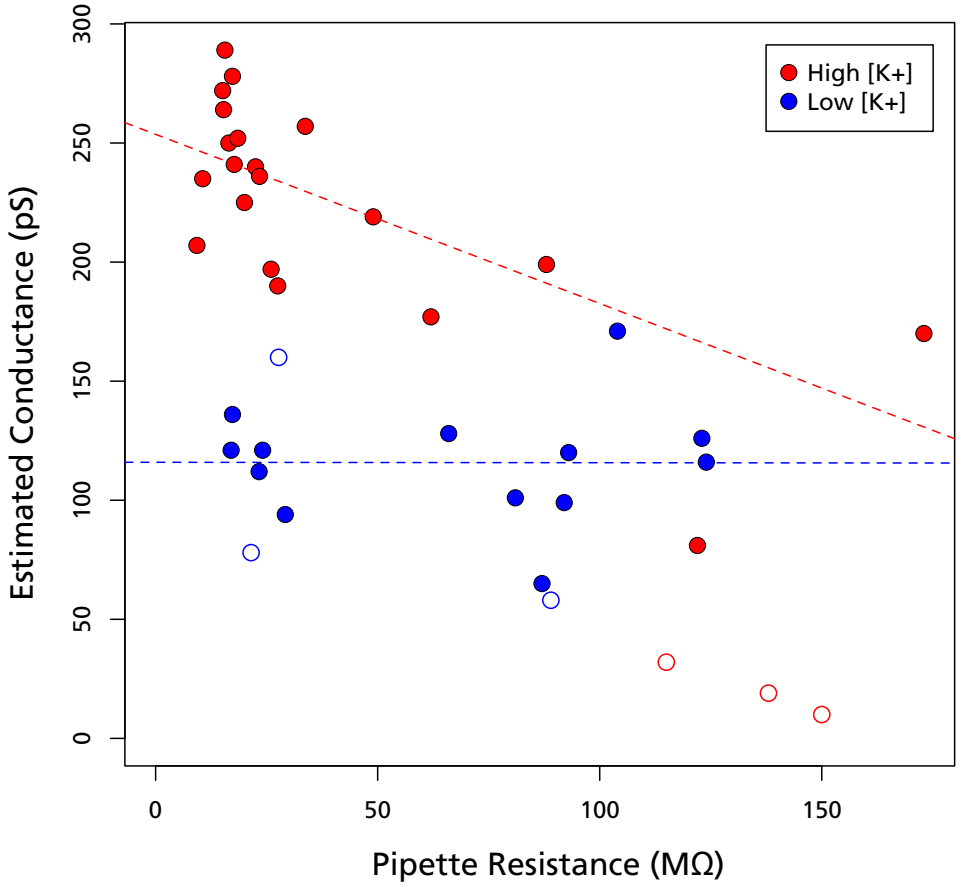

Figure 5.2: Variation of conductance estimates with tip resistance. Dashed lines show a linear regression. Points marked by open circles were excluded from the analysis because of poor recording quality.

The resulting conductance estimates for all successful recordings are shown in Figure 5.2, plotted against pipette resistance. As expected, the conductance estimates differ markedly with pipette filler, with the high $[K^+]$ solution mostly eliciting higher currents.

For the lower resistance recordings, the results are relatively consistent and the estimates are around the expected values, albeit with a fair amount of variance. At higher resistances, the low $[K^+]$ recordings are also spread around the correct value (Hille 2001). However, the high $[K^+]$ conductances decline markedly. The dotted lines show trends from a linear regression, although we do not mean to suggest by this that the effect is actually linear.

Both robust and OLS regressions were performed in this case, to check for susceptibility to outliers, but in fact the results were almost identical, so it is appropriate to report the OLS statistics. The resistance relation was found to be significant ($p = 3.7 \times 10^{-4}$), explaining about half of the variance in conductance (adjusted $R^2 = 0.49$). We therefore tentatively conclude that pipette resistance has some detectable effect on measured channel conductances. A possible mechanism for this is discussed in §5.2.

In a small number of cases, conductances were estimated from lower-quality recordings. These were excluded from the above analysis because the values were not considered sufficiently reliable. These results are shown as open circles in Figure 5.2. We note that they are consistent with the observed trend.

5.1.3 Qualitative variation

As previously discussed, a number of recordings were good enough to estimate a channel conductance. One example, recorded with the larger Harvard F patch pipette, is shown in Figure 5.3 as a point of comparison for the anomalous traces presented below. By contrast, a representative Sutter #77 empty recording is shown in Figure 5.4. A possible explanation for the prevalence of such recordings when using these small tips was suggested in §5.1.1.

Examples of an interesting class of artefact are shown in Figure 5.5. Here the initial current after opening decays rapidly to a lower level, apparently tending to an approximate steady state. During very brief closures the open current level does not noticeably change, but when the channel is closed for a longer period there is a recovery of the peak current, with the degree of recovery apparently depending on the closure duration.

The decay is more marked when several channels open simultaneously, as seen in Figure 5.6. In particular, the expanded regions in panels 5.6b and 5.6d suggest that the steepness of decay increases as each channel opens, implying that the time course is in some way dependent on the total conductance.

The apparent shape of the decay is not identical from one instance to another, especially in the case shown in Figure 5.6c, which exhibits a distinct

Figure 5.3: Good quality HEK-bslo recording, obtained using a Harvard F patch pipette. Pipette resistance was 27.5 MΩ. Recording was sampled at 10 kHz and filtered at 2 kHz.

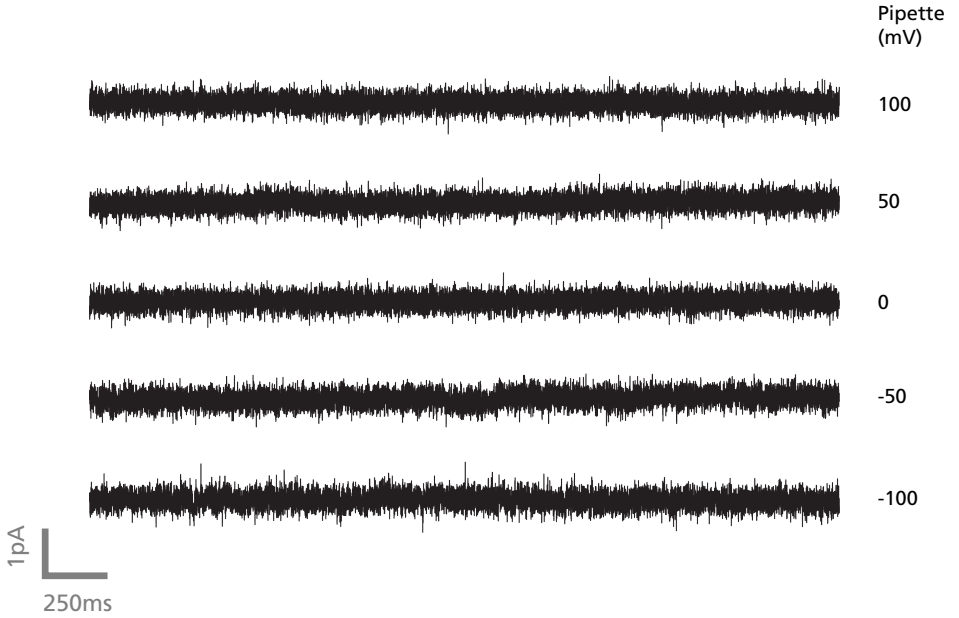

Figure 5.4: Empty HEK-bslo recording, obtained using a Sutter #77 SICM pipette. Pipette resistance was 75 MΩ. Recording was sampled at 10 kHz and filtered at 2 kHz.

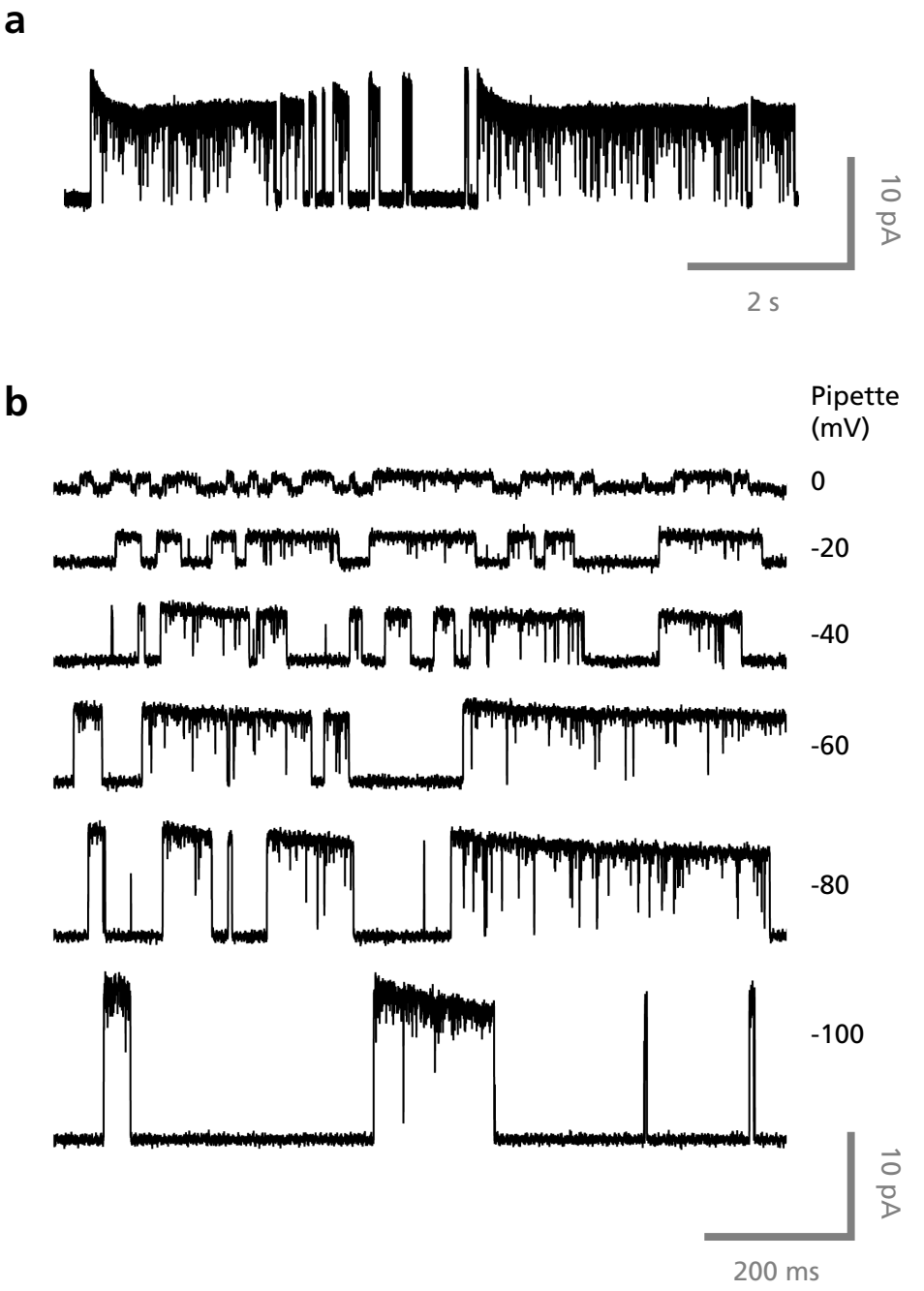

Figure 5.5: Current decaying after channel opening. The peak current appears to recover during closure. All traces are from the same recording, made with a 93 MΩ pipette, sampled at 10 kHz and filtered at 2 kHz. **a** A sustained (8 s) trace at single potential (–80 mV) with distinct decay. **b** Decay can also be seen over shorter durations and a range of voltages, though most closures here are not long enough for full recovery.

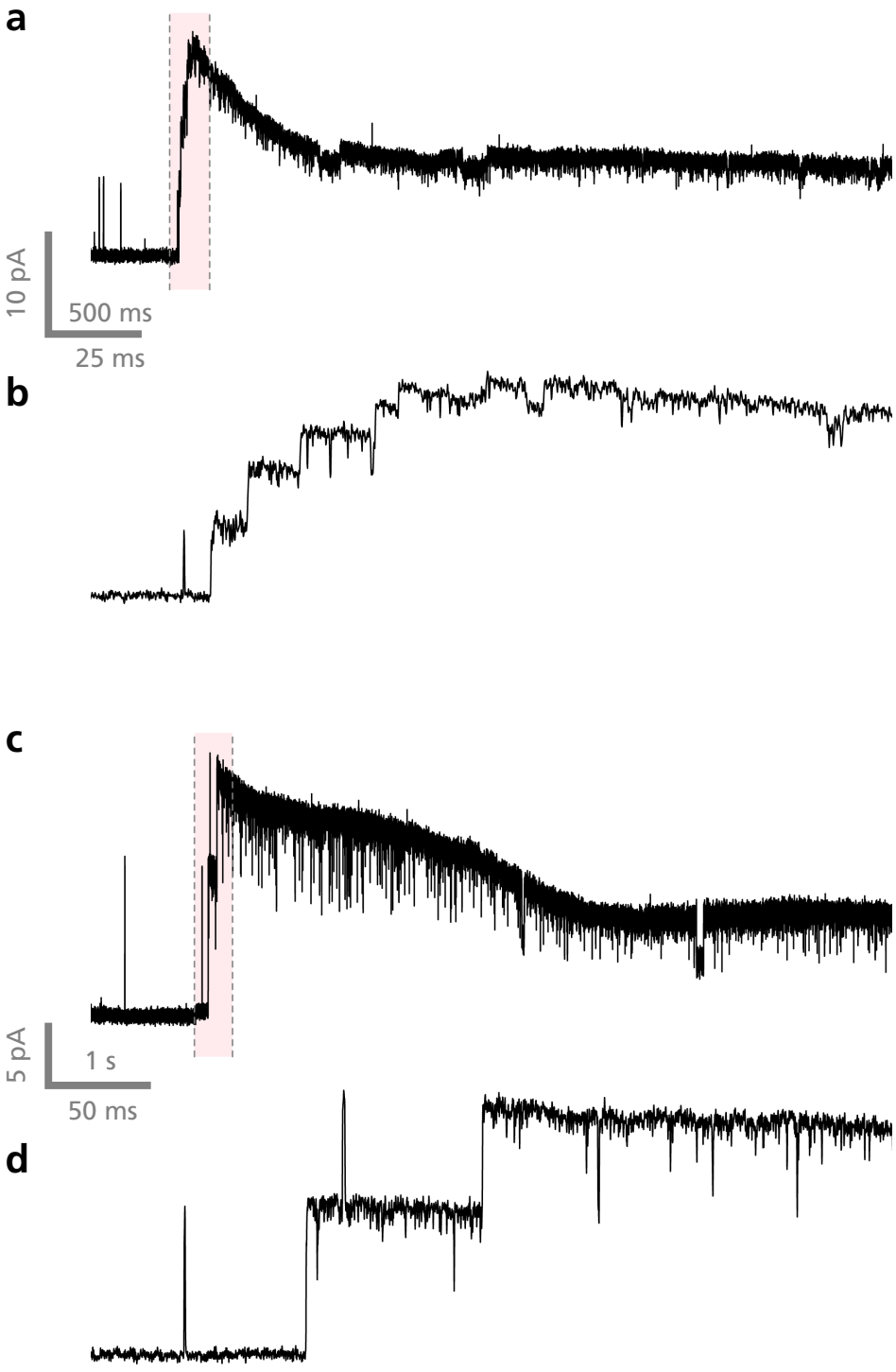

Figure 5.6: Current decay after multiple openings. Full decay curves are shown in **a** and **c**, while in **b** and **d** the highlighted regions are expanded 20× to show the sequential openings. Pipette resistance was 154 MΩ for **a** and **b**, 68 MΩ for **c** and **d**. Both recordings were sampled at 10 kHz and filtered at 2 kHz.

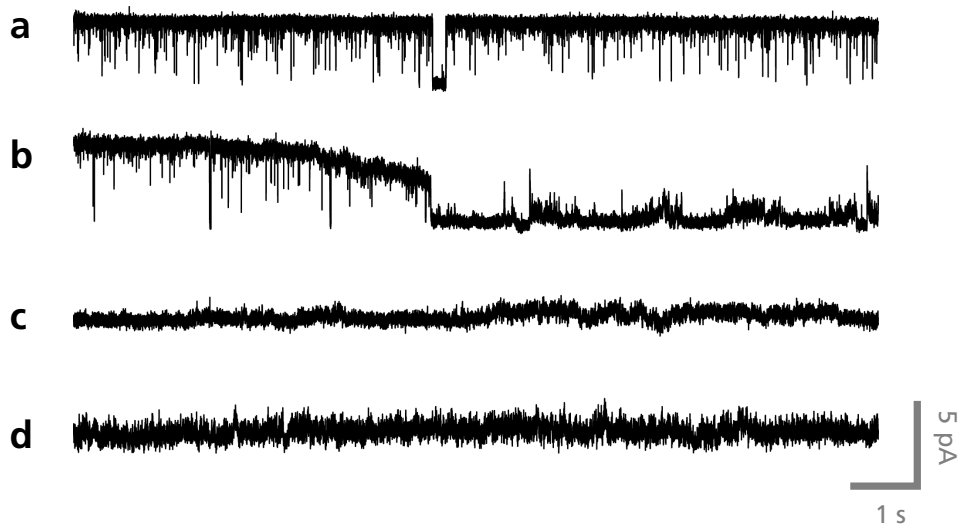

Figure 5.7: Visible change of recording state. **a** Stable recording immediately prior to state change, pipette potential –50 mV. **b** Pipette potential was changed to -100 mV and recording state altered after a few seconds. **c,d** Representative traces from the remainder of the recording, at –50 mV and –100 mV respectively. Pipette resistance was 93 MΩ. Recording was sampled at 10 kHz and filtered at 2 kHz.

'waver'.

The decay shape is locally self-consistent over short durations, inasmuch as segments starting from the same current level tend to follow the same time course towards the same steady state. However, the decay does not seem to be well modelled by a standard curve such as an exponential: fitting multiple successive openings like those in Figure 5.5a produces estimates for τ that differ by 3 orders of magnitude.

A different kind of artefact can be seen in Figure 5.7. Here, an apparently stable recording showing clear channel openings undergoes a visible transition to what seems to be a different state. Over the course of (in the case shown) $\sim$ 2 s, the current falters and collapses to a noisy and essentially flat level. In other recordings, such as the one shown in Figure 5.8, similarly occluded current behaviour can be observed, either present from the beginning or occurring later but without such an identifiable transition point. Once a recording is in this state it does not recover.

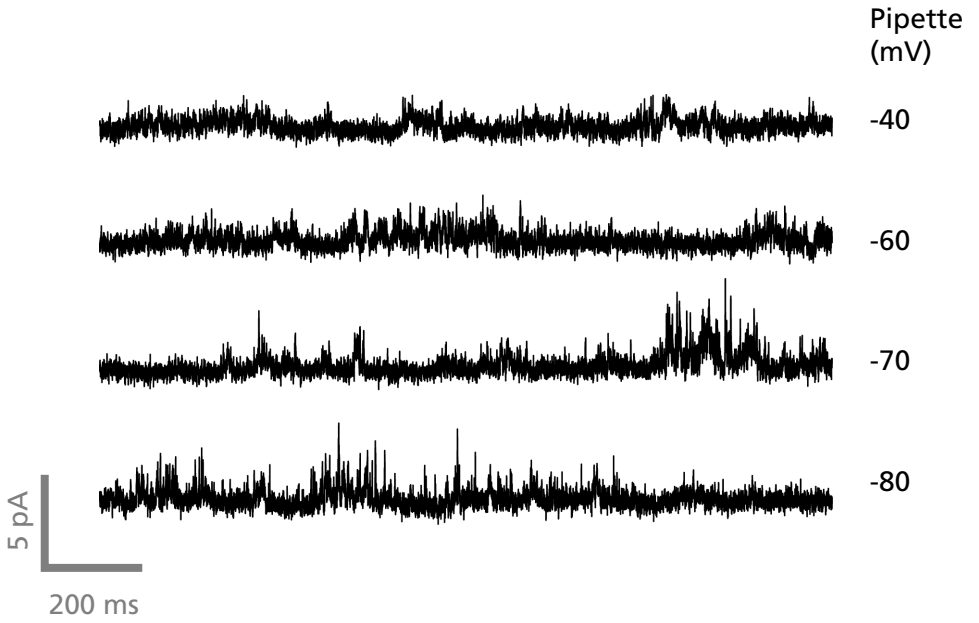

Figure 5.8: Poor recording. There is some semblance of activity but any well-defined single channel currents are obscured and no useful information can be obtained. Pipette resistance was 68 MΩ. Recording was sampled at 10 kHz and filtered at 2 kHz.

5.1.4 Vesicle formation might explain current behaviour

Poor recording quality is a common problem for electrophysiological experiments, and not in itself evidence of an interesting phenomenon. However, the apparent systematic difference in occurrence of these particular artefacts between small and large pipettes indicates that there might be an underlying cause that is affected by tip size.

The decaying current level during channel opening, and recovery during closure, are suggestive of some form of resource depletion and replenishment during these two states. The principal resource required for current flow through the channel is the charge-carrying ions themselves. In general we would expect these to be present in such numbers, and with sufficient mobility, that depletion is unlikely. A region of substantively different concentration in unconstrained bulk solution would be thermodynamically unfavourable. If, however, the ions were contained in a very small volume with restricted access, then the observed behaviour might result.

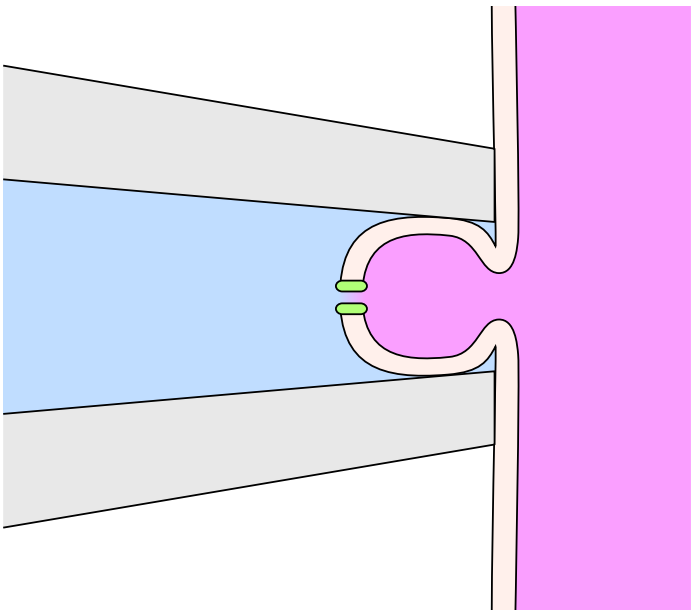

Figure 5.9: Vesicle formation is known to occur with larger pipette tips and could contribute to the strange recordings seen with SICM pipettes.

It is well known that a patch pipette does not sample a flat region of membrane, but instead tends to draw the membrane into the tip in what is classically described as an 'omega' shape (Figure 5.9). For traditional patch pipettes, this formation is large enough to be imaged with an optical microscope. The aperture in such cases is also large, and the interior of the vesicle can be reasonably considered to be continuous with the inside of the cell.

For our much smaller SICM pipettes, such vesicles would be too small to observe optically, and so we do not have direct pictorial evidence that they occur. If they were to do so, however, it is possible that the small aperture might present enough of an obstacle to the free flow of ions that the vesicle interior could become depleted. Such a vesicular configuration also suggests a possible mechanism for state transitions such as that seen in Figure 5.7b: blockage or closure of the vesicle aperture.

Thus, it is at least possible that the presence of vesiculation in very small pipette tips could give rise to many of the artefacts that we have seen. In the next section we consider this possibility more carefully.

5.2 Modelling current behaviour in the presence of a vesicle

To gauge the plausibility of our proposed explanation for the recording peculiarities, we constructed and investigated the simplified compartment model illustrated in Figure 5.10.

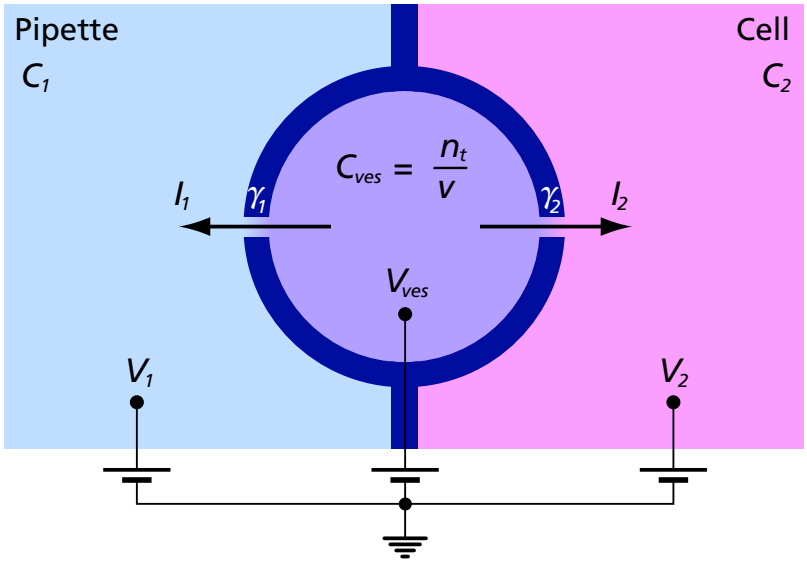

Figure 5.10: Schematic of compartments in the vesicle model. The vesicle is considered as a uniform volume of solution with currents flowing under the influence of concentration differences and applied voltages. C_{ves}, C_1 and C_2 are the ion concentrations in each compartment. V_{ves}, V_1 and V_2 are the respective voltages. γ_1 and γ_2 are the conductances between compartments, while I_1 and I_2 are the currents flowing through those conductances. The vesicle is of volume v and contains n_t ions.

5.2.1 Analytical description of the model

For the purposes of the model, we assume that only a single, monovalent cation species is present. There is an implicit assumption of electroneutrality, insofar as we exclude the contribution of excess charge to the membrane potential, but the counterions are not modelled. The vesicle is considered as a constant uniform volume v containing n_t ions at time t. The cell interior and the pipette are assumed to be of effectively infinite volume compared to the

vesicle, and the ion concentrations in each are taken as constant. The conductances between the vesicle and the other compartments, γ_i, are treated as ohmic. Currents through each conductance are driven by the difference between an applied voltage V_i, the membrane potential of the vesicle V_{ves}, and the Nernst equilibrium potential, calculated from the relevant far side concentration C_i and the vesicular concentration $C_{ves} = n_t/v$:

$$I_i = \gamma_i \left[(V_{ves} - V_i) - \frac{RT}{F} \ln \frac{C_i v}{n_t} \right] \tag{5.1}$$

where R, T and F take their traditional meanings. Over a small time interval δt, the number of ions flowing out of the vesicle will be the sum of the outward currents through all channels, scaled by the elementary charge e:

$$n_{t+\delta t} - n_t = -\sum_i \gamma_i \left[(V_{ves} - V_i) - \frac{RT}{F} \ln \frac{C_i v}{n_t} \right] \frac{\delta t}{e} \tag{5.2}$$

In the limit as $\delta t \to 0$, we obtain a non-linear, inhomogenous first-order differential equation for n:

$$\frac{\mathrm{d}n}{\mathrm{d}t} = \frac{RT}{Fe} \sum_i \gamma_i \ln \frac{C_i v}{n} - \frac{1}{e} \sum_i \gamma_i (V_{ves} - V_i)$$

This can be rearranged into the form

$$\frac{\mathrm{d}n}{\mathrm{d}t} + A \ln n = B \tag{5.3}$$

where A and B are constants derived from the model parameters:

$$A = \frac{RT}{Fe} \sum_i \gamma_i$$

$$B = \sum_i \frac{\gamma_i}{e} \left(\frac{RT}{F} \ln C_i v + V_i - V_{ves} \right)$$

Equation 5.3 is theoretically tractable, but not in closed form. Mathematica gives the solution as

$$n(t) = \exp\left(\frac{A \mathrm{Ei}^{(-1)} \left[-A \exp(-\frac{B}{A})(c_1 + t) \right] + B}{A} \right)$$

where c_1 is a constant of integration and Ei is the exponential integral function, given by

$$\mathrm{Ei}(x) = -\int_{-x}^{\infty} \frac{\exp(-t)}{t} \mathrm{d}t$$

5.2.2 Numerical implementation

The solution derived in the previous section is rather unwieldy and does not directly provide useful qualitative information about the current behaviour and how it is affected by the model parameters. In order to gain a better understanding of this, a numerical version of the model was implemented using the R language. The model was based on equations 5.1 and 5.2, and simulated the current under different sets of parameters.

The baseline parameter set, before any variation, was as follows: external and internal concentration C_1 and C_2, 150 mM; pipette potential V_1, –100 mV; external and internal conductances γ_1 and γ_2 were both 250 pS. Although the model is defined in terms of volume v, it was convenient to specify this in terms of a sphere radius r and calculate v from this internally; the default r was 75 nm. There was assumed to be no membrane potential and all the drop of V_1 was applied over the external channel, so $V_{ves} = V_2 = 0$.

The system was taken to be in equilibrium for times $t < 0$, with the external channel closed, $C_{ves} = C_2$ and $I_1 = I_2 = 0$. At $t = 0$ the channel opened.

The model was run using a time step of 10 µs, and a typical run duration of 10 ms.

These settings are somewhat arbitrary and were chosen primarily so that both the depletion effect itself and the results of varying the parameters would be clearly visible. While most of the values are not grossly unrealistic, there are certainly some departures from what we believe our typical experimental conditions to have been, as will be discussed below.

The result of one 10 ms run with only the baseline parameters is shown in Figure 5.11. As in the experimental traces of Figure 5.5, the peak current at opening decays rapidly towards a substantially lower steady-state value as the vesicle is depleted. However, the time course of the decay is about two orders of magnitude faster in the model than in our experimental results. We

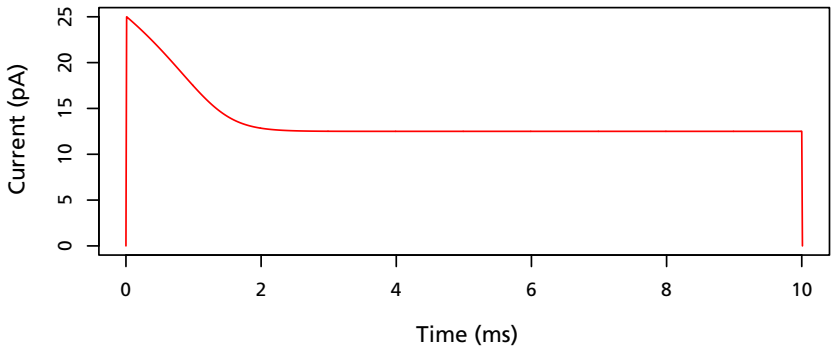

Figure 5.11: Time course of the measured (pipette side) current using the baseline parameters.

will return to this point shortly, but first we examine how the parameters affect the model.

Figure 5.12 shows the results of varying the parameters one at a time while keeping the others at their baseline value. Each coloured trace shows the pipette current for a particular value of the parameter. The actual parameter values used in each case are given in Table 5.2.

	Parameter	Values
a	External conductance γ_1 (pS)	400, 300, (250), 200, 150, 100, 75, 50, 25, 10, 5
b	Internal conductance γ_2 (pS)	5000, 2500, 1000, 500, (250), 150, 100, 50, 25, 10
c	Pipette concentration C_1 (mM)	1, 5, 10, 25, 50, 75, 100, 125, (150), 200, 250
d	Cell concentration C_2 (mM)	1, 5, 10, 25, 50, 75, 100, 125, (150), 200, 250
e	Pipette potential V_1 (mV)	–150, –125, (–100), –75, –50, –25, 0, 25, 50, 75, 100, 125, 150
f	Vesicle radius r (nm)	500, 400, 300, 250, 200, 150, 125, 100, (75), 50, 25

Table 5.2: Parameter values for traces in Figure 5.12. Values are listed in the order of traces from red to purple. Brackets denote the default value.

For the most part, the model results are intuitive. Concentration and voltage changes contribute to the effective driving force, while the conductances scale the current. Taken together, these parameters determine the peak cur-

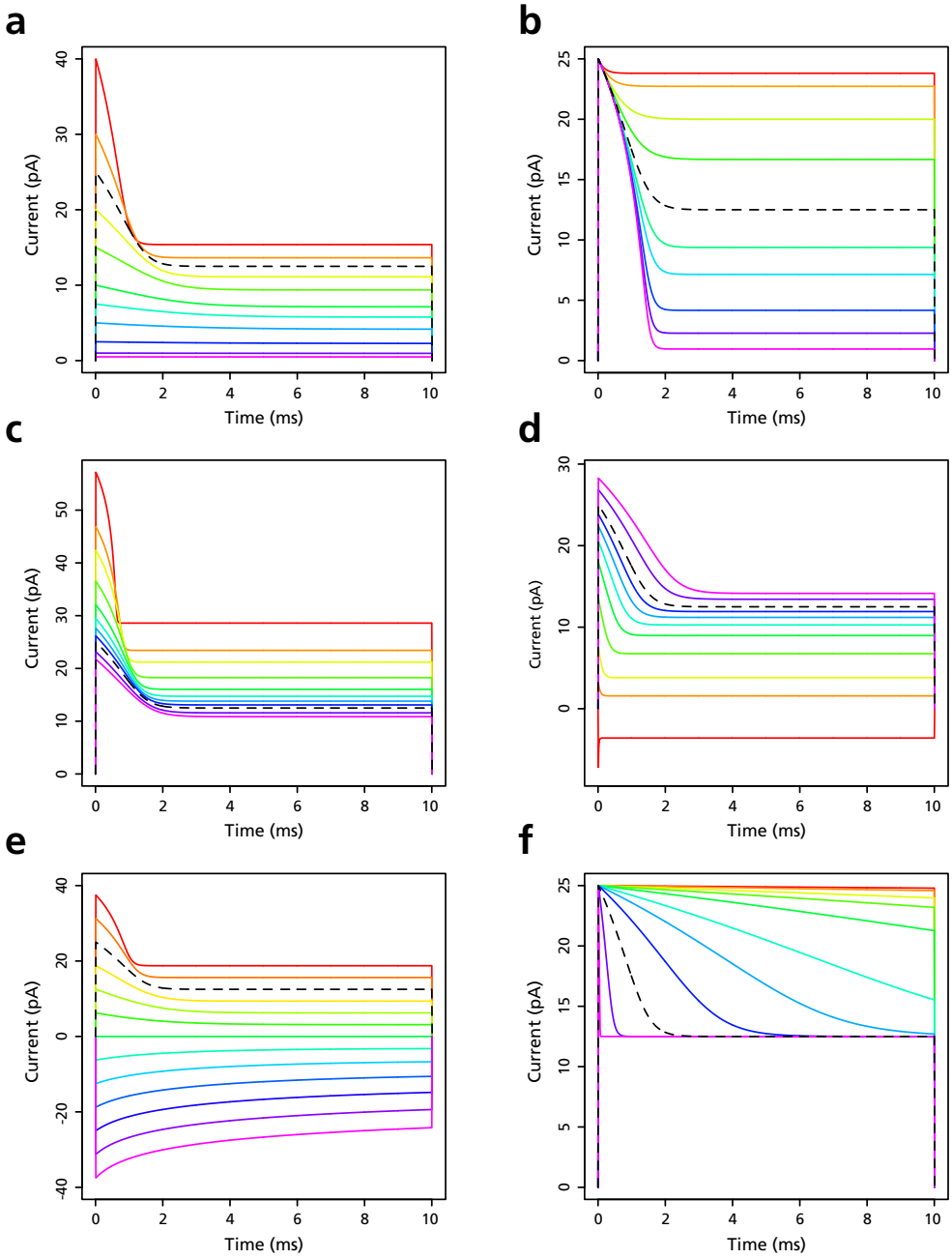

Figure 5.12: Single parameter variations of the vesicle model. Parameter values are listed in Table 5.2. The graphs show the time course of the external current I_1 with different values of: **a** External conductance γ_1 **b** Internal conductance γ_2 **c** Pipette concentration C_1 **d** Intracellular concentration C_2 **e** Pipette potential V_1 **f** Vesicle volume v. Dashed lines show the default parameter time course of Figure 5.11.

rent, the steady state current and the shape of the decay from one to the other. Specifically, the peak current depends only on γ_1 and the initial driving force across the channel, while the steady state current depends on both γ_1 and γ_2 (which, since we have assumed an ohmic response, are essentially just resistors in series) and the overall driving force between the inside of the cell and the pipette. There is some variation in the time course with the latter, but typically not orders of magnitude.

Within plausible ranges, these factors only contribute to a substantially slower time course when the currents flowing are themselves small. This is not generally relevant to the 'strange' experimental results that the model is intended to explain. In the context of a real recording, the currents need to be relatively large before the depletion effect becomes obvious above other behavioural variability.

An interesting feature of the decay curve is its asymmetrical response to changes in driving force, most visible in Figure 5.12e. This arises because the number of ions in the vesicle can never be less than zero. The force required to reduce C_{ves} increases hyperbolically as the ions run out, causing the current to fall steeply. There is no equivalent upper bound on concentration, so a current that is limited by the accumulation of a surplus of ions decays more gradually.

We have assumed that all of the applied pipette potential acts across γ_1. This is probably not the case in practice, although it is not clear *a priori* what a realistic division would be. To see how this would affect the behaviour, the model was run with the same –100 mV potential apportioned differently between the internal and external faces. Results are shown in Figure 5.13a. The split ranges from {–120 mV, +20 mV} for the top (red) curve to {–10 mV, –90 mV} for the bottom (purple), proceeding in steps of 10 mV. As in previous graphs, the dashed black line indicates the default setting.

Because the overall driving force from the cell to the pipette is unchanged in each case, the current tends to the same steady state level, but with different approach characteristics. If, as with the default values, most of the potential applies over γ_1, then the initial current is large, decaying rapidly to the steady state as γ_2 limits replenishment. If most of the potential applies instead over γ_2, the initial current is small and most of the force serves to charge up the vesicle with additional ions. The current then rises as the

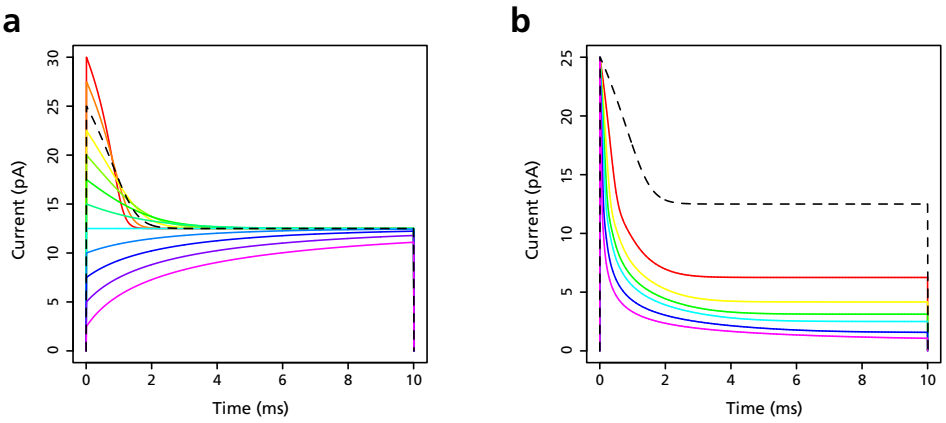

Figure 5.13: Voltage drop and spatial effects. **a** An applied pipette voltage of –100 mV is divided between the inner and outer membranes. The split goes from {–120 mV, +20 mV} for the top (red) trace, to {–10 mV, –90 mV} for the bottom (purple) in increments of 10 mV. **b** Emulating spatial effects by dividing the volume into smaller communicating compartments. The number of compartments is (red to purple): 3, 5, 7, 9, 15, 25.

surplus overflows through γ_1. We see the same asymmetry of curvature that was mentioned above, for the same reason.

The traces with most of the voltage drop over the channel are the ones that most resemble the phenomena we are trying to reproduce, so we continue with that assumption for the time being.

By contrast to the electrochemical parameters, the vesicle volume does not affect the steady state current. Instead it alters the time course, acting as a buffer for the overall current flow between the cell and the pipette. If there is a large volume of solution in the vesicle, the currents in and out take a long time to have an impact on the concentration. Conversely, if the volume is small, the vesicle provides very little buffering and the system is driven to steady state quickly.

We expect the volume to be constrained by the tip size, and thus be small. But, as noted above, the resultant time course in the model is very much faster than that observed in our actual 'strange' recordings. In order to get a decay on the observed scale we have to posit a volume that is large in comparison to the size of the tip (see §5.2.8).

The volume cannot be large without the distances involved becoming signif-

icant, which would be expected to affect the time course. We have assumed that the distance across the vesicle is short enough for perfect mixing to occur in negligible time. For comparison, we can estimate the diffusion time for the range of vesicle diameters modelled in Figure 5.12f. Treating just one dimension, such that $t \approx x^2/4D$, and taking $D = 1.96 \times 10^{-9}$ m^2/s for K^+ (Hille 2001), then the expected time to cross the smallest vesicle ($2r = 50$ nm) is 640 ns. This is very much shorter than our 10 µs simulation time step and the assumption of perfect mixing is not unreasonable. However, for the largest vesicle ($2r = 1$ µm), the estimated diffusion time is 250 µs. The vesicle would not be well-mixed on the time scale at which the behaviour occurs and we would expect a concentration gradient to arise.

As a crude simulation of what the effect of distance might be, we added a 'pseudo-spatial' component to the model by subdividing the vesicle volume into a series of separate sub-compartments. Between these were intermediate fluxes driven by concentration differences. Although not expressed in terms of physical distance, this division served to slow down communication across the space and remove the assumption of uniform internal concentration.

The results of using different numbers of sub-compartments are shown in Figure 5.13b. The most striking effect is to substantially steepen the initial decay, as the smaller volume in the outermost sub-compartment experiences a faster drop in concentration with outward current. In the traces shown there is also a noticeable lowering of the steady state current, though this has been exaggerated by setting the inter-compartment conductance fairly low (equal to the internal conductance γ_2) and thus significantly increasing the total resistance of the circuit.

The overall decay time is somewhat increased by the slowing of communication through all the sub-compartments. However, this increase is almost entirely in the shallowest part of the decay, when the current is already close to its steady state value. It does not seem that this effect could account for the much slower time course we have observed.

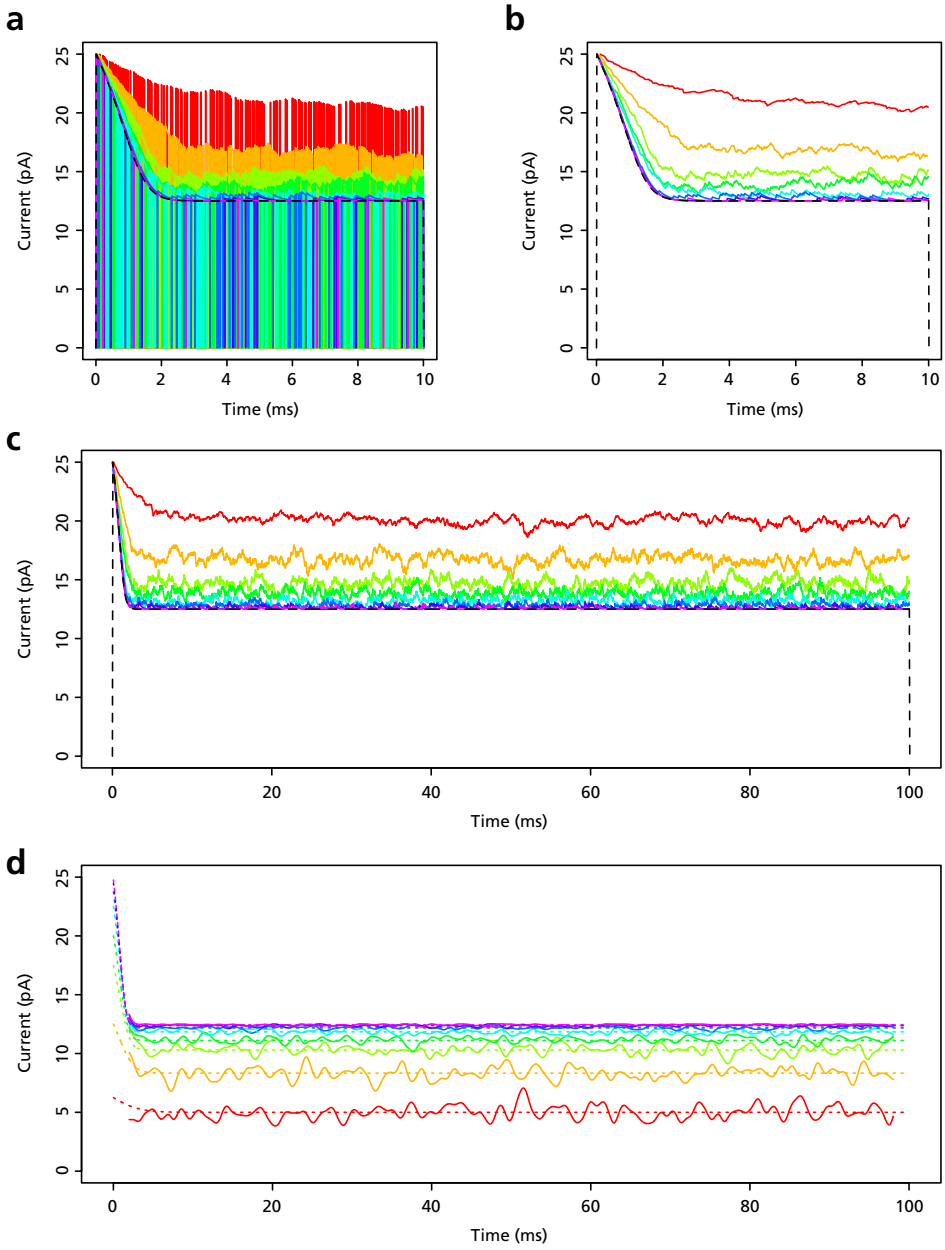

Figure 5.14: Varying P_{open} in the vesicle model. Values taken are (red to purple): 0.25, 0.5, 0.7, 0.8, 0.9, 0.95, 0.98, 0.99. Black dashed line indicates the default value 1, as before. Full current traces, including closures, are shown in **a**, while **b** and **c** show only the open state current. In **d** the current has been filtered with a Gaussian kernel ($\sigma_t = 0.5$ ms, $\sigma_f = 320$ Hz) to show the average current flow over both open and closed states. Dotted lines show the expected current where the channel does not close but instead γ_1 is scaled by the corresponding P_{open}.

5.2.3 Inclusion of stochastic effects

So far we have considered only what happens during a sustained opening of the channel, observing that a steady state is reached when the fluxes depleting and replenishing the vesicle are in balance. In practice, channels can change state frequently, disrupting this balance.

To observe how this might affect the current behaviour, a stochastic element was added to the model, switching on and off the channel conductance according to a specified open probability, P_{open}. Current traces for different P_{open} values are shown in Figure 5.14.

The conductance changes prevent the system from reaching a true steady state, but the current does settle down to fluctuate around an approximate steady average. Since the vesicle is replenished by I_2 whenever the channel is closed, the mean C_{ves} increases and the current that flows when the channel opens is correspondingly higher (Figure 5.14a–c).

Of course, the overall current flow nevertheless drops because it is flowing for less of the time, as shown in (Figure 5.14d). Here the simulated signal has been filtered by convolution with a Gaussian kernel to obtain a smoothed moving average (described in more detail later in this section).

Taken over the long term, the effective conductance of the channel is reduced in proportion to the fraction of the time it spends open, ie $\langle\gamma_1\rangle = P_{open} \cdot \gamma_1$. This conductance is one of the determinants of the steady state, so all else being equal we would expect to converge on the same average current as if the channel were permanently open with conductance $\langle\gamma_1\rangle$. This is indeed the case, as illustrated by the dotted lines in Figure 5.14d.

This model of channel openings as a Bernoulli process, with the channel state at any instant depending only on P_{open}, is useful for understanding the average behaviour of the system, but the results don't look very much like what we actually observe. In practice, we rely on there being some continuity between states at successive instants, so that at least some openings and closings last long enough to be distinguished.

In order to account for this, the model was extended to include a dependence on present state. Since we were primarily concerned with the qualitative behaviour of the model, rather than the kinetics of any real channel, only a simple two-state mechanism was considered. Separate rate constants

α and β were introduced to describe the stability of the open and closed states:

$$\text{open} \underset{\beta}{\overset{\alpha}{\rightleftharpoons}} \text{closed}$$

Treating the rates as transition probabilities over our simulation time step δt, we represented this as a Markov chain model with the following transition matrix:

$$\begin{array}{c} \\ \text{open} \\ \text{closed} \end{array} \begin{array}{c} \begin{array}{cc} \text{open} & \text{closed} \end{array} \\ \begin{pmatrix} 1-\alpha & \alpha \\ \beta & 1-\beta \end{pmatrix} \end{array}$$

We require that a stationary distribution exists. The long term P_{open} is then related to the rate parameters α and β by

$$P_{open} = \frac{\beta}{\alpha + \beta}$$

Given one rate parameter, say β, we can calculate the other to attain a given P_{open}:

$$\alpha = \frac{\beta(1 - P_{open})}{P_{open}} \tag{5.4}$$

The specified rate provides a control for the 'stickiness' of the channel state. Examples of its effect are shown in the left hand panels of Figure 5.15. We observe that the longer openings produced by reducing the transition probability span a greater portion of the depletion curve and are more likely to reach the true steady state current.

With the partial exception of the moving average shown in Figure 5.14d, all model currents have so far been presented in ideal form, as if they could be measured exactly. Although we have introduced an element of behavioural noise in the form of stochastic opening, we still have perfect knowledge of the channel state and current at every instant. Of course, this is not the case for a real recording. Experimental equipment will always have finite bandwidth and be subject to both intrinsic noise and contamination from other sources. The 1–10 µs time steps of our simulations are well beyond the temporal resolution of an ordinary patch clamp amplifier.

To get a better sense of how our predicted channel behaviour might manifest within a real recording, we added both noise and filtering to the model.

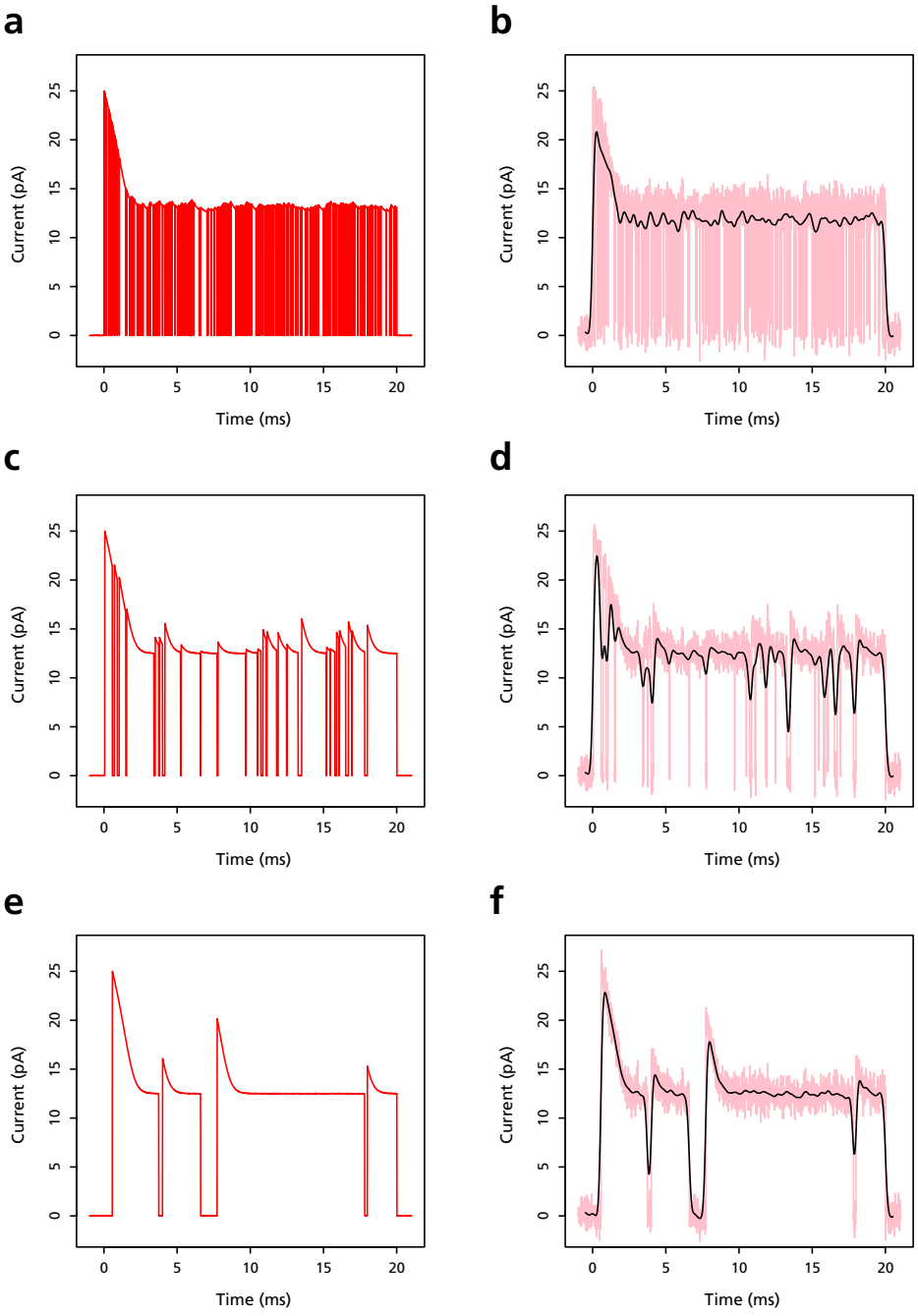

Figure 5.15: Two-state Markov chain model allows for more realistic patterns of opening. Stationary $P_{open} = 0.9$ in all cases, but the state change probabilities vary: **a,b** $\beta = 1$; **c,d** $\beta = 0.1$; **e,f** $\beta = 0.01$. Graphs on the left (**a**,**c**,**c**) show the ideal current generated by the model. On the right (**b**,**d**,**f**) are the corresponding signals after simulated 'measurement' by addition of 1 pA RMS noise (pink) and filtering by convolution with a Gaussian kernel (black, $\sigma_t = 125$ µs, $\sigma_f = 1.3$ kHz).

These factors were considered as issues of measurement rather than as fluctuations in the underlying processes generating the current, so they did not affect the internal state of the model, only its output.

Typical baseline noise in our real experiments was of the order 1 pA RMS. We simulated this by adding pseudo-random noise to the predicted current, distributed normally with mean 0 and standard deviation 1 pA.

Our real recordings were low-pass filtered at 1–2 kHz with a 4-pole Bessel filter and sampled at 10 kHz. In the simulation, low-pass filtering was implemented using a Gaussian convolution kernel, specified in terms of its time domain standard deviation σ_t and applied over a window of $(-4\sigma_t, 4\sigma_t)$. Ignoring artefacts due to the finite window, this translates to a frequency domain Gaussian with standard deviation

$$\sigma_f = \frac{1}{2\pi\sigma_t}$$

By convention, we take σ_f as the cut-off frequency for such a filter.

The right hand panels of Figure 5.15 show the current traces from the left hand panels with noise and filtering. The results are predictable. When β is high (Figure 5.15b), openings are short relative to the kernel width and we do not measure distinct states, only a reduced average current. As β decreases (Figure 5.15d) the closed states can be partially resolved, appearing as noise spikes on a background level closer to the true open state current. With low enough β (Figure 5.15f), individual openings can be distinguished, and the currents in both open and closed states are close to their predicted values.

At least in qualitative terms, this last trace resembles the recordings that suggested the vesicle hypothesis, such as those shown in Figures 5.5 and 5.6. Openings are sustained long enough for the current decay to be discerned, and there is time for significant recovery during the closed states.

5.2.4 Multiple channel openings

In several experimental records the patches contained multiple channels, so we were interested in the behaviour of the system as additional channels opened.

We considered first the ideal case with no stochastic behaviour or filtering. All channels were assumed to have the same unitary conductance $\hat{\gamma}_1$ and be subject to the same concentrations and voltage. Thus, k open channels would be equivalent to a single combined channel of conductance $\gamma_1 = k \cdot \hat{\gamma}_1$.

If, as in most of our previous simulations, the interior conductance γ_2 were of the same order as $\hat{\gamma}_1$, then with increasing k the external resistance would decrease and the steady state current would come to be dominated by γ_2. At the same time, the increased outward conductance would accelerate the decay towards that steady state, shortening the time course.

These effects would be even more pronounced for smaller γ_2. On the other hand, for very large γ_2, even with multiple external channels open the current would still be predominantly determined by γ_1.

This is indeed what we see in Figure 5.16a, which shows the model current with 12 channels opening in quick succession, simulated for different values of γ_2.

If we allow the channels to open and close stochastically then the situation is slightly more complicated because the random variation of γ_1 transiently changes the nominal steady state current. Nevertheless, provided the mean outward conductance

$$\langle \gamma_1 \rangle = P_{open} \cdot k \cdot \hat{\gamma}_1$$

is of a comparable order to γ_2 then we expect to see a similar, albeit noisier, collapse towards an approximately steady average level. An example is shown in Figure 5.16b. There is a clear formal similarity to the experimental traces from Figure 5.6, although of course the model version is more regular.

5.2.5 Effect of filtering on peak current detection

As already noted, the time courses predicted by the model are shorter than those observed in our 'strange' recordings. We defer discussion of the plausibility of this to §5.2.8, and first consider what the implications would be if the prediction were correct.

The primary determinant of decay time in the model is vesicle volume. If there is a large reservoir of solution buffering the fluxes between compartments, then the decay is slow. If there is only a little, it is fast.

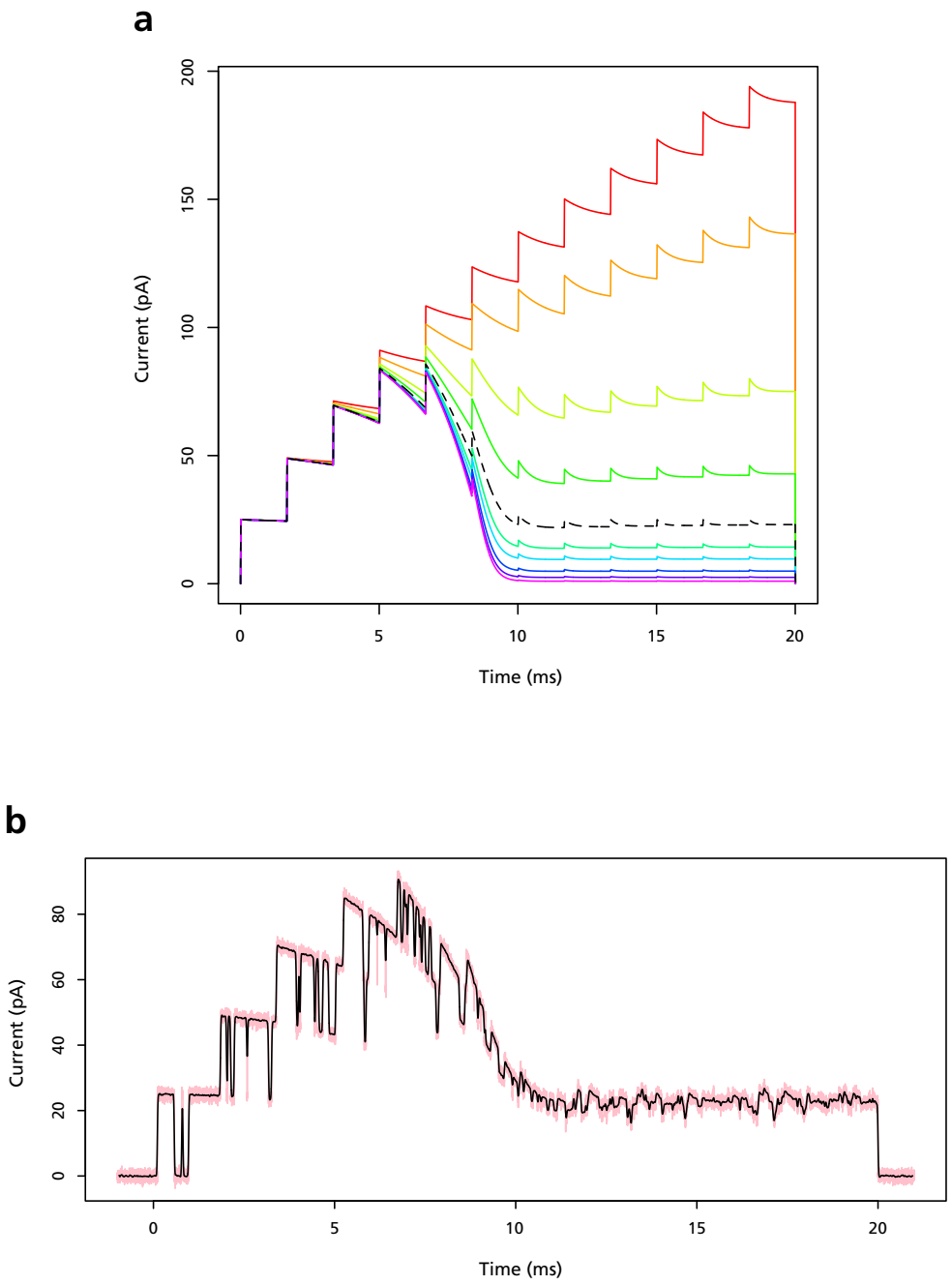

Figure 5.16: Multiple channel openings can drive current to apparent collapse. **a** As channels open, the increasing γ_1 accelerates the approach to steady state. Traces are shown for different values of interior conductance γ_2 as listed in Table 5.2. **b** Simulation with all default parameter values plus stochastic openings, noise and filtering ($P_{open} = 0.9$, $\beta = 0.01$, $\sigma_t = 125$ µs, $\sigma_f = 1.3$ kHz).

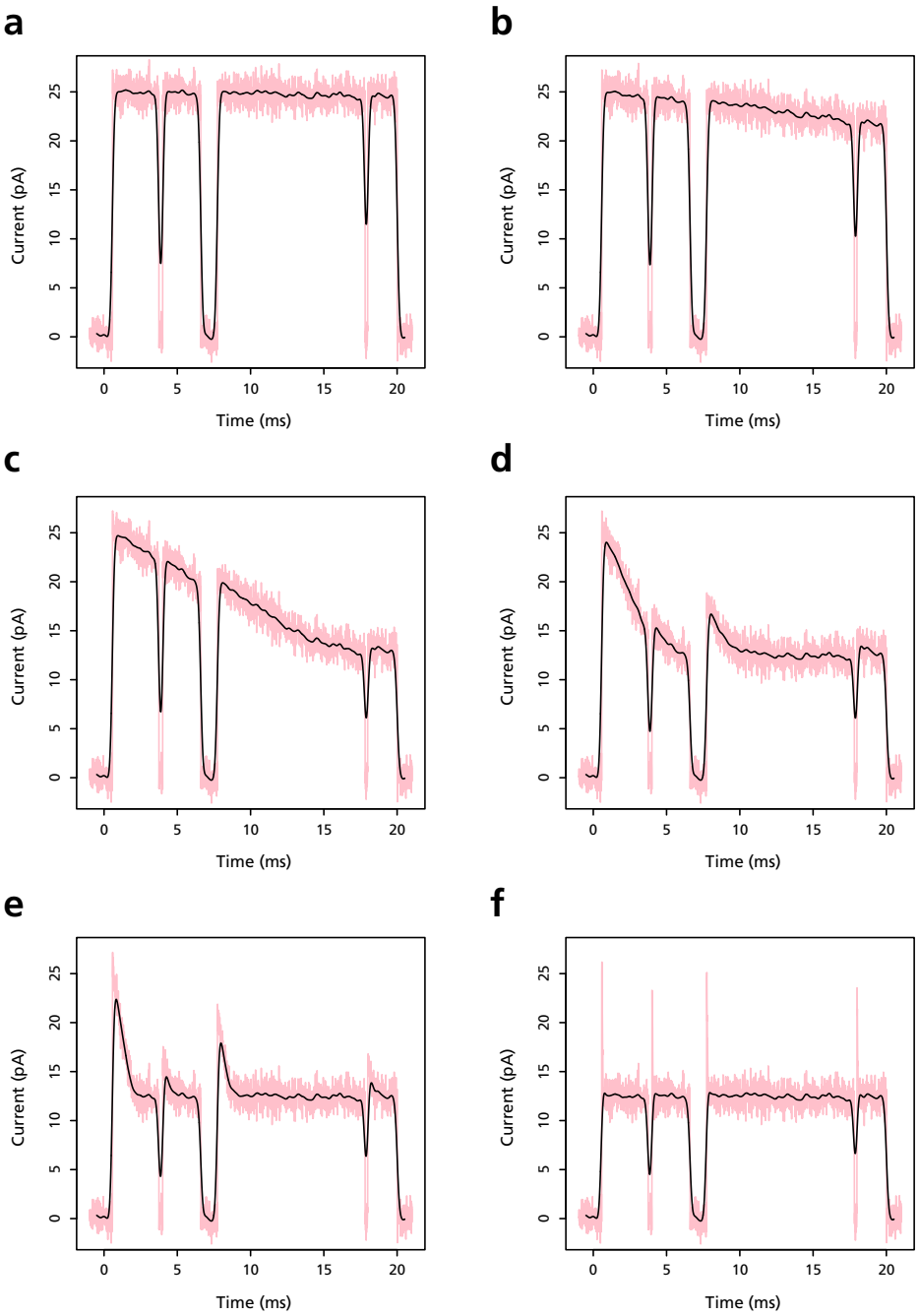

Figure 5.17: Vesicle volume affects detectability of depletion artefacts. Pink traces show the simulated noisy current, black lines the filtered signal ($P_{open} = 0.9$, $\beta = 0.01$, $\sigma_t = 125$ µs, $\sigma_f = 1.3$ kHz). Conditions are identical for each run except for the vesicle radius. **a** $r = 500$ nm; **b** $r = 250$ nm; **c** $r = 150$ nm; **d** $r = 100$ nm; **e** $r = 70$ nm; **f** $r = 30$ nm.

When looking at the variation of time course with volume in Figure 5.12f, only the simplest version of the model was used. There were no stochastic openings and no filtering. If the model is run with these additional factors included, the results look like those shown in Figure 5.17.

It appears that the visible symptoms of vesicle depletion can vary substantially depending on the vesicle volume, the channel kinetics and the filtering. The decay may appear slight and linear for large vesicles, while at smaller volumes the peaks become much more pronounced. Crucially, however, the trace can appear flat and ordinary not only when the vesicle is very large but also when it is very small, if the decay from peak occurs too fast to be measured with a realistic bandwidth.

The former situation is unproblematic, even if it can occur—and we might reasonably expect such a large vesicle to be accompanied by a much greater γ_2, reducing the impact even further.

The small vesicle case is of greater concern. In the model it occurs at almost exactly the size range we estimate for our SICM pipette tips. If it were to do so in practice, it would lead to apparently good recordings, without obvious artefacts, that systematically underestimated channel conductances. If the conductance were experimentally important, for example as evidence of channel identity, then such underestimation would become an issue.

Evidence of this kind of underestimation from some of the HEK bslo recordings has already been described in §5.1.2. Moreover, that effect showed a dependence on resistance, hence probably on tip size and perhaps in turn on the volume of a putative vesicle. Thus, the mechanism suggested by these simulations *could* provide an explanation for those results.

5.2.6 Estimating the conductance between the vesicle and the cell

If we assume that the initial peak and decay phase of the current passes undetected, and that instead the value recorded for each opening is the current at or near its steady state level, we can estimate the apparent current-voltage relationship that would be derived from the recording. Results from such simulations are shown in Figure 5.18. Here, the measured current was taken to be that reached after 50 ms.

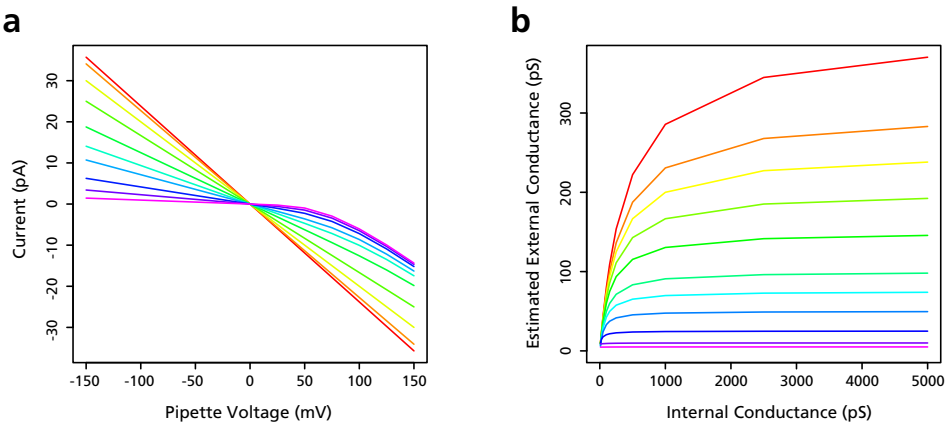

Figure 5.18: Effect of vesicle on conductance estimates. **a** IV curves estimated from current reached 50 ms after channel opening. External conductance γ_1 is set to the default 250 pS in all cases, while γ_2 takes a different value for each curve, following the values listed in Table 5.2. **b** Conductance estimates from the linear portion of simulated IV curves. Each coloured curve is for a constant γ_1, with values again taken from Table 5.2.

We see from Figure 5.18a that a simple linear relationship results as long as γ_2 is larger than γ_1. This is consistent with the assumption of ohmic behaviour. When γ_2 becomes small, there is some apparent inward rectification. This is not due to a change in the steady state conductance, but arises because the steady state has not been reached due to the slower decay. This effect has not been observed in practice.

To be consistent with the calculations used for experimental data, conductance estimates were calculated from the linear portion of the simulated IV curves, with the results shown in Figure 5.18b. Since we have excluded any regions for which time course effects come into play, the results are purely ohmic. The derived conductance in most cases is very close to that for a simple series circuit:

$$\gamma_{series} = \frac{\gamma_1 \gamma_2}{\gamma_1 + \gamma_2} \tag{5.5}$$

The few deviations from this, which only occur when both conductances are small, can be attributed to loss of numerical precision over the course of the simulation.

While it is doubtful such a neat relation holds in reality, it provides a useful approximation with which to test our assumption that the hypothetical

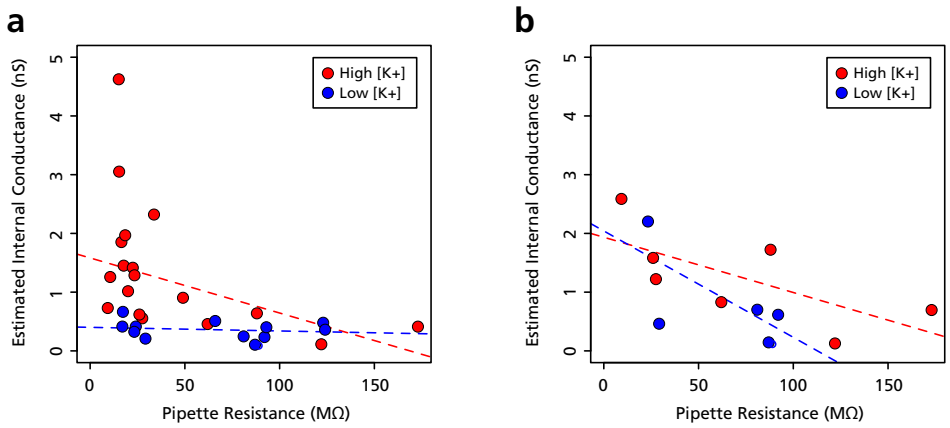

Figure 5.19: Estimated γ_2 decreases with pipette resistance. γ_2 is calculated relative to: **a** the largest measured γ_1; **b** the median γ_1. Dashed lines indicate trends from a robust linear fit.

internal conductance γ_2 decreases as pipette resistance rises. Revisiting the conductances presented in Figure 5.2, we can consider these as estimating the combined conductance γ_{series}. If we then assert a value of γ_1 we can calculate the corresponding γ_2:

$$\gamma_2 = \frac{\gamma_1 \gamma_{series}}{\gamma_1 - \gamma_{series}} \tag{5.6}$$

The results are sensitive to the choice of γ_1. By the nature of conductors in series, $\gamma_{series} < \gamma_1$. A valid estimate of γ_2 can only be obtained where this holds. Therefore, choosing γ_1 at least as large as the greatest measured conductance maximises the number of data points considered. However, this is likely to give undue weight to outlying observations. An alternative is to use the median as an estimator of the true conductance. Plots using both approaches are shown in Figure 5.19.

For the high $[K^+]$ recordings, both estimates give approximately the same results and we see the expected drop in γ_2 with pipette resistance.

For the low $[K^+]$ case, the situation is less clear cut: using the higher γ_1 estimate, and thus including all the data, the estimate of γ_2 is essentially flat. Using the median, and thus excluding half of the data, we see a marked downward slope. Given the relatively small number of points and the scatter of the original data we cannot draw any useful conclusions.

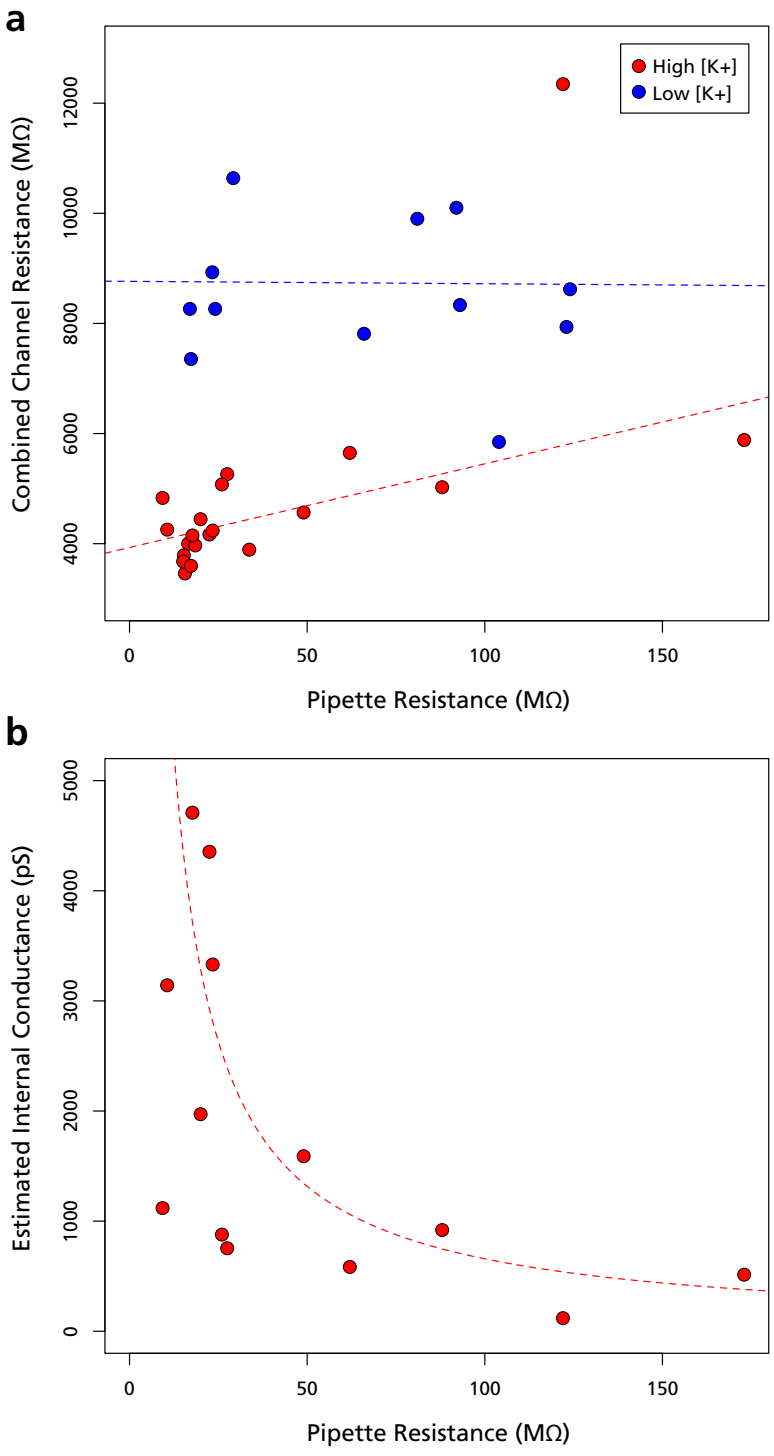

Figure 5.20: Relationship between internal channel resistance and pipette resistance. **a** Linear regressions for both high and low [K^+] data in terms of resistance. **b** High [K^+] regression parameters transformed back into conductance space.

Although straight trend lines are shown in Figure 5.19, a linear dependence between conductance and pipette resistance is unlikely. It is more plausible and convenient to consider both the internal channel and the pipette resistance in the same units, as seen in Figure 5.20a. This is essentially a reciprocal of Figure 5.2, and exhibits similar features.

There is again no evidence of a trend in the low [K^+] results, and the measurements are widely scattered. The regression intercept is 8764 MΩ, equivalent to 114 pS, very close to the expected conductance, but the fit is poor.

The high [K^+] results show a distinct resistance relationship that is well modelled by a robust linear fit in the observed range. The intercept is 3930 MΩ or 254 pS, again close to the expected value. The slope is 15.2. If we transform these parameters back into terms of the conductance of the interior channel, the results are as shown in Figure 5.20b. This provides a more convincing fit than the straight lines of Figure 5.19 and suggests that the linear resistance model may be useful in this case.

The pipette resistance arises from its geometry and we might expect that the internal channel resistance is, at least in part, similarly governed by its own. We have no direct information as to what that might be, but we assume that the vesicle exists inside the pipette and as such must be constrained by it. If a relationship does in fact exist between pipette resistance and the resistance of the internal channel, the obvious explanation is that it is a consequence of this shared dependence on geometry.

A simplistic model of the internal channel would be as a short cylindrical pore of the kind classically used to model ion channels themselves. The resistance for such a pore is determined by its length l and radius r (Hille 2001):

$$R_{pore} = \left(l + \frac{\pi r}{2}\right) \frac{\rho}{\pi r^2} \tag{5.7}$$

At small sizes the resistance will depend very steeply on the radius, just as it does with the pipette tip (§4.1.3). Calculating R_{pore} as both parameters vary (once again using $\rho = 51\ \Omega \cdot \text{cm}$) gives the results shown in Figure 5.21. To produce the resistance range observed in Figure 5.20a, the pore parameters would have to traverse the red to orange regions of Figure 5.21b.

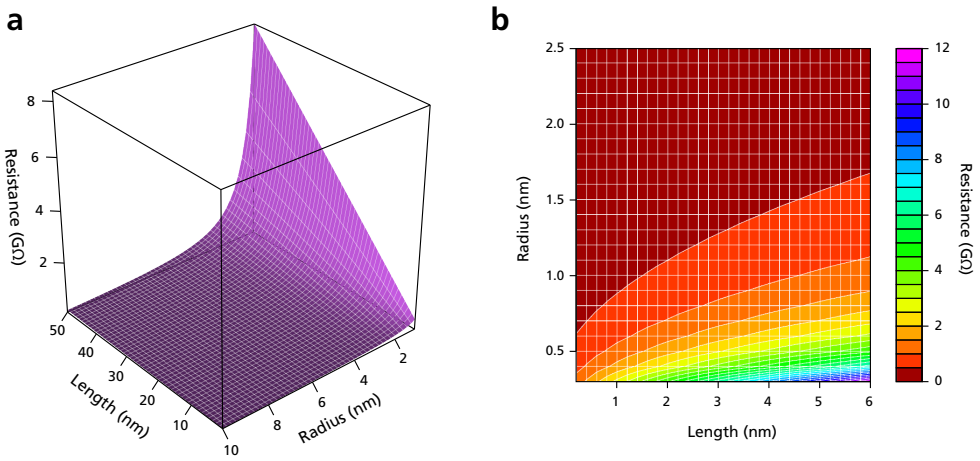

Figure 5.21: Variation of pore resistance with geometry, from Equation 5.7. **a** The overall shape of the relationship. Resistance is linear in l and increases hyperbolically as r becomes small. (Lower bound 1 nm for both parameters.) **b** A magnified view of a portion of the steepest region with small l and r.

Given the sensitivity of the pipette resistance to the tip radius, it is tempting to suggest that this is also what gives rise to the apparent change in R_{pore}. However, it is also possible that changes in the tip radius, by constraining the geometry of the vesicle, instead increase the effective length of the pore. At present there is insufficient data to separate these possibilities.

5.2.7 Stochastic behaviour of the internal conductance

In a final variation of the model, stochastic opening and closing were added to the inner conductance from the vesicle to the cell. As described in §5.1.3, some of our 'strange' recordings include apparent state changes that are suggestive of closure of the internal channel. We have no established mechanism on which to base the modelling of this, since the physical structure of the vesicle has not been measured. Indeed, there is no obvious way to make such a measurement that would take into account the dynamics of either the vesicle in general or the channel in particular.

Lacking any better model, the kinetics of the internal channel were modelled in the same way as the exterior one, via transition probabilities α and β, constrained to some long-term open probability P_{open}. The results for a

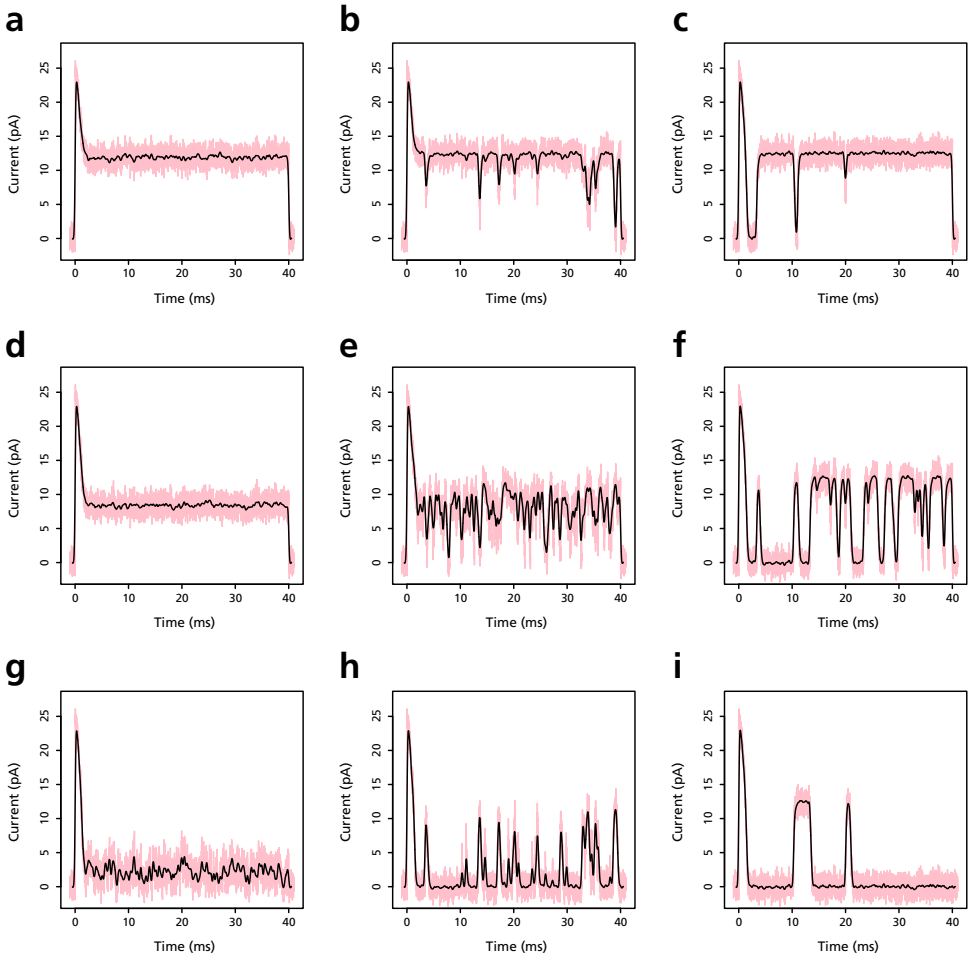

Figure 5.22: Varying P_{open} and β for the internal conductance. As before, 1 pA RMS noise has been added, with filtering by convolution with a Gaussian kernel ($\sigma_t = 125$ µs, $\sigma_f = 1.3$ kHz). **a** $P_{open} = 0.9$, $\beta = 0.9$; **b** $P_{open} = 0.9$, $\beta = 0.1$; **c** $P_{open} = 0.9$, $\beta = 0.01$; **d** $P_{open} = 0.5$, $\beta = 0.9$; **e** $P_{open} = 0.5$, $\beta = 0.1$; **f** $P_{open} = 0.5$, $\beta = 0.01$; **g** $P_{open} = 0.1$, $\beta = 0.1$; **h** $P_{open} = 0.1$, $\beta = 0.01$; **i** $P_{open} = 0.1$, $\beta = 0.001$.

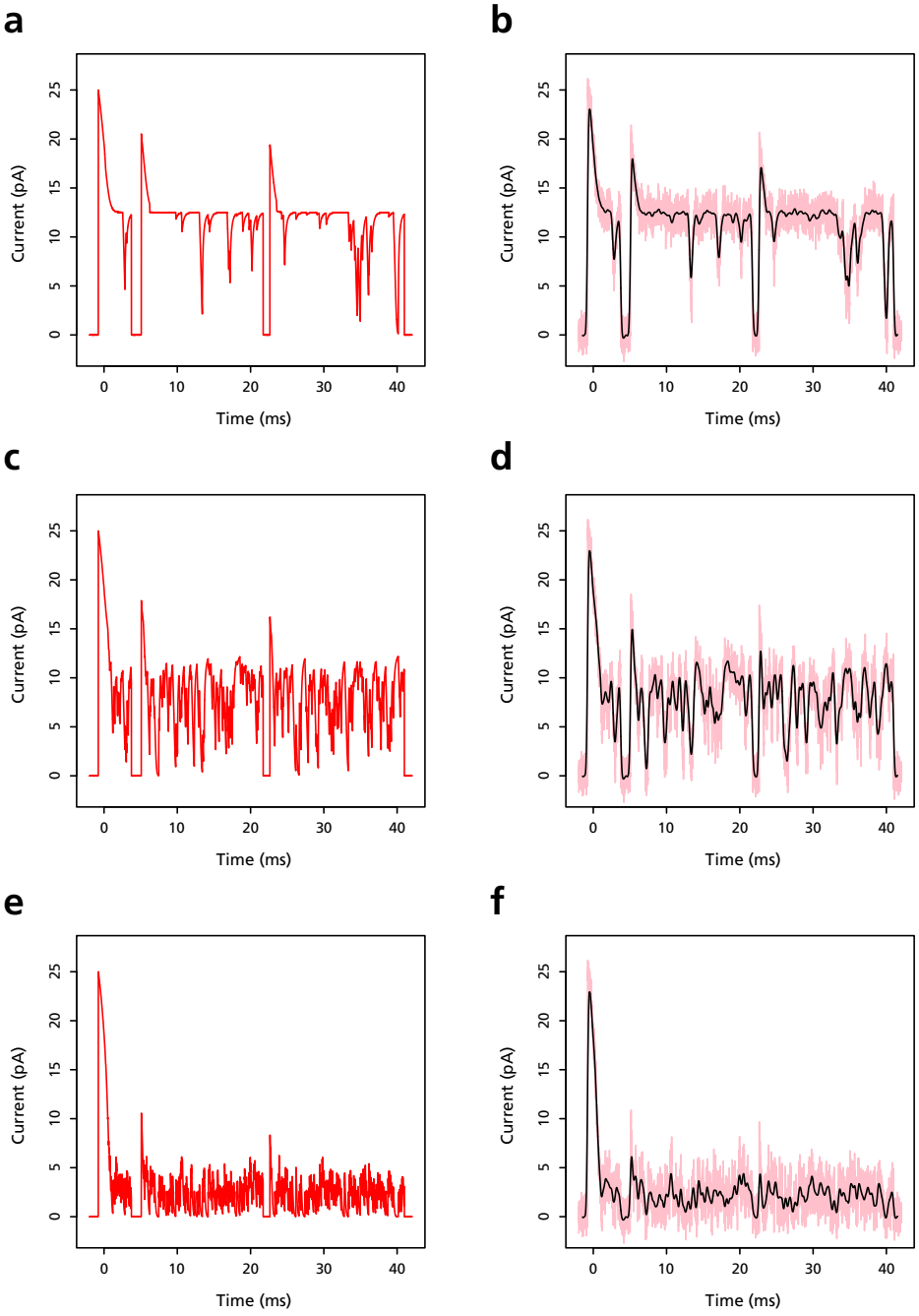

Figure 5.23: Stochastic openings on both side of the vesicle. External channel has $P_{open} = 0.9$, $\beta = 0.01$. Right hand panels have 1 pA RMS noise added and are filtered at $\sigma_t = 125$ µs, $\sigma_f = 1.3$ kHz. Internal channel has $\beta = 0.1$ and open probability: **a,b** $P_{open} = 0.9$; **c,d** $P_{open} = 0.5$; **e,f** $P_{open} = 0.1$.

number of parameter combinations on the internal side—with the external channel maintained at $P_{open} = 1$ for clarity—are shown in Figure 5.22, with noise and filtering as previously described. (Note that with $P_{open} = 0.1$, the values of β were necessarily constrained, so panels g–i use smaller β values than were applied in panels a–f.)

As with the external conductance, where β is high—so that the channel opens and closes very rapidly—individual events cannot be properly distinguished and only an ensemble effect manifests, equivalent to scaling the internal conductance γ_2 and increasing the level of noise. As β decreases, the events are more separable and the measured currents are closer to their true values.

The characteristic shape of an internal opening inverts that of an external, since the equilibrium during closure is the other way around. The current starts at 0 and rises to the steady state level. The model results still show an initial peak, because of the imposed start condition that $\gamma_1 = 0$ for $t < 0$ and hence $C_{ves} = C_2$. But otherwise the results, especially after filtering, look similar to normal channel openings. Once again, the apparent size of openings is dominated by the reduced steady state level rather than the true conductance of the channel.

If stochastic openings are allowed on both sides of the vesicle, the result is as shown in Figure 5.23. The general appearance of these simulations is similar to the poor or post state change records obtained experimentally, exemplified in Figures 5.7 and 5.8. However, the same would doubtless be true of other failure modes that we haven't modelled.

5.2.8 Relationship of vesicle volume to pipette geometry

According to our model, the time course of current decay depends principally on the volume of the vesicle. We have so far considered this abstracted from the actual geometry of the pipette. However, we expect the vesicle to exist inside the pipette tip and therefore be constrained by it. The tip geometry was estimated in Chapter 4 and we now use that to place some bounds on the vesicle.

The pipette interior resembles a truncated cone with a shallow cone angle. We assume that the membrane conforms to the shape of the glass walls for

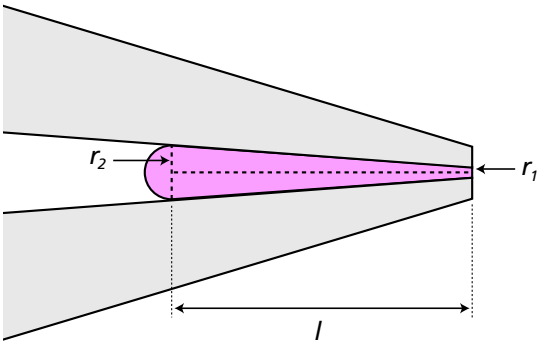

Figure 5.24: Vesicle geometry is constrained by the pipette tip, represented here as a truncated cone. Unless the length l is very short, the volume will be dominated by the conical portion.

some distance into the pipette, before closing off across the interior space. Because of surface tension within the membrane, we approximate the end region as a hemisphere. As illustrated in Figure 5.24, the combined shape is the classic 'omega' described by Sakmann and Neher (1983b). If the truncated cone has end radii $r_1 < r_2$ and length l, then the vesicle volume is:

$$v = \frac{\pi}{3}\left(2r_2^3 + l.(r_1^2 + r_2^2 + r_1 r_2)\right) \tag{5.8}$$

The tripartite geometric model from §4.1 suggests that within the tip head there should be a transition between the different cone angles associated with different OD:ID ratios. We do not know where this transition occurs, so instead calculate a range of possible volumes bounded by the two ratios, as shown in Figure 5.25. We expect that the actual volume will lie somewhere within the shaded region between the two curves.

Since the tip cone angle is shallow, r_2 increases slowly with l. The total volume is quickly dominated by the conical segment and thus depends primarily on the vesicle length.

It is known that for larger patch pipettes the vesicle may extend several µm into the tip (Sakmann and Neher 1983b; Suchyna et al. 2009). If this were to be replicated with the SICM pipettes, the vesicle volume could be large enough to account for the long decay times observed in recordings such as those seen in Figures 5.5 and 5.6. If, on the other hand, the vesicle length is

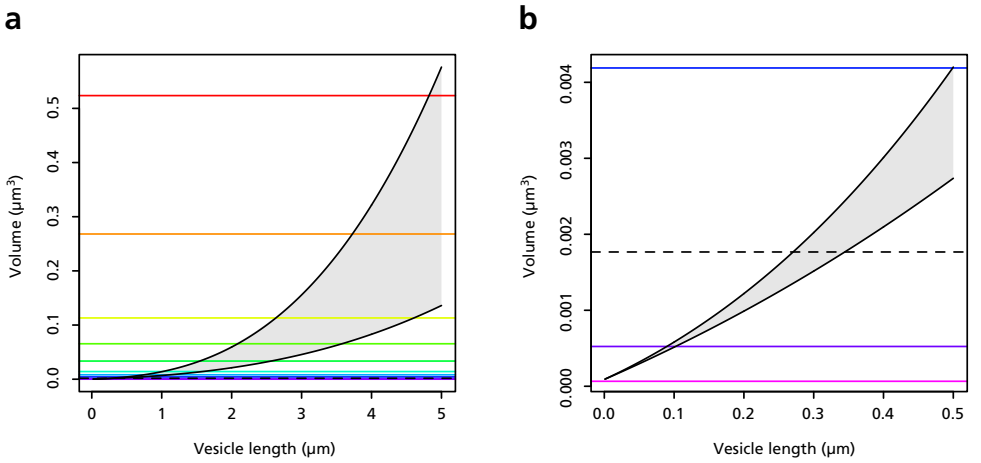

Figure 5.25: Vesicle volume as a function of length. Lower curve shows the volume assuming the thicker tip OD:ID is maintained, upper is for the thinner neck OD:ID. Actual volume will be somewhere in the grey area, depending on the location of the transition region between the ratios. Horizontal lines represent the volume values graphed in Figure 5.12f, equivalent to the sphere radii from Table 5.2f. The first 500 nm of **a** is magnified in **b** for visibility.

scaled in proportion to the much smaller tip opening size, then we would expect short decays that might escape detection, as discussed in §5.2.5.

Given that we see both kinds of phenomenon in our recordings, it is possible that vesicles occur with lengths spanning this whole range.

5.3 Discussion

The vesicle model produces results that are qualitatively similar to those observed in our control recordings, and also provides a potential, albeit speculative, explanation for the apparent tendency of some higher resistance pipettes to underestimate channel conductances.

Despite the addition of various complications, the model remains highly simplified and many details have been neglected that could be expected to influence the behaviour of real currents. Among the many absent factors are: the non-ohmic behaviour of ion channel currents, the capacitance of the pipette and membrane, the presence of multiple ion species, spatial aspects

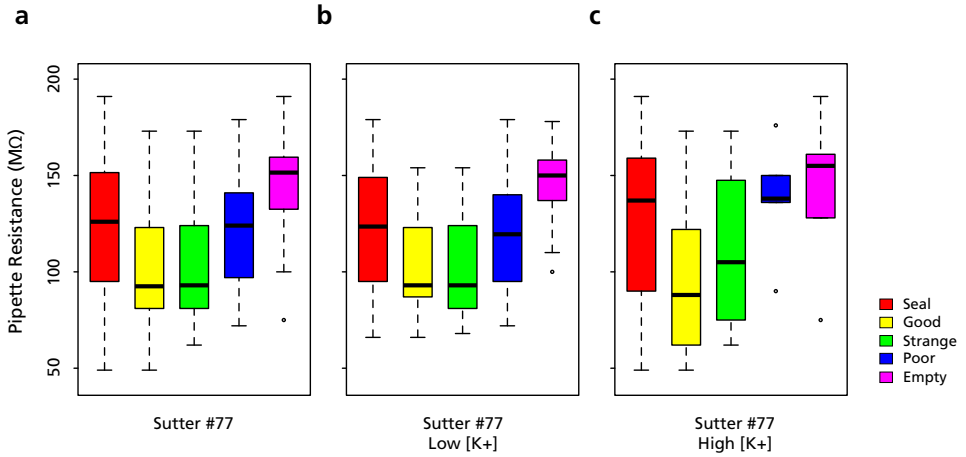

Figure 5.26: Resistance distribution by experimental outcome. Box plots show resistance ranges by category for: **a** all SICM pipette recordings; **b** those in low [K^+]; **c** those in high [K^+].

of diffusion, and imperfect mixing both inside and outside the vesicle. We must therefore treat any quantitative predictions with caution.

One possible qualitative prediction, however, is that the different abnormalities that occur in these recordings might vary according to the size, and hence the resistance, of the pipette. If the 'strange' decaying currents are indeed volume dependent, we would expect them to be more common among lower resistance pipettes, which would have larger tips and so be more likely to support larger vesicles. As resistance increases, decay artefacts might become less visible, and the smaller tips might be more prone to blocking of the vesicle opening. And very high resistance pipettes should be the most likely to sample membrane with no channels, producing empty recordings.

Pipette resistance distributions for different classes of recording are shown as boxplots in Figure 5.26. In each case, the leftmost (red) plot shows the distribution for the whole set of recordings, while the other plots show different subsets. It can be seen that there is indeed a progression up the resistance range as we proceed from good recordings to strange to poor to empty.

In conclusion, the control recording results and vesicle model presented in this chapter suggest that several issues need to be considered when applying the smart patch technique to practical problems.

Patch recording with small pipettes is subject to a number of errors and artefacts. Some of these are also found with large pipettes, but occur more frequently when the tip is fine. Other artefacts, notably the current decay we have hypothesised to be caused by ion depletion in a small vesicle, appear to be unique to small pipettes. Therefore, where possible within the constraints of imaging resolution, pipettes of lower resistance are more likely to produce satisfactory recordings.

Because of the reduced sampling area, there is a significantly lower probability of finding channels in a patch when using SICM pipettes compared to conventional patch pipettes. The degree to which this is problematic depends on the expected channel density in the target region. In cases where channels are present at high density and the aim is to isolate individual channels, for example for studying their gating kinetics, the small sampling area may be a desirable property. In many cases, however, it would be expected to increase the number of experiments required in order to obtain a useful number of successful recordings.

One particular, and previously unreported, consequence of the use of small pipettes is that channel conductances may not be estimated correctly. This effect is most likely to occur when the real channel conductance is large. It is notable that conductance estimates for the bslo channels in low $[K^+]$ solution, with an expected value around 100 pS, did not show evidence of systematic underestimation. The 200–250 pS conductance range of bslo in high $[K^+]$ is larger than most channels, so the impact of this problem may be limited, but it is nevertheless important to be aware of it.

Despite some potential pitfalls, the benefits of localised patching guided by SICM remain significant. We next attempt to apply the technique to a real problem of ion channel localisation in neurons.

Chapter 6

Application of smart patch to cerebellar terminals

As described in §1.2, the proposed explanation for the phenomenon of DPI requires the presence of functional NMDA receptors in the presynaptic terminals of cerebellar interneurons. We decided to apply the smart patch clamp technique to see if these receptors could be detected electrophysiologically in such terminals.

6.1 GAD65-EGFP cerebellar culture

SICM does not produce satisfactory images of brain slices, because of the residue of damaged tissue occluding the surface. Therefore, patching was performed in primary dissociated culture, where the phenomenon of DPI has also been observed.

Cerebellar basket and stellate cells can be readily recognised in slices by location and morphology. This is not the case in dissociated culture. To allow the correct cells to be identified, we made use of a transgenic mouse strain developed by Erdélyi et al. (2002). These mice express enhanced green fluorescent protein (EGFP) under the control of the promoter for the 65 kDa isoform of glutamic acid decarboxylase (GAD65), an enzyme used in the production of the inhibitory neurotransmitter γ-aminobutyric acid (GABA). GAD65 is expressed in many GABAergic neurons and a proportion of such

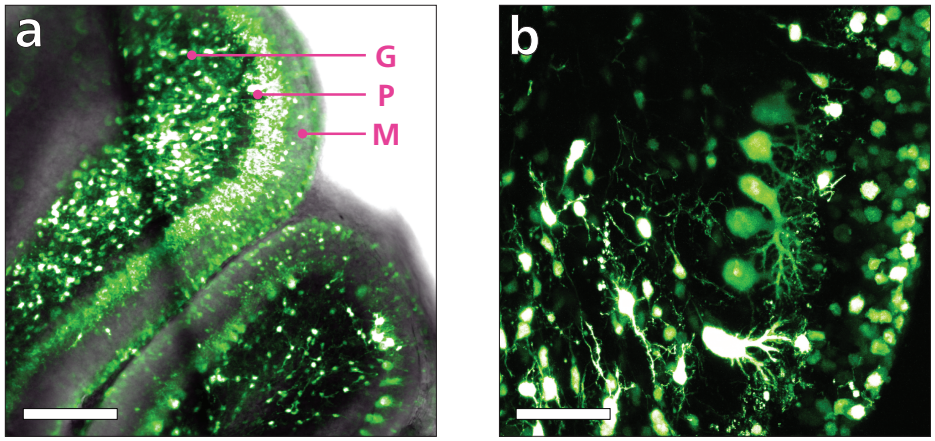

Figure 6.1: Confocal images of a parasagittal slice from the cerebellum of a GAD65-EGFP transgenic mouse. Fluorescent protein is expressed by inhibitory neurons in the molecular (M), Purkinje (P) and granule cell (G) layers of the cerebellar cortex. (Scale bars: **a** 200 µm; **b** 50 µm.)

cells also express EGFP in these transgenic mice. This provided a marker by which inhibitory neurons could be identified.

In slices from the cerebellar cortex, EGFP expression was observed as expected in molecular layer interneurons, Golgi neurons of the granule layer and in the much larger Purkinje cells (Figure 6.1).

These cells are known to have different survival rates in culture (Spatkowski and Schilling 2003). In order to determine the identity of EGFP-expressing cultured cells, antibody staining was performed for the characteristic interneuron protein parvalbumin (Figure 6.2). Of 20 green fluorescent cells examined, all 20 were also positive for parvalbumin. We therefore concluded that EGFP expression was a good indicator of interneuron identity in culture.

In addition to locating candidate cells, it was necessary to identify the presynaptic compartments within them. This was done from morphology and also by activity-dependent labelling with the styryl dye FM 4-64.

Many fluorescent neurons in culture exhibited a characteristic 'beaded' region, where a process became winding and branched, with many obvious varicosities. An example can be seen in Figure 6.2. (Note that the beaded process in this instance is not part of the neuron in the field of view but

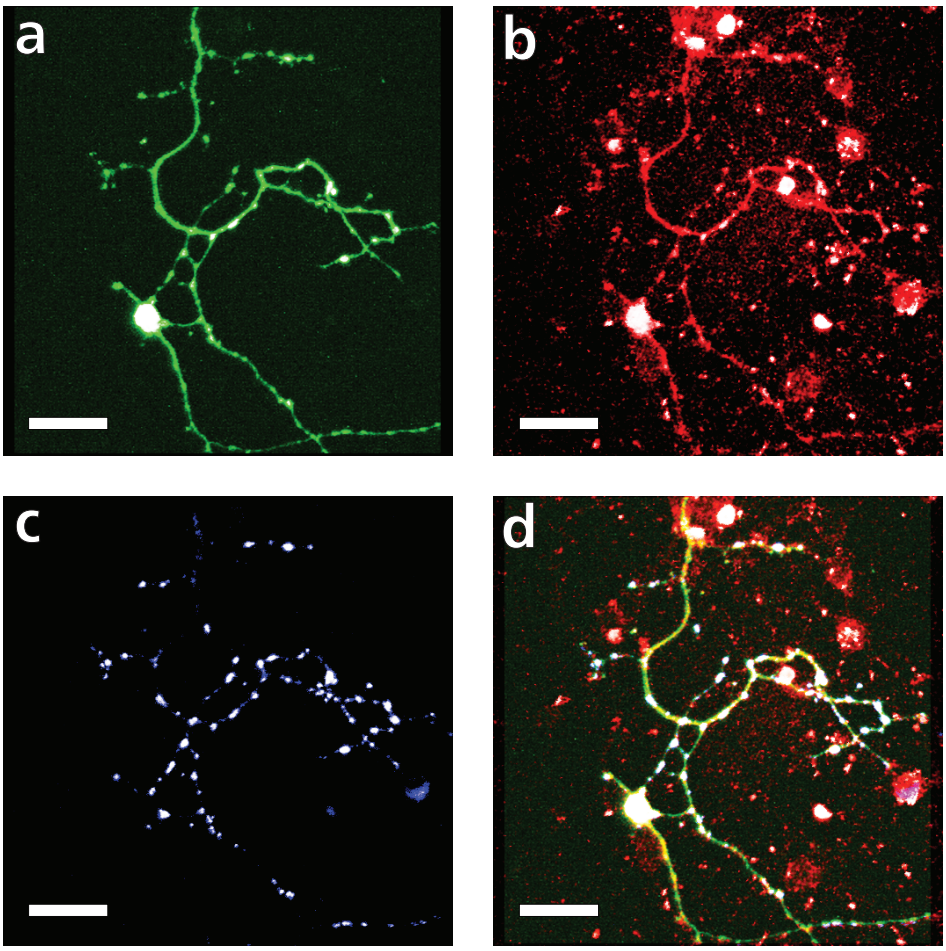

Figure 6.2: Interneuron and synaptic staining of GAD65-EGFP cerebellar culture shows colocalisation of the expressed EGFP (**a**, green) with parvalbumin (**b**, red) and VIAAT (**c**, blue). **d** Combined image with all three fluorophores overlaid. (Scale bars, 25 µm.)

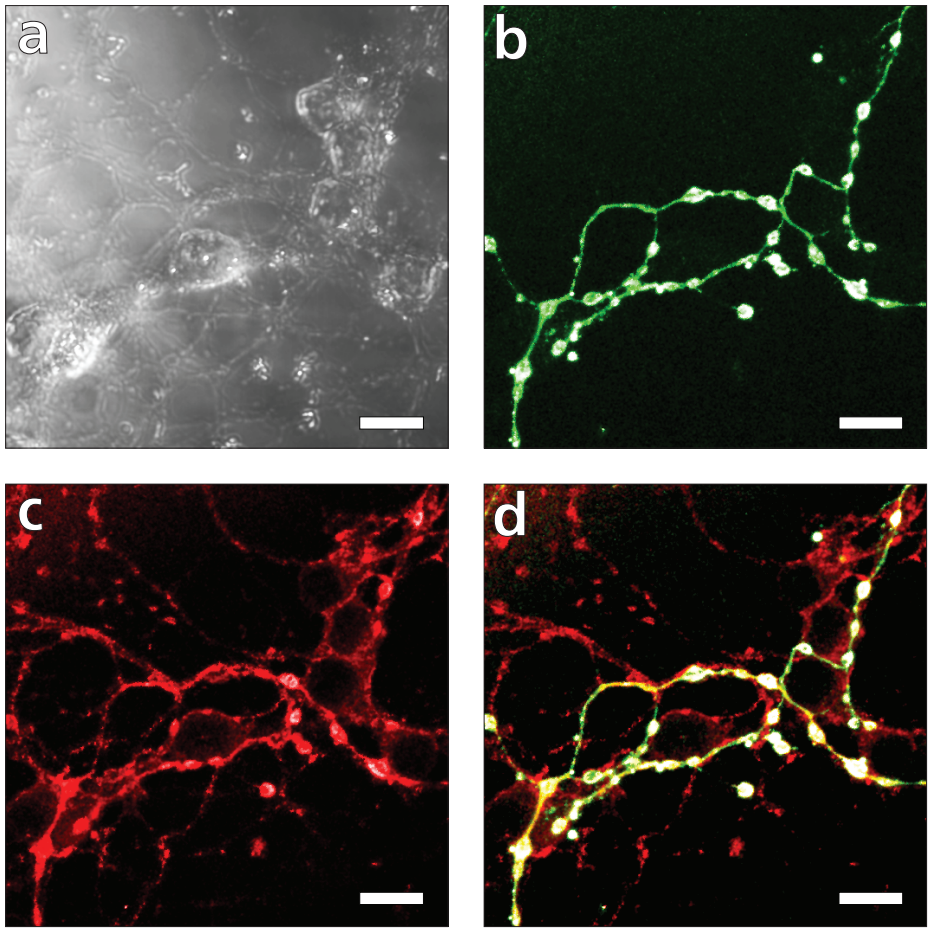

Figure 6.3: Axonal staining of GAD65-EGFP cerebellar culture. **a** Brightfield image of cultured cells. **b** Transgenically expressed EGFP. **c** Antibody staining for axonal marker Tau. **d** Combined image shows colocalisation of both fluorophores in 'beaded' region of putative synaptic boutons. (Scale bars, 10 µm.)

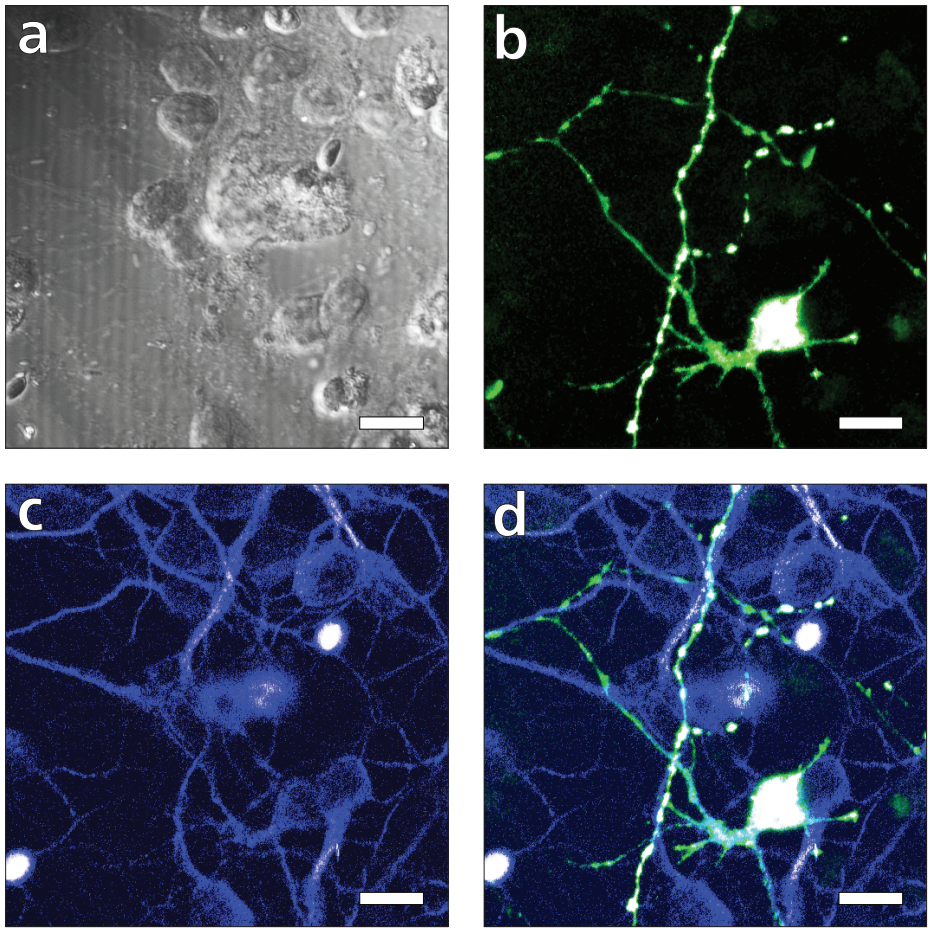

Figure 6.4: Dendritic staining of GAD65-EGFP cerebellar culture. **a** Bright-field image of cultured cells. **b** Transgenically expressed EGFP. **c** Antibody staining for dendritic marker MAP2. **d** Combined image shows MAP2 is not expressed in 'beaded' region. (Scale bars, 10 µm.)

extended from a second cell some distance away.) In this experiment, antibody staining was also performed for the vesicular inhibitory amino acid transporter protein (VIAAT), which localises to presynaptic boutons of inhibitory neurons (Dumoulin et al. 1999). As can be seen in panel 6.2c, VIAAT is present in the varicosities. Similar colocalisation was observed in 18 out of 20 EGFP-expressing cells.

Further antibody staining experiments were performed to confirm the identity of these beaded regions. The Tau protein is an axonal marker (Bradke and Dotti 2000). In all 20 cells examined, the beading was found to colocalise with Tau (Figure 6.3). Conversely, the microtubule-associated protein MAP2 occurs in dendritic and perikaryotic regions and not in axons (Bernhardt and Matus 1984). MAP2 did not colocalise with the beaded regions in any of 21 cells (Figure 6.4). We conclude that these regions are axonal and therefore these varicosities could be taken as putative bouton targets for smart patch clamping.

In many experiments, live cell staining with the activity dependent styryl dye FM 4-64 (§2.4.1) was also performed to identify regions of vesicular internalisation characteristic of presynaptic terminals. FM loading could give rise to high levels of background and so was not always conclusive, but it provided additional circumstantial evidence for target location.

6.2 Smart patching in cerebellar culture

6.2.1 Experimental variations

Methods for the preparation of GAD65-EGFP cerebellar cultures (§2.1.3), FM 4-64 loading (§2.4.1) and smart patch clamping (§2.7.1) are presented in Chapter 2. The culture protocol as described was the result of several rounds of refinement, and numerous variations were tried over the course of the project.

Cultures were initially plated at uniform density rather than in the X shape shown in Figure 2.1. Low density cultures exhibited very poor survival rates, while high density were too busy to find clearly identifiable and accessible terminals. The eventual plating pattern led to improved survival of

the culture as a whole while providing an extensive low density periphery containing some accessible cells and processes.

Different growth substrates were tested, including poly-L-lysine, poly-L-ornithine, laminin and poly-D-lysine without borate buffer. The borate-buffered poly-D-lysine produced the most consistent results, while laminin was wholly unsuccessful. Differences between the others were marginal.

The final protocol was somewhat unconventional insofar as a defined, serum-free medium was used for the initial plating and the first 24 hours of growth, while subsequent maintenance was in a serum-based medium. In a number of tests using different serum-based media immediately or serum-free media in the longer term, cultures tended to be very unhealthy. In particular, cells would frequently die *en masse* at around DIV 7–8. This is also the stage when synapses are believed to form, but we were unable to establish whether there was any causal relationship between these events. Addition of glutamate receptor antagonists to the culture medium did not appear to improve the cultures' survival, suggesting that the poor health was not trivially a result of excitotoxicity.

Most patch attempts were made using pipette filler solutions containing NMDA and glycine, with Mg^{2+} ions omitted and buffered to very low levels to avoid their block of NMDARs [22][23][24]. Because of the patch configuration it was not possible to exchange the external solution during recording, and thus we could not observe the response of a recorded channel to different drugs. The only intervention that could be readily made was to alter the applied pipette potential. NMDAR Mg^{2+} block is known to be voltage-dependent, relieved by depolarisation (Nowak et al. 1984). In the latter stages of the project it was realised that this could potentially provide a useful marker of channel identity. Accordingly, a subset of experiments were performed with Mg^{2+} explicitly included in the pipette filler [25], in the hope of observing voltage-dependent block.

Pipettes used were Intracel #95, Intracel #99 or Sutter #77 (§2.6.2). In many cases the tips were coated with Sylgard or ski-wax to reduce capacitance; retrospectively this appears to have significantly increased the rejection rate (131/318 compared to 36/131; $p = 0.007$, Fisher's exact test). In 42 of 449 cases positive pressure was applied to help keep the tip clear; this had no identifiable effect on success, but the number is small.

6.2.2 Rates of success and failure

Smart patch experiments with GAD65-EGFP cerebellar cultures were performed on 85 days over the course of 2 years. Overall experimental outcomes are summarised in Table 6.1, using a similar classification to that used for the HEK-bslo experiments in §5.1.1. Aggregate Sutter #77 results from the latter experiments are also reproduced in the table for comparison purposes.

It is clear that the neuronal results were generally poorer than those for HEK cells, with lower seal rates and fewer good recordings obtained. But this is not surprising given the much greater complexity of the preparations and much smaller and more specific patch targets. Candidate HEK cells could be identified quickly and easily, and patched with little concern for positional precision. By contrast, it would frequently take tens of minutes of searching to locate a potentially patchable interneuron in the culture, then further time to perform scans and match the topography to the fluorescence before deciding whether to attempt a patch. Throughout this process the pipette tip was vulnerable to blockage—requiring the experiment to be started over—or to contamination that could interfere with the seal.

Possibly due to the latter, perhaps because of the small size or some other as-yet unidentified property of the targets, even 'good' recordings were typically quite unstable and inconsistent. Only relatively short stretches were clear enough to analyse, and there was no way to be certain that the same

	Total	Intracel #95/#99	Sutter #77	HEK-bslo
Total Pipettes	449	308	141	98
Seal Attempted	144 (32%)	84 (27%)	60 (43%)	71 (72%)
Sealed	90 (63%)	45 (54%)	45 (75%)	60 (85%)
Good	9 (10%)	5 (11%)	4 (9%)	14 (23%)
Empty	20 (22%)	10 (22%)	10 (22%)	20 (33%)
Strange	13 (14%)	6 (13%)	7 (16%)	9 (15%)

Table 6.1: Outcomes of smart patching in cerebellar culture. Percentages are given with respect to the closest containing set, ie: Attempted as a proportion of Total; Sealed as a proportion of Attempted; Good, Empty and Strange as a proportion of Sealed.

channels were involved in each stretch. It is thus necessary to be cautious about any possible conclusions. Nevertheless, the results were interesting.

In view of the small number of useful recordings obtained, all 9 are presented below (§§6.2.4–6.2.6).

6.2.3 Proportion of empty recordings

If we compare the number of good recordings, in which channel activity can be clearly identified, to the number of empty recordings, in which it is clearly absent, we can extrapolate a crude metric of the channel density in the membrane. Poor or ambiguous recordings are excluded because we cannot say anything useful about the presence or absence of channels in those patches.

We assume that all recordings are drawn from comparable membrane populations. The evidence for this is circumstantial, but there is no reason to suspect the contrary. Some examples of empty recording locations are shown in Figure 6.5, for comparison with the location data for good recordings in Figures 6.6 & 6.10–6.18, below.

In the HEK-bslo experiments, there were 20 empty recordings compared to 14 good, while in the putative cerebellar terminals there were 20 empty to 9 good. Although this appears to suggest a slightly lower density of channels in the bouton membrane, the difference is not significant ($p = 0.4424$, Fisher's exact test). This is a potentially interesting result, because channel expression in transfected HEK cells is typically very high. If channels were to be present in synaptic boutons with comparable density, this could be expected to contribute to complex presynaptic behaviour.

6.2.4 Smart bouton recording #1

The first putative bouton recording is a special case. Dating from early in the project, it was performed without NMDA and glycine in the pipette solution. It is thus only peripherally relevant to the question at hand. Nevertheless, it is interesting in its own right, and exhibits some of the issues discussed in the previous chapter.

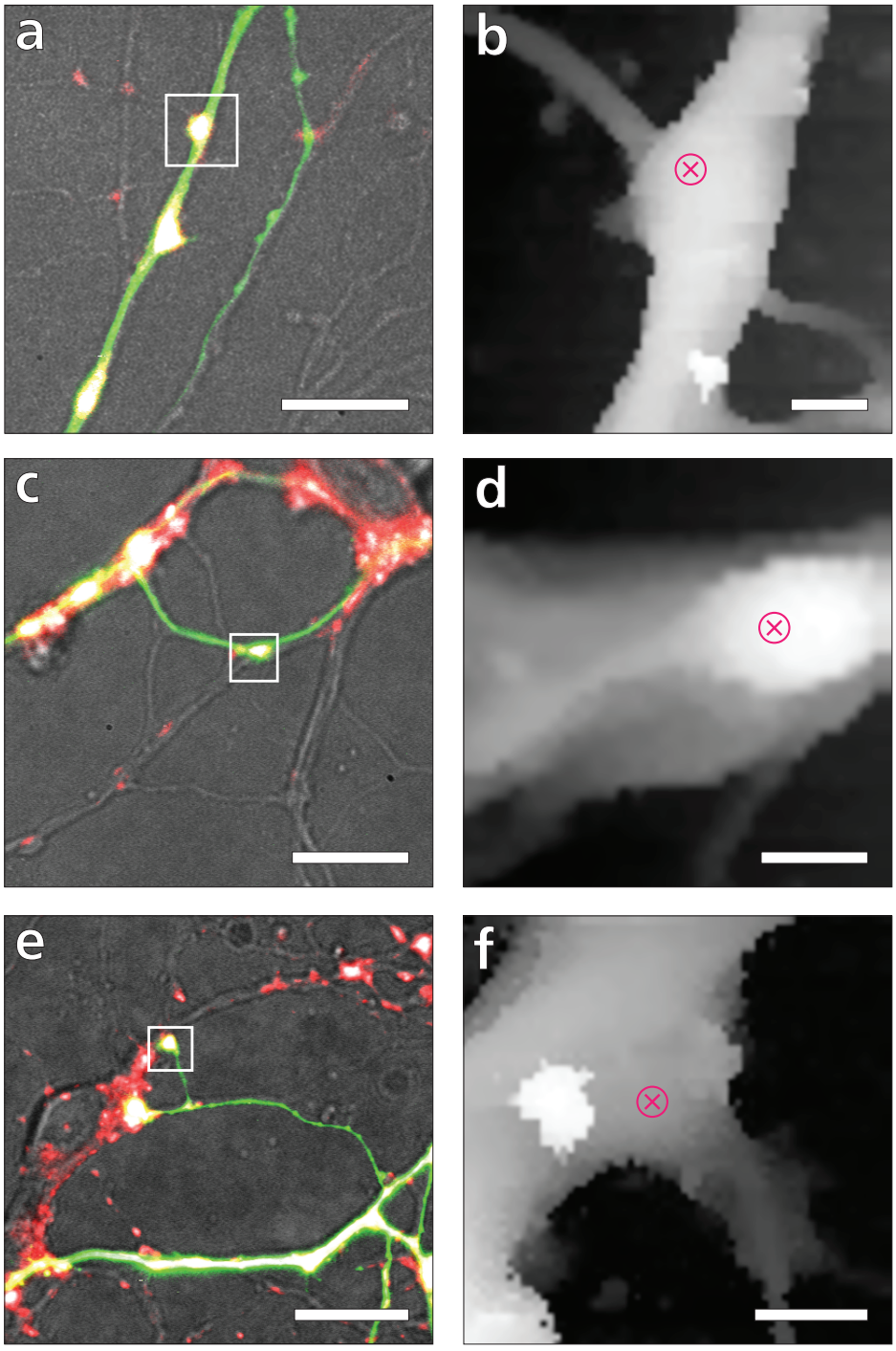

Figure 6.5: Locations of some empty recordings. **a,c,e** Optical images showing brightfield overlaid with EGFP and FM 4-64 fluorescence. Boxes mark scan areas. **b,d,f** Corresponding SICM images with markers indicating patch locations. (Scale bars a,c,e 10 µm, b,d,f 1 µm.)

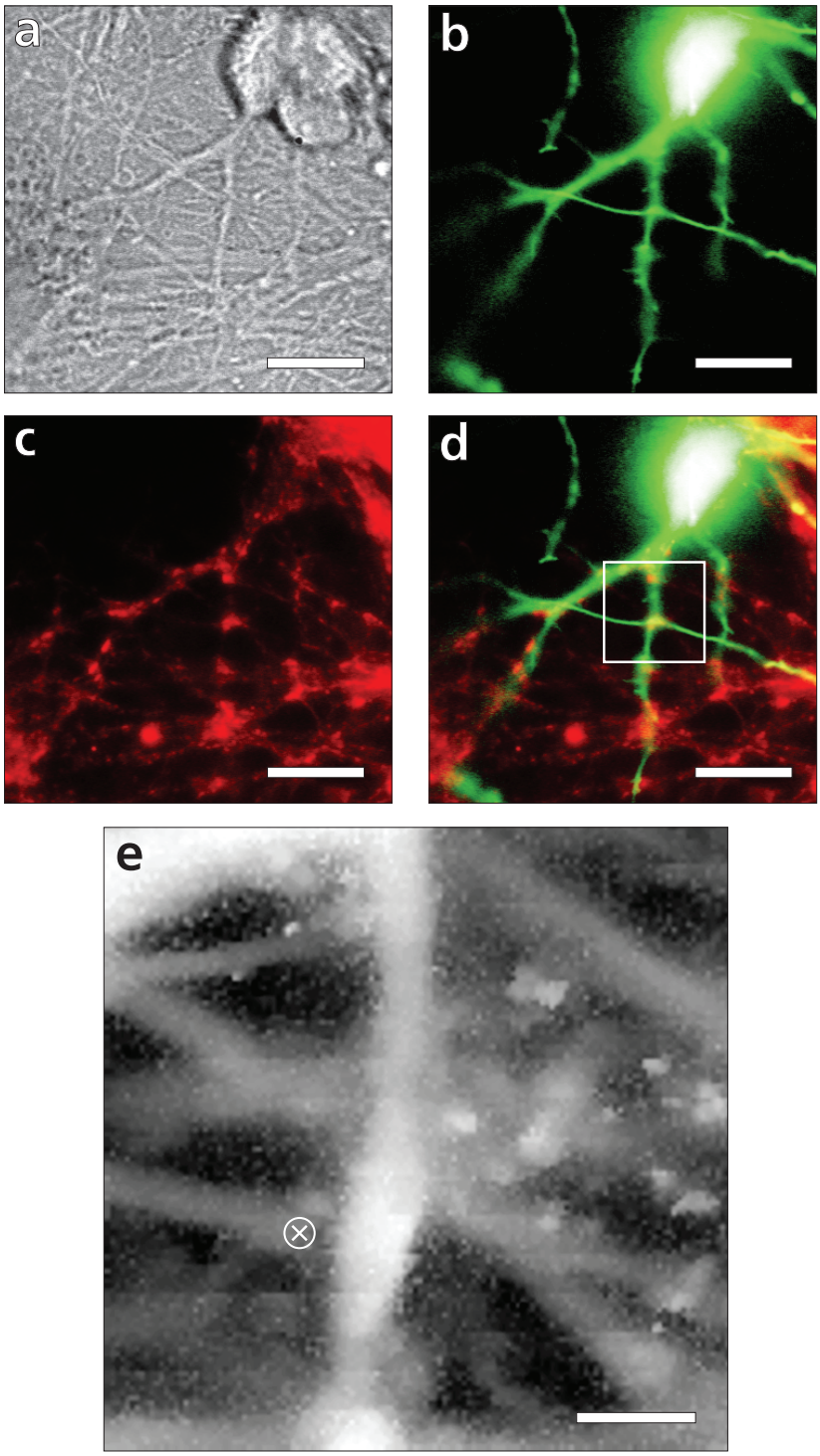

Figure 6.6: Location of smart recording #1. **a–c** Optical microscope images of brightfield, EGFP and FM 4-64 signals respectively. **d** Overlay of the three optical images, with box marking area of scan. **e** SICM image with marker indicating patch location. (Scale bars a–d 10 µm, e 1 µm.)

The recording location is shown in Figure 6.6. The culture was dense, with many criss-crossing processes. The chosen point was at the intersection of two EGFP-expressing processes, with FM 4-64 staining on both sides of the intersection suggesting the existence of synaptic connectivity. The larger process, roughly vertical in the images, appeared to be a proximal dendrite belonging to the visible soma, so the patch was made on the finer lateral process on the basis that it was more likely to be axonal.

The recorded trace was clean and stable. Openings occurred at very low frequency, in very short bursts with long gaps in between. Examples of individual bursts are shown in Figure 6.7a. Over the 40 min duration of the recording, there were 57 identified bursts with a total open time of 3.6 s, an aggregate P_{open} of about 1.5×10^{-3} (assuming only a single channel was present). The time course of pipette potential changes and events throughout the whole recording are depicted in Figure 6.7b–d.

Burst currents showed a distinctive decay similar to that seen in some HEK-bslo recordings and in the vesicle model in Chapter 5. If this decay indeed occurred by vesicular depletion, the initial peak current should most closely reflect the true channel conductance. Figure 6.8 shows an IV plot for these peaks.

There appears to have been some drift in the sizes of the measured currents over time. This has been illustrated by sequentially colour-coding the plotted points, from the earliest in green to the latest in purple. Linear fits are shown for subsets of points from both the beginning of the recording and the end, producing quite different conductance estimates. It is not clear what caused this change. It is possible that different channels were active at different times, although the gradual shift in value, visible especially at -75 mV, is not obviously discrete and may suggest the process was more continuous in nature. The -75 mV bursts have also been marked on the time course in Figure 6.7c to make the decline visible above the background variation due to voltage changes.

As can be seen from Figure 6.9a, neither the burst duration nor within-burst P_{open} exhibited voltage dependence. There was some evidence for bursts occurring more frequently at depolarised potentials (Figure 6.9b), with no openings at all at resting or hyperpolarised potentials. However, only a tiny fraction of the recording (197 of 2432 s, 8%) was spent at such potentials.

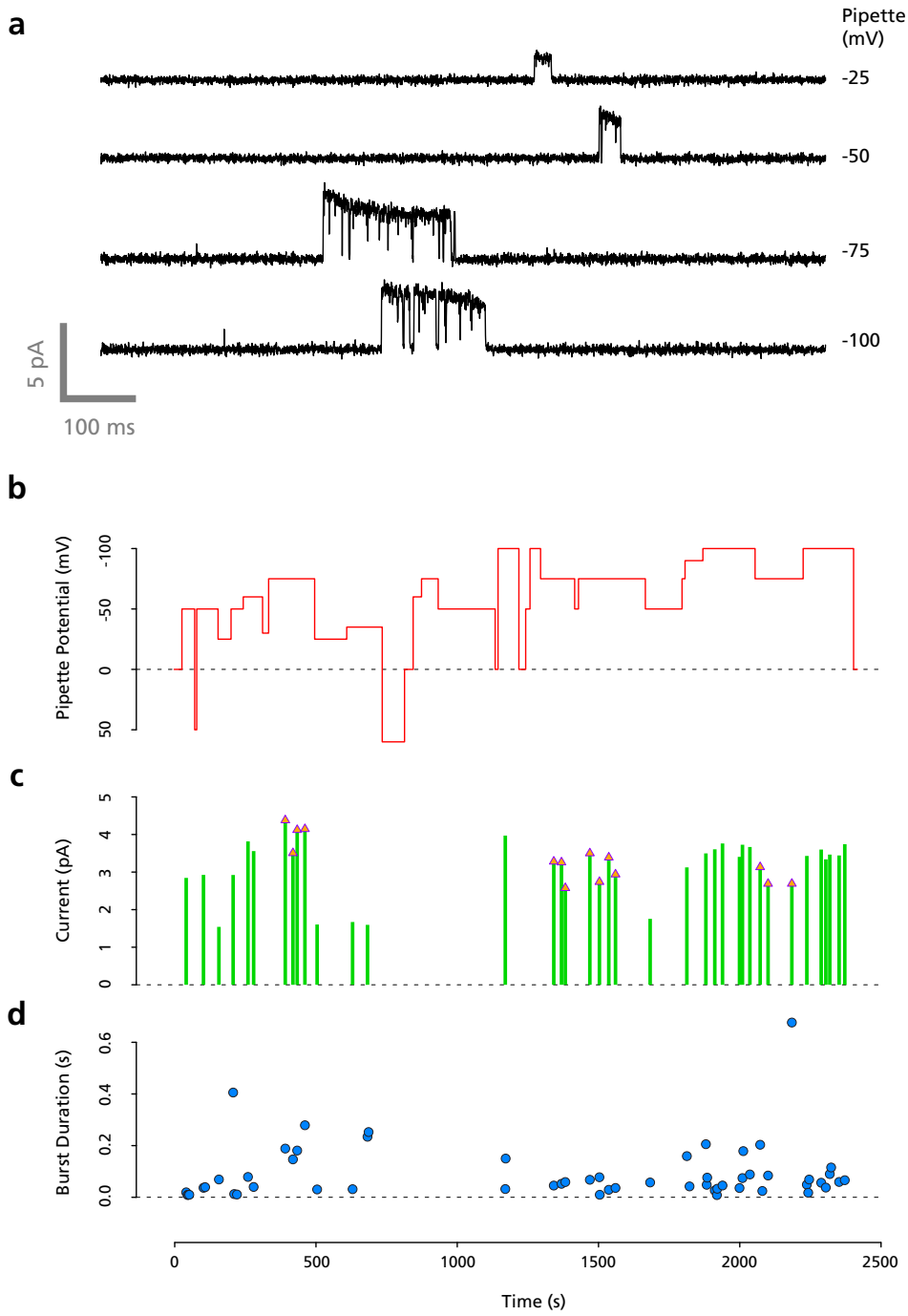

Figure 6.7: Overview of smart recording #1. **a** Example opening bursts at several voltages. Openings were very infrequent and exhibited current decay. **b** Changes in pipette potential over lifetime of recording. **c** Peak current at start of burst over lifetime of recording. Triangular markers indicate bursts occurring at a common pipette potential, –75 mV. **d** Duration of each burst over lifetime of recording.

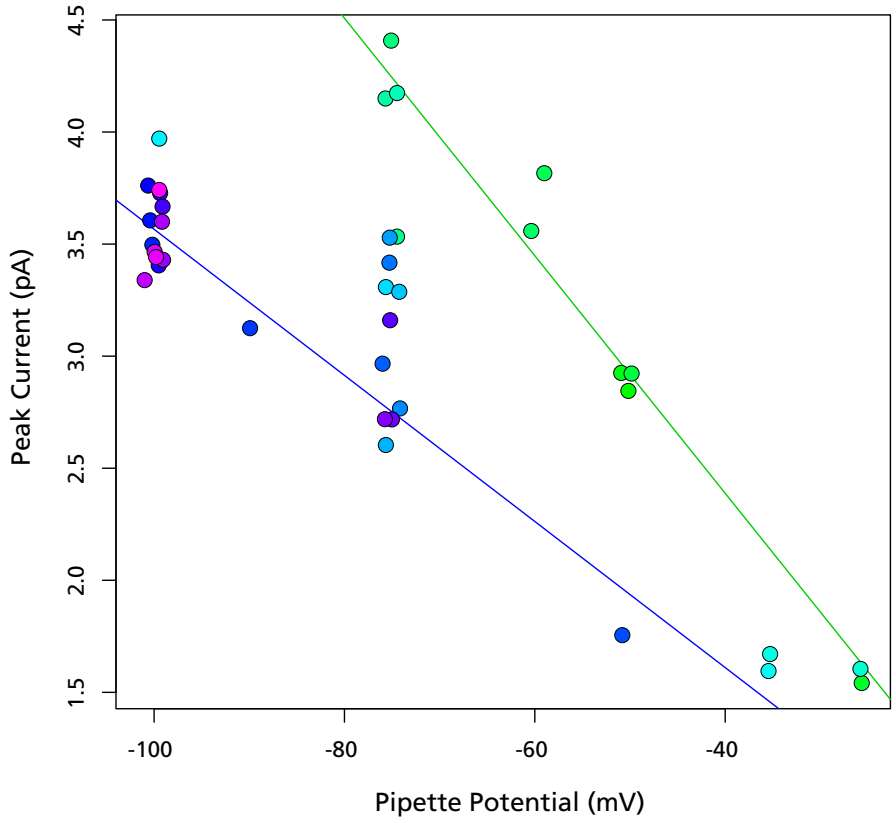

Figure 6.8: Peak current in relation to voltage. Points are coloured sequentially in order of recording, on a continuous hue scale from green to purple. Apparent channel conductance reduced over time. Lines were regressed from points at the beginning of the recording (green; slope 53 pS, reversal 5 mV) and the end (violet; slope 33 pS, reversal 10 mV).

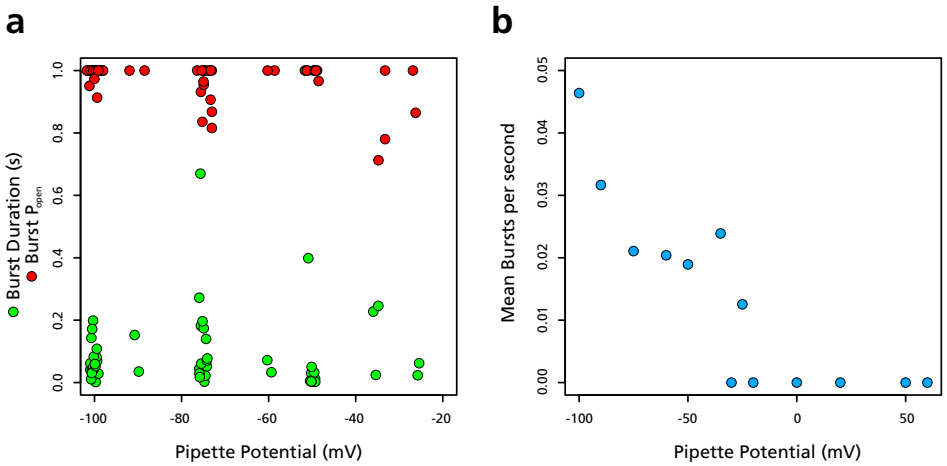

Figure 6.9: Burst duration (green) and the within-burst open probability (red) exhibited no identifiable voltage dependence (**a**), but there was some evidence of increased burst frequency at more depolarised potentials (**b**).

In the absence of either of its ligands, an NMDA receptor would not be expected to exhibit even the low rate of opening observed in this recording, and the conductance and kinetics are not distinctive enough to be able to offer any other strong candidate for the channel identity. It is not clear why the conductance appeared to change with time. Considering the model in Chapter 5, one possible cause could be a change in vesicle geometry, leading to a faster decay time and greater peak loss due to filtering. Irrespective of whether this is the case, the validity of the conductance estimates must be considered uncertain.

6.2.5 Smart recordings #2–#8

Seven cell-attached smart recordings from putative interneuron boutons were obtained in the presence of NMDA and glycine, and under similar experimental conditions. They are presented in a uniform format in Figures 6.10–6.16. For each figure, panels **a** and **b** show optical microscope images of the patch region, while panel **c** indicates the recording location selected within the SICM image. Several 1 s segments of current trace at different voltages are shown in panel **d**. An estimated current-voltage relationship is plotted in panel **e**, with individual observations shown in blue, median opening

currents at each voltage in red, error bars indicating the MAD, and a line showing a robust linear regression from all points.

For recordings #2–#7, Mg^{2+} was omitted from the pipette filler and EDTA added to chelate residual levels. Recording #8 included explicit $MgCl_2$ at 1.2 mM, sufficient to induce a near-saturating voltage-dependent block in NMDARs of all subunit compositions except for those including NR3 (Sasaki et al. 2002; Qian et al. 2004).

Summary results from these recordings are given in Table 6.2 and plotted in Figure 6.17.

#	Pipette Resistance (MΩ)	Estimated Conductance (pS)	Reversal Potential (mV)	Mg^{2+}	Multiple Channels
2	67	34 ± 2	-17 ± 4	×	✓
3	77	21 ± 1	-60 ± 7	×	×
4	110	20 ± 1	36 ± 6	×	✓
5	56	12 ± 1	-54 ± 11	×	✓
6	172	26 ± 3	-43 ± 12	×	✓
7	100	23 ± 2	-19 ± 5	×	✓
8	124	31 ± 4	-4 ± 9	✓	✓

Table 6.2: Summary results for smart cell-attached bouton recordings in the presence of NMDA and glycine.

In nearly all recordings there is evidence of more than one channel in the patch, either in the form of double openings or a very great disparity in opening behaviour. A striking example of the latter can be seen in the traces for recording #4 (Figure 6.12), where a very large opening at +50 mV is markedly out of keeping with those at other potentials; we will revisit this later in the chapter. It was often not possible to clearly distinguish which openings corresponded to different channels in the records. As a consequence, some conductance estimates may be distorted by contributions from more than one type. Given the small region of membrane sampled by the fine SICM pipette tip, the high incidence of multiple channels appears to support the suggestion from §6.2.3 that channel density in our target locations is unexpectedly high.

It can be seen from Figure 6.17a that the measured openings are of the right

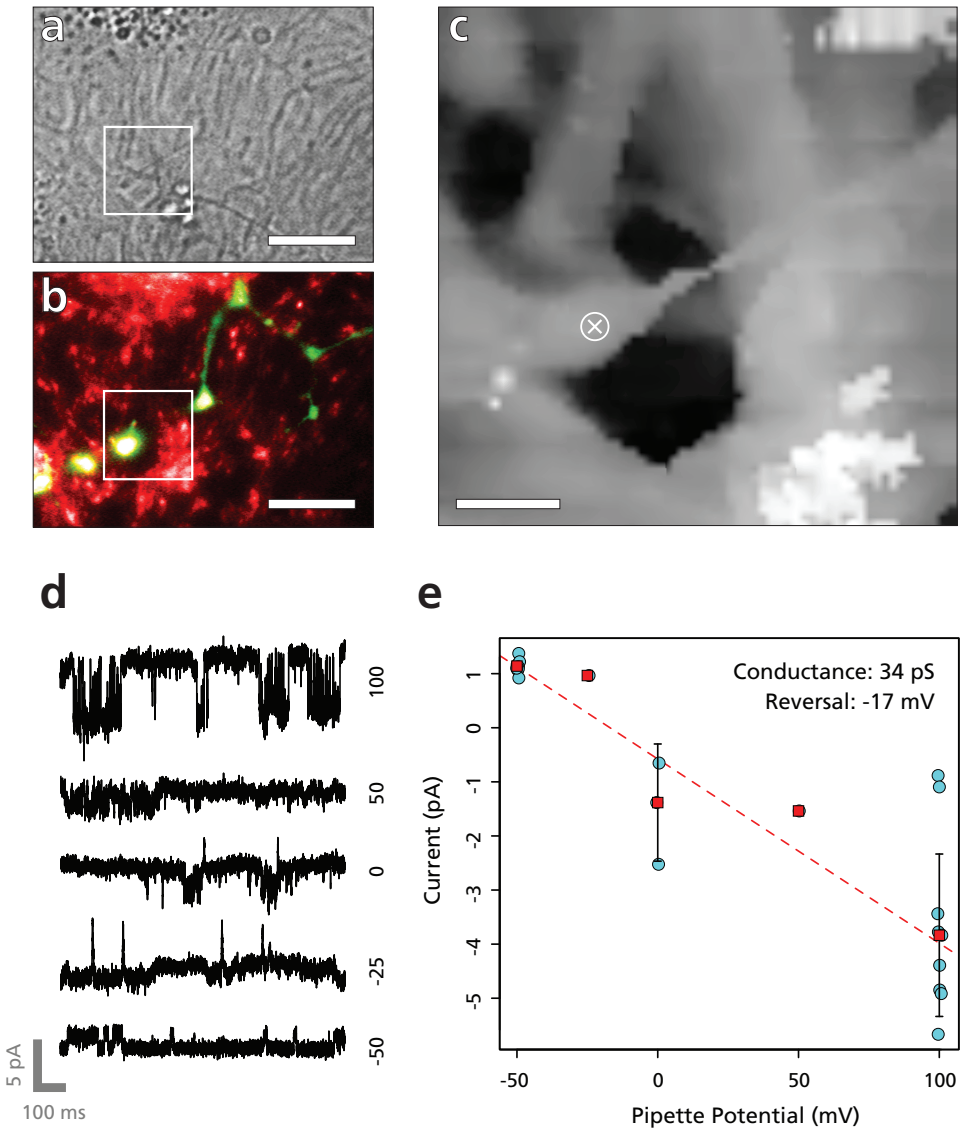

Figure 6.10: Smart recording #2. **a** Brightfield microscope image of the patch region. **b** Corresponding fluorescence image for EGFP (green) and FM 4-64 (red). **c** SICM image of the area marked on optical images, with marker indicating location of patch. **d** Example 1 s segments of trace for different pipette potentials. **e** Current-voltage plot of measurable openings. (Scale bars a,b 10 µm, c 2 µm.)

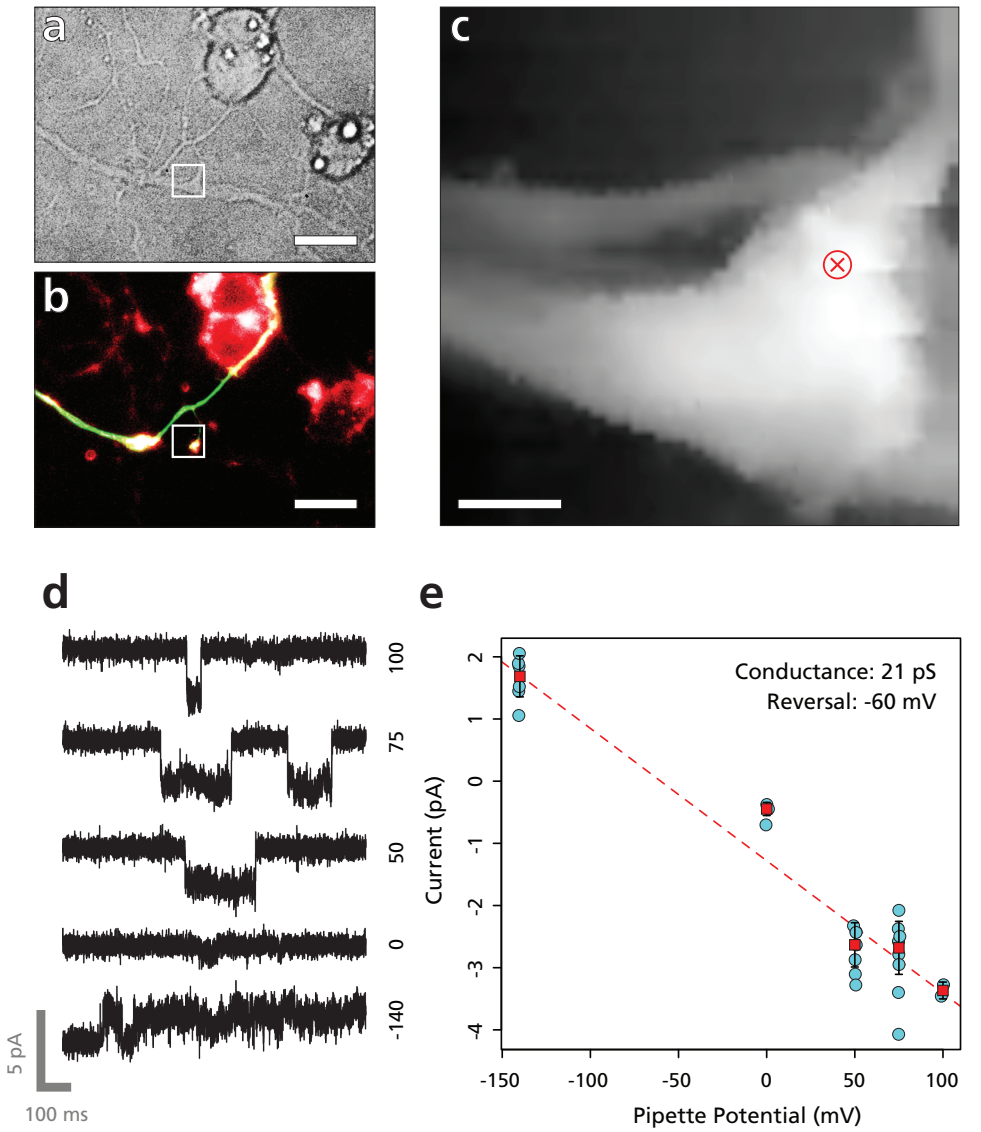

Figure 6.11: Smart recording #3. **a** Brightfield microscope image of the patch region. **b** Corresponding fluorescence image for EGFP (green) and FM 4-64 (red). **c** SICM image of the area marked on optical images, with marker indicating location of patch. **d** Example 1 s segments of trace for different pipette potentials. **e** Current-voltage plot of measurable openings. (Scale bars a,b 10 µm, c 1 µm.)

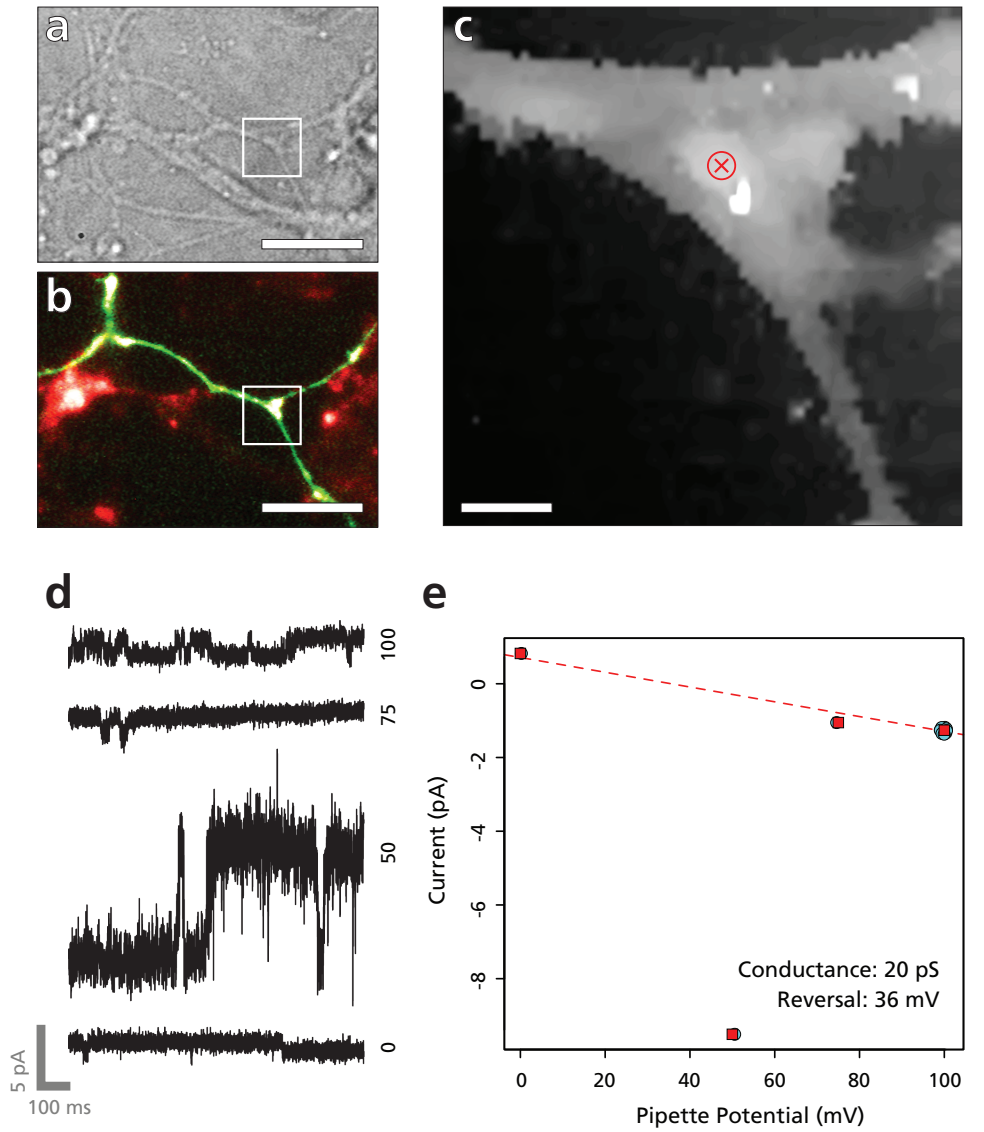

Figure 6.12: Smart recording #4. **a** Brightfield microscope image of the patch region. **b** Corresponding fluorescence image for EGFP (green) and FM 4-64 (red). **c** SICM image of the area marked on optical images, with marker indicating location of patch. **d** Example 1 s segments of trace for different pipette potentials. **e** Current-voltage plot of measurable openings. (Scale bars a,b 10 µm, c 2 µm.)

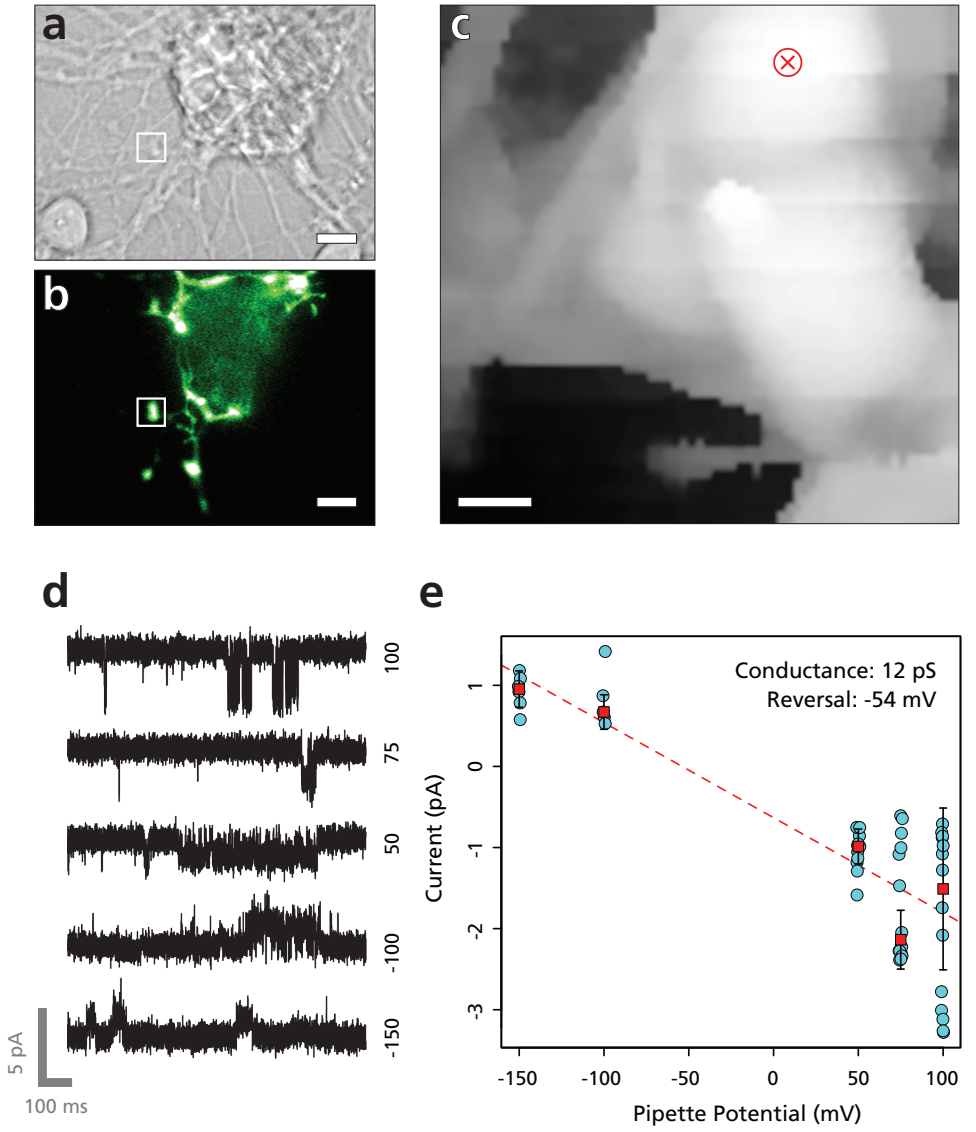

Figure 6.13: Smart recording #5. **a** Brightfield microscope image of the patch region. **b** Corresponding fluorescence image for EGFP. **c** SICM image of the area marked on optical images, with marker indicating location of patch. **d** Example 1 s segments of trace for different pipette potentials. **e** Current-voltage plot of measurable openings. (Scale bars a,b 10 µm, c 1 µm.)

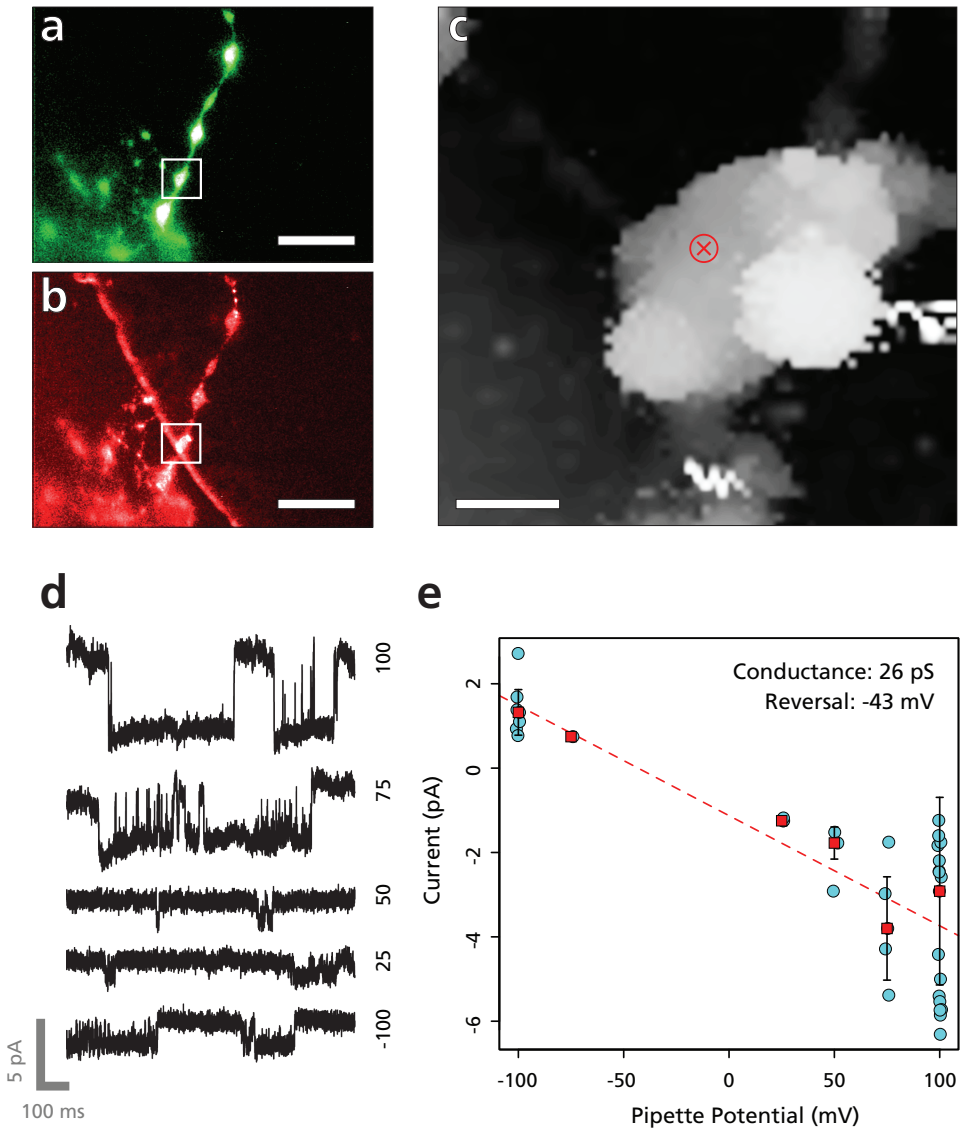

Figure 6.14: Smart recording #6. **a** EGFP fluorescence image of the patch region. **b** FM 4-64 fluorescence image of the patch region. **c** SICM image of the area marked on optical images, with marker indicating location of patch. **d** Example 1 s segments of trace for different pipette potentials. **e** Current-voltage plot of measurable openings. (Scale bars a,b 10 µm, c 1 µm.)

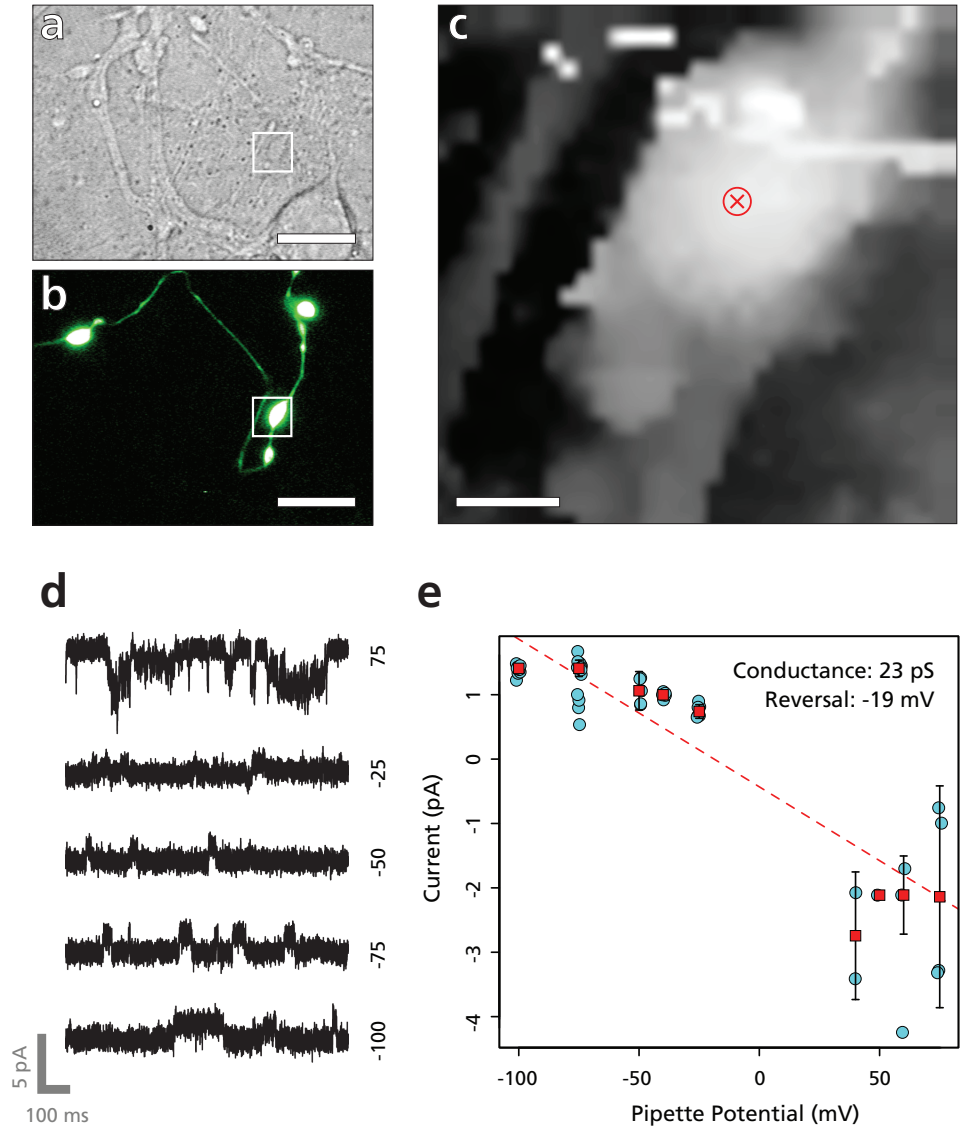

Figure 6.15: Smart recording #7. **a** Brightfield microscope image of the patch region. **b** Corresponding fluorescence image for EGFP. **c** SICM image of the area marked on optical images, with marker indicating location of patch. **d** Example 1 s segments of trace for different pipette potentials. **e** Current-voltage plot of measurable openings. (Scale bars a,b 10 µm, c 1 µm.)

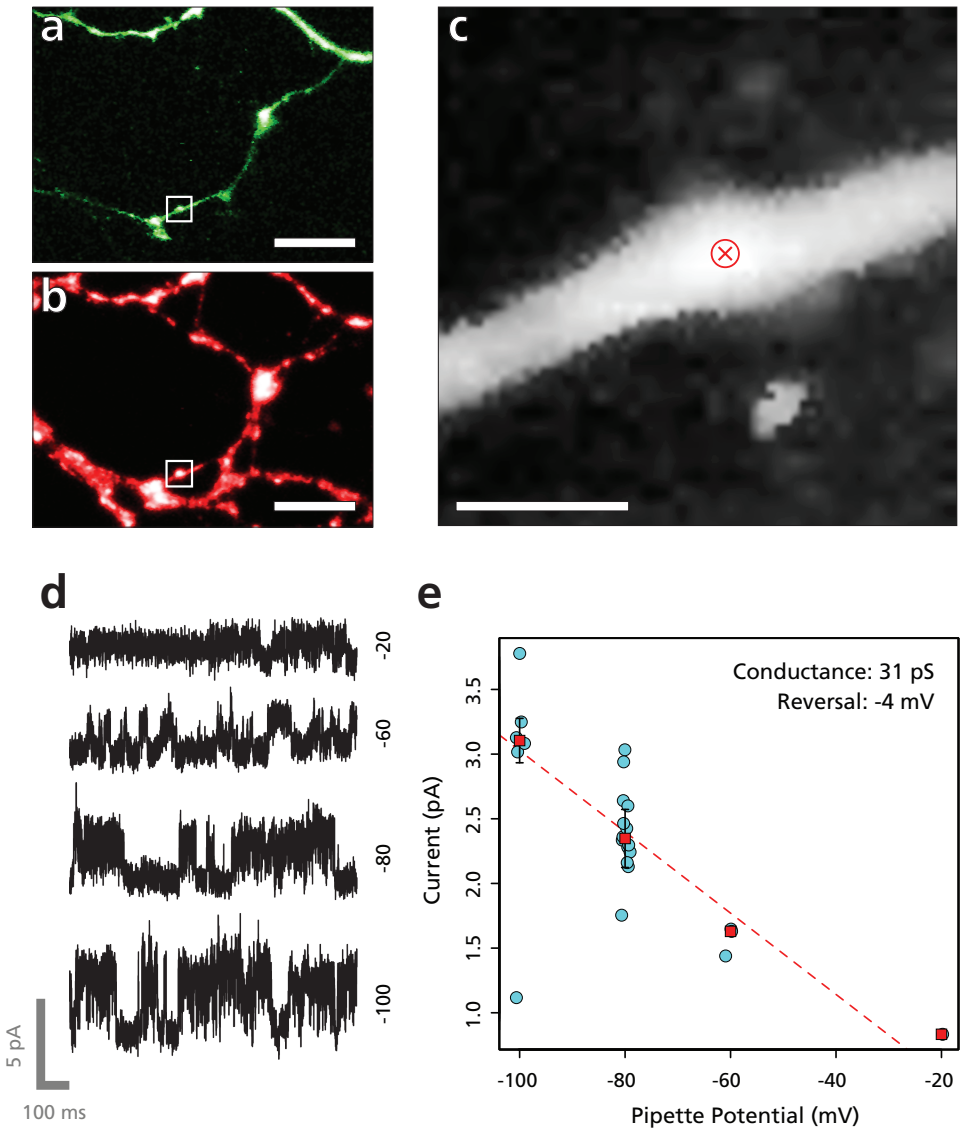

Figure 6.16: Smart recording #8. **a** EGFP fluorescence image of the patch region. **b** FM 4-64 fluorescence image of the patch region. **c** SICM image of the area marked on optical images, with marker indicating location of patch. **d** Example 1 s segments of trace for different pipette potentials. **e** Current-voltage plot of measurable openings. (Scale bars a,b 10 µm, c 1 µm.)

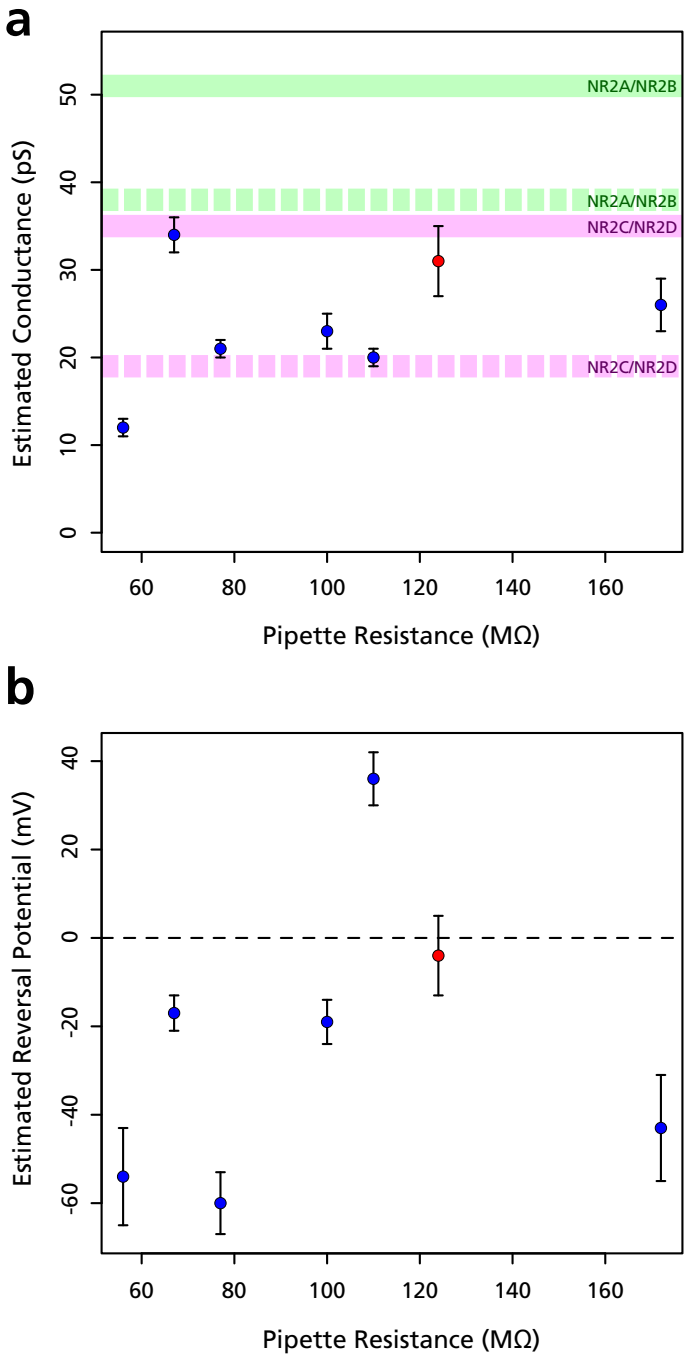

Figure 6.17: Summary plots of recording results from smart bouton patches with NMDA. **a** Conductance estimates plotted by pipette resistance. The red point is from recording #8, with Mg^{2+} in the pipette filler. Green bands show approximate expected conductances for NR2A/NR2B-containing receptors, magenta show those for NR2C/NR2D. **b** Corresponding reversal potential estimates.

order of magnitude to be NMDARs, but in most cases the correspondence is only approximate. We have previously noted that conductance estimates with high resistance pipettes may be unreliable. The data here show no evidence of a systematic relationship between estimated conductance and pipette resistance, of the kind seen in Chapter 5, but the number of recordings is small.

The spread of conductances and reversal potentials, along with differing gating kinetics apparent in the traces, suggest that the recordings do not all show the same kind of channel. Given the nature of the sample, such variation is to be expected. Since we were not able to change the pharmacological environment for these patches, there is little basis on which to establish channel identity unless the channel behaviour has a very distinctive character. NMDARs exhibit distinct gating patterns and sub-levels, but long stretches of clear data are required in order to distinguish these features, and we were unable to obtain such evidence from these traces.

In the case of recording #8, we would expect Mg^{2+} to induce a substantial voltage-dependent block in a (non-NR3-containing) NMDAR. Some voltage dependence is indeed observed, with fewer and shorter openings seen at less depolarised potentials and none at all when the pipette is at 0 mV or higher. However, there is insufficient data from this recording to enable a rigorous analysis. Useful numbers of openings are only seen at –100 mV and –80 mV. These openings are more flickery than would typically be expected from NMDARs in such conditions, but NMDAR gating is complex and can inhabit different modes (Popescu and Auerbach 2003; Schorge et al. 2005).

6.2.6 Smart recording #9

The final smart recording showed no channel activity in cell-attached mode but was successfully excised as an inside-out patch. The location and sample traces are illustrated in Figure 6.18. The experimental conditions were the same as for recording #8, with Mg^{2+} present in the pipette.

The openings that occurred after excision were large and quite variable, showing distinct fluctuations in the open state current and more than one subconductance state. The IV plot shown in Figure 6.18 is based on current estimates for the largest open state, as far as that could be distinguished.

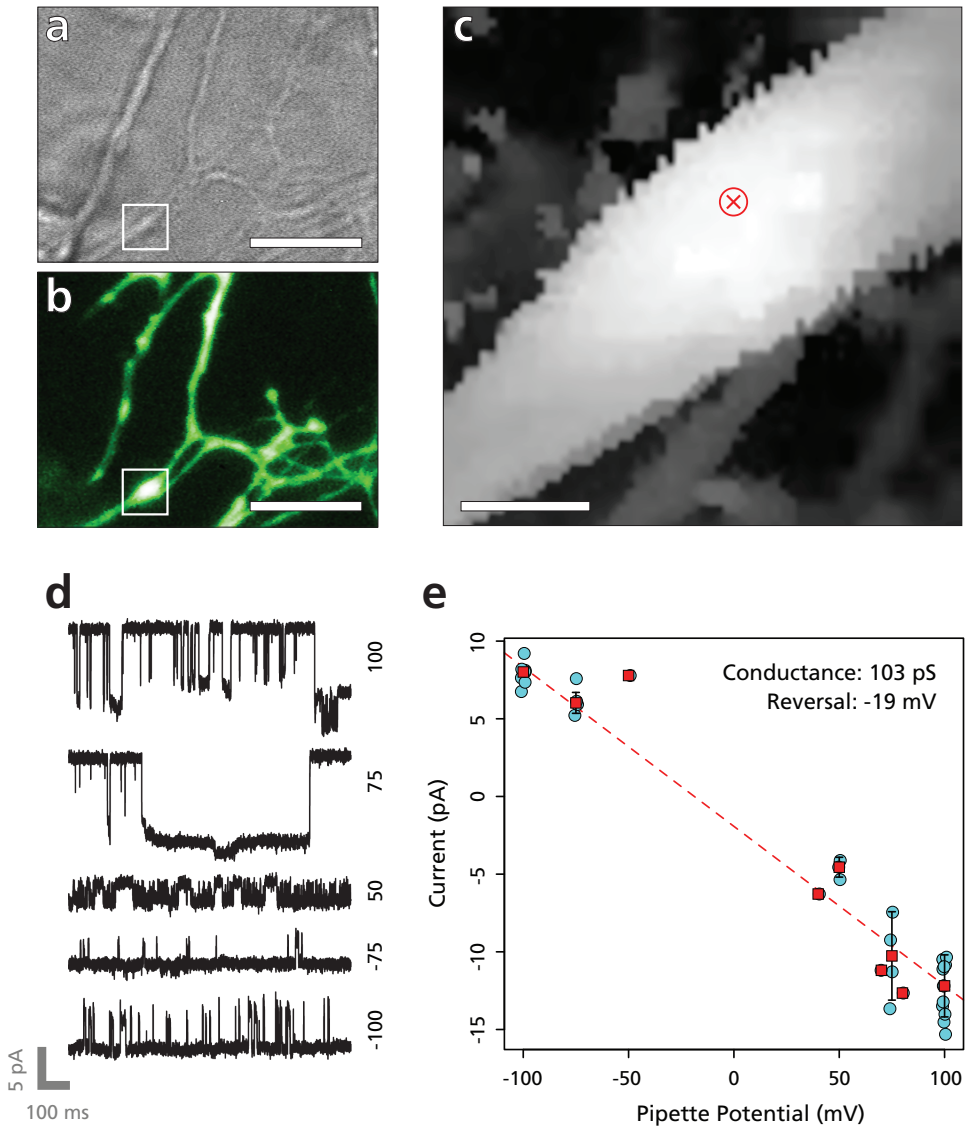

Figure 6.18: Smart recording #9. Pipette resistance was 139 MΩ. **a** Bright-field microscope image of the patch region. **b** Corresponding fluorescence image for EGFP. **c** SICM image of the area marked on optical images, with marker indicating location of patch. **d** Example 1 s segments of trace for different pipette potentials. **e** Current-voltage plot of measurable openings. (Scale bars a,b 10 µm, c 1 µm.)

There is no sign of any magnesium block, but in any case the currents are far too large for an NMDAR. The true channel identity is uncertain, but as with recording #4 we will revisit the question later in this chapter.

6.3 Recording with large pipettes

A number of localised patches were also attempted in these cultures using Harvard F (large) pipettes like those in Chapter 5. SICM imaging was not possible at a useful resolution in these cases, due to the larger tip size, so location was chosen solely on the basis of optical evidence. The SICM positioning system was then used under manual control to place the pipette directly over the selected target before lowering to the surface with the Z piezo to patch.

These recordings were attempted in similar conditions to those in the previous section. FM 4-64 loading was not used; the location was chosen on the basis of morphology observed under EGFP fluorescence. The red fluorescence imaging band was used instead for Alexa Fluor 568 in the pipette filler. This allowed better visualisation of the pipette tip under the microscope when aligning the patch, and also potentially allowed the patched location to be retrospectively confirmed by going to the whole cell configuration and letting the dye fill the cell.

Other than the inclusion of the Alexa 568, the pipette filler solution was the same as for smart recordings #8 and #9, with Mg^{2+} present (solution [25]).

	Big Pipette Bouton	Big Pipette Soma	Small Pipette Bouton
Total Pipettes	108	46	449
Seal Attempted	72 (67%)	33 (72%)	144 (32%)
Sealed	16 (22%)	18 (55%)	90 (63%)
Good	2 [5] (13% [31%])	4 (22%)	9 (10%)
Empty	0 (0%)	0 (0%)	20 (22%)
Strange	0 (0%)	0 (0%)	13 (14%)

Table 6.3: Outcomes of large pipette patching in cerebellar culture. Percentages are calculated with respect to the containing group, as before.

Success rates for these experiments are shown in Table 6.3. For comparison, the SICM pipette results are reproduced, and the table also includes counts from some attempts to patch directly onto the cell body with the same large pipettes and cultures.

Interestingly, the proportion of successful seals on putative boutons appears to be markedly lower than with SICM pipettes. It is possible this is due to the larger size of the tip in comparison to the target, or to less accurate targetting in the absence of a topographic scan.

It is also notable that none of the large pipette recordings, either from terminals or the soma, were clearly empty, and none showed the strange artefacts observed with small pipettes. The counts remain small, so these differences are probably not significant. Considering bouton recordings only, Fisher's exact test gives $p = 0.073$; taking the bouton and soma recordings together gives $p = 0.004$, but it is not clear such an aggregate comparison is meaningful. Nevertheless, the observations are certainly consistent with the idea that empty and strange recordings are related to tip geometry.

Of the 16 recordings obtained, 5 were reasonably clean and showed definite channel activity. However, 3 of these were too short-lived to provide reliable estimates of conductance, reversal potential or kinetics. Despite these failures, and the poor sealing, the rate of useful recordings is comparable to that for the smart patch experiments and the potential advantages significant.

Although the whole cell configuration was achieved in both the cases presented below, the ion concentrations in the pipette were not suited to acquiring data in that mode—it was purely a means of confirming location. While some recordings were made, the quality was poor and they did not generate useful information.

The first of the two good recordings was obtained from the beaded varicosity indicated in Figure 6.19. Images from after patching show the desired Alexa fill, confirming the patch was on this cell. Cell health was visibly reduced after patching. This occurred in all cases and was to be expected given the influx of pipette solution designed for extracellular use.

Single channel data from this recording are shown in Figure 6.20. There appear to be multiple channels, although one channel predominates, especially at depolarised potentials. The conductance is relatively low for an NMDAR and the openings are particularly short and flickery at negative

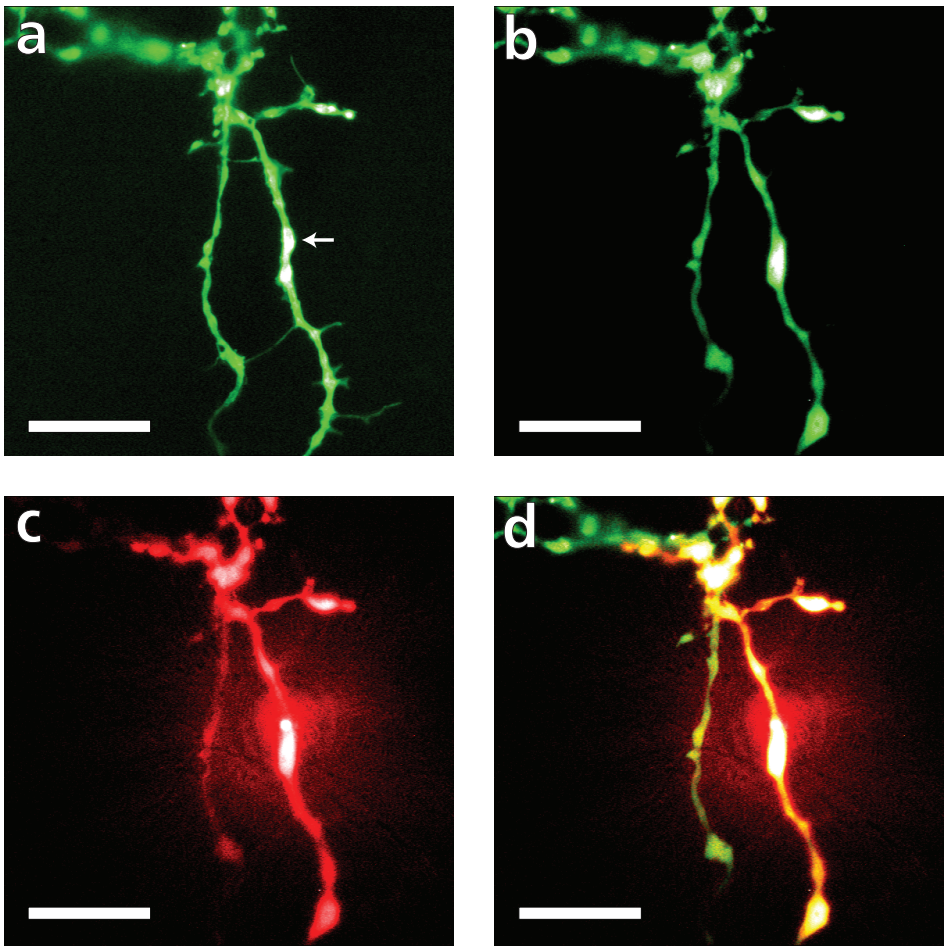

Figure 6.19: Location of big pipette recording #1. **a** EGFP fluorescence before patching. Arrow marks position of patch. **b** EGFP fluorescence after patching. **c** Alexa Fluor 568 fluorescence after patching. **d** Combined image showing both EGFP and Alexa Fluor 568. (Scale bars 10 µm.)

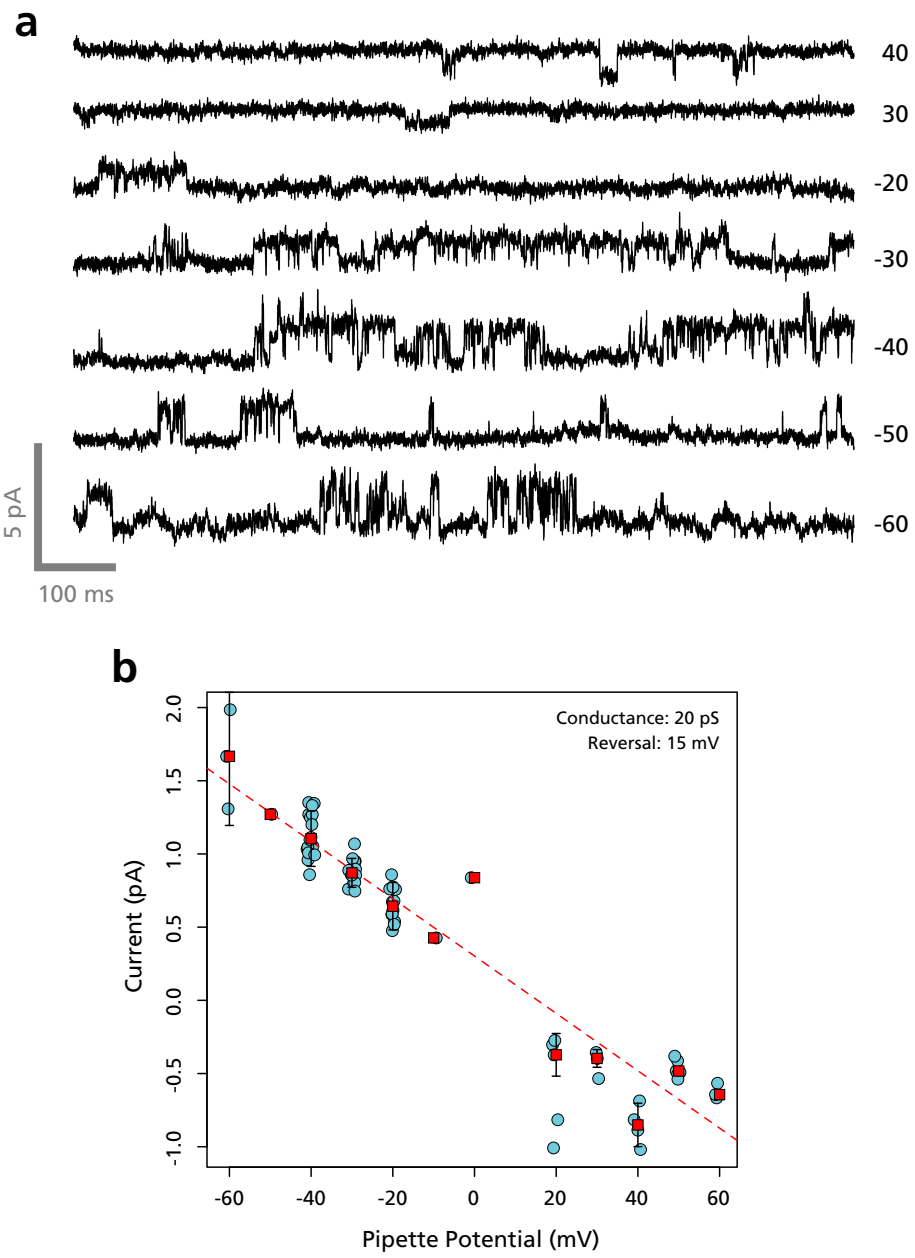

Figure 6.20: Big pipette recording #1. Pipette resistance was 26.4 MΩ. Recording was sampled at 10 kHz and filtered at 2 kHz. **a** Trace segments showing channel openings at several potentials. **b** Current-voltage plot of measured openings. Red points indicate median values, error bars the corresponding MAD.

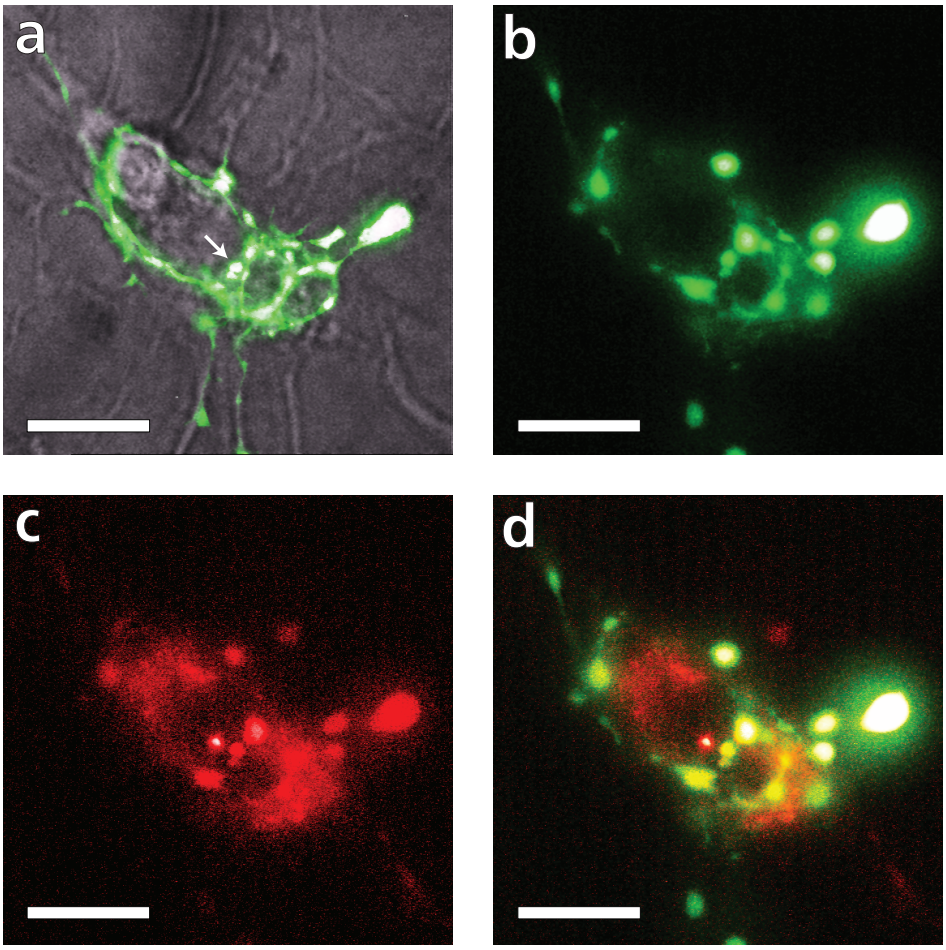

Figure 6.21: Location of big pipette recording #2. **a** Brightfield overlaid with EGFP fluorescence before patching. Arrow marks position of patch. **b** EGFP fluorescence after patching. **c** Alexa Fluor 568 fluorescence after patching. **d** Combined image showing both EGFP and Alexa Fluor 568. (Scale bars 10 µm.)

pipette potentials, the opposite of the effect expected with Mg^{2+} present. The estimated reversal potential, 15 ± 1 mV, is unusual among our presynaptic patches in being somewhat hyperpolarised; however, since the resting membrane potential is not known, no strong conclusions can be drawn from this. In short, the channel identity is uncertain but its profile means it is unlikely to be an NMDAR.

The second interesting recording was obtained from the location indicated in

Figure 6.21. The beaded process shown was wrapped around a small cluster of other neurons, apparently making synapses onto them. Such formations, comparable to the 'basket' structures found *in vivo*, occurred often in our cultures. The candidate varicosity was chosen because focussing up and down indicated that it was uppermost of all those present and thus most likely to be accessible to the pipette.

After recording in cell-attached mode and going whole cell, Alexa fill was slow and incomplete, so the locational evidence is less conclusive than in Figure 6.19. Nevertheless, filling did occur into the EGFP-expressing processes, and not into the soma of the underlying cell. (The very bright small red spot seen near to the patch location in Figure 6.21c–d seems not to have been part of the EGFP interneuron and is apparently unconnected to the other filled regions.) As in the previous case, the patched cell was in poor health after the recording, its former well-defined varicosities having swollen as blebs.

The current record obtained from this cell was complex and certainly contained multiple channels. However, several stretches showed a large channel with very distinctive gating behaviour and these were selected for analysis. Examples of this behaviour can be seen in Figure 6.22a.

The channel appeared to undergo long open periods during which it flickered rapidly between at least two different conductance states. The current-voltage relationship for both these states is graphed in Figure 6.22b, while 6.22c shows the state occupancy, which appears to be largely independent of voltage though with possibly lower P_{open} at more extreme voltages.

The estimated conductances, 246 ± 5 pS and 356 ± 7 pS, are very high and effectively limit the identity of the channel to two candidates: the maxi-anion channel or the voltage-dependent anion channel (VDAC). The latter was originally thought to be expressed only in the outer membrane of mitochondria, but is now known also to occur in the plasma membrane, possibly targeted to this location by an alternative exon splicing (Bàthori et al. 1999; Buettner et al. 2000). This form is sometimes referred to as 'pl-VDAC' or 'VDACpl'. VDAC and the maxi-anion channel have similar characteristics and for a time were suggested to be one and the same (Dermietzel et al. 1994; Bahamonde and Valverde 2003; Elinder et al. 2005). This is now considered unlikely (Sabirov et al. 2006; Sabirov and Okada 2008), but the molecular

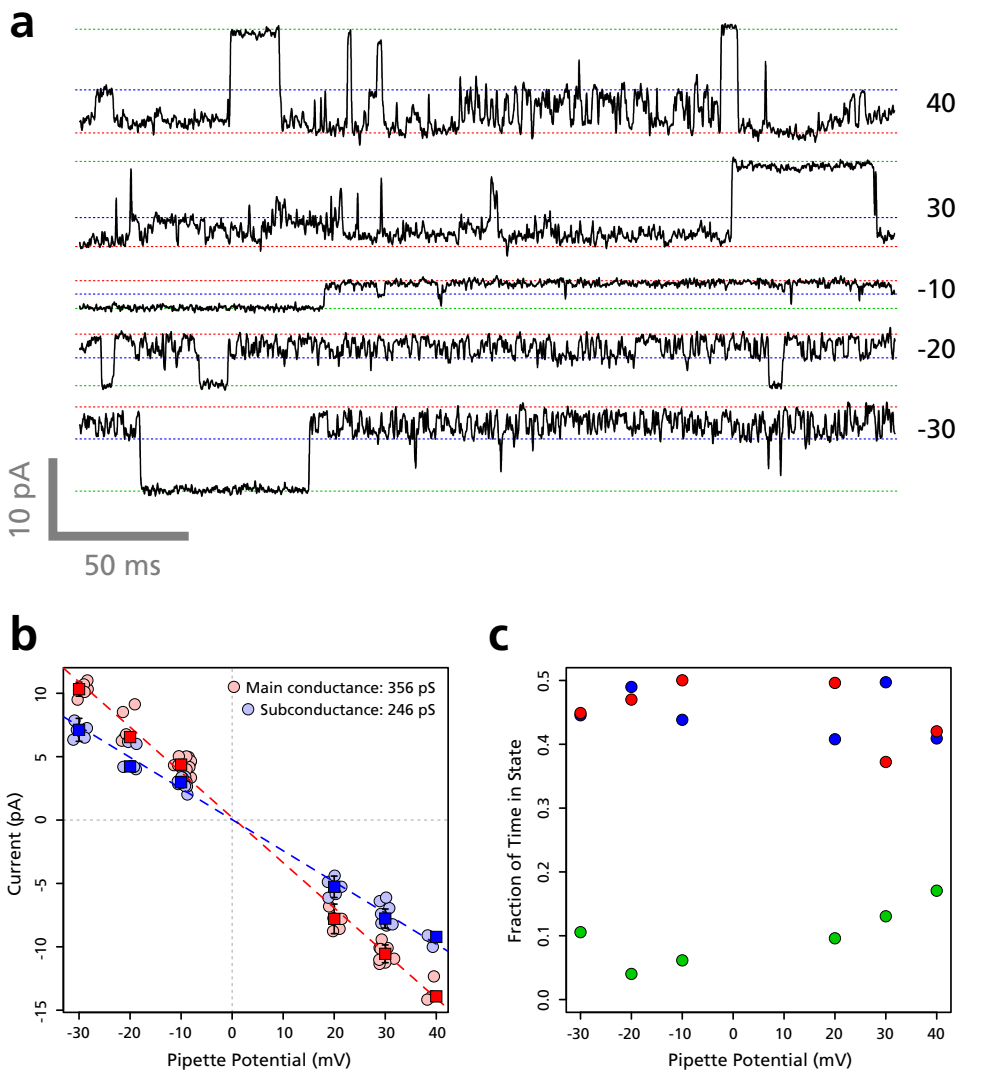

Figure 6.22: Big pipette recording #2. Pipette resistance was 33.7 MΩ. Recording was sampled at 10 kHz and filtered at 2 kHz. **a** Trace segments showing channel openings at several potentials. Dotted lines indicate levels of the closed (green), subconductance (blue) and fully open (red) states. **b** Current-voltage plot of measured levels of both main and subconductance states. **c** State occupancy is largely independent of pipette potential. Green dots indicate time spent in the closed state; blue, time in the subconductance state; red, time in the fully open state.

identity of the maxi-anion channel remains unknown.

The two cannot be distinguished on the basis of the data we have. The estimated reversal potential of our channel, close to 0, is consistent with either identification, and both VDAC and the maxi-anion channel exhibit multiple high-occupancy subconductance states (Schwarze and Kolb 1984; Krouse et al. 1986; Jalonen 1993; Akanda and Elinder 2006).

Similar large-conductance anion channels have been observed in many different tissues, including spinal neurons (Hussy 1992), glia (Gray et al. 1984; Liu et al. 2007), an immortalised hippocampal cell line (Akanda and Elinder 2006) and primary hippocampal culture (Akanda et al. 2008). Because of the similarities in electrophysiological behaviour and the lack of clear molecular markers for the maxi-anion channel, it is not always clear which channel was observed. Detailed localisation information is typically sparse, but an exception is the localisation of maxi-anion channels to the T-tubule openings and Z-lines in mature cardiomyocytes, which was demonstrated by Dutta et al. (2008) using the smart patch clamp technique.

Neither VDAC nor the maxi-anion channel has previously been suggested to have a presynaptic role, so the apparent presence of such a channel in this recording was unexpected.

In the light of the putative identity of this channel, we reexamined the unusually large openings seen in two of the small pipette recordings presented earlier (Figures 6.12d and 6.18d).

The opening in recording #4 seemed short-lived and was originally thought to occur at only a single voltage level (Figure 6.12d). However, it was noted that the first change of pipette potential, from 0 mV to +50 mV, was accompanied by a very large change in current out of proportion with the leak current elsewhere. 40 s prior to this change there was an apparent small opening that had not closed, and this appeared to be balanced by an eventual closure at the higher potential. This extended opening had not been identified earlier because of its long duration. The sequence of events is shown in Figure 6.23, omitting the long stretches between events.

The apparent currents through the opening at the two voltages were 1.1 pA and 17.9 pA, with 8.9 pA in the intermediate state. The conductance was estimated at 336 pS, with a subconductance level of 167 pS and reversal potential of –3 mV. These values must be treated with caution—errors cannot even

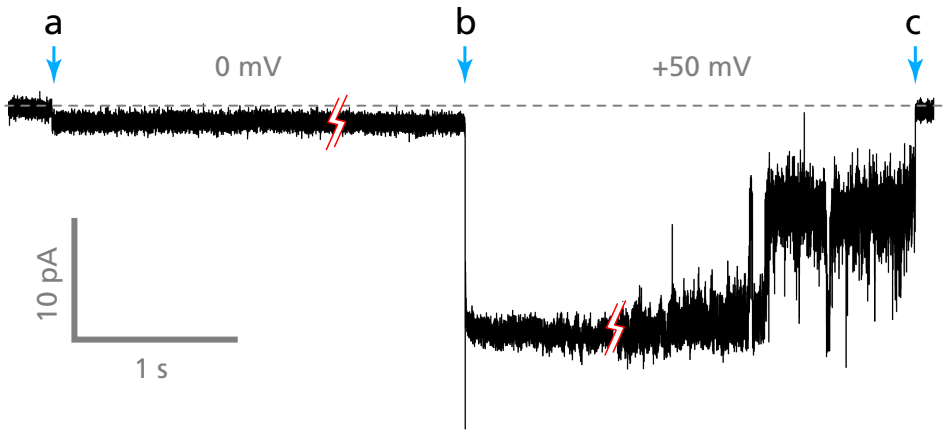

Figure 6.23: Possible maxi-anion channel activity from smart recording #4. **a** Initial channel opening. Pipette potential at 0 mV is close to the reversal potential so current is small (1.1 pA). **b** Channel is still open when pipette potential is changed to +50 mV, causing a very large increase in current. **c** Channel finally closes via an intermediate subconductance state (main current 17.9 pA, substate current 8.9 pA). (Duration: a–b 40 s; b–c 63 s.)

be estimated because there are only two measurements. Nevertheless, the main conductance appears very close to that observed in the large pipette recording, and the reversal potential is also near to the expected value. The subconductance in this instance is quite different, but similar levels have been observed by others (Krouse et al. 1986; Olesen and Bundgaard 1992; Sun et al. 1993).

The openings in recording #9 are of smaller apparent magnitude, and the estimated conductance of 103 ± 3 pS, while still large, is much lower than would be expected from a maxi-anion channel. Nevertheless, some of the gating behaviour looks comparable, notably periods of very fast flickering between open states with very few visits to the fully closed state, as illustrated in Figure 6.24. Comparable flickery changes do not occur separately, supporting the interpretation that they are indeed different conductance states of the same channel rather than openings of another independent channel. All the channel activity also seems to have been prompted by patch excision, which has been reported as characteristic for maxi-anion channels (Sabirov and Okada 2008).

Many of the openings show evidence of current decay reminiscent of the

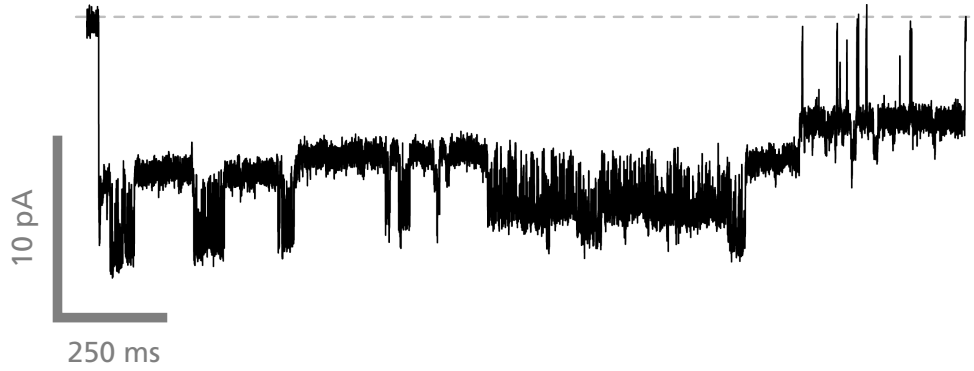

Figure 6.24: Possible maxi-anion channel activity from smart recording #9. The channel flickers rapidly between open states, with very few full closures. Pipette potential +100 mV.

strange recordings in Chapter 5. The HEK-bslo control experiments and the vesicle model in that chapter suggested there could be a tendency to underestimate conductance with SICM pipettes, especially when both the pipette resistance and the channel conductance are high. In this case the resistance was 139 MΩ, and the currents were certainly large. So it is *possible* that conductance was underestimated and the channel was indeed a maxi-anion. However, such thoughts are clearly speculative.

Even if the conductance estimates here are unreliable, the openings are evidently large and at least for recording #4 there is no other ready candidate for the channel identity. A note of caution must be sounded, however, because of the extended period for which the openings appear to be sustained at higher voltages. VDAC and maxi-anion channels are often found to inactivate rapidly at such potentials (Schwarze and Kolb 1984; Jalonen 1993; Sabirov and Okada 2008), although there are some reports of a distinct subpopulation that does not do so (Gray and Ritchie 1986; Sonnhof 1987).

6.4 Discussion of results

We have demonstrated that patch clamp recordings can be obtained from presynaptic boutons by using SICM for positional control. This can be done both with classic high resistance SICM pipettes and also with lower resis-

tance patch pipettes similar to those more usually used for single channel recording. The former provide for better locational precision through the use of SICM topographic imaging. However, they can be more fragile and prone to blockage, and their use increases the susceptibility to recording artefacts and uncertainties of the sort described in Chapter 5.

Using larger pipettes appears to offer comparable chances of successful patching, while at the same time opening up the possibility of more versatile experimental techniques. As a preliminary example, we managed to achieve the whole-cell configuration and use it to confirm the patch location with a tracer dye. The potential benefits of extending this approach to making targetted whole-compartment recordings are substantial.

The low rate of acquiring usable recordings means that the limitations of the cell-attached configuration can be problematic. Particularly in the case of small pipette recordings, where the accuracy of the current measurements may be open to question, the inability to apply different pharmacological interventions makes channel identification difficult. The ability to operate in a configuration such as whole-cell or outside-out that allows exchange of the external medium would be an important step toward mitigating this problem.

The relative frequencies of good and clearly-empty recordings when using fine-tipped pipettes offers some evidence of a high local channel density. Further evidence is provided by the fact that nearly all records contained multiple channels, as inferred from the presence of double openings. Both lines suggest that the number of channels in the membrane of our putative boutons could be surprisingly large, perhaps not far removed from that found in conditions of artificially-elevated expression such as our HEK-bslo experiments. If this were indeed the case then it might have significant effects on the complexity of presynaptic behaviour and its role in modulating synaptic transmission. This is certainly a possibility that merits further investigation.

Despite the appearance in several records of channels with conductances similar to NMDARs, we have not been able to reach any strong conclusions as to their identity. The complexity of NMDAR behaviour, which can include shifts between different gating modes (Popescu and Auerbach 2003; Schorge et al. 2005), makes it particularly difficult to make a convincing

identification within the constraints of cell-attached recording, unless exceptionally long, stable recordings can be obtained.

By contrast, VDAC and the maxi-anion channel are more identifiable. On the basis of conductance, we can be reasonably certain one of these channels was present in one of the large pipette recordings, and perhaps in two of the smart patches as well. The presence of such a large conductance channel in a presynaptic location raises interesting questions as to its functional role. The opening of this channel would be expected to have a significant impact on the chemical environment in a compartment as small as a presynaptic bouton.

Chapter 7

Discussion

7.1 Applicability of the techniques

7.1.1 Hopping mode SICM allows imaging of neuronal networks

The implementation of hopping probe SICM is complex and there are potential drawbacks in terms of speed of image acquisition. Nevertheless, the greatly reduced occurrence of lateral collisions enables imaging of much more convoluted and delicate samples than were previously possible (Novak et al. 2009). Speed problems can be somewhat mitigated by judicious use of lower-resolution sampling and stepwise zooming into small target areas.

Using these techniques, we have been able to image the intricate networks of processes found in neuronal cultures and gain access to their synaptic connections. Such locations cannot generally be identified by topography alone, but SICM combines well with optical microscopy and well-established fluorescent labelling methods.

The resolution of SICM imaging is critically dependent on the pipette tip geometry. Our SEM measurements and models of expected pipette resistance suggest that tip apertures may tend to be smaller than is often estimated, due to a thickening of the glass walls. We propose that the traditional assertion that OD:ID ratio is conserved throughout a pulled pipette is incorrect. While it is not clear that this result generalises to all glass types and puller units, it may offer an explanation for reports of SICM images apparently

exhibiting a somewhat higher resolution than models would predict for tips whose size has been estimated using the conserved OD:ID assumption (Novak et al. 2009).

The current-distance relationship on which SICM is based is traditionally modelled as the approach to an ideal surface that is flat, rigid and perfectly insulating. The predicted relationship accords well with measured approaches to similarly ideal targets, but our experiments indicate that there is significant deviation from the prediction when the pipette is operated close to the surface of a real cell. This does not invalidate SICM imaging of biological samples—manifestly, that does work—but strongly implies that to image cells reliably very low set points should be used.

It is not clear how the deviation arises. One possibility is that the pipette tip is colliding with the cell and causing some deformation that allows a current to continue flowing. Alternatively, the pipette may be interacting not with the plasma membrane itself, but with poorly-insulating components of the extracellular matrix. These could then form a conducting envelope around the tip, alleviating the current drop as the pipette descends towards and even through the cell surface. Such suggestions are speculative and further investigation is required before the true cause can be established.

7.1.2 Limitations of patching with SICM pipettes

Patch clamp recordings are usually made with low resistance pipettes, typically in the range 2–5 MΩ. This allows better control of the experimental conditions and ensures that the measured current is dominated by the properties of the ion channels rather than those of the pipette.

Smart patching entails the use of much finer pipettes, with resistances of 60–150 MΩ or even higher, in order to obtain a satisfactory SICM imaging resolution. Such pipettes present some difficulties for patch clamp recording. The small tip size usually restricts their use to the cell-attached configuration, which limits the experimental manipulations that are possible. It also means that only a very small region of membrane can be sampled, reducing the likelihood of detecting channels that are not present at high density.

In control experiments with transfected HEK cells, and also to a lesser extent in recordings from neuronal compartments, several unusual features were

observed in the single channel currents. These did not appear to reflect actual channel behaviour, but instead were artefacts of the recording process.

A model was developed to explain these artefacts in terms of the formation of partially-enclosed vesicles inside the pipette tip. Such vesicles are well known to occur within larger patch pipettes. While they have not been directly observed within SICM pipettes due to the small size, it is likely that they would exist there also. The behaviour of currents predicted by the vesicle model was comparable to artefacts observed in smart patch recordings, lending circumstantial support to the hypothesis that such vesicles do indeed occur.

An important implication of the vesicle model is that estimates of electrical properties such as conductance and reversal potential obtained from such recordings may be unreliable. The degree of uncertainty depends on the vesicle geometry, about which we have little direct information. For modelling purposes the geometry was treated as static, but that is unlikely to be true in practice. Detailed study of the behaviour of gigaseal patches by Suchyna et al. (2009) suggests that the membrane geometry can be dynamically affected by factors such as the pipette potential, and that there is also often a gradual 'creep' over time. Such effects could have significant impact on the results of smart patch recordings. While this does not invalidate the technique, it does mean that data interpretation requires care.

7.1.3 Localised patching is possible with larger pipettes using SICM positioning

As an alternative to sharp SICM electrodes, we also attempted recordings with more conventional patch pipettes. In this case the imaging capabilities of the SICM were not used and instead it was treated only as a precise positioning system. Patch success rates were lower using this approach, perhaps because of the reduced targeting information and the greater size of the pipette tip compared to the bouton. Nevertheless, useful recordings could be obtained and fewer experimental constraints were imposed.

Using larger pipettes helped to restore some of the advantages of conventional patch clamping while still retaining relatively high positional accuracy. The artefacts seen using SICM pipettes did not occur. The sampled

area of membrane was higher and we did not encounter any clearly empty patches.

Although we acquired useful data only in the cell-attached configuration, we were able to go whole cell and retrospectively trace the patch location with fluorescent dye. It therefore seems likely that this approach could be used successfully for whole compartment recordings and potentially for pulling outside-out patches. Both of these configurations would allow for exchange of the external medium and therefore better characterisation of the channels.

7.2 Presynaptic patching

Our primary goal in recording from presynaptic locations in cerebellar interneurons was to demonstrate the presence of NMDARs, as implied by the phenomenon of DPI. Despite the acquisition of a number of successful recordings from likely presynaptic sites, using both small and large pipettes, direct evidence for the presence of functional NMDARs in these locations remained elusive. This does not exclude the possibility that such channels were in fact present, but no sufficiently characteristic behaviour was observed. Due to the limitations of the cell-attached configuration and the relatively low patch success rate, the range of pharmacological interventions necessary to unambiguously separate out NMDAR activity could not be performed.

Nevertheless, the results suggest two other interesting conclusions that merit further investigation. The first is that the density of active channels in the presynaptic membrane appears to be remarkably high. This result is consistent with the recordings from cerebellar interneuron boutons by Southan and Robertson (1998, 2000), who found large voltage-dependent K^+ currents, and by Fiszman et al. (2005, 2007), who reported smaller but still notable presynaptic currents elicited by agonists for several classes of glutamate receptor, including NMDARs.

Considering the small volume of a bouton, currents through even a single open channel could have a significant impact on the local ionic environment. The apparent presence of comparatively large numbers of channels of several different types suggests that mechanisms of presynaptic control may be more varied than is usually supposed.

The possible presence of a very large conductance channel, either a VDAC or a maxi-anion channel, further complicates the picture. If such channels were to be present in the bouton plasma membrane with any consistency, this would be an interesting and quite unexpected discovery. The contribution of such a channel to bouton behaviour could be substantial.

VDAC and maxi-anion channels and are usually reported to have a significant voltage dependence, opening readily near the resting membrane potential and inactivating as the potential moves away. However, we did not see obvious inactivation of the large conductance channels in our traces. Whether this is because the channels in question are of a subtype that does not inactivate (Gray and Ritchie 1986; Sonnhof 1987) or whether it was in some way an artefact of the recording context is uncertain. Maxi-anion channels are also reported to be at least partially gated by mechanical or osmotic stresses, with much higher probability of opening when subjected to pathological stimuli, notably patch excision. It is possible that this gating dominates in patches from small compartments such as ours.

If the channel were to be constitutively active, it would be expected to play a significant role in setting the membrane potential in the bouton. If, on the other hand, the channel were active only under pathological conditions, then it could perhaps play a homeostatic or apoptotic role; both functions have been reported previously in other cell types (Shimizu et al. 2001; Elinder et al. 2005; Akanda et al. 2008).

Although Cl^- ions would likely constitute much of its traffic, the maxi-anion channel is also notably permeable to various organic anions and has been implicated in ATP signalling in a number of cell types (Bell et al. 2003; Dutta et al. 2004; Liu et al. 2008). It is conceivable that it fulfils such a role in our presynaptic boutons, although the exact nature of that role remains obscure. ATP is known to be co-released with GABA from some synapses (Jo and Schlichter 1999; Jo and Role 2002), but there is no evidence to date of that being the case in cerebellar interneurons.

While the molecular identity of the maxi-anion channel is unknown, that is not the case for VDAC, and several antibodies exist. Thus it may be possible to distinguish which channel is present using immunocytochemistry. It would be necessary to ensure the binding was strictly extracellular, since VDAC is found ubiquitously in mitochondria.

7.3 Future work

All the presynaptic recordings described here were obtained from cultured cerebellar interneurons from GAD65-EGFP mice. It is possible that some of the difficulties encountered in obtaining reliable patches were due to an intrinsic property of these particular cells, rather than with the technique more generally. This concern is somewhat mitigated by the fact that patches have been successfully obtained from similar terminals in culture (Fiszman et al. 2005, 2007) and in slices (Southan and Robertson 1998, 2000), although there are always differences in the specifics of the preparation. In any case, it is certainly possible that other cell types or preparations would be more amenable to localised patching by this method. This possibility merits further investigation, since detailed knowledge of channel populations in any small compartment is likely to be informative.

A small number of exploratory experiments with other cell types and preparations have been performed in our laboratory, but so far the results are too sparse to draw any substantive conclusions. Further work in this direction is required.

For nearly any region of specialised membrane investigated this way, in presynaptic terminals or elsewhere, detailed information about the native channel population can only be obtained if suitable pharmacological interventions can be performed. Since there is limited scope for this in the cell-attached configuration, other patch modes need to be utilised. Recordings from whole boutons or from outside-out patches should provide better information and we believe these to be possible using larger pipettes.

One particularly interesting avenue that we have only just begun to explore is a protocol that combines the imaging resolution advantages of SICM pipettes with the patch recording benefits of a lower resistance. In this approach, first suggested by Pavel Novak and colloquially termed 'hop & chop', a high resistance pipette is first used to obtain the topographic map, just as for the smart patch protocol. The tip is then carefully sheared away by controlled collision with an empty region of glass coverslip, leaving a bigger, lower-resistance aperture for patching. Because the same pipette is used in both phases, the lateral position of the enlarged tip remains very close to that of the original and the recorded topography can still be used for XY targeting. The process of breaking also eliminates any contaminants

that may have previously accumulated at the tip, which could otherwise interfere with sealing.

With developments such as this, SICM should be able to fulfil its potential as a tool not only for imaging but also for precise electrophysiological study of small cellular structures.

Appendix A

Software and source code

A.1 IMG file format

SICM data generated by the ICnano system is saved in IonScope IMG files, a custom format based loosely on an earlier AFM/STM image format called ECS. The format retains a number of legacy features that are not relevant to SICM images, but is also distinct enough to be incompatible with existing ECS reading code.

IMG files consist of an 830-byte descriptive header, followed by a table of 16-bit unsigned integer samples. The samples represent the voltage applied to the piezo, or the ion current or other signal sampled by the ADC, scaled according to the particular hardware configuration of the SICM. Attributes from the header must be used to convert the data into physical units.

Multibyte numeric values are stored in little-endian order. Floating point numbers in the header use the Pascal Real format, a non-IEEE 48-bit floating point format with 1 sign bit, 39 bits of fraction and 8 of exponent.

A partial list of the most useful header fields is given in Table A.1. A complete definition, together with C and Perl code for reading IMG files, can be found on the CD in the directory `SICM`. This directory also contains compiled versions (`sicmdump.exe` for Windows and `sicmdump` for Mac) of a command-line utility for converting IMG data to tab-delimited text suitable for import into programs such as Matlab, R or Excel.

The nature of the samples may be determined from the first letter of the

Offset	Field Name	Type	Notes
0	version	Int16	Always 50
2	xdim	Int16	Number of samples across
4	ydim	Int16	Number of samples down
6	fsdHVA	Real48	Voltage range of the piezo amplifier (V)
12	fsdDAC	Real48	Voltage range of the DAC (V)
18	fsdADC	Real48	Voltage range of the ADC (V)
30	piezoCalX	Real48	X piezo sensitivity
36	piezoCalY	Real48	Y piezo sensitivity
42	piezoCalZ	Real48	Z piezo sensitivity
56	scanSize	Real48	Width of the scan ($\times$10 nm)
666	modeStr	Char[41]	String describing the scan type

Table A.1: Important fields in the IMG file header

modeStr field. If it is 'T', the image contains topographic data, if it is 'C' the samples are of the ion current, and if 'A' then it is some other signal sampled from an auxiliary ADC input.

For topographic images, the sample data can be converted to µm using the following formula:

$$\text{microns} = \frac{\text{sample} \times \text{piezoCalZ} \times \text{fsdDAC} \times \text{fsdHVA}}{32767}$$

For current or auxiliary signals there is insufficient data in the file to map the samples to their true physical units, but the values can be converted to the voltage received at the ADC like this:

$$\text{voltage} = \frac{\text{sample} \times \text{fsdADC}}{32767}$$

The full lateral piezo range can be determined from the header information as follows for X:

$$\text{micronsX} = 2 \times \text{piezoCalX} \times \text{fsdDAC} \times \text{fsdHVA}$$

and equivalently for Y with appropriate substitutions.

Samples are stored in the file in bottom-up order: the first xdim samples are the bottom row of the image, the next xdim are the next up from the bottom, and so on.

An unconverted sample value of 0 indicates that the pixel was not sampled, typically because the scan was halted before completion. In images that have been recorded with compressed sampling, an unconverted value of 0x7fff (32767) indicates placeholder pixels that have not been filled in by the default bilinear interpolation.

A.2 IonView

IonView is a viewer for IonScope IMG files on Apple Mac OS X computers. A Quick Look plug-in is also included, to allow IMG files to be previewed within the Mac OS X Finder and other applications. IonView was written in Objective-C using the Cocoa framework and compiled using Apple XCode 3.2.1. It requires Mac OS X 10.6 (Snow Leopard) to run.

The current IonView version at the time of writing is 0.86a. The compiled application can be found on the CD in the `IonView` directory, with source code in `IonView/source`. Updated versions will be made available online at http://walkytalky.net/ionview/.

IonView is a document-based application, structured according to the model-view-controller pattern. The principal classes are IonModel, which holds the SICM image data; IonImageView, IonGLView and IonInfoPanelController, which provide three different views onto the model data; and IonDocument, which binds the model and views together and provides some top-level user interface support.

Loading and analysis of IMG file data is provided by the IonModel class. Topographic data is maintained internally in double-precision floating point format with sizes in µm, as opposed to the hardware-dependent 16-bit unsigned integer samples of the original files. In addition to the raw data, the model maintains a version interpolated using bicubic spline interpolation with overshoot avoidance based on Heckbert (1985) and spot filtering for noise spikes. There is also support for adding non-destructive decorations to the image, such as positional markers.

IonImageView provides 2D greyscale display, with several viewing options and the ability to select regions of the data for export or analysis. The view can be switched between raw and interpolated data, and markers can optionally be displayed.

IonGLView provides 3D display of the image data using OpenGL. The image can be rotated and zoomed using the mouse, and a variety of display options are provided.

The IonInfoPanelController class provides access to the image file header information in textual form.

IonDocument manages the image window and user interaction for things like opening documents, copying data to the clipboard, and exporting. Writing the IMG format is not supported, but data can be exported to many popular image formats or to delimited text for import into other programs. Sequences of images can be combined and exported as QuickTime movies.

To build the application, use the supplied project file `IonView.xcodeproj`.

A.3 Vesicle model

R code for the vesicle model discussed in Chapter 5 can be found in the directory `Vesicle` on the CD. The model code is contained in the file `phys.r`. This is a relatively large file with many functions, but a lot of these are concerned with generation of figures or exploration of different parameter ranges. They serve mainly as somewhat-automated wrappers around a few core model functions and need not be described here.

The most basic unit of the model is the function `comp.step`, which implements a single time step of Equation 5.2. It is assumed that the step, `dt`, is sufficiently small that all forces driving the movement of ions can be taken as constant for its duration. The function returns the ion currents in and out of the compartment over `dt` and the updated vesicle concentration afterwards.

`comp.step` is called repeatedly by the main model function `vesicle.t`. This first initialises all the model parameters and creates a number of data structures to hold the simulation state and results. It then adjusts any variable parameters, allowing for such effects as stochastic changes in channel state, before invoking `comp.step` to advance the model fractionally. After many iterations of this process the simulation completes and the results for all the time steps are returned.

Both of these functions generate data without producing any plots. The workhorse plotting function is `vesicle.vary`, which calls `vesicle.t` and

plots the results. `vesicle.vary` can loop over multiple sets of parameters to plot them together on the same axes, but is also used to plot only a single simulation time course. Several other functions use `vesicle.vary` to do their plotting.

As discussed in §5.2.3, filtering and noise are not treated as part of the internal model state, but are added to the generated 'ideal' data afterwards. Filtering by any supplied convolution kernel is supported by `vesicle.vary`, but it does not allow for the addition of noise. `vesicle.filter` supports both, and again is used by several other functions to do their plotting. The Gaussian convolution kernel is generated by the `blur.kernel` function.

A.4 Other source code

A number of R scripts are provided in the `R` directory of the CD. The file `resist.r` contains functions used in Chapter 4 to estimate the pipette resistance from geometry according to the analytical approximation of Snell (1969). The functions in `approach.r` were used to plot approach curves. Functions used in the analysis and presentation of the HEK-bslo data in Chapter 5 are in `bk.r`. Electrophysiological traces were plotted and analysed using the functions in `ephys.r`.

The `Matlab/boost` directory contains functions used to demonstrate the effect of the hopping mode boustrophedon scan sequence in Chapter 3.

References

Omolabake Abimbola Adenle and William J Fitzgerald. Simulating Imaging with the Scanning Ion-Conductance Microscope. In *27th IEEE EMBS Annual International Conference*, pages 3410–3413, Shanghai, September 2005.

Nesar Akanda and Fredrik Elinder. Biophysical Properties of the Apoptosis-Inducing Plasma Membrane Voltage-Dependent Anion Channel. *Biophysical Journal*, 90(12):4405–4417, June 2006.

Nesar Akanda, Roshan Tofighi, Johan Brask, Christoffer Tamm, Fredrik Elinder, and Sandra Ceccatelli. Voltage-dependent anion channels (VDAC) in the plasma membrane play a critical role in apoptosis in differentiated hippocampal neurons but not in neural stem cells. *Cell Cycle*, 7(20):3225–3234, October 2008.

Thomas R Albrecht and Calvin F Quate. Atomic resolution imaging of a nonconductor by atomic force microscopy. *Journal of Applied Physics*, 62 (7):2599–2602, October 1987.

S Alexander, L Hellemans, O Marti, J Schneir, V Elings, Paul K Hansma, Matt Longmire, and John Gurley. An atomic-resolution atomic-force microscope implemented using an optical lever. *Journal of Applied Physics*, 65 (1):164–167, January 1989.

M Amrein, A Stasiak, H Gross, E Stoll, and G Travaglini. Scanning Tunneling Microscopy of recA-DNA Complexes Coated with a Conducting Film. *Science*, 240(4851):514–516, April 1988.

D Anselmetti, R Lüthi, E Meyer, T Richmond, M Dreier, J E Frommer, and H-J Güntherodt. Attractive-mode imaging of biological materials with dynamic force miroscopy. *Nanotechnology*, 5:87–94, 1994.

E A Ash and G Nicholls. Super-resolution aperture scanning microscope. *Nature*, 237(5357):510–512, June 1972.

R Bachelot, P Gleyzes, and A C Boccara. Reflection-mode scanning near-field optical microscopy using an apertureless metallic tip. *Applied Optics*, 36(10):2160–2170, April 1997.

Maria I Bahamonde and Miguel A Valverde. Voltage-dependent anion channel localises to the plasma membrane and peripheral but not perinuclear mitochondria. *Pflügers Archiv*, 446:309–313, June 2003.

Fadi Issam Baida, Daniel Courjon, and Hartmut Beilefeldt. Compact standalone near-field optical microscope combined with force detection. *Applied Optics*, 37(10):1808–1813, April 1998.

A M Baró, R Miranda, J Alamán, N García, Gerd Binnig, Heinrich Rohrer, Christoph Gerber, and J L Carrascosa. Determination of surface topography of biological specimens at high resolution by scanning tunneling microscopy. *Nature*, 315:253–254, May 1985.

György Bàthori, Isabella Parolini, Francesco Tombola, Ildikò Szabò, Angela Messina, Marta Oliva, Vito De Pinto, Michael Lisanti, Massimo Sargiacomo, and Mario Zoratti. Porin Is Present in the Plasma Membrane Where It Is Concentrated in Caveolae and Caveolae-related Domains. *Journal of Biological Chemistry*, 274(42):29607–29612, October 1999.

Phillip Darwin Bell, Jean-Yves Lapointe, Ravshan Sabirov, Seiji Hayashi, Janos Peti-Peterdi, Ken-ichi Manabe, Gergely Kovacs, and Yasunobu Okada. Macula densa cell signaling involves ATP release through a maxi anion channel. *Proceedings of the National Academy of Sciences of the United States of America*, 100(7):4322–4327, April 2003.

R Bernhardt and A Matus. Light and electron microscopic studies of the distribution of microtubule-associated protein 2 in rat brain: a difference between dendritic and axonal cytoskeletons. *Journal of Comparative Neurology*, 226(2):203–221, June 1984.

Eric Betzig and Jay K Trautman. Near-Field Optics: Microscopy, Spectroscopy, and Surface Modification Beyond the Diffraction Limit. *Science*, 257(5067):189–195, July 1992.

Eric Betzig, Aaron Lewis, Alec Harootunian, Michael Isaacson, and E Kratschmer. Near-field scanning optical microscopy (NSOM). *Biophysical Journal*, 49(1):269–279, January 1986.

Eric Betzig, P L Finn, and J S Weiner. Combined shear force and near-field scanning optical microscopy. *Applied Physics Letters*, 60(20):2484–2486, May 1992.

Magdalena Bezanilla, Barney Drake, Evgeny Nudler, Mikhail Kashlev, Paul K Hansma, and Helen G Hansma. Motion and enzymatic degradation of DNA in the atomic force microscope. *Biophysical Journal*, 67(6): 2454–2459, December 1994.

Gerd Binnig and Heinrich Rohrer. Scanning tunneling microscopy. *Surface Science*, 126:236–244, 1983.

Gerd Binnig, Heinrich Rohrer, Christoph Gerber, and E Weibel. Surface Studies by Scanning Tunneling Microscopy. *Physical review letters*, 49(1): 57–61, July 1982a.

Gerd Binnig, Heinrich Rohrer, Christoph Gerber, and E Weibel. Tunneling through a controllable vacuum gap. *Applied Physics Letters*, 40(2):178–180, 1982b.

Gerd Binnig, Heinrich Rohrer, Christoph Gerber, and E Weibel. 7x7 Reconstruction on Si(111) Resolved in Real Space. *Physical review letters*, 50(2): 120–123, January 1983.

Gerd Binnig, CF Quate, and C Gerber. Atomic force microscope. *Physical review letters*, 56(9):930–933, March 1986.

Christian A Bippes, Andrew D L Humphris, Martin Stark, Daniel J Muller, and Harald Janovjak. Direct measurement of single-molecule viscoelasticity in atomic force microscope force-extension experiments. *European Biophysics Journal*, 35(3):287–292, October 2005.

B L Blackford, M H Jericho, P J Mulhern, C Frame, G Southam, and T J Beveridge. Scanning tunneling microscope imaging of hoops from the cell sheath of the bacteria methanospirillum hungatei and atomic force microscope imaging of complete sheathes. *Journal of Vacuum Science and Technology B*, 9(2):1242–1247, March 1991.

Max Born and Emil Wolf. *Principles of Optics: Electromagnetic theory of propagation, interference and diffraction of light 7th (Expanded) Edition*. Cambridge University Press, Cambridge, 1999.

J G G Borst and Bert Sakmann. Calcium influx and transmitter release in a fast CNS synapse. *Nature*, 383(6599):431–434, October 1996.

J G G Borst, F Helmchen, and Bert Sakmann. Pre- and postsynaptic whole-cell recordings in the medial nucleus of the trapezoid body of the rat. *Journal of Physiology*, 489(3):825–840, December 1995.

Frank Bradke and Carlos G Dotti. Differentiated neurons retain the capacity to generate axons from dendrites. *Current Biology*, 10(22):1467–1470, November 2000.

F Braet, C Seynaeve, R de Zanger, and E Wisse. Imaging surface and submembranous structures with the atomic force microscope: a study on living cancer cells, fibroblasts and macrophages. *Journal of Microscopy*, 190 (3):328–338, June 1998.

Kenneth T Brown and Dale G Flaming. *Advanced Micropipette Techniques for Cell Physiology*. John Wiley and Sons, Chichester, 1986.

Andreas Bruckbauer, Liming Ying, Alison M Rothery, Yuri E Korchev, and David Klenerman. Characterization of a Novel Light Source for Simultaneous Optical and Scanning Ion Conductance Microscopy. *Analytical Chemistry*, 74(11):2612–2616, June 2002a.

Andreas Bruckbauer, Liming Ying, Alison M Rothery, Dejian Zhou, Andrew I Shevchuk, Chris Abell, Yuri E Korchev, and David Klenerman. Writing with DNA and Protein Using a Nanopipet for Controlled Delivery. *Journal of the American Chemical Society*, 124(30):8810–8811, July 2002b.

Andreas Bruckbauer, Dejian Zhou, Liming Ying, Yuri E Korchev, Chris Abell, and David Klenerman. Multicomponent submicron features of biomolecules created by voltage controlled deposition from a nanopipet. *Journal of the American Chemical Society*, 125(32):9834–9839, August 2003.

Andreas Bruckbauer, Peter S James, Dejian Zhou, Ji Won Yoon, David Excell, Yuri E Korchev, Roy Jones, and David Klenerman. Nanopipette Delivery

of Individual Molecules to Cellular Compartments for Single-Molecule Fluorescence Tracking. *Biophysical Journal*, 93(9):3120–3131, August 2007.

Reinhard Buettner, Georg Papoutsoglou, Eliana Scemes, David C Spray, and Rolf Dermietzel. Evidence for secretory pathway localization of a voltage-dependent anion channel isoform. *Proceedings of the National Academy of Sciences of the United States of America*, 97(7):3201–3206, March 2000.

Carlos Bustamante, James Vesenka, Chun Lin Tang, William Rees, Martin Guthold, and Rebecca Keller. Circular DNA Molecules Imaged in Air by Scanning Force Microscopy. *Biochemistry*, 31(1):22–26, 1992.

H J Butt, K H Downing, and Paul K Hansma. Imaging the membrane protein bacteriorhodopsin with the atomic force microscope. *Biophysical Journal*, 58(6):1473–1480, December 1990.

Leda Chang, Thomas Kious, Max Yorgancioglu, David Keller, and Janet Pfeiffer. Cytoskeleton of living, unstained cells imaged by scanning force microscopy. *Biophysical Journal*, 64(4):1282–1286, April 1993.

Jason M Christie and Craig E Jahr. Dendritic NMDA Receptors Activate Axonal Calcium Channels. *Neuron*, 60(2):298–307, October 2008.

Lilia A Chtcheglova, Fatmahan Atalar, Ugur Ozbek, Linda Wildling, Andreas Ebner, and Peter Hinterdorfer. Localization of the ergtoxin-1 receptors on the voltage sensing domain of hERG K+ channel by AFM recognition imaging. *Pflügers Archiv : European Journal of Physiology*, 456(1): 247–254, February 2008.

Beverley A Clark, Pablo Monsivais, Tiago Branco, Michael London, and Michael Häusser. The site of action potential initiation in cerebellar Purkinje neurons. *Nature Neuroscience*, 8(2):137–139, January 2005.

R V Coleman, B Drake, Paul K Hansma, and G Slough. Charge-Density Waves Observed with a Tunneling Microscope. *Physical review letters*, 55 (4):394–397, July 1985.

David P Corey and Charles F Stevens. Science and technology of patch-recording electrodes. In Sakmann and Neher (1983a), chapter 3, pages 53–68.

Sarah E Cross, Yu-Sheng Jin, Jianyu Rao, and James K Gimzewski. Nanomechanical analysis of cells from cancer patients. *Nature Nanotechnology*, 2 (12):780–783, December 2007.

D C Dahn, M O Watanabe, B L Blackford, and M H Jericho. Scanning tunneling microscopy imaging of biological structures. *Journal of Vacuum Science and Technology A*, 6(2):548–552, March 1988.

P J de Pablo, J Colchero, J Gómez-Herrero, and A M Baró. Jumping mode scanning force microscopy. *Applied Physics Letters*, 73(22):3300–3302, November 1998.

Samantha Juo Li Del Linz. *Scanning ion conductance microscopy: modelling and approaches to studying peptide secretion*. PhD thesis, University College London, 2011.

Marie Laure Delignette-Muller, Regis Pouillot, Jean-Baptiste Denis, and Christophe Dutang. *fitdistrplus: Help to fit of a parametric distribution to non-censored or censored data*, 2010. R package version 0.1-3.

Patrick Delmas, Fe C Abogadie, Noel J Buckley, and David A Brown. Calcium channel gating and modulation by transmitters depend on cellular compartmentalization. *Nature Neuroscience*, 3(7):670–678, July 2000.

Rolf Dermietzel, Theng-Khing Hwang, Reinhard Buettner, Andreas Hofer, Elisabeth Dotzler, Marian Kremer, Rainer Deutzmann, Friedrich P Thinnes, Glenn I Fishman, David C Spray, and Detlef Siemen. Cloning and in situ localization of a brain-derived porin that constitutes a large-conductance anion channel in astrocytic plasma membranes. *Proceedings of the National Academy of Sciences of the United States of America*, 91(2):499–503, January 1994.

Marco A Diana, Carole Levenes, Ken Mackie, and Alain Marty. Short-term retrograde inhibition of GABAergic synaptic currents in rat Purkinje cells is mediated by endogenous cannabinoids. *Journal of Neuroscience*, 22(1): 200–208, 2002.

B Drake, R Sonnenfeld, J Schneir, and Paul K Hansma. Tunneling microscope for operation in air or fluids. *Review of Scientific Instruments*, 57(3): 441–445, March 1986.

B Drake, C B Prater, A L Weisenhorn, S A C Gould, Thomas R Albrecht, Calvin F Quate, D S Cannell, Helen G Hansma, and Paul K Hansma. Imaging Crystals, Polymers, and Processes in Water with the Atomic Force Microscope. *Science*, 243(4898):1586–1589, March 1989.

Yves F Dufrêne and Peter Hinterdorfer. Recent progress in AFM molecular recognition studies. *Pflügers Archiv : European Journal of Physiology*, 456(1): 237–245, December 2007.

Ian C Duguid and Trevor G Smart. Retrograde activation of presynaptic NMDA receptors enhances GABA release at cerebellar interneuron–Purkinje cell synapses. *Nature Neuroscience*, 7(5):525–533, May 2004.

Ian C Duguid, Yuriy Pankratov, Guy W J Moss, and Trevor G Smart. Somatodendritic Release of Glutamate Regulates Synaptic Inhibition in Cerebellar Purkinje Cells via Autocrine mGluR1 Activation. *Journal of Neuroscience*, 27(46):12464–12474, November 2007.

Andréa Dumoulin, Philippe Rostaing, Cécile Bedet, Sabine Lévi, Marie-Françoise Isambert, Jean-Pierre Henry, Antoine Triller, and Bruno Gasnier. Presence of the vesicular inhibitory amino acid transporter in GABAergic and glycinergic synaptic terminal boutons. *Journal of cell science*, 112(6): 811–823, March 1999.

Peter R Dunkley, Paula A Jarvie, John W Heath, Grahame J Kidd, and John A P Rostas. A Rapid Method for Isolation of Synaptosomes on Percoll Gradients. *Brain research*, 372:115–129, 1986.

C Durkan and I V Shvets. 40 nm resolution in reflection-mode SNOM with A - 685 nm. *Ultramicroscopy*, 61:227–231, 1995.

Amal K Dutta, Ravshan Z Sabirov, Hiromi Uramoto, and Yasunobu Okada. Role of ATP-conductive Anion Channel in ATP Release from Neonatal Rat Cardiomyocytes in Ischemic or Hypoxic Conditions. *Journal of Physiology*, 559(3):799–812, July 2004.

Amal K Dutta, Yuri E Korchev, Andrew I Shevchuk, Seiji Hayashi, Yasunobu Okada, and Ravshan Z Sabirov. Spatial Distribution of Maxi-Anion Channel on Cardiomyocytes Detected by Smart-Patch Technique. *Biophysical Journal*, 94(5):1646–1655, March 2008.

Jackie Edry-Schiller, Simona Ginsburg, and Rami Rahamimoff. A Bursting Potassium Channel in Isolated Cholinergic Synaptosomes of Torpedo Electric Organ. *Journal of Physiology*, 439:627–647, 1991.

Martin A Edwards, Cara G Williams, Anna L Whitworth, and Patrick R Unwin. Scanning Ion Conductance Microscopy: a Model for Experimentally Realistic Conditions and Image Interpretation. *Analytical Chemistry*, 81 (11):4482–4492, June 2009.

Fredrik Elinder, Nesar Akanda, R Tofighi, S Shimizu, Y Tsujimoto, S Orrenius, and S Ceccatelli. Opening of plasma membrane voltage-dependent anion channels (VDAC) precedes caspase activation in neuronal apoptosis induced by toxic stimuli. *Cell Death and Differentiation*, 12(8):1134–1140, April 2005.

P A Engel and D B Millis. Study of surface topography in impact wear. *Wear*, 75:423–442, 1982.

Ferenc Erdélyi, G Sekerkova, Z Katarova, N Hájos, J Pálhalmi, T F Freund, E Mugnaini, and Gábor Szabó. GAD65-GFP Transgenic Mice Expressing GFP in the GABAergic Nervous System. *FENS Abstract*, 1:A011.3, 2002.

U C Fischer and Dieter W Pohl. Observation of Single-Particle Plasmons by Near-Field Optical Microscopy. *Physical review letters*, 62(4):458–461, January 1989.

Ulrich C Fischer. Optical characteristics of 0.1 µm circular apertures in a metal film as light sources for scanned ultramicroscopy. *Journal of Vacuum Science and Technology B*, 3(1):386–390, January 1985.

Ulrich C Fischer, U T Dürig, and Dieter W Pohl. Near-field optical scanning microscopy in reflection. *Applied Physics Letters*, 52(4):249–251, January 1988.

Mónica L Fiszman, Andrea Barberis, Congyi Lu, Zhanyan Fu, Ferenc Erdélyi, Gábor Szabó, and Stefano Vicini. NMDA Receptors Increase the Size of GABAergic Terminals and Enhance GABA Release. *Journal of Neuroscience*, 25(8):2024–2031, February 2005.

Mónica L Fiszman, Ferenc Erdélyi, Gábor Szabó, and Stefano Vicini. Presynaptic AMPA and kainate receptors increase the size of GABAergic ter-

minals and enhance GABA release. *Neuropharmacology*, 52(8):1631–1640, June 2007.

Ian D Forsythe. Direct patch recording from identified presynaptic terminals mediating glutamatergic EPSCs in the rat CNS, in vitro. *Journal of Physiology*, 479(3):381–387, September 1994.

Ian D Forsythe, Tetsuhiro Tsujimoto, Margaret Barnes-Davies, Matthew F Cuttle, and Tomoyuki Takahashi. Inactivation of Presynaptic Calcium Current Contributes to Synaptic Depression at a Fast Central Synapse. *Neuron*, 20(4):797–807, April 1998.

Monika Fritz, Manfred Radmacher, Jason P Cleveland, Miriam W Allersma, Russell J Stewart, Ralph Gieselmann, Paul Janmey, Christoph F Schmidt, and Paul K Hansma. Imaging Globular and Filamentous Proteins in Physiological Buffer Solutions with Tapping Mode Atomic Force Microscopy. *Langmuir*, 11(9):3529–3535, 1995.

Nicholas A Geisse, Sean P Sheehy, and Kevin Kit Parker. Control of myocyte remodeling in vitro with engineered substrates. *In Vitro Cellular & Developmental Biology - Animal*, 45(7):343–350, February 2009.

Levi A Gheber, Jeeseong Hwang, and Michael Edidin. Design and optimization of a near-field scanning optical microscope for imaging biological samples in liquid. *Applied Optics*, 37(16):3574–3581, June 1998.

Franz J Giessibl. Atomic resolution of the silicon (111)-(7x7) surface by atomic force microscopy. *Science*, 267(5194):68–71, January 1995.

Franz J Giessibl. AFM's path to atomic resolution. *Materials Today*, 8(5): 32–41, May 2005.

Ziv Gil, Shai D Silberberg, and Karl L Magleby. Voltage-induced membrane displacement in patch pipettes activates mechanosensitive channels. *Proceedings of the National Academy of Sciences of the United States of America*, 96 (25):14594–14599, December 1999.

P Gleyzes, A C Boccara, and R Bachelot. Near field optical microscopy using a metallic vibrating tip. *Ultramicroscopy*, 57:318–322, 1995.

Maike Glitsch and Alain Marty. Presynaptic effects of NMDA in cerebellar Purkinje cells and interneurons. *Journal of Neuroscience*, 19(2):511–519, January 1999.

Julia Gorelik, Yuchun Gu, Hilmar A Spohr, Andrew I Shevchuk, Max J Lab, Sian E Harding, Christopher R W Edwards, Michael Whitaker, Guy W J Moss, David C H Benton, Daniel Sanchez, Alberto Darszon, Igor Vodyanoy, David Klenerman, and Yuri E Korchev. Ion channels in small cells and subcellular structures can be studied with a smart patch-clamp system. *Biophysical Journal*, 83(6):3296–3303, December 2002a.

Julia Gorelik, Andrew I Shevchuk, M Ramalho, M Elliott, C Lei, C F Higgins, Max J Lab, David Klenerman, Nina Krauzewicz, and Yuri E Korchev. Scanning surface confocal microscopy for simultaneous topographical and fluorescence imaging: application to single virus-like particle entry into a cell. *Proceedings of the National Academy of Sciences of the United States of America*, 99(25):16018–16023, December 2002b.

Julia Gorelik, Andrew I Shevchuk, Gregory I Frolenkov, Ivan A Diakonov, Max J Lab, Corne J Kros, Guy P Richardson, Igor Vodyanoy, Christopher R W Edwards, David Klenerman, and Yuri E Korchev. Dynamic assembly of surface structures in living cells. *Proceedings of the National Academy of Sciences of the United States of America*, 100(10):5819–5822, May 2003.

Julia Gorelik, Yanjun Zhang, Daniel Sanchez, Andrew I Shevchuk, Gregory I Frolenkov, Max J Lab, David Klenerman, Christopher R W Edwards, and Yuri E Korchev. Aldosterone acts via an ATP autocrine/paracrine system: the Edelman ATP hypothesis revisited. *Proceedings of the National Academy of Sciences of the United States of America*, 102(42):15000–15005, October 2005.

Julia Gorelik, Nadire N Ali, Andrew I Shevchuk, Max J Lab, Catherine Williamson, Sian E Harding, and Yuri E Korchev. Functional characterization of embryonic stem cell-derived cardiomyocytes using scanning ion conductance microscopy. *Tissue engineering*, 12(4):657–664, April 2006.

P T Gray and J M Ritchie. A voltage-gated chloride conductance in rat cultured astrocytes. *Proceedings of the Royal Society of London Series B*, 228 (1252):267–288, August 1986.

P T A Gray, S Bevan, and J M Ritchie. High Conductance Anion-Selective Channels in Rat Cultured Schwann Cells. *Proceedings of the Royal Society B: Biological Sciences*, 221(1225):395–409, June 1984.

Yuchun Gu, Julia Gorelik, Hilmar A Spohr, Andrew I Shevchuk, Max J Lab, Sian E Harding, Igor Vodyanoy, David Klenerman, and Yuri E Korchev. High-resolution scanning patch-clamp: new insights into cell function. *FASEB Journal*, 16(7):748–750, May 2002.

Karl H Guenther, Peter G Wierer, and Jean M Bennett. Surface roughness measurements of low-scatter mirrors and roughness standards. *Applied Optics*, 23(21):3820–3836, November 1984.

A C Hall, G R Tibbs, J O Dolly, W R Lieb, and Nicholas P Franks. A simple method for recording single-channel activity from synaptic plasma membranes. *J Neurosci Meth*, 49:81–91, 1993.

James E Hall. Access resistance of a small circular pore. *The Journal of general physiology*, 66(4):531–532, October 1975.

Owen P Hamill, Alain Marty, Erwin Neher, Bert Sakmann, and Frederick J Sigworth. Improved Patch-Clamp Techniques for High-Resolution Current Recording from Cells and Cell-Free Membrane Patches. *Pflügers Archiv*, 391(2):85–100, August 1981.

Helen G Hansma. Surface biology of DNA by atomic force microscopy. *Annual Review Physical Chemistry*, 52:71–92, 2001.

Helen G Hansma, R L Sinsheimer, J Groppe, T C Bruice, V Elings, G Gurley, M Bezanilla, I A Mastrangelo, P V C Hough, and Paul K Hansma. Recent advances in atomic force microscopy of DNA. *Scanning*, 15(5):296–299, 1993.

Paul K Hansma, B Drake, O Marti, S A Gould, and C B Prater. The scanning ion-conductance microscope. *Science*, 243(4891):641–643, February 1989.

Paul K Hansma, J P Cleveland, M Radmacher, D A Walters, P E Hillner, M Bezanilla, M Fritz, D Vie, H G Hansma, C B Prater, J Massie, L Fukunaga, J Gurley, and V Elings. Tapping mode atomic force microscopy in liquids. *Applied Physics Letters*, 64(13):1738–1740, March 1994.

Patrick Happel and Irmgard D Dietzel. Backstep scanning ion conductance microscopy as a tool for long term investigation of single living cells. *Journal of Nanobiotechnology*, 7(1):7, 2009.

Patrick Happel, G Hoffmann, S A Mann, and Irmgard D Dietzel. Monitoring cell movements and volume changes with pulse-mode scanning ion conductance microscopy. *Journal of Microscopy*, 212(Pt 2):144–151, November 2003.

Alec Harootunian, Eric Betzig, Michael Isaacson, and Aaron Lewis. Super-resolution fluorescence near-field scanning optical microscopy. *Applied Physics Letters*, 49(11):674–676, September 1986.

Eugene Hecht. *Optics, 4th Edition*. Pearson Education, San Francisco, 2002.

Paul Heckbert. Non-overshooting Hermite cubic splines for keyframe interpolation. Technical report, Three Dimensional Animation Systems Group, Computer Graphics Laboratory, New York Institute of Technology, February 1985.

E Henderson, P G Haydon, and D S Sakaguchi. Actin Filament Dynamics in Living Glial Cells Imaged by Atomic Force Microscopy. *Science*, 257(5078): 1944–1946, September 1992.

Bertil Hille. *Ion channels of excitable membranes, 3rd edition*. Sinauer Associates, Sunderland Massachussetts, 2001.

Peter Hinterdorfer, Werner Baumgartner, Hermann J Gruber, Kurt Schilcher, and Hansgeorg Schindler. Detection and localization of individual antibody-antigen recognition events by atomic force microscopy. *Proceedings of the National Academy of Sciences of the United States of America*, 93: 3477–3481, April 1996.

Alan L Hodgkin and Andrew F Huxley. A Quantitative Description of Membrane Current and its Application to Conduction and Excitation in Nerve. *Journal of Physiology*, 117(4):500–544, August 1952a.

Alan L Hodgkin and Andrew F Huxley. The Components of Membrane Conductance in the Giant Axon of Loligo. *Journal of Physiology*, 116(4): 473–496, April 1952b.

Alan L Hodgkin and Andrew F Huxley. Currents Carried by Sodium and Potassium Ions Through the Membrane of the Giant Axon of Loligo. *Journal of Physiology*, 116(4):449–472, April 1952c.

Bart W Hoogenboom, Kitaru Suda, Andreas Engel, and Dimitrios Fotiadis. The Supramolecular Assemblies of Voltage-dependent Anion Channels in the Native Membrane. *Journal of Molecular Biology*, 370(2):246–255, July 2007.

Hao Huang and Angélique Bordey. Glial Glutamate Transporters Limit Spillover Activation of Presynaptic NMDA Receptors and Influence Synaptic Inhibition of Purkinje Neurons. *Journal of Neuroscience*, 24(25): 5659–5669, June 2004.

Nicolas Hussy. Calcium-activated chloride channels in cultured embryonic Xenopus spinal neurons. *Journal of Neurophysiology*, 68(6):2042–2050, December 1992.

Bernard Jaffe, William R Cook, and Hans Jaffe. *Piezoelectric Ceramics*. Academic Press, New York, 1971.

Tuula Jalonen. Single-channel characteristics of the large-conductance anion channel in rat cortical astrocytes in primary culture. *Glia*, 9(3):227–237, November 1993.

Young-Hwan Jo and Lorna W Role. Coordinate Release of ATP and GABA at In Vitro Synapses of Lateral Hypothalamic Neurons. *Journal of Neuroscience*, 22(12):4794–4804, June 2002.

Young-Hwan Jo and Rémy Schlichter. Synaptic corelease of ATP and GABA in cultured spinal neurons. *Nature Neuroscience*, 2(3):241–245, March 1999.

D H Jones and A I Matus. Isolation of Synaptic Plasma Membrane from Brain by Combined Flotation-Sedimentation Density Gradient Centrifugation. *Biochimica et Biophysica Acta*, 356:276–287, 1974.

Masanobu Kano, U Rexhausen, J Dreessen, and Arthur Konnerth. Synaptic excitation produces a long-lasting rebound potentiation of inhibitory synaptic signals in cerebellar Purkinje cells. *Nature*, 356(6370):601–604, April 1992.

Sandor Kasas, Neil H Thomson, Bettye L Smith, Helen G Hansma, Xingshu Zhu, Martin Guthold, Carlos Bustamante, Eric T Kool, Mikhail Kashlev, and Paul K Hansma. Escherichia coli RNA Polymerase Activity Observed Using Atomic Force Microscopy. *Biochemistry*, 36(3):461–468, January 1997.

Bernard Katz and Ricardo Miledi. The Effect of Calcium on Acetylcholine Release from Motor Nerve Terminals. *Proc R Soc B*, 161(985):496–503, February 1965.

Petr Klapetek, David Nečas, and Christopher Anderson. Gwyddion user guide. http://gwyddion.net/, 2004–2010.

David Klenerman, Yuri E Korchev, and Simon J Davis. Imaging and characterisation of the surface of live cells. *Current Opinion in Chemical Biology*, 15:1–8, April 2011.

Maarten H P Kole, Susanne U Ilschner, Björn M Kampa, Stephen R Williams, Peter C Ruben, and Greg J Stuart. Action potential generation requires a high sodium channel density in the axon initial segment. *Nature Neuroscience*, 11(2):178–186, January 2008.

Yuri E Korchev, C Lindsay Bashford, Mihailo Milovanovic, Igor Vodyanoy, and Max J Lab. Scanning ion conductance microscopy of living cells. *Biophysical Journal*, 73(2):653–658, August 1997a.

Yuri E Korchev, Mihailo Milovanovic, C Lindsay Bashford, D C Bennett, Elena V Sviderskaya, Igor Vodyanoy, and Max J Lab. Specialized scanning ion-conductance microscope for imaging of living cells. *Journal of Microscopy*, 188(Pt 1):17–23, October 1997b.

Yuri E Korchev, Julia Gorelik, Max J Lab, Elena V Sviderskaya, Caroline L Johnston, Charles R Coombes, Igor Vodyanoy, and Christopher R W Edwards. Cell volume measurement using scanning ion conductance microscopy. *Biophysical Journal*, 78(1):451–457, 2000a.

Yuri E Korchev, Yuri A Negulyaev, Christopher R W Edwards, Igor Vodyanoy, and Max J Lab. Functional localization of single active ion channels on the surface of a living cell. *Nature Cell Biology*, 2(9):616–619, September 2000b.

Yuri E Korchev, Meera Raval, Max J Lab, Julia Gorelik, Christopher R W Edwards, Trevor Rayment, and David Klenerman. Hybrid scanning ion conductance and scanning near-field optical microscopy for the study of living cells. *Biophysical Journal*, 78(5):2675–2679, May 2000c.

Mauri E Krouse, Gavan T Schneider, and Peter W Gage. A large anion-selective channel has seven conductance levels. *Nature*, 319(1):58–60, January 1986.

Jean-Jacques Lacapère, David L Stokes, and Didier Chatenay. Atomic force microscopy of three-dimensional membrane protein crystals. Ca-ATPase of sarcoplasmic reticulum. *Biophysical Journal*, 63(2):303–308, August 1992.

M G Langer, A Koitschev, H Haase, U Rexhausen, J K Heinrich Hörber, and J P Ruppersberg. Mechanical stimulation of individual stereocilia of living cochlear hair cells by atomic force microscopy. *Ultramicroscopy*, 82: 269–278, 2000.

Marc Lavallée, Otto F Schanne, and Normand C Hébert, editors. *Glass Microelectrodes*. John Wiley and Sons, New York, 1969.

José R Lemos and Martha C Nowycky. Two Types of Calcium Channels Coexist in Peptide-Releasing Vertebrate Nerve Terminals. *Neuron*, 2:1419–1426, May 1989.

Aaron Lewis, Michael Isaacson, Andrew Muray, and Alec Harootunian. Scanning optical spectral microscopy with 500Å spatial resolution. *Biophysical Journal*, 41:405a, 1983.

Aaron Lewis, Michael Isaacson, Alec Harootunian, and Andrew Muray. Development of a 500 Å spatial resolution light microscope: I. light is efficiently transmitted through $\lambda/16$ diameter apertures. *Ultramicroscopy*, 13: 227–232, 1984.

Nancy Fidler Lim, Martha C Nowycky, and Richard J Bookman. Direct measurement of exocytosis and calcium currents in single vertebrate nerve terminals. *Nature*, 344(6265):449–451, March 1990.

S M Lindsay and B Barris. Imaging deoxyribose nucleic acid molecules on a metal surface under water by scanning tunneling microscopy. *Journal of Vacuum Science and Technology A*, 6(2):544–547, March 1988.

Hong-Tao Liu, Ravshan Z Sabirov, and Yasunobu Okada. Oxygen-glucose deprivation induces ATP release via maxi-anion channels in astrocytes. *Purinergic Signalling*, 4(2):147–154, September 2007.

Hong-Tao Liu, Abduqodir H Toychiev, Nobuyuki Takahashi, Ravshan Z Sabirov, and Yasunobu Okada. Maxi-anion channel as a candidate pathway for osmosensitive ATP release from mouse astrocytes in primary culture. *Cell Research*, 18(5):558–565, May 2008.

Hsue-Yang Liu, Fu-Ren F Fan, Charles W Lin, and Allen J Bard. Scanning Electrochemical and Tunneling Ultramicroelectrode Microscope for High-Resolution Examination of Electrode Surfaces in Solution. *Journal of the American Chemical Society*, 108(13):3838–3839, June 1986.

Isabel Llano, Nathalie Leresche, and Alain Marty. Calcium entry increases the sensitivity of cerebellar Purkinje cells to applied GABA and decreases inhibitory synaptic currents. *Neuron*, 6(4):565–574, April 1991.

Rodolfo R Llinás, M Sugimori, and R B Silver. The Concept of Calcium Concentration Microdomains in Synaptic Transmission. *Neuropharmacology*, 34 (11):1443–1451, 1995.

S A Mann, G Hoffmann, A Hengstenberg, W Schuhmann, and Irmgard D Dietzel. Pulse-mode scanning ion conductance microscopy–a method to investigate cultured hippocampal cells. *Journal of Neuroscience Methods*, 116(2):113–117, May 2002.

S A Mann, J W Meyer, and Irmgard D Dietzel. Integration of a scanning ion conductance microscope into phase contrast optics and its application to the quantification of morphological parameters of selected cells. *Journal of Microscopy*, 224(Pt 2):152–157, November 2006.

Anders Mannelquist, Hideki Iwamoto, Gábor Szabó, and Zhifeng Shao. Near-field optical microscopy with a vibrating probe in aqueous solution. *Applied Physics Letters*, 78(14):2076–2078, April 2001.

Anders Mannelquist, Hideki Iwamoto, Gábor Szabó, and Zhifeng Shao. Near field optical microscopy in aqueous solution: implementation and characterization of a vibrating probe. *Journal of Microscopy*, 205(1):53–60, January 2002.

Y Martin, C C Williams, and H K Wickramasinghe. Atomic force microscope-force mapping and profiling on a sub 100-Å scale. *Journal of Applied Physics*, 61(10):4723–4729, May 1987.

Marco Martina, Gui Lan Yao, and Bruce P Bean. Properties and Functional Role of Voltage-Dependent Potassium Channels in Dendrites of Rat Cerebellar Purkinje Neurons. *Journal of Neuroscience*, 23(13):5698–5707, July 2003.

Alain Marty and Isabel Llano. Modulation of inhibitory synapses in the mammalian brain. *Current Opinion in Neurobiology*, 5(3):335–341, June 1995.

Viswanathan Meenakshi, Yelizaveta Babayan, and Teri W Odom. Benchtop Nanoscale Patterning Using Soft Lithography. *Journal of Chemical Education*, 84(11):1795–1798, November 2007.

Gerhard Meyer and Nabil M Amer. Novel optical approach to atomic force microscopy. *Applied Physics Letters*, 53(12):1045–1047, September 1988.

Ricardo Miledi. Release Induced by Injection of Calcium Ions into Nerve Terminals. *Proc R Soc B*, 183(1073):421–425, July 1973.

Clemens Möller, Mike Allen, Virgil Elings, Andreas Engel, and Daniel J Muller. Tapping-Mode Atomic Force Microscopy Produces Faithful High-Resolution Images of Protein Surfaces. *Biophysical Journal*, 77(2):1150–1158, August 1999.

John W Moore, Norman Stockbridge, and Monte Westerfield. On the Site of Impulse Initiation in a Neurone. *Journal of Physiology*, 336:301–311, 1983.

F Moreno-Herrero, J Colchero, J Gómez-Herrero, A M Baró, and J Ávila. Jumping mode atomic force microscopy obtains reproducible images of Alzheimer paired helical filaments in liquids. *European Polymer Journal*, 40 (5):927–932, May 2004.

Vincent T Moy, Ernst-Ludwig Florin, and Hermann E Gaub. Intermolecular Forces and Energies Between Ligands and Receptors. *Science*, 266(5183): 257–259, October 1994.

Daniel J Muller and Andreas Engel. Atomic force microscopy and spectroscopy of native membrane proteins. *Nature Protocols*, 2(9):2191–2197, September 2007.

Hiroshi Muramatsu, Norio Chiba, Katsunori Homma, Kunio Nakajima, Tatsuaki Ataka, Satoko Ohta, Akihiro Kusumi, and Masamichi Fujihira. Near-field optical microscopy in liquids. *Applied Physics Letters*, 66(24): 3245–3247, June 1995a.

Hiroshi Muramatsu, Norio Chiba, Takeshi Umemoto, Katsunori Homma, Kunio Nakajima, Tatsuaki Ataka, Satoko Ohta, Akihiro Kusumi, and Masamichi Fujihira. Development of near-field optic/atomic-force microscope for biological materials in aqueous solutions. *Ultramicroscopy*, 61: 265–269, December 1995b.

Erwin Neher and Bert Sakmann. Single-channel currents recorded from membrane of denervated frog muscle fibres. *Nature*, 260(5554):799–802, April 1976.

J J Nordmann, J P Desmazes, and D Georgescauld. The Relationship Between the Membrane Potential of Neurosecretory Nerve Endings, as Measured by a Voltage-Sensitive Dye, and the Release of Neurohypophysial Hormones. *Neuroscience*, 7(3):731–737, 1982.

Pavel Novak, Chao Li, Andrew I Shevchuk, Ruben Stepanyan, Matthew Caldwell, Simon Hughes, Trevor G Smart, Julia Gorelik, Victor P Ostanin, Max J Lab, Guy W J Moss, Gregory I Frolenkov, David Klenerman, and Yuri E Korchev. Nanoscale live-cell imaging using hopping probe ion conductance microscopy. *Nature Methods*, 6(4):279–281, April 2009.

Linda Nowak, P Bregestovski, Philippe Ascher, A Herbet, and A Prochiantz. Magnesium gates glutamate-activated channels in mouse central neurones. *Nature*, 307(5950):462–465, 1984.

Hans Oberleithner, Edna Brinckmann, Gerhard Giebisch, and John Geibel. Visualizing life on biomembranes by atomic force microscopy. *Kidney international*, 48(4):923–929, October 1995.

F Oesterhelt, D Oesterhelt, M Pfeiffer, A Engel, H E Gaub, and Daniel J Muller. Unfolding Pathways of Individual Bacteriorhodopsins. *Science*, 288(5463):143–146, April 2000.

F Ohnesorge and Gerd Binnig. True Atomic Resolution by Atomic Force Microscopy Through Repulsive and Attractive Forces. *Science*, 260(5113): 1451–1456, June 1993.

John Aloysius O'Keefe. Resolving Power of Visible Light. *Journal of the Optical Society of America*, 46(5):359, May 1956.

S P Olesen and M Bundgaard. Chloride-selective channels of large conductance in bovine aortic endothelial cells. *Acta physiologica Scandinavica*, 144 (2):191–198, February 1992.

V Parpura, P G Haydon, and E Henderson. Three-dimensional imaging of living neurons and glia with the atomic force microscope. *Journal of cell science*, 104:427–432, February 1993.

David Pastré, Hideki Iwamoto, Jie Liu, Gábor Szabó, and Zhifeng Shao. Characterization of AC mode scanning ion-conductance microscopy. *Ultramicroscopy*, 90(1):13–19, December 2001.

Joe D Piper, Chao Li, Chien-Jung Lo, Richard Berry, Yuri Korchev, Liming Ying, and David Klenerman. Characterization and Application of Controllable Local Chemical Changes Produced by Reagent Delivery from a Nanopipet. *Journal of the American Chemical Society*, 130(31):10386–10393, August 2008.

Thomas A Pitler and Bradley E Alger. Postsynaptic spike firing reduces synaptic GABAA responses in hippocampal pyramidal cells. *Journal of Neuroscience*, 12(10):4122–4132, October 1992.

Dieter W Pohl, W Denk, and M Lanz. Optical stethoscopy: image recording with resolution /20. *Applied Physics Letters*, 44(7), April 1984.

Gabriela Popescu and Anthony Auerbach. Modal gating of NMDA receptors and the shape of their synaptic response. *Nature Neuroscience*, 6(5):476–483, May 2003.

Constant A J Putman, Kees O van der Werf, Bart G de Grooth, Niek F van Hulst, and Jan Greve. Tapping mode atomic force microscopy in liquid. *Applied Physics Letters*, 64(18):2454–2456, May 1994.

Anqi Qian, Amy L Buller, and Jon W Johnson. NR2 subunit-dependence of NMDA receptor channel block by external Mg2+. *Journal of Physiology*, 562(2):319–331, October 2004.

R Development Core Team. *R: A Language and Environment for Statistical Computing*. R Foundation for Statistical Computing, Vienna, Austria, 2010. URL http://www.R-project.org. ISBN 3-900051-07-0.

M Radmacher, RW Tillmann, M Fritz, and HE Gaub. From molecules to cells: imaging soft samples with the atomic force microscope. *Science*, 257 (5078):1900–1905, September 1992.

M Radmacher, J P Cleveland, M Fritz, H G Hansma, and Paul K Hansma. Mapping interaction forces with the atomic force microscope. *Biophysical Journal*, 66(6):2159–2165, June 1994.

Rami Rahamimoff, Susan A DeRiemer, Bert Sakmann, Herbert Stadler, and Nilly Yakir. Ion channels in synaptic vesicles from Torpedo electric organ. *Proceedings of the National Academy of Sciences of the United States of America*, 85:5310–5314, July 1988.

Ede A Rancz, Taro Ishikawa, Ian C Duguid, Paul Chadderton, Séverine Mahon, and Michael Häusser. High-fidelity transmission of sensory information by single cerebellar mossy fibre boutons. *Nature*, 450(7173):1245–1248, December 2007.

Matthew N Rasband, James S Trimmer, Thomas L Schwarz, S Rock Levinson, Mark H Ellisman, Melitta Schachner, and Peter Shrager. Potassium Channel Distribution, Clustering, and Function in Remyelinating Rat Axons. *Journal of Neuroscience*, 18(1):36–47, January 1998.

Johannes Rheinlaender and Tilman E Schäffer. Image formation, resolution, and height measurement in scanning ion conductance microscopy. *Journal of Applied Physics*, 105(9):094905, 2009.

Johannes Rheinlaender, Nicholas A Geisse, Roger Proksch, and Tilman E Schäffer. Comparison of Scanning Ion Conductance Microscopy with Atomic Force Microscopy for Cell Imaging. *Langmuir*, 27(2):697–704, January 2011.

Matthias Rief, Mathias Gautel, Filipp Oesterhelt, Julio M Fernandez, and Hermann E Gaub. Reversible Unfolding of Individual Titin Immunoglobulin Domains by AFM. *Science*, 276(5315):1109–1112, May 1997a.

Matthias Rief, Filipp Oesterhelt, Berthold Heymann, and Hermann E Gaub. Single Molecule Force Spectroscopy on Polysaccharides by Atomic Force Microscopy. *Science*, 275(5304):1295–1297, February 1997b.

Kit T Rodolfa, Andreas Bruckbauer, Dejian Zhou, Andrew I Shevchuk, Yuri E Korchev, and David Klenerman. Nanoscale pipetting for controlled chemistry in small arrayed water droplets using a double-barrel pipet. *Nano Letters*, 6(2):252–257, July 2006.

Alison M Rothery, Julia Gorelik, Andreas Bruckbauer, W Yu, Yuri E Korchev, and David Klenerman. A novel light source for SICM–SNOM of living cells. *Journal of Microscopy*, 209(2):94–101, February 2003.

Ravshan Z Sabirov and Yasunobu Okada. The maxi-anion channel: a classical channel playing novel roles through an unidentified molecular entity. *The Journal of Physiological Sciences*, 59(1):3–21, December 2008.

Ravshan Z Sabirov, Tatiana Sheiko, Hongtao Liu, Defeng Deng, Yasunobu Okada, and William J Craigen. Genetic Demonstration That the Plasma Membrane Maxianion Channel and Voltage-dependent Anion Channels Are Unrelated Proteins. *Journal of Biological Chemistry*, 281(4):1897–1904, January 2006.

Bert Sakmann and Erwin Neher, editors. *Single Channel Recording, 1st edition*. Plenum Press, New York, 1983a.

Bert Sakmann and Erwin Neher. Geometric parameters of pipettes and membrane patches. In *Single Channel Recording, 1st edition* Sakmann and Neher (1983a), chapter 2, pages 37–51.

Bert Sakmann and Erwin Neher, editors. *Single Channel Recording, 2nd edition*. Plenum Press, New York, 1995.

Daniel Sanchez, Uma Anand, Julia Gorelik, Christopher D Benham, Chas Bountra, Max J Lab, David Klenerman, Rolfe Birch, Praveen Anand, and Yuri E Korchev. Localized and non-contact mechanical stimulation of dorsal root ganglion sensory neurons using scanning ion conductance microscopy. *Journal of Neuroscience Methods*, 159(1):26–34, January 2007.

Yasnory F Sasaki, Thomas Rothe, Louis S Premkumar, Saumya Das, Jiankun Cui, Maria V Talantova, Hon-Kit Wong, Xiandi Gong, Shing Fai Chan, Dongxian Zhang, Nobuki Nakanishi, Nikolaus J Sucher, and Stuart A Lipton. Characterization and comparison of the NR3A subunit of the NMDA receptor in recombinant systems and primary cortical neurons. *Journal of Neurophysiology*, 87(4):2052–2063, April 2002.

J Schneir and Paul K Hansma. Scanning Tunneling Microscopy and Lithography of Solid Surfaces Covered with Nonpolar Liquids. *Langmuir*, 3(5): 1025–1027, 1987.

Stephanie Schorge, Sergio Elenes, and David Colquhoun. Maximum likelihood fitting of single channel NMDA activity with a mechanism composed of independent dimers of subunits. *Journal of Physiology*, 569(2): 395–418, October 2005.

Sebastian Schrot, Christian Weidenfeller, Tilman E Schäffer, Horst Robenek, and Hans-Joachim Galla. Influence of Hydrocortisone on the Mechanical Properties of the Cerebral Endothelium In Vitro. *Biophysical Journal*, 89(6): 3904–3910, December 2005.

W Schwarze and H-A Kolb. Voltage-dependent kinetics of an anionic channel of large unit conductance in macrophages and myotube membranes. *Pflügers Archiv*, 402(3):281–291, 1984.

Shmuel Shalom, Klony Lieberman, Aaron Lewis, and Sidney R Cohen. A micropipette force probe suitable for near-field scanning optical microscopy. *Review of Scientific Instruments*, 63(9):4061–4065, September 1992.

Andrew I Shevchuk, Julia Gorelik, Sian E Harding, Max J Lab, David Klenerman, and Yuri E Korchev. Simultaneous measurement of Ca2+ and cellular dynamics: combined scanning ion conductance and optical microscopy to study contracting cardiac myocytes. *Biophysical Journal*, 81(3): 1759–1764, September 2001.

Andrew I Shevchuk, Gregory I Frolenkov, Daniel Sanchez, Peter S James, Noah Freedman, Max J Lab, Roy Jones, David Klenerman, and Yuri E Korchev. Imaging Proteins in Membranes of Living Cells by High-Resolution Scanning Ion Conductance Microscopy. *Angewandte Chemie International Edition*, 45(14):2212–2216, March 2006.

Andrew I Shevchuk, Phil Hobson, Max J Lab, David Klenerman, Nina Krauzewicz, and Yuri E Korchev. Imaging Single Virus Particles on the Surface of Cell Membranes by High-Resolution Scanning Surface Confocal Microscopy. *Biophysical Journal*, 94(10):4089–4094, January 2008.

Shigeomi Shimizu, Yosuke Matsuoka, Yasuo Shinohara, Yoshihiro Yoneda, and Yoshihide Tsujimoto. Essential Role of Voltage-dependent Anion Channel in Various Forms of Apoptosis in Mammalian Cells. *Journal of Cell Biology*, 152(2):237–250, January 2001.

Wonchul Shin and Kevin D Gillis. Measurement of Changes in Membrane Surface Morphology Associated with Exocytosis Using Scanning Ion Conductance Microscopy. *Biophysical Journal*, 91(6):L63–L65, June 2006.

Peter Shrager. Sodium channels in single demyelinated mammalian axons. *Brain research*, 483:149–154, 1989.

Sanjeev G Shroff, Donald R Saner, and Ratneshwar Lal. Dynamic micromechanical properties of cultured rat atrial myocytes measured by atomic force microscopy. *American Journal of Physiology - Cell Physiology*, 269(1): C286–C292, July 1995.

R L W Smithson, T G Stange, D F Evans, R D Edstrom, and W A Hendrickson. AFM and STM of organic macromolecules. In Wickramasinghe (1991), pages 219–231.

Fred M Snell. Some electrical properties of fine-tipped pipette microelectrodes. In Lavallée et al. (1969), chapter 7, pages 111–123.

Richard Sonnenfeld and Paul K Hansma. Atomic-Resolution Microscopy in Water. *Science*, 232(4747):211–213, April 1986.

U Sonnhof. Single voltage-dependent K+ and Cl channels in cultured rat astrocytes. *Canadian Journal of Physiology and Pharmacology*, 65(5):1043–1050, May 1987.

J Sotres, A Lostao, C Gómez-Moreno, and A M Baró. Jumping mode AFM imaging of biomolecules in the repulsive electrical double layer. *Ultramicroscopy*, 107(12):1207–1212, November 2007.

Andrew P Southan and Brian Robertson. Patch-clamp recordings from cerebellar basket cell bodies and their presynaptic terminals reveal an asymmetric distribution of voltage-gated potassium channels. *Journal of Neuroscience*, 18(3):948–955, February 1998.

Andrew P Southan and Brian Robertson. Electrophysiological characterization of voltage-gated K(+) currents in cerebellar basket and purkinje cells: Kv1 and Kv3 channel subfamilies are present in basket cell nerve terminals. *Journal of Neuroscience*, 20(1):114–122, 2000.

Andrew P Southan, Neil P Morris, Gary J Stephens, and Brian Robertson. Hyperpolarization-activated currents in presynaptic terminals of mouse cerebellar basket cells. *Journal of Physiology*, 526 Pt 1:91–97, July 2000.

Gabriele Spatkowski and Karl Schilling. Postnatal dendritic morphogenesis of cerebellar basket and stellate cells in vitro. *Journal of Neuroscience Research*, 72(3):317–326, May 2003.

Andrej-Nikolai Spiess and Christian Ritz. *qpcR: Modelling and analysis of real-time PCR data*, 2010. URL http://CRAN.R-project.org/package=qpcR. R package version 1.3-3.

Martin Stark, Reinhard Guckenberger, Andreas Stemmer, and Robert W Stark. Estimating the transfer function of the cantilever in atomic force microscopy: A system identification approach. *Journal of Applied Physics*, 98(11):114904, 2005.

G J Stuart, H U Dodt, and Bert Sakmann. Patch-clamp recordings from the soma and dendrites of neurons in brain slices using infrared video microscopy. *Pflügers Archiv*, 423(5-6):511–518, June 1993.

Greg J Stuart and Michael Häusser. Initiation and Spread of Sodium Action Potentials in Cerebellar Purkinje Cells. *Neuron*, 13:703–712, September 1994.

Greg J Stuart and Bert Sakmann. Active propagation of somatic action potentials into neocortical pyramidal cell dendrites. *Nature*, 367(6458):69–72, January 1994.

Thomas M Suchyna, Vladislav S Markin, and Frederick Sachs. Biophysics and Structure of the Patch and the Gigaseal. *Biophysical Journal*, 97(3): 738–747, August 2009.

Xiao Ping Sun, Stephane Supplisson, and Emeran Mayer. Chloride channels in myocytes from rabbit colon are regulated by a pertussis toxin-sensitive G protein. *The American Journal of Physiology*, 264(4 Pt 1):G774–85, April 1993.

E H Synge. A suggested method for extending the microscopic resolution into the ultra-microscopic region. *Philosophical Magazine*, 6(35):356–362, August 1928.

E H Synge. An application of piezo-electricity to microscopy. *Philosophical Magazine*, 13(83):297–300, February 1932.

Bela Szabo, Michal J Urbanski, Tiziana Bisogno, Vincenzo Di Marzo, Aitziber Mendiguren, Wolfram U Baer, and Ilka Freiman. Depolarization-induced retrograde synaptic inhibition in the mouse cerebellar cortex is mediated by 2-arachidonoylglycerol. *Journal of Physiology*, 577(1):263–280, September 2006.

Yasufumi Takahashi, Yu Hirano, Tomoyuki Yasukawa, Hitoshi Shiku, Hiroshi Yamada, and Tomokazu Matsue. Topographic, Electrochemical, and Optical Images Captured Using Standing Approach Mode Scanning Electrochemical/Optical Microscopy . *Langmuir*, 22(25):10299–10306, December 2006.

Yasufumi Takahashi, Yumi Murakami, Kuniaki Nagamine, Hitoshi Shiku, Shigeo Aoyagi, Tomoyuki Yasukawa, Makoto Kanzaki, and Tomokazu Matsue. Topographic imaging of convoluted surface of live cells by scanning ion conductance microscopy in a standing approach mode. *Physical Chemistry Chemical Physics*, 12(34):10012, 2010.

E Clayton Teague, Fredric E Scire, Saul M Baker, and Stephen W Jensen. Three-dimensional stylus profilometry. *Wear*, 83:1–12, 1982.

Philip Thomas and Trevor G Smart. HEK293 cell line: a vehicle for the expression of recombinant proteins. *Journal of Pharmacological and Toxicological Methods*, 51(3):187–200, 2005.

R Toledo-Crow, P C Yang, Y Chen, and M Vaez-Iravani. Near-field differential scanning optical microscope with atomic force regulation. *Applied Physics Letters*, 60(24):2957–2959, June 1992.

G Tosello, H N Hansen, F Marinello, and S Gasparin. Replication and dimensional quality control of industrial nanoscale surfaces using calibrated AFM measurements and SEM image processing. *CIRP Annals - Manufacturing Technology*, 59(1):563–568, 2010.

Rafael Vázquez, F Javier Rubio-Sierra, and Robert W Stark. Transfer Function Analysis of a Surface Coupled Atomic Force Microscope Cantilever System. In *Proceedings of the American Control Conference*, pages 532–537, June 2006.

W N Venables and B D Ripley. *Modern Applied Statistics with S*. Springer, New York, Fourth edition, 2002. URL http://www.stats.ox.ac.uk/pub/MASS4. ISBN 0-387-95457-0.

P Vincent, Clay M Armstrong, and Alain Marty. Inhibitory synaptic currents in rat cerebellar Purkinje cells: modulation by postsynaptic depolarization. *Journal of Physiology*, 456:453–471, October 1992.

Lu-Yang Wang, Erwin Neher, and Holger Taschenberger. Synaptic Vesicles in Mature Calyx of Held Synapses Sense Higher Nanodomain Calcium Concentrations during Action Potential-Evoked Glutamate Release. *Journal of Neuroscience*, 28(53):14450–14458, December 2008.

H Kumar Wickramasinghe, editor. *AIP Conference Proceedings 241: Scanned Probe Microscopy*, New York, 1991. American Institute of Physics.

H Kumar Wickramasinghe. Scanning probe microscopy: Current status and future trends. *Journal of Vacuum Science and Technology A*, 8(1):363–368, January 1990.

H Kumar Wickramasinghe. Progress in scanning probe microscopy. *Acta Materialia*, 48(1):347–358, January 2000.

D L Worcester, R G Miller, and P J Bryant. Atomic force microscopy of purple membranes. *Journal of Microscopy*, 152(3):817–821, December 1988.

Hiroshi Yamada, Hikaru Fukumoto, Tetsuya Yokoyama, and Tohru Koike. Immobilized Diaphorase Surfaces Observed by Scanning Electrochemical Microscope with Shear Force Based TipSubstrate Positioning. *Analytical Chemistry*, 77(6):1785–1790, March 2005.

Liming Ying, Andreas Bruckbauer, Dejian Zhou, Julia Gorelik, Andrew I Shevchuk, Max J Lab, Yuri E Korchev, and David Klenerman. The scanned nanopipette: a new tool for high resolution bioimaging and controlled deposition of biomolecules. *Physical Chemistry Chemical Physics*, 7(15):2859–2866, August 2005.

Takayuki Yoshida, Kouichi Hashimoto, Andreas Zimmer, Takashi Maejima, Kenji Araishi, and Masanobu Kano. The cannabinoid CB1 receptor mediates retrograde signals for depolarization-induced suppression of inhibition in cerebellar Purkinje cells. *Journal of Neuroscience*, 22(5):1690–1697, March 2002.

Russell Young, John Ward, and Fredric Scire. The Topografiner: An Instrument for Measuring Surface Microtopography. *Review of Scientific Instruments*, 43(7):999–1011, July 1972.

M G Youngquist, R J Driscoll, T R Coley, W A Goddard, and J D Baldeschwieler. STM of DNA in UHV. In Wickramasinghe (1991), pages 154–158.

J A Zasadzinski, J Schneir, J Gurley, V Elings, and Paul K Hansma. Scanning tunneling microscopy of freeze-fracture replicas of biomembranes. *Science*, 239(4843):1013–1015, February 1988.

Yanjun Zhang, Julia Gorelik, Daniel Sanchez, Andrew I Shevchuk, Max J Lab, Igor Vodyanoy, David Klenerman, Christopher R W Edwards, and Yuri E Korchev. Scanning ion conductance microscopy reveals how a functional renal epithelial monolayer maintains its integrity. *Kidney international*, 68(3):1071–1077, September 2005.

Q Zhong, D Inniss, K Kjoller, and V B Elings. Fractured polymer/silica fiber surface studied by tapping mode atomic force microscopy. *Surface Science Letters*, 290(1-2):L688–L692, June 1993.

Robert S Zucker and Wade G Regehr. Short-term synaptic plasticity. *Annual Review of Physiology*, 64(1):355–405, March 2002.